# UNIVERSITÉ DE STRASBOURG

*ÉCOLE DOCTORALE physique et Chimie-Physique (ED182)*

**Institut de Physique et Chimie des Matériaux de Strasbourg.**

# THÈSE présentée par :


## Luis Enrique PARRA LOPEZ


soutenue le : **07 Juillet 2021**

pour obtenir le grade de : **Docteur de l'université de Strasbourg**

Discipline/ Spécialité : Nano-physique

# Tailoring the luminescence of atomically-thin semiconductors at the sub-nanometer scale.

**THÈSE dirigée par :**

| | |
|---|---|
| **M. BERCIAUD Stéphane** | Professeur, université de Strasbourg. |
| **M. SCHULL Guillaume** | Directeur de recherche, IPCMS-CNRS, université de Strasbourg. |

**RAPPORTEURS :**

| | |
|---|---|
| **M. BAUDIN Emmanuel** | Maître de conférence, LPENS. |
| **M. URBASZEK Bernhard** | Directeur de recherche, INSA-Toulouse. |

---

**AUTRES MEMBRES DU JURY :**

| | |
|---|---|
| **M. NOVOTNY LUKAS** | Professeur, ETH-Zurich. |
| **Mme. VIART Nathalie** | Professeur, Université de Strasbourg. |
| **M. SCHULER Bruno** | Chercheur, EMPA. |

# Remerciements

When I started my Bachelor's in physics in Venezuela, my aim was clear: I wanted to study cosmology and learn about string theory and all the theoretical physicist fuss. I wanted to investigate phenomena at the largest scale possible and I didn't see myself as an experimentalist. I even remember saying to my friends "I will never do optics", "I will never do experimental physics". At that time I wouldn't even imagine that I'd end up doing an experimental Ph.D. focused on nano-optics and that I would be happy to do so. It is thanks to the many people I encountered during my career that I discovered this marvelous field and I am really happy with my choice, and it is thanks to every single person that supported me and was there for me, that today I can say that I am a Doctor. There is nothing like a "self-made person" and I hope that in the following lines I can thank most of the people that contributed to making me who I am today.

First of all, I would like to thank Dr. Emmanuel Baudin and Dr. Bernhard Urbaszek, for accepting to examine and review my manuscript. I appreciate the time and effort they put into it. I would like to also extend my gratitude to the other members of the jury, who fostered an ambiance of scientific discussion with their interesting questions and remarks: Dr. Lukas Novotny, Dr. Nathalie Viart, Dr. Bruno Schuler, and Dr. Eric le Moal.

I would like to continue by thanking my supervisors Guillaume Schull and Stéphane Berciaud. Without them, I would have never enjoyed my Ph.D. and I couldn't have learned as much as I did. Their creativity, scientific spirit, kindness, and complementary qualities made my stay at the IPCMS a joy. I can not be more thankful to have had such amazing supervisors both in scientific as well as in human terms, and I am glad to have you as friends. I want to thank you for your patience, your encouragement, and your support even in hard times for me. You made me feel welcomed and as a part of a big family and I'll always be thankful for that.

It goes without a say that two people were essential for succeeding in my Ph.D.: Michael Chong and Etienne Lorchat. Etienne trained me in the art of making samples the alsatian way. You taught me not to get discouraged from passing several days in a cleanroom trying to get a good sample. Beyond that, you were always helpful in the lab and always ready for a scientific discussion. Your determination and hard work are admirable and I hope you have nothing but success in your future! It was a pleasure meeting you. An STM can be a terrifying machine when one knows nothing. Luckily for me, Michael was there to help. He was the person I interacted with the most during my master internship and helped me look for single-photon sources (which sadly we never found...yet). I enjoyed a lot our experiments together and I can't thank you enough for

all the nice conversations, jokes, and random things we listened to or discussed during the experiments. You became a really good friend and I feel lucky to have met you and worked with you.

I would also like to thank all of the members of the "2D-team" I had the pleasure to interact with. Loic "El Presidente", you have incredible intuition and you are clearly in love with science (and "hunting lions"). I wish you nothing but success and may you continue "liquifying excitons" and playing your nano-drums. I would also like to thank Leo Colombier who not only was a great colleague but also like an older brother. With the passing of the years, we have become good friends and I wish you good luck with your amazing family. I want to thank Aditya Singh, despite arriving at a difficult experiment and at the beginning of the first confinement, you were always keeping a good mood. It was a pleasure to stay late in the lab fighting lasers with you. Finally, I would like to thank the newest members of our team: Arnaud Gloppe who joined as a permanent and two new Ph.D. students, Joanna and Aditi. I hope you do great science! I wish you nothing but the best.

Getting through my Ph.D. required more than scientific support, and I have many people to thank for listening and supporting me throughout my thesis. Among them, there is a person who has become one of my best friends: Benjamin Doppagne or "Ben Ben". Ben, I am deeply grateful to have met you, you are an incredibly intelligent and kind person and my stay in France was definitely better thanks to you. You are among the persons I appreciate the most and I hope you have a great future by continuing teaching newer generations and hopefully inspiring new future scientists. From our discussions at the cafeteria, at the office, and in the lab, to our trips to "café des langues" and the Netherlands. Spending time with you was always a great experience. You were always there during my Ph.D. and always ready to help. Even when I was panicking because the tip holder "spontaneously" fell and bend inside the vacuum chamber. Thanks a lot for these years and I hope we continue our friendship well beyond.

As the years passed by, new group members arrived on the "STM-side" and I couldn't be happier to have met them. First, there is Anna, who joined as a postdoc in the middle of my Ph.D. I am glad to have met you Anna, your intelligence, knowledge, kindness, and eagerness to help really made the days of "looking in the dark" much better. From playing with lasers while listening to great hits of the 90s to discussing science, it is always a pleasure to pass time with you. Thank you for an amazing friendship. A bit later, the younger member of our group arrived: Kirill. Kirill, you are an amazing person and you are always ready to help. I enjoyed all the laughs in the office while "training birds", all of our discussions regarding "diplomacy", all the memes, and of course the chess. Even on the most discouraging days, you'll pass by the lab and make the time less discouraging. I hope you have a great future. Thank you. Finally, by the end of my Ph.D., I had the pleasure to meet Tomas Neuman. We immediately got along. Thank you for forcing me

to explore Alsace, to make energy diagrams, and for your humor and kindness. You were someone that I could always count on. I hope the future holds only good things for you and may you not cross tape while you bike again. I would also like to thank "les limots". Laurent Limot, Benjamin Verlhac ("Big ben"), Nicolas Bachelier, Leo Garnier ("Yeso") and Alex Fetida for the great laughs that we had over the years. I would like to end this paragraph by thanking Shuiyan and Song for their great mood and I hope that in whatever you do in the future, you keep that positive energy.

Among the many people I interacted with during my Ph.D., I would like to express my sincere gratitude to Fabrice Scheurer, Virginie Speisser, and Michelangelo Romeo. Thank you for all of the help over the years, you really are the backbone of the group and a big part of why it feels not like a group but like a big family. I would also like to thank the ST-Nano cleanroom members: Sabine Siegwald, Romain Bernard, and Hicham Majjad for all the technical support during my Ph.D.

My work was also possible thanks to different collaborations. First, I want to thank our collaborators at LCPNO in INSA Toulouse: Cédric Robert, Délphine Lagarde, and Xavier Marie for their measurements on time-resolved photoluminescence. Second, I want to thank our collaborators at University of La Sapienza in Rome: Tullio Scopigno, Carino Ferrante, and of course, Giorgio di Batista with whom I had the pleasure to work with. You are an amazing person and you will achieve great things in science. I also want to thank our collaborators at ISMO in Paris: Eric le Moal, Délphine Pommier, and Remi Bretel for the STM measurements performed at room temperature. Finally, I would like to thank Kenji Watanabe and Takashi Taniguchi for providing us with high-quality hexagonal Boron Nitride.

During my university years, I had the pleasure to meet great professors whose kindness and motivation help me remember why I wanted to study physics. I want to thank in particular Thierry Charitat and Guillaume Weick. I have already told you, but you are amazing professors and persons. I am lucky to have been your student. I would also like to thank two professors that were extremely important for my formation back in Venezuela: Celso Ladera and Rita Gianvitorrio. Muchísimas gracias profesores, su paciencia, didáctica, pasión por la ciencia y cálidad humana han sido una gran motivación para estudiar física.

También quiero agradecer a mis amigos de "por allá". Muchas gracias Mauricio Gomez y Gustavo Kufatty, es un placer tenerlos como amigos y recuerdo con mucha añoranza nuestras discusiones en COF y en clases de mécanica cuántica. Me acuerdo cuando creamos nuestros "libro de preguntas difíciles" y todo lo que he aprendido gracias a ustedes durante todos estos años. En especial, quisiera agradecer a Mauricio, quien ha estado conmigo desde que llegamos a Francia y siempre dispuesto a ayudar. Estoy seguro que el futuro les depara mucho éxito. Quisiera también agradecer a mis hermanos de corazón, ustedes han estado conmigo desde siempre y me han apoyado en todo. Muchas gracias

Lore, Eduardo y Juan por su amistad y por los buenos momentos compartidos, ya sea en la punta, en tepe, como en linea. Siempre estaré agradecido por su amistad y por todo el apoyo que me han dado con el pasar de los años. Finalmente a mi otra "hermana", Vero, espero que podamos vernos en el futuro y que logres cumplir todas tus metas. Luego estan mis amigos de "por acá". Mati, eres una persona de un talento innato y de una amabilidad increíble. Ha sido un placer pasar estos años contigo tanto como colega como amigo. Te deseo lo mejor para tu futuro. Camilo, o mejor dicho "So", estudiar contigo fue un placer, muchas gracias por las risas y las discusiones tanto científicas como absurdas. Espero que continuemos esta amistad y que logres todos tus objetivos. I would also like to thank Sebastien Ferry, Alain Ferry and Valerie Quieti for a great friendship since I came to Strasbourg. There are many other people that I would like to thank and it is all the friends I have meet throughout the years: Ines Rachid and Daniel Ajoy whom I met during my first years in Strasbourg and which I appreciate immensely. Then there is Caroline, Saurabh, Anais, Frenni, Niklas, Morgado, Christoph Breitenstein, Sigrid Korf-Breitenstein, among many others who made my stay here much better.

Finalmente, quisiera agradecer a mi familia que durante toda mi vida han estado detrás de mí apoyandome, a mis abuelos, a mis primos y a mis tios. En especial quiero agradecer a mi Mamá que desde niño puso mi educación como prioridad. Incluso en los momentos dificiles, me llevaba a pasear por librerias, para que pudiera leer libros de ciencia que de otra manera no podriamos comprar. Muchas gracias por apoyarme en todas las decisiones, incluso cuando todo parecia que no iba a funcionar. Sin tí no hubiera podido llegar donde estoy. Otra persona a quien estaré eternamente agradecido es Jaime Casas. Muchísimas gracias Jaime por todo el apoyo durante estos años. Estaré siempre agradecido y espero que sepas que cuentas conmigo también. Muchas gracias por apoyarnos y por ayudarme a llegar donde estoy. También quisiera agradecer a mi tía Sandra (QEPD) quien desde pequeño me apoyó para perseguir mis pasiones. Recuerdo ir a la casa de la música con ella cuando era un niño. Sin duda una persona que admiro y que extraño, muchas gracias tía. Por último quiero agradecer a mi hermana Laura, durante todos estos años tu siempre estuviste conmigo. Mucho exito hermana en todo lo que te propongas. Gracias.

At last, I want to thank a person whom I shared my life with and that I am incredibly lucky to have: Julia Breitenstein. Thank you for making my life better, thank you for always being there. I can't thank you enough for all of the support and for being my rock. Without you, I couldn't have gotten where I am now.

Direction de la **recherche**
et de la **valorisation**
Collège **doctoral**
Université de Strasbourg

# Déclaration sur l'honneur
# *Declaration of Honour*

J'affirme être informé que le plagiat est une faute grave susceptible de mener à des sanctions administratives et disciplinaires pouvant aller jusqu'au renvoi de l'Université de Strasbourg et passible de poursuites devant les tribunaux de la République Française.

Je suis conscient(e) que l'absence de citation claire et transparente d'une source empruntée à un tiers (texte, idée, raisonnement ou autre création) est constitutive de plagiat.

Au vu de ce qui précède, **j'atteste sur l'honneur que le travail décrit dans mon manuscrit de thèse est un travail original et que je n'ai pas eu recours au plagiat ou à toute autre forme de fraude.**

*I affirm that I am aware that plagiarism is a serious misconduct that may lead to administrative and disciplinary sanctions up to dismissal from the University of Strasbourg and liable to prosecution in the courts of the French Republic.*

*I am aware that the absence of a clear and transparent citation of a source borrowed from a third party (text, idea, reasoning or other creation) is constitutive of plagiarism.*

*In view of the foregoing,* ***I hereby certify that the work described in my thesis manuscript is original work and that I have not resorted to plagiarism or any other form of fraud.***

**Nom :** Parra Lopez

**Prénom :** Luis Enrique

**Ecole doctorale :** ED-182

**Laboratoire :** IPCMS

**Date :** 09/10/2021

# Contents

Chapter 0

# Resumé

## 0.1 Introduction

Les matériaux 2D sont des cristaux lamellaires liés de manière covalente et maintenus ensemble par des interactions de van-der-Waals. Depuis la première isolation du graphène en utilisant l'exfoliation mécanique [1], une toute nouvelle panoplie de matériaux 2D a été découverte. Ces couches atomiquement fines présentent un large éventail de propriétés allant des métaux bidimensionels comme le graphène, aux semi-conducteurs comme les dichalcogénures de métaux de transition (TMD) et aux isolants comme le nitrure de bore hexagonal (hBN). Cet ensemble de propriétés uniques, combiné à leur finesse atomique, fait des materiaux 2D des systèmes intéressants tant pour la recherche fondamentale que pour les applications. En outre, leur minceur atomique les rend également très sensibles à leur environnement local.

Une autre propriété remarquable des matériaux 2D est l'absence de liaisons pendantes sur leurs surfaces. Cela nous permet de les empiler facilement et de former de nouveaux matériaux artificiels appelés **hétérostructures de van-der-Waals (vdW)**. Historiquement, la première hétérostructure de vdW consistait en un empilement d'une couche de graphène sur une terrasse de hBN [2]. Le caractère inerte du hBN, ainsi que ses terrasses atomiquement plates, ont fourni un substrat idéal pour le graphène, ce qui a permis d'améliorer ses propriétés conductrices. Cela a marqué le début de " l'ère de van-der-Waals ", où une nouvelle génération d'hétérostructures a été créée, présentant des différentes propriétés émergentes [3]. Par exemple, la supraconductivité a été démontrée dans des hétérostructures composées de deux ou trois couches de graphène empilées les unes sur les autres et décalées en rotation [4, 5].

Ces phénomènes émergents sont une conséquence du couplage intercouche inhérent à ces empilements. En effet, la nature atomiquement fine de ses composants et la séparation sous-nanométrique entre les couches font des hétérostructures de vdW des plateformes idéales pour étudier les interactions de champ proche. En allant plus loin, nous voudrions exploiter ces effets de proximité pour créer de nouveaux matériaux aux propriétés accordables. Ceci est particulièrement prometteur dans le cas des hétérostructures constituées de dichalcogénures de métaux de transition (TMD) semi-conducteurs, dont les propriétés optiques uniques en font des briques idéales pour les dispositifs optoélectroniques.

Cependant, les défauts, les adsorbats et le désordre diélectrique peuvent jouer un rôle important dans la photophysique des hétérostructures de vdW à base des TMD. En effet, les propriétés optiques des TMD sont définies par des excitons fortement liés avec un rayon de Bohr de l'ordre de $\sim$ 1 nm. Ceci signifie que la dynamique sous-jacente peut être fortement modifiée par des inhomogénéités à l'échelle du nanomètre. Un exemple intéressant est le piégeage des excitons dans les motifs de Moiré résultant de l'orientation relative entre différents matériaux 2D. Il a été démontré que ces excitons piégés se comportent comme des sources de photons uniques dans les TMDs [6, 7]. Par conséquent, afin d'étudier les propriétés intrinsèques des matériaux 2D et des hétérostructures vdW, il est nécessaire de disposer de sondes sensibles capables de caractériser les propriétés photophysiques des TMD, avec une résolution à l'échelle du nanometre à la fois *dans le plan* et *hors du plan*.

L'objectif de cette thèse est de **accorder les propriétés des matériaux bidimensionnels à l'échelle sous-nanométrique**. Cela implique de développer des stratégies qui nous permettent d'accéder au couplage entre differentes couches et d'étudier l'effet des inhomogénéités sur les propriétés optiques des hétérostructures de vdW. Comme nous le verrons tout au long de ce manuscrit, un système idéal pour mener à bien ces études est celui d'une monocouche de TMD empilée sur une couche du graphène. En effet, les propriétés optiques de cette hétérostructure sont définies par des mécanismes de transfert d'énergie efficaces se produisant à l'interface [8, 9, 10]. Par exemple, à température ambiante, le rendement d'émission du TMD est massivement réduit à proximité du graphène. De plus, en raison du décalage de réseau entre les couches et du manque de contrôle sur l'alignement rotationnel entre les réseaux, des motifs de Moiré peuvent apparaître, induisant une modulation locale du potentiel de surface. Ces motifs, combinés aux défauts et aux contaminants créés lors du processus de fabrication de l'échantillon, constituent un environnement riche pour étudier la dynamique excitonique. Au cours de nos recherches, nous allons traiter les questions suivantes :

- Quelle est la nature du mécanisme de couplage intercouche entre les TMD et le graphène ?
- Quel est l'effet de ce couplage sur la luminescence des TMD ?
- Dans quelle mesure existe-t-il un transfert de charge entre differentes couches d'une heterostructure de vdW?
- Pouvons-nous exploiter ce couplage pour accorder la luminescence des TMD ?
- Quel est l'effet des défauts et des adsorbats sur la luminescence des TMD ?
- Peut-on étudier l'effet des motifs de moiré sur l'émission excitonique ?

Pour réaliser ces études, nous utiliserons des spectroscopies optiques afin de caractériser de manière approfondie le couplage entre les couches dans l'hétérostructure TMD/graphène. Par exemple, en utilisant la spectroscopie de photoluminescence spatialement et temporellement résolue, nous pouvons sonder directement la dynamique excitonique. Cette technique consiste en la photogénération d'excitons, et nous permet d'obtenir des informations sur les échelles de temps dans lesquelles le transfert d'énergie se produit. Nous complementerons ces études en utilisant également la diffusion inélastique de la lumière. C'est ce qu'on appelle la spectroscopie Raman, qui nous fournit des informations sur la structure, les contraintes et les tendances de dopage du matériau.

Cependant, ces techniques ne nous permettent pas d'étudier l'effet de l'environnement nanoscopique *dans le plan*. De telles investigations requièrent une résolution qui ne peut pas être atteinte avec des techniques limitées par la diffraction. C'est pourquoi nous avons utilisé une approche unique impliquant la résolution ultime fournie par un microscope à effet tunnel (STM) travaillant à basse température et dans des conditions d'ultravide pour exciter et sonder la luminescence de l'hétérostructure. Dans ces conditions, nous pouvons atteindre une résolution spatiale supérieure de 3 ordres de grandeur à celle des spectroscopies optiques. Cette technique est connue sous le nom de luminescence induite par le STM (STML).

Expérimentalement, cela nécessite que les échantillons étudiés soient compatibles avec les mesures STM. De plus, le champ électromagnétique à l'intérieur d'une jonction STM est loin d'être trivial, et certains processus peuvent entraver l'émission intrinsèque. Par exemple, en raison de la présence du substrat métallique, les voies de recombinaison non radiatives deviennent efficaces. Cette question a déjà été explorée dans le contexte des molécules uniques, où différentes stratégies de découplage ont dû être développées afin d'observer la luminescence intrinsèque : [11, 12]. Pour les monocouches de TMDs, l'état de l'art pointe vers un compromis entre résolution et émission intrinsèque. En effet, la luminescence intrinsèque induite par STM (STM-L) des TMDs a été observée uniquement à température ambiante et à l'air [13, 14, 15]. Dans ces conditions, il n'est pas possible d'obtenir la résolution requise pour nos expériences. En revanche, à basse température et sous ultravide (UHV), il est possible d'obtenir facilement des informations avec résolution atomique. Cependant, la luminescence observée dans ces expériences est d'origine extrinsèque [16, 17]. Par conséquent, la première question à laquelle notre expérience devrait s'attaquer est liée à la faisabilité de l'émission intrinsèque des TMD tout en préservant la résolution atomique.

Ce projet a débuté en 2017 sous la forme d'une collaboration entre l'équipe de Stéphane Berciaud, focalisée sur les propriétés des matériaux 2D, et l'équipe de Guillaume Schull, focalisée sur la luminescence induite par STM. L'idée était de combiner l'expertise des deux équipes pour étudier l'origine des sources de photons uniques (qui reste à ce jour inconnue) dans les TMD monocouches en utilisant la STM-L. Notre point de départ était

un article publié par Krane *et al.* [16] dans lequel une tentative d'obtention de STM-L intrinsèque d'une monocouche de TMD a été faite. Dans cet article, la luminescence observée était d'origine extrinsèque, suggérant que la proximité de l'électrode métallique nécessaire pour effectuer une mesure STM éteignait fortement la luminescence du TMD. Cela nous a motivés à concevoir des architectures qui pourraient contourner ces limitations tout en préservant les propriétés des TMDs. Cependant, cela s'est avéré être un défi puisque dans toutes nos expériences, aucune STM-L provenante des TMDs n'a pu être observée. Enfin, dans une collaboration avec l'équipe d'Eric le Moal à Paris, le STML de monocouches de TMD a été observé à température ambiante et à l'air [13]. Pour éviter le couplage avec les électrodes, ils ont utilisé un substrat non plasmonique. La principale limitation restait cependant l'obtention simultanée d'une résolution atomique, ce qui n'est pas possible dans ces conditions. À ce stade de mon doctorat, nous avions étudié la photophysique de l'hétérostructure du TMD/graphène de manière approfondie. La suite logique était d'étudier cette hétérostructure à l'échelle atomique avec le STM. L'espoir était que le graphène (1LG) agisse comme une couche de découplage tout en fournissant un substrat atomiquement plat pour le TMD. De plus, la séparation relativement petite entre le TMD et le substrat métallique nous permettrait de bénéficier d'une amélioration du champ EM fourni par la jonction STM (voir chapitre 2). Dans ces conditions, nous avons rapporté la STM-L intrinsèque de semi-conducteurs atomiquement fins avec une résolution atomique pour la première fois. Ce faisant, nous avons mis les bases de futures recherches sur les mécanismes de champ proche qui affectent la dynamique excitonique dans les hétérostructures de vdW.

Cette thèse est divisée en 5 chapitres. Dans le chapitre 1, je présente une brève introduction des principales propriétés des matériaux 2D. Dans le chapitre 2, j'explique en détail les techniques expérimentales utilisées au cours de ma thèse. Dans le chapitre 3, je présente nos résultats concernant les propriétés optiques des hétérostructures TMD/1LG et je montre que l'on peut exploiter le couplage entre les couches pour obtenir des spectres d'émission du TMD caracterisés par une raie unique et étroite. Dans le chapitre 4, je présente nos résultats concernant la luminescence induite par STM des hétérostructures TMD/1LG à des températures cryogéniques. Enfin, dans le chapitre 5, je conclus la thèse et donne une perspective. Dans la suite, je vais resumer les points le plus importantes des chapitres 3 et 4.

## 0.2 Chapitre 3: Accordement de la luminescence des monocouches de TMDs avec graphene

Dans ce chapitre, nous présentons les résultats des études spectroscopiques des hétérostructures composées par une monocouche de TMD empilée sur une monocouche du graphene.

Nous discuterons les mécanismes de couplage en champ proche et l'étendue de leurs effets sur les propriétés optiques de l'hétérostructure. Ensuite nous aborderons le filtrage du PL à basse température ainsi que un aperçu microscopique de la dynamique excitonique à basse température. Les résultats présentés dans ce chapitre ont donné lieu à deux publications sur lesquelles j'étais co-auteur [9] et premier auteur [10].

### 0.2.1 Mécanismes de couplage

Grâce à leur nature atomiquement fine et aux distances sous-nanométriques entre les couches, les hétérostructures de VdW sont sensibles aux phénomènes qui se produisent à l'interface entre les couches. Ces phénomènes peuvent dominer les propriétés optiques et électroniques de l'hétérostructure. Leur compréhension est de la plus haute importance car ils peuvent nous fournir des informations précieuses sur les processus de champ proche à l'interface. Un exemple central de cette interaction est celui des TMD monocouches empilées sur une couche de graphène. Ces hétérostructures sont connues pour présenter une réduction massive de 2 ordres de grandeur du signal de luminescence à température ambiante. Cette réduction est une conséquence directe des mécanismes de couplage de champ proche caractéristiques des hétérostructures TMD/graphene.

Cette réduction suggère que le mécanisme de couplage ouvre des voies de recombinaison non-radiative vers le graphène qui réduisent la durée de vie excitonique dans le TMD. Le mécanisme exact par lequel cette recombinaison se produit reste débattu. Une discussion détaillée des possibles mécanismes se produisant à l'interface entre le TMD et le graphène peut être trouvée à la section 3.2. Pour l'instant, nous pouvons les résumer comme suit :

**Transfert de charge:**

Comme son nom l'indique, cela se produit lorsque les porteurs de charge du TMD (ou du graphène) sont transférés vers le graphène (TMD). Ce processus doit respecter la conservation de l'énergie et de la quantité de mouvement et entraîne à la fois une réduction de la luminescence et un dopage des couches. Notez que cela peut se produire "dans l'obscurité" (transfert de charge statique) ou sous illumination (transfert de charge photoinduit). Les deux processus ont été rapportés dans des hétérostructures TMD/graphène. Cependant, le transfert de charge photoinduit a été exclu comme candidat pour expliquer le facteur d'extinction à temperature ambiante, car il se produit dans des échelles de temps plus longues que les meilleures estimations pour l'échelle de temps du transfert d'énergie.

**Transfert d'energie:**

Ce mécanisme se produit lorsqu'au lieu qu'une charge se transfère physiquement d'une couche à l'autre, l'exciton entier transfère son énergie à un état excitonique dans la deux-

ième couche. Ce type de transfert d'énergie est médié par l'interaction de Coulomb. Si le transfert se produit par l'interaction dipôle-dipôle, il est appelé transfert d'énergie de Förster (FRET) et s'il se produit par l'effet tunnel des charges, il est connu sous le nom de transfert d'énergie de Dexter (DET). Remarquez que le DET ressemble à un mécanisme de transfert de charge, mais dans le cas du DET, il n'y a pas de transfert net de charge.

#### État de séparation des charges à courte durée de vie

Récemment, un nouveau mécanisme a été proposé [18]. Il s'agit d'un processus photoinduit qui se produit lorsque les électrons et les trous ont des probabilités differentes de transfert vers le graphene. Par conséquent, il existe un état transitoire dans lequel les porteurs photoexcités se trouvent effectivement dans des couches différentes. Dans cet état, le TMD et le graphène sont tous deux chargés. Ce processus a été observé dans les hétérostructures $WS_2$/graphène dans des régimes de densité excitonique élevée. Notez que ceci est un processus de transfert de charge, cependant, puisqu'il se produit typiquement sur de courtes échelles de temps ($\sim$ 1 ps) l'état final est équivalent à un processus de transfert d'énergie.

### 0.2.2 Filtrage de la luminescence des TMDs avec graphene

Comme mentionné précédemment, le couplage entre les couches adjacentes peut modifier radicalement les propriétés optiques des hétérostructures vdW. En effet, leur luminescence sera largement définie par la compétition entre la recombinaison radiative et les processus de transfert d'énergie et de charge tels que le FRET, le DET ou les états séparés de charge à courte durée de vie. Cette compétition peut entraîner une extinction importante du signal de photoluminescence, comme on peut le constater à température ambiante (voir 3.1). Cependant, une étude détaillée de la dynamique excitonique dans ces conditions peut être complexe car d'autres processus non radiatifs ne peuvent être négligés. Par conséquent, cela nous motive à étudier l'hétérostructure à des températures cryogéniques où la durée de vie excitonique est réduite à quelques ps [19] et déterminée uniquement par la recombinaison radiative (voir section 1.5.2). Cela présente une situation intéressante, car dans ces conditions, la recombinaison radiative se produit dans la même échelle de temps que le transfert d'énergie vers le graphène et cela aura des conséquences fondamentales dans les spectres de PL à basse température des TMDs.

#### Phenomenologie

La figure 1 montre des spectres de PL typiques de monocouches de $MoSe_2$, $WSe_2$, $MoS_2$ et $WS_2$ encapsulées par hBN (panneau supérieur) et des heterostructures TMD/1LG encapsulées par hBN des mêmes TMDs (panneau inférieur). Tous les spectres ont été normalisés et les facteurs d'échelle entre le pic correspondant à la recombinaison radiative de l'exciton

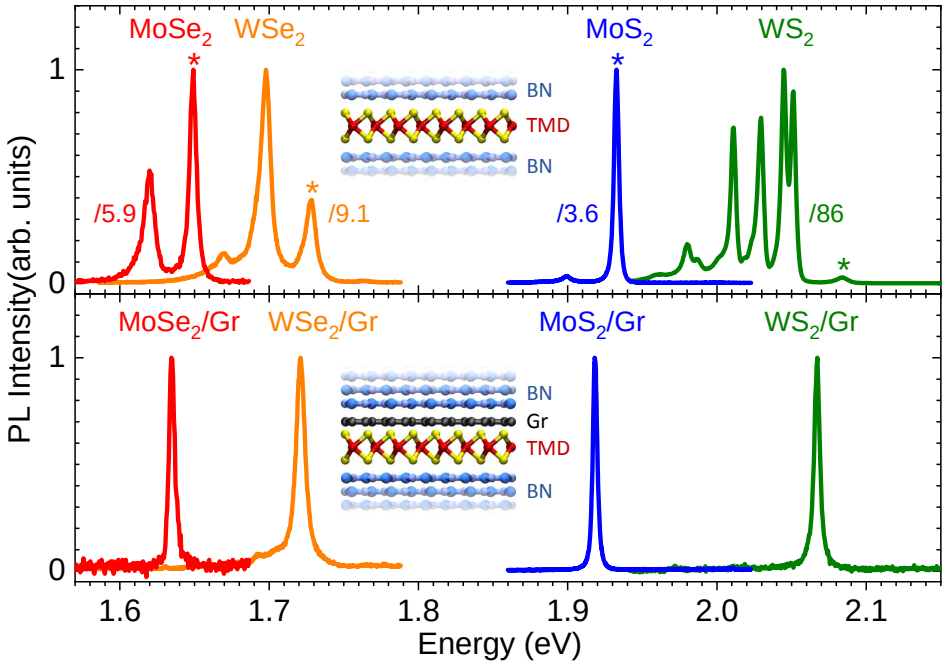


Figure 1: **Filtrage de la luminescence des TMD à 15 K.** En haut : spectres PL de $MoSe_2$, $WSe_2$, $MoS_2$ et $WS_2$ encapsulés par hBN. En bas : Spectre PL de $MoSe_2$/1LG, $WSe_2$/1LG, $MoS_2$/1LG et $WS_2$/1LG encapsulés par hBN. Les spectres sont normalisés par rapport au maximum d'émission et le facteur d'échelle entre la contrepartie TMD et TMD/1LG est indiqué dans le panneau supérieur pour chaque spectre. La résonance correspondant à $X^0$ est marquée d'un astérisque. Tous les spectres ont été enregistrés à 15 K sous excitation laser cw à 2,33 eV ($MoSe_2$, $WS_2$, $MoS_2$) et 1,96 eV ($WSe_2$).

neutre (marquée d'un astérisque), et le pic unique dans les spectres des heterostructures TMD/1LG sont indiqués à côté de chaque spectre dans le panneau supérieur. Dans le cas du TMD "seul", les spectres sont composés de deux ou plusieurs pics provenants de la recombinaison radiative de différentes particules excitoniques. Comme prévu, les TMDs dits "bright" ($MoSe_2$, $MoS_2$) présentent des spectres composés de deux pics que nous attribuons à l'exciton neutre $X^0$ et au trion $X^*$ situé à plus basse énergie. Les TMDs dits "dark" ($WSe_2$ et $WS_2$), d'autre part, présentent les mêmes deux pics ainsi qu'une multitude d'autres résonances de plus basse énergie provenant d'autres espèces excitoniques telles que les excitons sombres, les biexcitons, les excitons localisés, entre autres (voir section 1.7 pour plus des détails).

Dans le panneau inférieur, les spectres sont étonnamment différents. Au lieu d'un grand nombre de pics, nous observons des lignes d'émission uniques et étroites pour tous les TMD couplés au graphène. Ceci est frappant car même les spectres complexes tels que ceux de $WSe_2$ et $WS_2$ ne présentent pas ces contributions de basse énergie. Néanmoins, nos observations restent qualitativement les mêmes pour toutes les hétérostructures TMD/1LG : spectres d'émission à ligne unique et à ligne étroite. De plus, pour toutes les hétérostructures TMD/1LG, les raies simples apparaissent décalées d'environ 10 meV

vers le rouge par rapport à la raie $X^0$ dans le spectre du TMD seul. De plus, ces lignes présentent des profils lorentziens avec des largeurs de l'ordre de $\sim 5$ meV, ce qui suggère une réduction du déphasage dans l'heterostructure. L'énergie et la largeur de ces pics sont obtenues par un ajustement lorentzien et sont reportées dans le tableau 1.

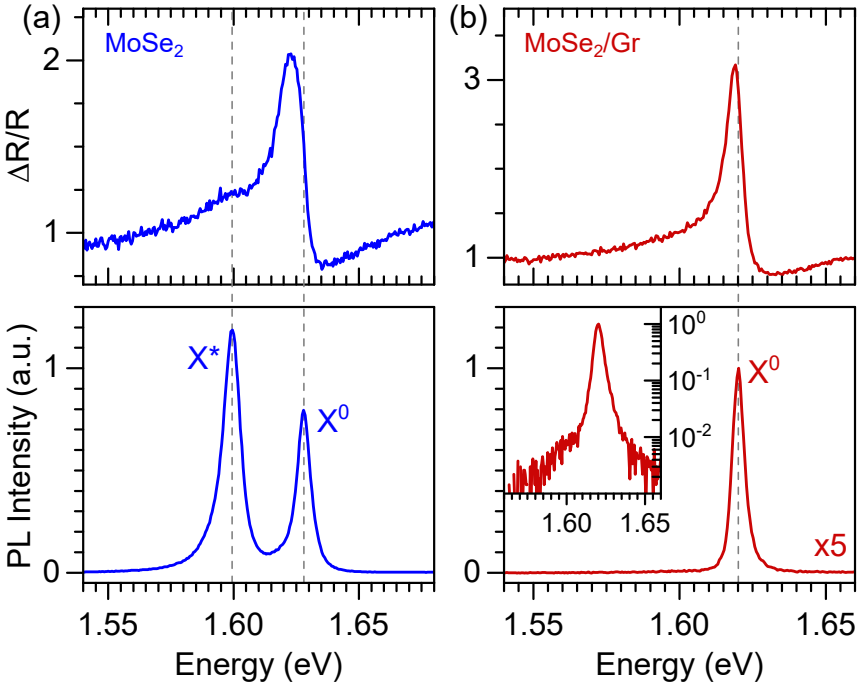


Figure 2: **Identification de $X^0$.** Spectres de DR (en haut) et PL (en bas) de $MoSe_2$ (a) et de $MoSe_2$/1LG (b) encapsulés par hBN. Les spectres ont été acquis à une température de 4 K, dans le régime d'excitation linéaire et en utilisant une laser continuu avec une energie de 2,33 eV.

Afin d'identifier l'origine de cette émission à ligne unique, nous avons mesuré les spectres de photoluminescnece (PL) et de reflectance differentielle (DR) d'un échantillon. Pour des raisons de simplicité, nous nous sommes concentrés sur le cas du $MoSe_2$. Les figures 2a et b montrent les spectres DR (en haut) et PL (en bas) des zones de $MoSe_2$ et $MoSe_2$/1LG encapsulées par hBN. Comme avant, les spectres du TMD seul présentent deux résonances associées à $X^0$ et $X^*$ (marquées par les lignes pointillées grises). En revanche, nous n'observons qu'une seule résonance intense dans le TMD/1LG à la fois en DR et en PL. Cela suggère que la résonance dans le spectre de TMD/1LG pourrait provenir d'un $X^0$ écranté. En effet, le décalage vers le rouge pourrait être compris en termes d'écrantage diélectrique dû à la présence de graphène [20]. Afin de prouver notre hypothèse selon laquelle le caractère monoligne du spectre TMD/1LG provient de la recombinaison radiative du $X^0$, nous avons étudié la PL en fonction de la température (T). La figure 3 montre l'énergie d'émission de cet échantillon en fonction de la température. Nous pouvons voir que l'émission provenant du TMD/1LG est systématiquement située entre les lignes $X^0$ et $X^*$ du spectre du TMD seul. Par conséquent, nous pouvons attribuer sans risque la ligne d'émission unique dans l'hétérostructure à la recombinaison de $X^0$.

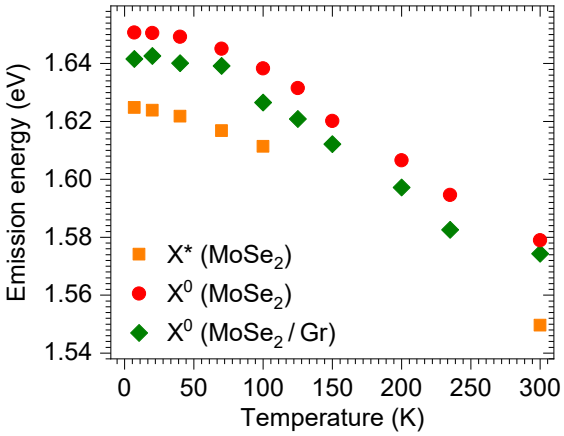


Figure 3: **Étude de la PL en fonction de la température sur un échantillon de $MoSe_2$/1LG encapsulée par hBN.** Énergie d'emission des lignes correspondantes à l'exciton ($X^0$) et le trion ($X^*$) du $MoSe_2$ en fonction de la température. Toutes les données ont été enregistrées dans le régime linéaire en utilisant un laser continuu à 2,33 eV.

Maintenant que nous avons identifié l'origine de la raie unique, nous pouvons nous concentrer sur les facteurs d'extinction. Pour ce faire, nous allons definir deux facteurs d'extinction différents qui seront utiles pour comprendre nos mesures. Tout d'abord, définissons le facteur d'extinction des excitons $Q_{X^0}$ en termes des intensités intégrées provenat des $X^0$ dans $MoSe_2$ ($I_{X^0}$) et $MoSe_2$/1LG ($I'_{X^0}$) tel que :

$$Q_{X^0} = \frac{I_{X^0}}{I'_{X^0}}$$

En connaisant cette valeur, nous pouvons obtenir des informations concernant le transfert d'énergie de la population des excitons froids vers le graphène. Les valeurs de $Q_{X^0}$ trouvées dans les échantillons de la figure 1 sont présentées dans le tableau 1. Nous observons des facteurs d'extinction modérés proches d'un ordre de grandeur. Cette réduction par rapport aux facteurs d'extinction observés à température ambiante n'est pas surprenante. Elle est une conséquence directe du raccourcissement de la durée de vie radiative à basse température.

Le deuxième facteur d'extinction qui sera utile est le facteur d'extinction total $Q_{\text{tot}}$. Cette valeur met en relation l'intensité totale intégrée dans les spectres du TMD seul avec l'intensité intégrée provenant de la recombinaison de l'exciton dans TMD/1LG de telle sorte que :

$$Q_{\text{tot}} = \frac{I_{\text{tot}}}{I'_{X^0}}$$

$Q_{\text{tot}}$ nous donne des informations sur la dynamique de la population excitonique chaude créée quelques instants après l'excitation (figure 3.17). Dans le TMD, les excitons chauds peuvent subir une relaxation entraînant la formation de différentes espèces excitoniques. En revanche, dans la TMD/1LG, les excitons chauds ne peuvent former que

des excitons neutres. Les $Q_{\text{tot}}$ calculés pour les échantillons de la figure 1 sont présentés dans le tableau 1. Comme nous pouvons le voir, ces valeurs sont plus grandes que $Q_{X^0}$, ce qui suggère une voie de désintégration non radiative supplémentaire impliquant le transfert des excitons chauds vers le graphène.

| | $E_{\text{X}^0}$ (eV) | $\Gamma_{\text{X}^0}$ (meV) | $Q_{\text{X}^0}$ | $Q_{\text{tot}}$ |
|---|---|---|---|---|
| $MoS_2$ | 1.933 | 4.0 | 3.9 | 4.3 |
| $MoS_2$/1LG | 1.918 | 3.5 | | |
| $MoSe_2$ | 1.649 | 5.6 | 7.1 | 13.6 |
| $MoSe_2$/1LG | 1.635 | 4.4 | | |
| $WS_2$ | 2.084 | 9.7 | 3.0 | 227 |
| $WS_2$/1LG | 2.067 | 4.3 | | |
| $WSe_2$ | 1.728 | 8.7 | 3.7 | 21 |
| $WSe_2$/1LG | 1.721 | 7.2 | | |

Table 1: **Valeurs caractéristiques d'emission des échantillons présentés dans la figure 1** Énergie d'émission maximale ($E_{\text{X}^0}$), largeur totale à mi-hauteur ($\Gamma_{\text{X}^0}$) correspondantes à la ligne d'émission $X^0$ pour les spectres de PL des quatre échantillons encapsulées par hBN présentés sur la figure 1. Les données ont été extraites à travers des ajustements lorentziens dans le cas de $MoSe_2$/graphene et d'un ajustement avec une fonction de Voigt pour le $MoSe_2$ seul.

### Neutralisation du TMD

Au cours du processus de fabrication d'une hétérostructure de van der Waals, une redistribution des charges peut se produire lors du contact entre les couches. En conséquence, le dopage natif de chacune des couches change. Cela peut avoir un impact sur les espèces excitoniques chargées telles que le trion. En effet, à faible flux incident, les trions se forment lorsque les excitons interagissent avec les dopants natifs. Par conséquent, l'absence du $X^*$ dans le spectre d'emission du TMD/1LG pourrait indiquer une réduction du dopage due à une redistribution de charges entre les couches. Pour étayer cette hypothèse, nous devons exclure les autres scénarios qui pourraient expliquer ce comportement. Au total, il existe trois scénarios qui pourraient expliquer l'absence de trions (figures 1 et 2) dans l'hétérostructure :

1. **Le TMD est dopé et le graphène empeche l'émission de trions.**

   Dans ce scénario, le transfert d'énergie vers le graphène est plus efficace que la recombinaison radiative du $X^*$. Cependant, nos observations (figure 2) nous permettent de mettre une borne inférieure pour le facteur d'extinction égal à $Q_{X^*} = \frac{I_{X^*}}{I'_{X^*}} \sim 10^2 - 10^3$. Cela implique une réduction de la durée de vie du trion à 100

fs tandis que le $X^0$ conserve une durée de vie de l'ordre de la ps. Cette valeur est extrêmement courte pour de telles quasi-particules. Ceci est confirmé par l'absence de la résonance $X^*$ dans le spectre de DR, ce qui suggère que les trions ne sont pas formés efficacement. Ces observations nous permettent d'exclure sans risque ce scénario.

2. **Le TMD est dopé et le graphène empeche la formation de trions.**

   Dans ce scénario, les excitons chauds sont transférés au graphène avant de pouvoir former des trions. En effet, dans les TMD, l'excitation non résonante entraîne la création d'une population excitonique hors équilibre. Cette population se relaxe rapidement vers les bords de la bande et se retrouve en dehors du cône de lumière [21]. Ensuite, ces excitons dits " chauds " se relaxent à nouveau vers le cône de lumière par émission de phonons, ce qui entraîne la formation d'excitons et de trions. Cependant, on sait que les $X^0$ et les $X^*$ se forment dans la même échelle de temps [19]. Cela signifie que nous devrions observer un facteur d'extinction similaire pour les deux espèces, ce qui n'est clairement pas compatible avec nos résultats. Par conséquent, nous pouvons exclure sans risque le scénario 2 également.

3. **Le TMD est neutralisé par le graphène.**

   La seule possibilité restante et la plus susceptible d'être correcte est la troisième. Ici, le graphène agit comme un réservoir d'électrons et de trous et neutralise complètement le TMD par transfert de charge statique. Ce transfert de charge se produit sans photoexcitation et augmente légèrement l'énergie de Fermi du graphène. Nous nous attendons à ce que cet effet de neutralisation se produise pour toutes les TMD, indépendamment de leur nature "bright" ou "dark".

#### Filtrage des espèces excitoniques à longue durée de vie

Enfin, dans le cas des quasi-particules qui ne sont pas chargées, leur absence peut être comprise en termes de dynamique excitonique dans l'hétérostructure. En effet, toutes les espèces excitoniques susmentionnées ont des durées de vie caractéristiques de l'ordre de 100 ps. Ces durées de vie sont beaucoup plus longues que le transfert d'énergie vers le graphène [19, 22, 23, 24]. En conséquence, la voie de désintégration de ces espèces est principalement non radiative.

### 0.2.3 Dynamique excitonique à basse temperature dans TMD/1LG

Nous allons maintenant étudier en détail la dynamique excitonique dans l'hétérostructure. Pour ce faire, nous avons effectué des mesures de PL résolue en temps (TRPL) au LCPNO Toulouse en collaboration avec Cédric Robert, Delphine Lagarde et Xavier Marie. Les

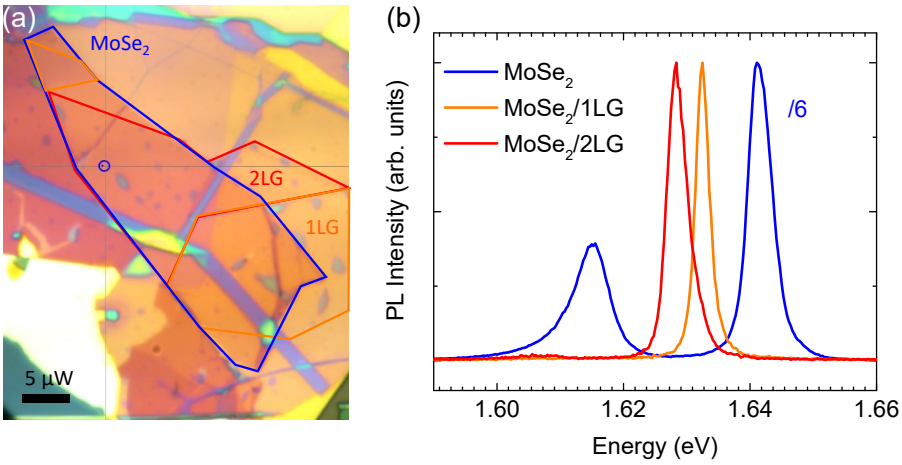


Figure 4: **Spectre the PL à basse température de $MoSe_2$/1LG encapsulée par hBN et déposé sur $SiO_2$**(a) Image de microscopie optique d'un échantillon composé par trois zones: $MoSe_2$, $MoSe_2$/1LG et $MoSe_2$/2LG encapsulées par hBN. (b) spectres de PL correspondants aux trois zones principales de l'hétérostructure. Les spectres ont été enregistrés à 14 K, en utilisant une excitation laser à 1,96 eV continue et sous une intensité proche de 100 $\mu$W/$\mu$m$^2$.

échelles de temps de ces phénomènes nécessitent une installation avec une résolution temporelle plus élevée que celle que nous pouvons atteindre dans notre setup. Pour réaliser ces mesures, ils ont utilisé une camera "streak" dont le principe de fonctionnement est décrit dans la section 2.3.4. Pour faciliter l'analyse, nous utiliserons un modèle simple consistant en un système à trois niveaux composé d'un niveau des excitons chauds ($X^h$) correspondant à la population d'excitons en dehors du cône de lumière, d'un niveau d'excitons froids ($X^0$) correspondant aux excitons qui peuvent se recombiner radiativement et d'un état fondamental. Ce modèle est expliqué en detail dans la section 3.4.1.

La figure 4 montre une image optique (a) et trois spectres de PL (b) d'un échantillon presentant 3 zones caracteristiques: Une monocouche de $MoSe_2$, une heterostructure $MoSe_2$/1LG et une heterostructure $MoSe_2$/2LG. Tous les zones ont été entierement encapsulées par hBN. Cet échantillon a été concu de sorte que le temps de recombinaision radiative ($\tau_{X^0}^{\text{rad}}$) soit aussi long que possible. Ceci peut être fait en choisissant de manière appropriée l'épaisseur du hBN inférieur dans les échantillons supportés par $SiO_2$. En effet, le taux de décroissance radiative peut être accordé par un effet de type Purcell au moyen d'une cavité optique définie par la géométrie hBN/$SiO_2$/Si. Ensuite, en choisissant l'épaisseur du hBN inférieur, nous pouvons contrôler les modes du champ electromagnétique dans la cavité [25] (voir section 1.5.2). L'échantillon a été fabriqué avec une terrase hBN inférieur de 110 nm d'épaisseur afin de maximiser la durée de vie radiative excitonique comme indiqué dans la référence [25].

Dans la zone correspondante à $MoSe_2$ seul, nous observons deux pics situées à $1,642 \pm 0,001$ eV et $1,615 \pm 0,003$ eV correspondants à $X^0$ et $X^*$ respectivement. Nous confir-

mons le couplage entre le TMD et les couches de graphène puisque nous retrouvons l'effet de filtrage attendu à la fois dans la zone de $MoSe_2$/1LG et dans la zone du $MoSe_2$/2LG. La résonance $X^0$ est située à $1,633 \pm 0,1$ eV pour la première et à $1,628 \pm 0,1$ eV pour la seconde. Les spectres de TRPL correspondant à l'émission de l'exciton neutre dans chaque zone sont présentés sur la figure 5. Tous les spectres ont été enregistrés à 14 K et avec un laser d'énergie 1,72 eV qui est inférieure à l'état $X^0_{2s}$. Ceci est fait pour éviter une modification de la dynamique excitonique du à la presence des états excitonique à plus haut energie. Dans le TMD seul, montré sur la figure 5a, nous observons un temps de montée de $11 \pm 8$ ps et un temps de descente similaire. Nous attribuons ces valeurs au temps de relaxation vers le cône de lumière ($\tau_{\text{rel}}$), et le temps de vie du $X^0$ ($\tau_{X^0}$). La grande incertitude que nous observons est due à la similitude de $\tau_{\text{rel}}$ et $\tau_{X^0}$ (voir équation (3.5)). Par conséquent, l'ajustement devient difficile et il existe de multiples combinaisons de paramètres qui peuvent fonctionner aussi bien. Nous constatons que le meilleur ajustement se produit lorsque les deux temps sont égaux à 11 ps. En revanche, pour $MoSe_2$/1LG et $MoSe_2$/2LG, nous observons des temps de montée et de descente beaucoup plus faibles. Comme l'effet de la cavité est de modifier la recombinaison radiative, nous ne nous attendons pas à un changement de la dynamique de formation. En d'autres termes, nous associons le temps de montée au temps de relaxation modifié dans le graphène, et le temps de décroissance au temps de vie de $X^0$ dans l'heterostructure ($\tau'_{X^0}$). Toutes ces valeurs sont reportées dans le tableau 2. Quantitativement, nous avons mesuré $\tau'_{rel} < 1$ ps, ce qui est inférieur à la résolution que nous pouvons atteindre, et $\tau'_{X^0} = 2.3 \pm 0.2$ ps dans $MoSe_2$/1LG. De façon remarquable, nous avons mesuré une durée de vie légèrement plus courte : $\tau'_{X^0} = 1.75 \pm 0.1$ ps dans $MoSe_2$/2LG. À titre de référence, les spectres PL pris aux mêmes endroits que les mesures TRPL sont présentés sur la figure 5d. Tous les spectres sont normalisés à l'intensité de la ligne $X^0$ et le facteur d'échelle entre les spectres est indiqué en bleu. Nous notons le même facteur d'échelle pour $MoSe_2$/1LG et MoSe2/2LG. Concentrons-nous d'abord sur la réduction du temps de relaxation. A partir de notre modèle de système à trois niveaux, nous pouvons estimer une limite pour le temps de transfert des excitons chauds de $\tau^h_G < 1$ ps. Cependant, cette valeur doit être prise avec précaution car nous sommes trop proches de la résolution de notre montage et donc le temps de montée mesuré est discutable. Ce qui ressort clairement de cette mesure est que le transfert de $X^h$ est un mécanisme très efficace qui domine entièrement la dynamique des excitons chauds. Nous avons effectué des mesures similaires sur l'échantillon de $MoSe_2$ montré dans la figure 1. Cet échantillon n'est pas optimisé pour maximiser $\tau_{X^0}$ et pourtant presente des temps caracteristiques plus courts. Ces mesures sont également présentées dans le tableau 2.

Avant de poursuivre la discussion, il est important de souligner que l'attribution des temps de montée et de descente dans le cas de $MoSe_2$/1LG et $MoSe_2$/2LG pourrait être remise en question. En effet, dans les TMD seuls, il n'y a pas de tels problèmes puisqu'on

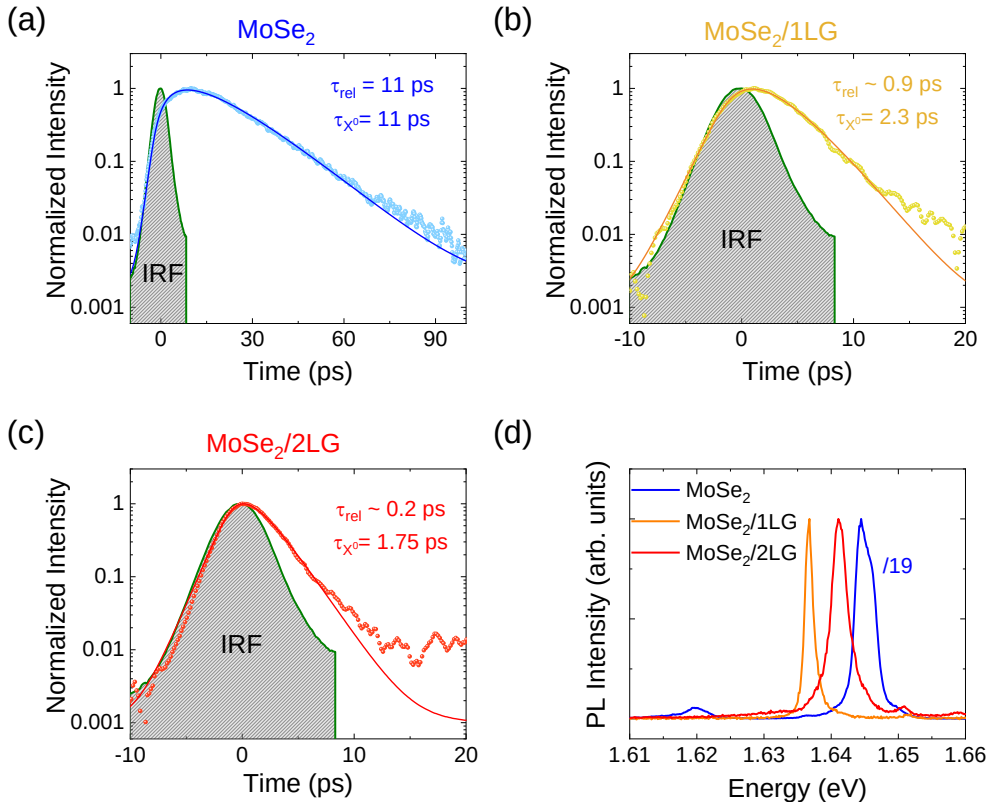


Figure 5: **Dynamique excitonique à basse température.** TRPL de l'émission de l'exciton neutre dans la zone de $MoSe_2$ (a) $MoSe_2$/1LG (b) and $MoSe_2$/2LG (c). (d) Spectres de PL correspondatns aux zones du $MoSe_2$, $MoSe_2$/1LG and $MoSe_2$/2LG. Tous les spectres ont été enregistrés à 14K et avec un laser pulsé à 722 nm dans le régime linéaire.

peut toujours comparer ces temps avec le temps de montée du $X^*$ et à partir de là identifier $\tau_{X^0}$. Dans les hétérostructures, aucun $X^*$ n'est formé et cette comparaison ne peut donc pas être faite. Cela signifie qu'a priori nous pourrions être dans une situation où le temps de montée dans la figure 5 correspond à $\tau_{X^0}$ et le temps de descente à $\tau_{rel}$. De plus, nous ne sommes pas en mesure de résoudre complètement le temps de montée car nous sommes limités par la résolution de notre installation. Il est donc nécessaire d'effectuer des mesures supplémentaires dans le domaine fs afin d'obtenir des informations sur cette échelle de temps.

Concentrons-nous maintenant sur les durées de vie excitoniques. La réduction de $11 \pm 8$ ps dans la TMD seul à $\sim 2$ ps dans l'hétérostructure, indique que la dynamique est dominée par le transfert d'énergie du TMD au graphène. Ceci est cohérent avec le facteur d'extinction plus élevé observé dans la PL par rapport à l'échantillon de $MoSe_2$ étudié dans la figure 1. En effet, nous mesurons $Q_{X^0}^{\mathrm{1LG}} = 19 \pm 7$ et $Q_{X^0}^{\mathrm{2LG}} = 15 \pm 4$ pour $MoSe_2$/1LG et $MoSe_2$/2LG respectivement. De même, nous avons mesuré $Q_{\mathrm{tot}}^{\mathrm{1LG}} = 37 \pm 12$ et $Q_{\mathrm{tot}}^{\mathrm{2LG}} = 28 \pm 9$. Finalement, avec ces valeurs, nous pouvons maintenant procéder

à l'estimation du temps de transfert d'energie vers le graphène. Pour ce faire, nous devons estimer $\tau_{X^0}^{\mathrm{rad}}$ dans l'hétérostructure en exploitant la relation entre la durée de vie de recombinaison radiative et l'énergie de liaison (Voir section 3.3.9) :

$$\frac{\tau_{X^0}^{rad}}{\tau_0^{rad}} \propto \left(\frac{E_b}{E_b'}\right)^2 \tag{1}$$

Où $\tau_0^{rad}$ correspond au temps de recombinaison radiative des excitons dans la zone du TMD seul, $\tau_{X^0}^{rad}$ est le temps de recombinaison radiative des excitons dans la zone TMD/1LG et $E_b$ et $E_b'$ sont les énergies de liaison respectives. L'estimation des énergies de liaison est expliquée en détail dans la section 3.3.9. À partir de cette expression nous pouvons déduire un temps de recombinaison radiative modifié dû au graphène de:

$$\tau_{X^0}^{\mathrm{rad}} \approx 26 \text{ ps}$$

Grâce à ces résultats, nous pouvons donner une estimation conservatrice des temps caratéristiques du transfert d'énergie égale à $\tau_{1LG} \approx 2.5$ ps et $\tau_{2LG} \approx 1.9$ ps pour la mono- et la bicouche de graphène respectivement. Ce résultat suggère que le transfert vers le 2LG est plus efficace que vers le 1LG. Nous avons répété le même calcul pour l'échantillon de la figure 1 et obtenu des valeurs similaires, bien qu'un peu plus grandes (voir tableau 2).

| | Substrat | $\tau_{X^0}$ (ps) | $\tau_{\mathrm{rel}}$ (ps) | $\tau_{X^0}^{\mathrm{rad}}$ (ps) | $\tau_{\mathrm{G}}$ (ps) |
|---|---|---|---|---|---|
| $hBN/MoSe_2$ | hBN$^\star$ | 11 | 11 | 11 | – |
| $hBN/MoSe_2$/1LG | | 2.3 | $< 1$ | 26 | 2.5 |
| $hBN/MoSe_2$/2LG | | 1.75 | $< 1$ | 26 | 1.9 |
| $hBN/MoSe_2$/hBN | Quartz | 2.4 | 5.1 | 2.4 | – |
| $hBN/MoSe_2$/1LG/hBN | | 2.2 | $\leq 1.5$ | 5.7 | 3.6 |

Table 2: Paramètres de la TRPL extraits des figures 3.18 et 5 et temps de transfert estimés.

Maintenant que nous connaissons le temps de transfert, nous pouvons estimer le rendement quantique attendu et le comparer au facteur d'extinction que nous observons pour les deux échantillons. L'estimation de ces facteurs est expliquée en détail dans la section 3.4.5 et les résultats sont résumés dans le tableau 3.

Nous observons des rendements allant de 6% dans l'échantillon déposé sur $SiO_2$ jusqu'à 50% dans l'échantillon supporté par le quartz. Ce contraste n'est pas une surprise puisque le premier a été conçu pour être affecté au maximum par le transfert d'énergie vers le graphène et donc afficher de faibles rendements d'émission. Il est intéressant de noter que dans les deux cas, il y a une désaccord entre $\eta_{X^0}$ et $Q_{X^0}$. Nous observons des facteurs

| | Substrat | $\eta_{X^0}$ | $Q_{X^0}$ | $Q_{\text{tot}}$ |
|---|---|---|---|---|
| hBN/$MoSe_2$/1LG | hBN$^\star$ | 8 % | 19 | 37 |
| $MoSe_2$/2LG | hBN$^\star$ | 6 % | 15 | 28 |
| hBN/$MoSe_2$/1LG/hBN | Quartz | 50 % | 7.1 | 20 |

Table 3: Rendements estimés pour l'échantillon de $MoSe_2$/1LG encapsulé par hBN et déposé sur du hBN et sur du quartz. Le symbole "étoile" indique que le substrat est composé d'une terrasse de hBN inférieur de 110 nm d'épaisseur, déposé sur un substrat de $SiO_2$/Si.

de quenching compatibles avec des rendements beaucoup plus faibles. Nous concluons qu'une partie significative du quenching provient du transfert d'énergie de la population d'exciton chaud vers le graphène, qui affecte la formation d'excitons (voir section 3.4.6).

## 0.3 Chapitre 4: Luminescence induite par STM de semi-conducteurs atomiquement fins.

Dans le chapitre précédent, nous avons vu que l'on peut accorder la luminescence des TMD en exploitant leur interaction avec une couche de graphène. En consequence, l'émission de ces hétérostructures est caractérisé par l'emission provenante de l'exciton neutre. Cet effet de filtrage dépend de manière sensible du "gap de van der Waals" sous-nanométrique qui sépare les couches et donc nous permet de contrôler la luminescence avec précision atomique *hors du plan*. Cependant, l'excitation est par nature limitée par la diffraction et pourtant limite les investigations avec une résolution atomique *dans le plan*. Par exemple, nous ne pouvons pas étudier l'impact des inhomogénéités locales telles que les défauts ou les adsorbats sur la luminescence excitonique à l'échelle nanométrique. En outre, certaines de ces inhomogénéités sont des candidats pour des sources de photons uniques (SPS) dans les TMD. On peut également s'interroger sur l'impact sur la dynamique des excitons des motifs moirés émergents dans les hétérostructures. Pour aller plus loin, il pourrait être intéressant de modifier le substrat ou même d'utiliser des adsorbats nanoscopiques tels que des clusters métalliques pour améliorer la luminescence d'un matériau. Pour surmonter les limitations liées aux techniques limitées par la diffraction, nous pouvons utiliser un STM à la fois comme une sonde et un moyen d'excitation. En effet, la luminescence induite par le STM (dite STML) permet de sonder les propriétés optiques d'un materiau avec la résolution fournie par le STM. Bien que quelques travaux fondamentaux aient rapporté des données STML sur des monocouches de TMD (voir section 4.2), les propriétés excitoniques des hétérostructures de VdW restent à explorer dans des expériences combinant de hautes résolutions spectrales (sub meV) et spatiales (sub-atomiques). Dans ce

chapitre, je présenterai nos résultats concernant la première observation de luminescence intrinsèque d'hétérostructures vdW dans une jonction STM à basse temperature et sous ultra-vide.

### 0.3.1 STM-L des differents TMDs

Au cours des 5 dernières années, différentes tentatives ont été faites pour obtenir des STML à partir de TMD. Ces approches visent le même objectif : l'étude de la luminescence intrinsèque des TMDs avec une résolution atomique. Les observations principales de ces études peuvent être résumées de la facon suivante: les techniques in-vaccuo réalisées à basse température fournissent des interfaces propres sur lesquelles la résolution atomique peut être facilement obtenue. Cependant, cette même interface propre semble entraîner l'extinction de l'émission intrinsèque du TMD. En revanche, les techniques ex-situ réalisées à température ambiante semblent bénéficier des contaminants (par exemple, l'eau) qui agissent comme des couches de découplage, et par conséquent, la luminescence provenant des excitons peut être observée à température ambiante. En outre, les approches à température ambiante bénéficient de l'utilisation d'optiques avec ouverture numérique plus importants que celles à basse temperature. Ceci augmente considérablement l'efficacité de la collection de lumière. Cependant, aucune résolution atomique n'est observée, et les paramètres requis pour exciter les couches peuvent entraîner la destruction partielle du TMD.

Par conséquent, pour étudier les propriétés excitoniques des hétérostructures de VdW avec de hautes résolutions spectrales (sub meV) et spatiales (sub-atomiques) simultanément, il faudrait une stratégie compatible avec les mesures à basse température et qui découple suffisamment la monocouche pour pouvoir observer de la luminescence intrinsèque.

#### Commentaire sur les mécanismes d'émission

Dans les expériences réalisées par Pommier (section 4.2.2) et Peña (section 4.2.3), différents mécanismes d'excitation ont été envisagés. Dans la première, le transfert d'énergie des électrons par effet tunnel vers les TMDs a entraîné la formation des excitons. Dans le second, l'injection de charges dans la bande de conduction était le coupable. L'attribution de la luminescence des TMD à un mécanisme donné est basée sur les paramètres expérimentaux nécessaires pour générer l'émission. Chacun de ces mécanismes requiert un ensemble différent de conditions que nous pouvons utiliser pour les identifier. Par exemple, le transfert d'énergie nécessite que la polarisation appliquée $V_0$ soit au moins aussi grande que la bande interdite optique ($E_{X^0}$) du TMD. En d'autres termes:

$$e|V_0| \geq E_{X^0} \tag{2}$$

Remarquez que cette condition est vraie pour les deux polarités. D'autre part, l'injection de charge nécessite au moins un alignement entre le niveau de Fermi d'une électrode et la bande de conduction ou de valence du TMD. Par conséquent, un lien direct entre la luminescence et les spectres dI/dV est attendu. De plus, le seuil de luminescence dans un mécanisme d'injection de charge devrait dépendre de la polarité de la polarisation appliquée.

### 0.3.2 L'échantillon

Toutes les expériences de ce chapitre ont été réalisées sur un échantillon constitué d'une monocouche de $MoSe_2$ empilé sur plusieurs couches ($< 4$ couches) de graphene ( FLG) en utilisant la méthode de transfert à sec (Pour plus de détails, voir le chapitre 2). Cette hétérostructure a ensuite été déposée sur un film de Au(111) déposé sur mica produit par Phasis Sàrl. Une image optique de l'échantillon et un schéma sont présentés dans les figures 6a et 6b. Dans cette configuration, les couches de graphène peuvent agir comme un élément de découplage, empêchant l'extinction de l'émission du TMD par le substrat d'or tout en fournissant simultanément une interface plate. Parallèlement, la courte distance entre le TMD et l'or ( 1 nm pour $MoSe_2$ supporté par 3LG) peut préserver une partie de l'amélioration plasmonique fournie par le substrat. Après le depôt de l'échantillon sur l'or, il est rapidement introduit dans la chambre de préparation du STM (voir chapitre 2) et recuit pendant une journée entière à 200°C et sous ultravide.

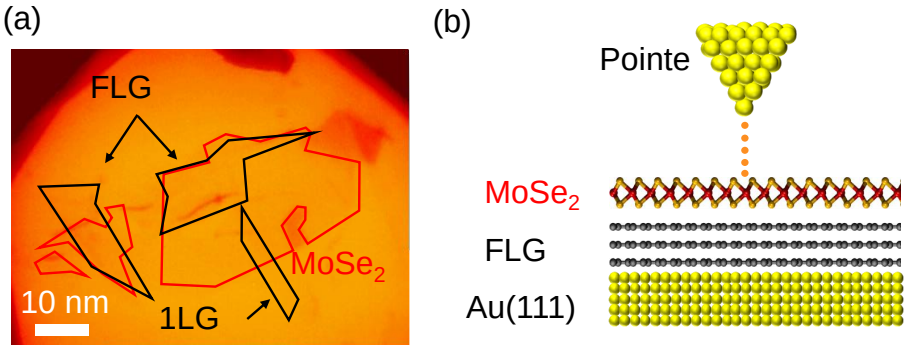


Figure 6: **Échantillon de $MoSe_2$/FLG/Au (111).** (a) Image optique d'un échantillon composé par une monocouche de $MoSe_2$ sur graphene multicouche (FLG) déposé sur un film de Au(111). (b) Schéma de l'échantillon dans la jonction STM.

#### Morphologie de la surface

La figure 7a montre une image STM à courant constant enregistrée à 6 K sur la surface du $MoSe_2$/FLG. En général, nous observons des zones plates de taille $\sim 20 \times 20$ nm$^2$ entourées de plis et de bulles. Ces structures résultent de l'adaptation de l'hétérostructure à la surface de Au(111) sous-jacente et de la présence de résidus issus du processus de

fabrication. Les figures b et c montrent des exemples d'images STM avec résolution atomique enregistrées sur deux des zones plates de l'échantillon. Dans les deux cas, nous mesurons un paramètre de maille de $3.3 \pm 0.2$ Å, ce qui correspond à la constante de maille du $MoSe_2$. La principale différence entre ces zones est l'apparition d'un motif moiré dans (c), résultant des orientations relatives entre la couche du TMD et le graphène. Remarquez que dans l'image présentée dans 7b, la résolution atomique peut être obtenue mais sans signature du motif moiré. Cela suggère un couplage plus fort entre le TMD et le FLG dans la région moirée (figure 7c) que dans celles où le moiré est absent. Nous avons mis en évidence le réseau primitif du motif moiré et déterminé qu'il est cohérent avec un angle relatif de $\sim 5$ °. Un modèle de ce motif est représenté sur la figure 7d. Nous avons superposé deux réseaux hexagonaux correspondants au $MoSe_2$ et au FLG. Au voisinage de la plupart des bulles, les conditions d'imagerie deviennent instables. Dans certaines de ces régions, nous observons une faible sensibilité du courant tunnel à la distance entre l'échantillon et la pointe. Par exemple, des variations d'un ordre de grandeur du courant ont été observées pour des variations de distance de l'ordre de 1 nm. Cela suggère des effets électrostatiques où la couche est poussée ou tirée par la pointe STM. Dans ces zones, le risque d'écraser la pointe dans le substrat est élevé.

### 0.3.3 STM-L de $MoSe_2$/1LG

La figure 4.7a montre un spectre STML obtenu sur une zone plane de taille $10 \times 10$ nm$^2$ sur la surface de $MoSe_2$/FLG (figure 4.7b). Le spectre est composé de deux résonances nettes séparées par 30 meV. Nous avons ajusté ces lignes en utilisant des profils de Voigt et obtenu $E_1 = 1.659$ eV$\pm 1$ meV et $\Gamma_1 = 11 \pm 1$ meV pour le premier pic, et $E_2 = 1.630$ eV$\pm 1$ meV et $\Gamma_2 = 14 \pm 1$ meV pour le second. Une comparaison avec les mesures PL sur le même échantillon nous permet d'attribuer ces pics à $X^0$ et $X^*$, respectivement. Pour toutes nos mesures, nous estimons un rendement quantique de $\sim 10^{-8}$ photons/e$^-$ en supposant une efficacité de détection de $\sim 15\%$ (voir section 2.5.7). En outre, un courant relativement faible ($< 100$ pA) a dû être utilisé afin de préserver l'intégrité de la couche de TMD. La faible efficacité de cette émission, ainsi que la nécessité d'utiliser des courants d'excitation modérés pourraient expliquer en partie la difficulté d'observer la luminescence intrinsèque des TMD lors des tentatives précédentes. La faiblesse de cette émission souligne également la nécessité de disposer d'une configuration permettant l'alignement précis in-situ de la lentille par rapport à la zone d'échantillon sondée (section 2.5.7).

Il est intéressant de noter que le spectre STML est lisse et ne présente pas de résonances multiples, contrairement à son homologue en PL. C'est une conséquence directe de la nature locale de l'excitation. En effet, on n'est pas sensible au moyennage spatial qui est au cœur des mesures optiques. Cependant, il y a toujours des signatures d'élargissement inhomogène dans les pics. En effet, même si nous observons des largeurs beaucoup plus

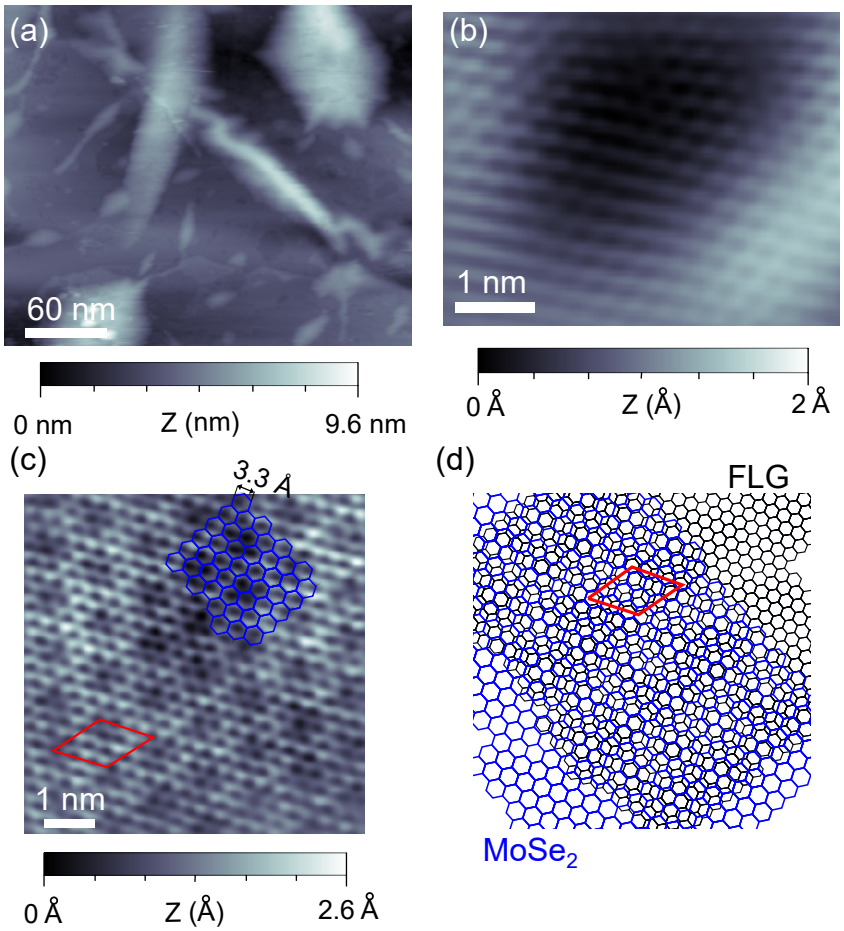


Figure 7: **Morphologie de la surface.** (a)Image STM enregistrée à courant constant de la surface $MoSe_2$/FLG. L'hétérostructure s'adapte au substrat situé en dessous, ce qui entraîne des bulles et des ondulations. Les paramètres d'acquisition de cette image sont -2.2 V et 4 pA. Images STM enregistrées avec résolution atomique sur des zones planes (b) et (c). Un paramètre de maille de 3.3 Å est mesuré en accord avec le paramètre attendu pour $MoSe_2$. Un motif moiré résultant de l'orientation relative entre le TMD et le graphène peut être observé en (c), suggérant une meilleure qualité de l'interface TMD/1LG qu'en (b). (d) Modèle du motif moiré. La cellule primitive de ce motif est indiquée en rouge. Les paramètres d'acquisition des images étaient -1.3 V, 10 pA pour l'image (b) et -1.4 V, 6 pA pour l'image (c).

fines que celles obtenues en PL, ces valeurs sont encore loin de la largeur homogène attendue pour $MoSe_2$/1LG ($\sim$ 300 $\mu$eV). Au contraire, la qualité de l'interface entre l'hétérostructure et l'Au(111) contribue probablement à l'élargissement du pic. De plus, la présence de plasmons peut également jouer un rôle dans le raccourcissement des durées de vie excitonique par l'effet Purcell.

La figure 4.7c montre un spectre de conductance différentielle pris dans la même zone. À partir de ce spectre, nous avons déterminé une valeur pour la bande interdite de transport de $2.2 \pm 0,1$ eV dans toute la région échantillonnée (cette valeur ne varie pas en fonction de la position de la pointe par rapport au motif moiré). Cette valeur coincide à ce qui a été rapporté dans des systèmes similaires [26]. De plus, la proximité entre le niveau

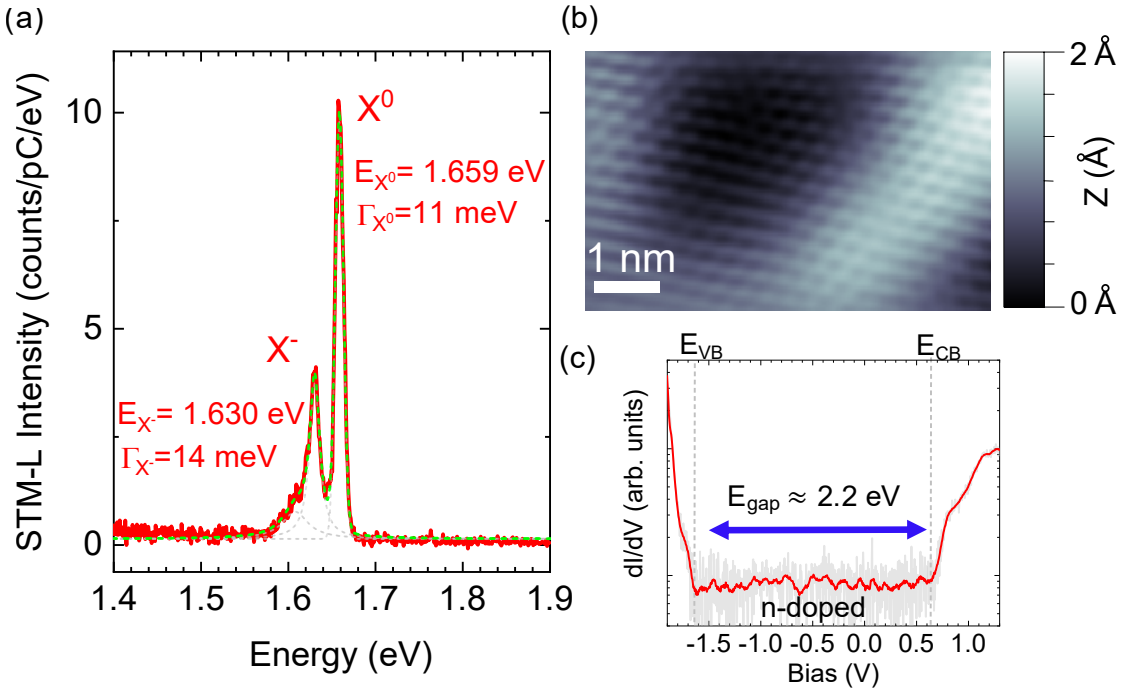


Figure 8: **Premier spectre STML de $MoSe_2$.**(a) Spectre de STML correspondant à l'hétérostructure $MoSe_2$/FLG/Au(111) (en rouge). Les paramètres d'acquisition sont -2.8 V et 90 pA. Chaque pic est ajusté avec des profils de Voigt (en gris pointillé), l'ajustement cumulatif est représenté par une ligne verte pointillée. Les paramètres extraits de chaque ajustement sont indiqués à côté de la résonance correspondante. (b) Image STM avec résolution atomique de la zone sur laquelle le spectre a été enregistré. Cette image a été acquise sous une tension de -1.3 V et à un courant de 10 pA.(c) Spectre de conductance différentielle pris sur la région explorée. Le spectre est représenté sur une échelle logarithmique afin de faciliter la détermination de l'apparition de la bande. Les données brutes sont représentées en gris. Pour plus de clarté, nous avons lissé ces données, et le résultat est montré en rouge. À partir de ce spectre, nous avons déterminé une bande interdite électronique de 2,2 eV.

de Fermi et la bande de conduction indique que la couche de $MoSe_2$ est dopée n. Ceci n'est pas surprenant puisque les couches de $MoSe_2$ exfoliées sont censées porter un dopage n résiduel [27, 28, 29]. Cette mesure, ainsi que le spectre STML, nous permet de tirer deux conclusions. Premièrement, la résonance du trion provient probablement d'un trion chargé négativement ($X^-$). Nous pouvons exclure sans risque les trions " induits par le courant " puisque le courant employé lors de cette acquisition (90 pA) correspond au passage moyen d'un électron toutes les 2 ns. Ceci est bien supérieur à la durée de vie caractéristique des excitons et des trions dans le $MoSe_2$ et le $MoSe_2$/1LG, dont nous avons vu qu'elle est de $\sim$ 2 ps (Voir la section 3.4). Deuxièmement, nous pouvons estimer l'énergie de liaison locale des excitons en soustrayant simplement la bande interdite électronique de la bande interdite optique obtenue à travers le STML. Nous estimons une différence moyenne entre la bande interdite STS et la bande interdite optique de $\sim$ 540 meV. Remarquez qu'il s'agit du premier exemple où l'énergie de liaison peut être déduite de mesures électroniques et

photoniques simultanées à résolution atomique, évitant tout effet de moyenne d'ensemble.

Cette valeur se situe dans les limites des énergies de liaison rapportées pour des systèmes similaires, estimées à partir de la comparaison entre les mesures STS et PL à grande échelle (voir tableau 4.2). Cependant, elle dépasse largement les énergies de liaison déduites des mesures purement optiques (voir chapitre 3). Cela invite à une réinterprétation sur ce qu'on mésure à travers la STS. Une discussion sur ce point peut être trouvée dans les chapitres 2 et 4. Nous tenons à souligner que ce résultat reste la première observation de l'émission intrinsèque des TMDs avec une résolution atomique.

**Homogeneité de l'emission: dependance spatiale**

Afin d'explorer l'effet de l'environnement local et d'assurer la reproductibilité de nos mesures, nous avons acquis plusieurs spectres à différents endroits de l'échantillon. En particulier, nous nous sommes concentrés sur trois régions plates dans l'hétérostrucuture avec une taille caractéristique de $5 \times 5$ nm$^2$ . Un schéma de ces régions et des images STM à courant constant avec résolution atomique sont présentés sur la figure 9a. Pour distinguer les mesures effectuées sur chaque région, nous leur avons attribué des numéros de 1 à 3, comme indiqué sur la figure. Les régions 1 et 2 sont situées à quelques dizaines de nm l'une de l'autre tandis que la région 3 est séparée des autres par plus de 1 $\mu$m. Une sélection de spectres STML acquis dans chaque région est présentée sur la figure 4.8b. Les positions correspondantes sur lesquelles les spectres ont été enregistrés sont indiquées dans les images STM par les marques colorées.

Discutons d'abord des régions 1 et 2. En général, nous observons que la position et la largeur des résonances restent inchangées pour de petites distances de séparation. Dans la région 2, nous observons un motif moiré indiquant une meilleure interface TMD/FLG que dans la région 1. Par conséquent, nous observons une diminution de la largeur des pics de 11 meV dans la région 1 à 9 meV dans la région 2. L'image acquise dans la région 3 révèle également un motif moiré. De manière surprenante, nous observons un décalage massif de la raie $X^0$ vers le rouge de 70 meV. Notez que des variations aussi importantes de l'émission $X^0$ ont été observées dans PL (figure 4.5). La différence entre les données STML acquises dans la région 2 et la région 3 ne peut être attribuée à une interface TMD/FLG différente et indique plutôt que c'est l'interface entre l'hétérostructure et le substrat d'or qui est en jeu. L'écran diélectrique induit par la proximité d'un environnement métallique est connu pour générer un redécalage substantiel des lignes d'émission des TMD (un phénomène que nous avons discuté pour l'interface $MoSe_2$/Au dans la référence [9]). Nous supposons que le changement de l'énergie d'émission de la ligne $X^0$ provient de ce phénomène qui indique donc une meilleure interface entre l'hétérostructure et le substrat de Au dans la région 3. Ceci est également cohérent avec la diminution de la largeur des raies d'émission de 11 meV dans la région 1 à 4 meV dans la région 3 (précisons qu'il s'agit de la valeur la plus étroite à notre connaissance pour des échantillons non en-

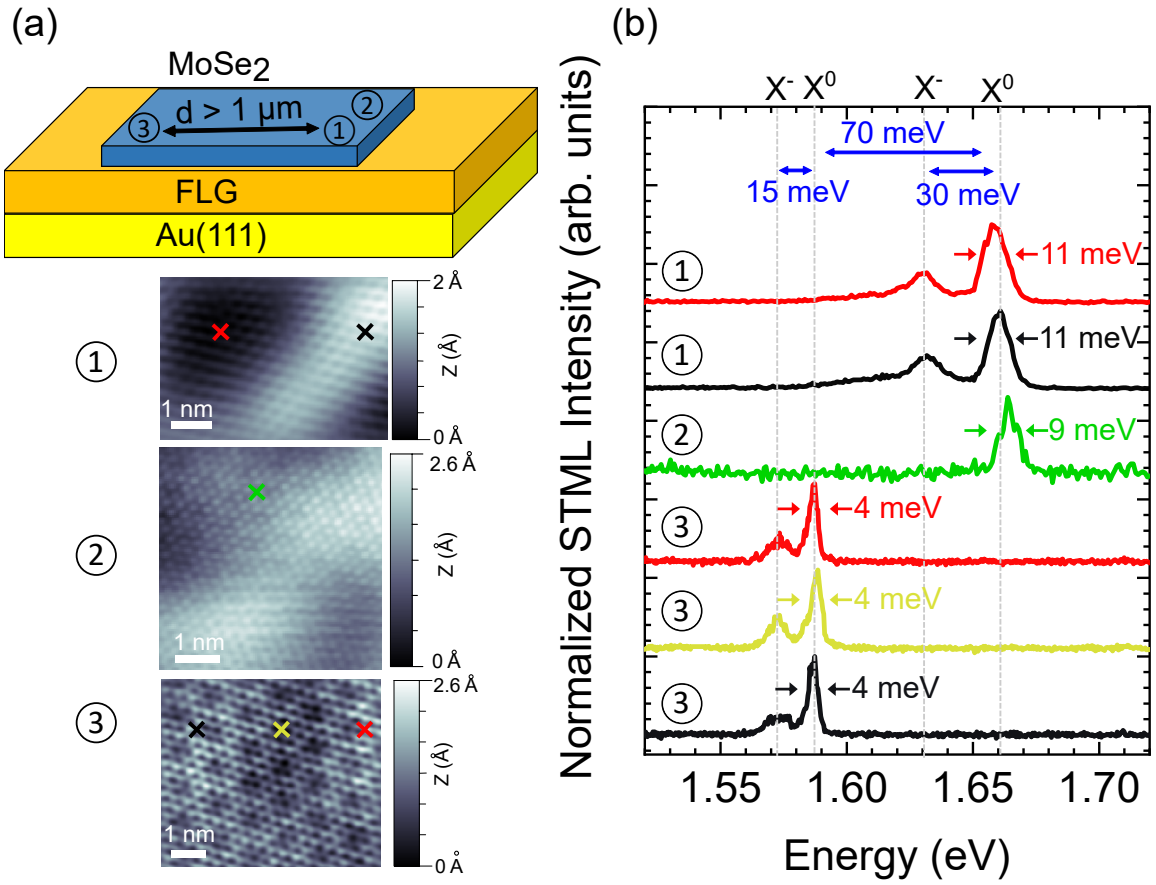


Figure 9: **Dépendance spatiale de l'émission.**Haut : Schéma de l'hétérostructure. Nous nous sommes concentrés sur trois régions, marquées de 1 à 3. Les régions 1 et 2 correspondent à la même zone alors que la région 3 est située à plus de 1 $\mu$m. Les images à résolution atomique de chaque région sont présentées dans la partie inférieure de la figure (a). Les paramètres d'acquisition pour ces images étaient de haut en bas : -1.3 V, 10 pA (région 1), -1.4 V, 4.1 pA (région 2) et -1.4 V, 6 pA pour la région 3. (b) Spectres de STML sélectionnés enregistrés sur les régions 1 (trois spectres en haut) et 2 (deux spectres en bas). Les positions correspondantes sur lesquelles les spectres ont été acquis sont indiquées sur les images STM et suivent les marques colorées. Les spectres sont caractérisés par deux résonances séparées de 30 meV (15 meV) dans les régions 1 et 2 (région 3). Les paramètres d'acquisition pour les spectres étaient : -2.8 V, 90 pA (région 1), -2.8 V 100 pA (région 2) et -2.9 V 90 pA (région 3).

capsulés). En effet, l'élargissement de la raie d'émission se produit lorsque les TMD sont situés dans un environnement inhomogène. Une ligne d'émission fine est une indication d'interfaces $MoSe_2$/FLG/Au(111) plus homogènes. Suivant un raisonnement similaire, les lignes d'émission étroites décalées vers le rouge peuvent également être attribuées à des excitons localisés, qui peuvent être dus à des défauts (absents dans l'image de la région 3) ou à des excitons piégés dans le motif moiré. En effet, l'émission de ce type d'excitons peut être très étroite ($< 1$ meV) en raison de leur longue durée de vie. Ici, la présence du graphène peut réduire leur durée de vie à quelques ps, résultant en des largeurs de lignes proches de quelques $\sim$ meV. Dans l'ensemble, ces observations indiquent que la qualité de

l'interface, que ce soit au sein de l'hétérostructure ou entre l'hétérostructure et la surface Au, joue un rôle crucial dans l'émission provenant des excitons.

Discutons maintenant du pic à basse énergie qui accompagne la ligne $X^0$ observée dans les spectres de la figure 4.8b. Dans la région 1, le pic décalé vers le rouge de 30 meV peut facilement être attribué à un trion. Le dopage n identifié dans le spectre dI/dV de la figure 4.7 suggère un trion chargé négativement ($X^-$). La disparition de ce trion dans la région 2 peut être bien expliquée par la meilleure interface avec le graphène qui conduit à un transfert de charge statique entre les couches comme discuté dans le chapitre 3. Dans la région 3, un pic apparaît à nouveau mais il est situé à 15 meV sous $X^0$ au lieu de 30 meV. Dans le paragraphe précédent, nous avons conclu que la région 3 est affectée par un écrantage massif dû au meilleur couplage avec le substrat d'or. Comme observé pour $MoSe_2$/1LG dans la figure 3.13, un écrantage accru réduit l'énergie de liaison des trions. Nous attribuons donc la caractéristique énergétique inférieure de 15 meV dans la région 3 à un trion écranté. Nous pouvons sans risque exclure les biexcitons comme candidats dû au bas courant utilisé pour les mesures. Dans la région 3, la bonne interface avec le substrat d'or a un effet direct sur la redistribution des électrons dans l'hétérostructure TMD/FLG qui peut conduire à un plus grand dopage n par rapport à la région 2 où le trion est absent. Cela fournit les conditions nécessaires pour la formation de trions et explique la présence de la ligne $X^-$ dans la région 3.

Il est intéressant de noter qu'à l'intérieur de chaque région, nous n'observons aucun changement appréciable dans la position des résonances sur des distances aussi grandes que 30 nm, même à différents points du motif moiré. Une explication possible de ce phénomène est liée à la période du motif lui-même. En effet, dans notre cas, la périodicité du motif moiré est comparable au rayon de Bohr excitonique dans les TMD. Cela pourrait signifier que les excitons " ressentent " l'effet de moyenne du super-réseau. Les conclusions tirées dans cette section sont basées sur un nombre solide mais limité d'ensembles de données. Compte tenu de la complexité des processus en jeu et de la morphologie très changeante de l'échantillon à l'échelle de 5 à 100 nm, une attribution définitive des différentes caractéristiques spectrales - en particulier celle identifiée comme $X^-$ - nécessite des recherches supplémentaires sur des échantillons $MoSe_2$/FLG/Au(111) présentant des interfaces plus homogènes.

Dans le cas des zones inhomogènes contenant des bulles et des ondulations, les mesures STM deviennent instables. En effet, il existe des situations où les bulles sont suffisamment découplées des électrodes pour rendre les mesures STM presque impossibles. Cependant, il pourrait être intéressant d'étudier l'émission de tels défauts macroscopiques et d'observer la modification qu'ils produisent dans la luminescence du TMD. La figure 10a montre une vue en 3D d'une aire de $50 \times 40 nm^2$ contenant une zone plate à côté d'une bulle de 1 nm d'hauteur. Des spectres de STML correspondants aux deux endroits marqués par des croix (bleu sur la bulle, rouge sur la zone plate) sont présentés sur la figure 10b. Le spectre

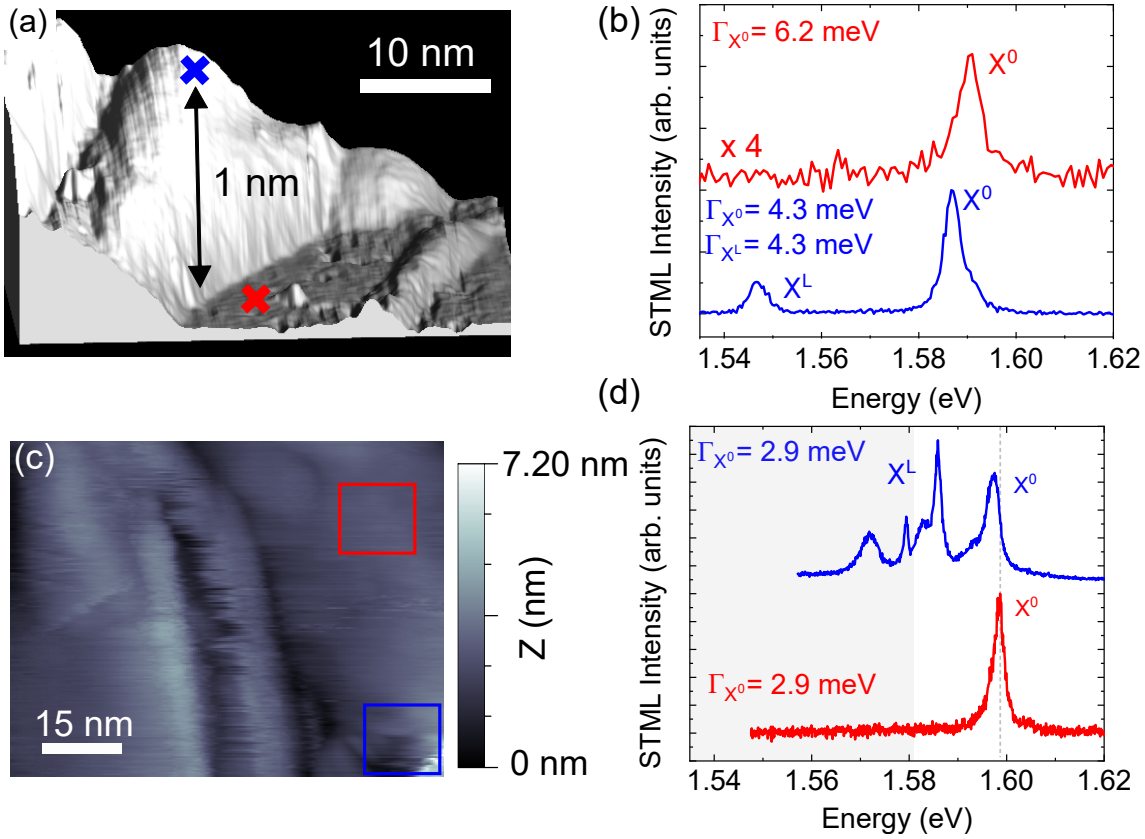


Figure 10: **Émission non-homogène dans les TMD**(a) Image STM d'une surface $MoSe_2$/FLG présentant une bulle. L'image a été acquise sous une tension de -2.1V et un courant de 4 pA. Un inset montre un profil de la surface pris le long de la ligne reliant les marques bleues et rouges. (b)Spectres de STML normalisés enregistrés aux positions marquées dans l'image précédente. Le facteur d'échelle entre le pic $X^0$ dans les deux spectres est de 4, et indiqué dans le panneau supérieur. Le spectre rouge (bleu) a été acquis sous une tension de -3.2 V et un courant de 4 pA (10 pA). (c) Image STM des surfaces $MoSe_2$/FLG montrant un pli et une partie endommagée de la couche. Les paramètres d'acquisition étaient -1.85 V et 5 pA.(d) Spectres de STML pris lors du balayage des zones entourées par les carrés colorés. Dans la zone endommagée, le spectre est composé de nombreux pics provenant d'excitons localisés. Les deux spectres ont été acquis sous une tension de -1.85 V et un courant de 5 pA.

enregistré sur la zone plate est composé d'une résonance située à 1.590 eV. Cette résonance est attribuée à la recombinaison radiative du $X^0$. Dans la bulle (représentée en bleu), nous observons deux pics situés à 1.587 eV et 1.547 eV. Le premier pic correspond à un $X^0$ décalé vers le rouge, probablement dû à la contrainte légèrement plus élevée dans la bulle. Le pic inférieur n'est visible qu'au voisinage de la bulle, et nous l'associons à un exciton localisé $X^L$. La multiplication par 3 du signal STML sur la bulle est une conséquence du caractère découplé de cette dernière qui réduit le transfert d'énergie vers le substrat. De plus, l'apparition de $X^L$ suggère que l'exciton est émis à proximité immédiate de la pointe, car les spectres acquis à quelques nm de distance fournissent des caractéristiques

d'émission différentes.

Le signal STML change radicalement à proximité d'inhomogénéités plus prononcées telles que des plis et des fissures dans la couche. Les figure 10c et d montrent respectivement une image STM d'une zone contenant ce type de défauts et des spectres STML correspondants. Les spectres STML ont été acquis lors du balayage des zones affichés sur la figure 10c. Dans la région de référence (zone rouge), le spectre est composé d'une seule résonance correspondant à $X^0$. En revanche, dans la région anormale (zone bleue), nous observons un spectre STML composé de plusieurs résonances avec des largeurs allant de 2.9 meV pour $X^0$, jusqu'à $\sim$ 700 $\mu$eV pour $X^L$. Des observations similaires ont été rapportées dans les TMDs avec des contraintes importantes [30]. Ces pics proviennent d'états semblables à des quantum dots qui peuvent se comporter comme des sources de photons uniques. Des mesures de corrélation seraient nécessaires pour confirmer cette hypothèse.

**Mécanisme d'emission**

Examinons maintenant le processus physique qui donne lieu à la luminescence. Dans ce but, un étude de la dépendance en tension de l'émission est cruciale car cette caractéristique est généralement différente en fonction du mécanisme d'excitation. Dans tous les spectres STML présentés jusqu'à présent, une tension négative a été utilisée. Nous avons également étudié des tensions allant de 1.6 V à 3.5 V et des variations de courant d'au moins deux ordres de grandeur. Aucune émission de lumière n'a été observée dans tout l'espace de paramètres exploré. Ceci suggère déjà un mécanisme médié par l'injection de porteurs dans la bande de conduction ou de valence. Pour explorer davantage ce mécanisme, nous avons enregistré une série de spectres à différentes tensions négatives (illustrées sur la figure 11b) enregistrés à la position indiquée sur la figure 11a. Les lignes pointillées grises marquent les positions des résonances $X^0$ et $X^-$. Nous observons de l'émission de lumière à environ -1.65 V. À cette tension et jusqu'à -1.7 V, seuls des pics de faible énergie situés 30 à 50 meV sous la ligne $X^0$ sont observés. Ces pics peuvent être attribués soit à des excitons localisés et/ou à des trions et peuvent provenir des inhomogénéités de l'entourage observées dans l'image STM. En augmentant la tension, nous observons un changement drastique dans la forme des spectres. En effet, la raie d'emission associée à $X^0$ apparaît à une tension de -1.75 V et devient dominante pour des tensions plus élévés. De plus, les pics à basse énergie liées aux excitons et trions localisés disparaissent entièrement. Ce phénomène est probablement lié à l'effet Purcell dû à la proximité de la pointe à l'échantillon et il est discuté dans la section 4.5.5. Pour le moment, concentrons-nous sur l'émission de $X^0$. La figure 11c montre un spectre de conductance différentielle pris au même endroit que le spectre de STML. Nous avons superposé à ce spectre l'intensité intégrée de la raie $X^0$ en fonction de la tension appliquée. L'accord entre les tendances de la conductance et l'intensité indique que les excitons sont excités plus efficacement

lorsque nous augmentons la tension à partir du maximum de la bande de valence. En fait, le début de la bande coïncide très bien avec le début de l'émission $X^0$.

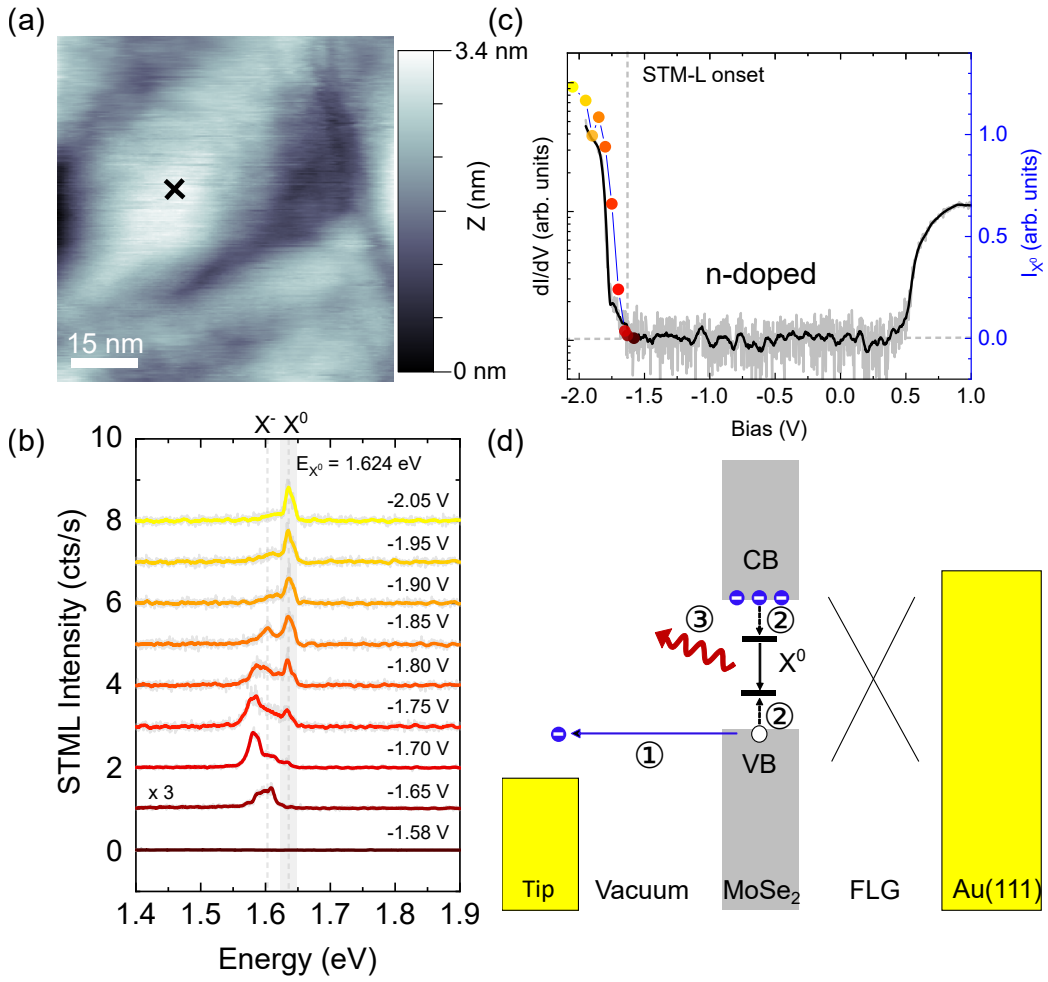


Figure 11: **Mécanisme d'excitation.**(a) Image STM d'une zone sur la surface $MoSe_2$/FLG. L'image a été acquise sous une tension de -2 V et un courant de 5 pA.(b)Spectres de STML enregistrés à différentes polarisations sur la position marquée en (a). Les lignes pointillées correspondent à la position des résonances $X^0$ et $X^-$. Ces spectres ont été enregistrés à un courant de 30 pA. (c) Spectre de conductance différentielle pris au même endroit que dans (b). Le spectre est superposé avec l'intensité intégrée de la ligne $X^0$ en fonction de la tension appliquée. L'accord entre les deux supporte un scénario d'injection de charge pour le mécanisme d'excitation. Le code de couleur correspond à celui utilisé dans la figure (b). (d) Diagramme énergétique du mécanisme d'excitation. Premièrement, un électron est extrait de la bande de valence, laissant un trou derrière lui. Ensuite, un exciton est formé lorsque les électrons natifs du TMD se lient au trou. Enfin, l'exciton se recombine et émet un photon.

Cette observation, ainsi que l'absence de STML à tension positive, suggère une émission provenant de l'injection de trous dans la bande de valence. Nous proposons un mécanisme d'excitation en trois étapes (figure 11d) :

1. **Injection de trous:** Lorsque la tension correspond au début de la bande de valence, un électron peut être extrait, laissant derrière un trou chargé positivement.

2. **Formation d'éxcitons:** Ce trou interagit ensuite de manière électrostatique avec les dopants natifs dans l'hétérostructure. D'après le spectre dI/dV, nous pouvons déduire que la couche est dopée n. Par conséquent, l'interaction de Coulomb entre les électrons natifs et le trou entraîne la formation d'excitons. Remarquez que ce processus est également valable pour la formation de trions. En effet, lors de la formation de l'exciton, il peut arriver qu'il interagisse avec les dopants natifs et forme un trion.

3. **Recombinaison radiative** Une fois formé, $X^0$ peut se recombiner de manière radiative, ce qui se traduit par la luminescence observée.

La figure 4.10d présente un diagramme énergétique résumant ce processus.

## 0.4 Conclusion

Dans ce manuscrit, nous avons présenté l'étude du couplage entre couches dans les hétérostructures TMD/graphène à l'échelle sub-nm. Cette thèse est basée sur deux chapitres principaux. Le chapitre 3 est consacré à l'étude du couplage entre couches dans les hétérostructures TMD/graphène à l'aide de spectroscopies optiques. Le chapitre 4 est consacré à l'étude des propriétés optiques des TMD/graphène en utilisant le STML.

Dans le chapitre 3, nous avons montré que le couplage avec le graphène a deux effets majeurs sur les propriétés de luminescence de la TMD. Il s'agit de la neutralisation complète de la TMD due au graphène et d'un filtrage résultant du transfert d'énergie des espèces excitoniques à longue durée de vie vers le graphène. Par conséquent, les spectres PL à basse température de différentes TMD présentent une ligne d'émission unique et étroite provenant de l'exciton neutre. Ce processus est également vrai pour les TMDs présentant des excitons sombres qui ne respectent pas la conservation du spin. Nos résultats suggèrent que le mécanisme à l'origine du couplage entre couches dans les TMD/graphène est compatible avec le transfert d'énergie de Dexter.

En outre, nous avons montré que le graphène offre des voies de recombinaison non radiatives efficaces pour les excitons dans le cône de lumière ainsi que pour les excitons chauds ayant un momentum en dehors du cône de lumière. En utilisant une approche combinée entre la spectroscopie de photoluminescence résolue dans le temps, la spectroscopie de réflectance différentielle et la spectroscopie de photoluminescence résolue dans l'espace, nous avons pu estimer un temps de transfert des excitons froids vers le graphène de l'ordre de $\tau_G \sim$ quelques ps.

De manière remarquable, tous les effets physiques (filtrage, réduction de la liaison, extinction du PL, etc...) que nous observons se produisent en utilisant une seule couche de graphène. En bref, l'ajout de couches supplémentaires de graphène et/ou d'une couche supérieure de hBN affecte marginalement les processus physiques susmentionnés. Cela

établit le TMD/1LG comme une hétérostructure photostable qui peut être facilement contactée et qui est compatible avec les études STML.

Dans le chapitre 4, nous avons poursuivi nos recherches sur les hétérostructures TMD/FLG en utilisant la STML à basse température et sous ultravide. Nous avons pu démontrer pour la première fois, la luminescence intrinsèque induite par un STM d'une hétérostructure vdW tout en préservant la résolution atomique. Un objectif qui, jusqu'à présent, n'avait pas été atteint. Nous avons ensuite exploité la résolution ultime fournie par la STML pour étudier l'effet de l'environnement atomique sur la luminescence du TMD.

Tout d'abord, nous avons montré que l'interface entre le TMD et le graphène joue un rôle important dans l'élargissement des lignes d'émission. Dans les interfaces propres, un motif de moiré a été observé ainsi qu'une réduction des largeurs des pics de 11 meV dans les zones sans motif de moiré jusqu'à 4 meV dans les meilleures zones que nous avons trouvées. Ces largeurs sont comparables à celles obtenues dans des échantillons encapsulés par hBN de haute qualité. Deuxièmement, nous avons montré que la qualité des interfaces (par exemple, TMD/FLG et FLG/Au) joue un rôle important dans les propriétés d'émission de l'hétérostructure. Nos résultats suggèrent que l'interface entre l'hétérostructure et l'or, définit fortement l'écrantage ressenti par les excitons. Ceci peut être mis en évidence à la fois dans la PL et la STML, où des variations de l'énergie d'émission excitonique de l'ordre de 70 meV ont été observées.

Enfin, nous avons pu explorer l'effet des défauts macroscopiques tels que les bulles et les fissures dans le TMD sur l'émission excitonique. Nous avons observé que ces inhomogénéités donnent lieu à des spectres STML composés de différents pics qui peuvent provenir d'excitons localisés. Il est intéressant de noter que certains de ces défauts macroscopiques affichent des spectres avec des pics avec largeurs proches de 700 $\mu$eV. Cela mérite des investigations plus approfondies car ils pourraient être un signe des sources de photon uniques présents dans les TMDs. Nos résultats nous permettent de mieux comprendre l'origine des spectres complexes observées avec des techniques macroscopiques comme la PL.

Enfin, nous avons étudié le mécanisme qui donne lieu à la luminescence observée. Une dépendance de la tension a révélé que l'émission excitonique est induite par l'injection de trous dans le $MoSe_2$. Ceci n'est possible qu'en raison du caractère dopé n du TMD qui agit comme un réservoir d'électrons avec lequel le trou peut interagir. De plus, nous avons observé des signes de contrôle à l'échelle atomique de la luminescence des TMD. En modifiant la distance pointe-échantillon, nous avons observé l'émission de différentes espèces excitoniques, ce qui suggère une interaction non négligeable entre les excitons et la pointe métallique. Dans l'ensemble, nos études établissent le TMD/graphène comme une plateforme pour étudier l'interaction lumière-matière à l'échelle nanométrique.

# Introduction

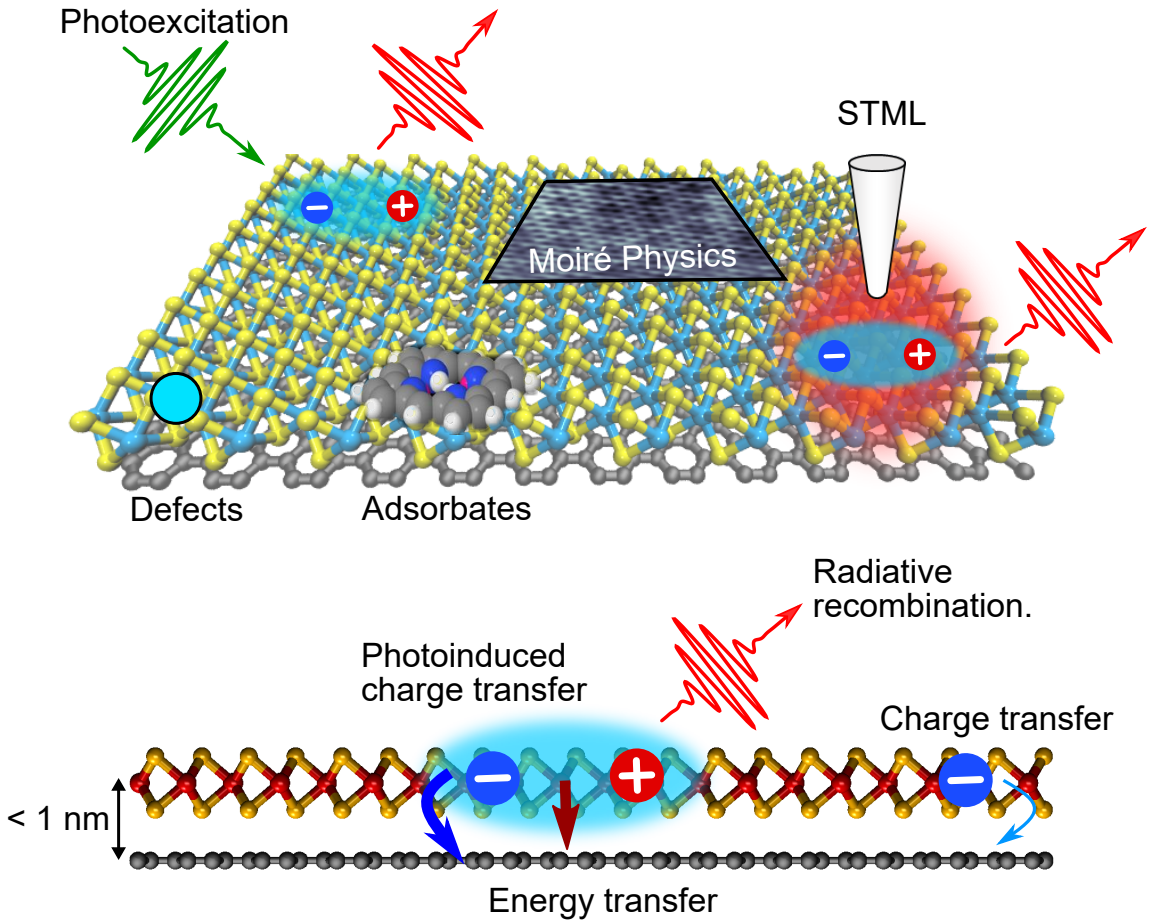


Figure 12: **Tailoring the luminescence of atomically thin semiconductors at the sub-nm scale.** Top: 3D-scheme of a monolayer TMD/graphene heterostructure. Exciton generation occurs either through photoexcitation (green wavy arrow) or using an STM current. We can identify the different nanoscopic environments an exciton can experience. These are defects, adsorbates and Moiré patterns among others. Bottom: Interlayer coupling mechanisms that can arise at the interface of the heterostructure. These are charge transfer, energy transfer and electron redistribution.

## 0.5 Motivation

2D materials are covalently bound layered crystals held together by van-der-Waals interactions. Ever since the first isolation of graphene with the scotch tape technique [1], a whole new toolkit of 2D materials has been fabricated. These atomically thin layers display a wide range of properties ranging from 2D metals such as graphene, semiconductors

such as transition metal dichalcogenides (TMDs) and insulators such as hexagonal boron nitride (hBN). These unique set of properties combined with their atomically thin nature is what makes 2D-layered structures such interesting systems both for fundamental research and applications. Moreover, their atomically thin nature also makes them highly sensitive to their local environment.

Another remarkable property of 2D materials is the absence of dangling bonds on their surfaces. This allows us to readily stack them and form new artificial materials called **van-der-Waals (vdW) heterostructures**. Since the 2D toolkit is extensive, one has a large number of possible architectures to explore. Historically, the first vdW heterostructure was created few years after the seminal work of Novoselov and Geim on graphene [1]. This heterostructure consisted of a stack of graphene on top of hBN [2]. The inert character of hBN, together with its atomically flat terraces, provided an ideal substrate for graphene, resulting in improved conductive properties. This marked the beginning of the "van-der-Waals era," where a new generation of heterostructures was created displaying an increasing set of emerging properties [3]. For instance, superconductivity was demonstrated in twisted bilayers, and trilayers of graphene [4, 5].

These emerging phenomena are a consequence of the interlayer coupling inherent to these stackings. Indeed, the atomically thin nature of its components and the sub-nm interlayer separation make vdW heterostructures ideal platforms to investigate near-field interactions. Going further, one would like to exploit these proximity effects to create new materials with tunable properties. This is particularly promising in the case of heterostructures made of semiconducting transition metal dichalcogenides (TMDs), whose unique optical properties make them ideal bricks for optoelectronic devices.

However, defects, adsorbates, and dielectric disorder can play an important role in the photophysics of TMD-based vdW heterostructures. Indeed, the optical properties of TMDs are defined by tightly bound excitons with a typical Bohr radius of $\sim 1$ nm meaning that the underlying dynamics can be strongly modified due to nm-scale inhomogeneities. An interesting example is the trapping of excitons in the Moiré patterns arising from the relative orientation between different 2D materials. These trapped excitons have been shown to behave as single-photon sources in TMDs [6, 7]. Therefore, to unveil the intrinsic properties of 2D materials and vdW heterostructures, one needs sensitive probes capable of characterizing the photophysical properties of TMDs, with both *in-plane* and *out-of plane* nm-scale resolution.

The aim of this thesis is to **tailor the properties of 2D materials at the sub-nm scale**. This implies developing strategies that allow us to access interlayer coupling and investigate the effect of inhomogeneities in the properties of vdW heterostructures. As we shall see throughout this manuscript, an ideal system to carry out these studies is a TMD monolayer stacked onto graphene. Indeed, the optical properties of this heterostructure are defined by efficient energy transfer mechanisms occurring at the interface [8, 9, 10]. For

instance, at room temperature, the emission yield of the TMD is massively reduced in the proximity of graphene. Moreover, due to the lattice mismatch between the layers and the lack of control on the rotational alignment between the lattices, Moiré patterns can appear, inducing a local modulation of the surface potential. These patterns, combined with defects and contaminants created during the fabrication process of the sample, provide a rich environment to study the excitonic dynamics. In our investigations, we will delve into the following questions:

- What is the nature of the interlayer coupling mechanism between TMD and graphene?
- What is the effect of this coupling in the luminescence of the TMD?
- To which extent is there a charge transfer between the layers?
- Can we exploit this coupling to tune the luminescence of the TMDs?
- What is the effect of defects and adsorbates in the luminescence of TMDs?
- Can we probe the effect of Moiré patterns on excitonic emission?

First, we can use optical spectroscopies to thoroughly characterize the interlayer coupling in the TMD/graphene heterostructure. For instance, using spatially- and time-resolved photoluminescence spectroscopy, we can directly probe the excitonic dynamics. This technique consists on the photogeneration of excitons, and it allows us to obtain information in the timescales in which the energy transfer occurs. We will complement this by using the inelastic scattering of light as well. This is known as Raman spectroscopy, and it provides us with information regarding the structure, strain, and doping trends of the material. Both approaches allow us to build a picture of the interlayer coupling in TMD/graphene.

However, these techniques do not allow us to investigate the effect of the *in-plane* nanoscopic landscape. Such investigations require a resolution that can not be achieved with diffraction-limited techniques. This is why we used a unique approach involving the ultimate resolution provided by a scanning tunneling microscope (STM) working at low temperatures and ultra-high-vacuum conditions to excite and probe the luminescence of the heterostructure. In these conditions, we can achieve a spatial resolution 3 orders of magnitude better than with optical spectroscopies. This technique is known as STM-induced luminescence (STML).

Experimentally, this requires that the investigated samples are compatible with STM measurements. Moreover, the electromagnetic field inside an STM junction is far from being trivial, and there can be processes that hinder intrinsic emission. For instance, due to the presence of the metallic substrate, non-radiative decay paths become efficient. This has been explored before in the context of single molecules where different decoupling

strategies needed to be developed in order to observe intrinsic luminescence [11, 12]. For monolayer TMDs, the current state of the art points towards a trade-off between resolution and intrinsic emission. Indeed, intrinsic STM-induced luminescence (STM-L) of TMDs has been observed only at room temperature and at air [13, 14, 15]. Under these conditions, it is not possible to obtain the required resolution for our experiments. On the other hand, at low temperatures and under ultra-high vacuum (UHV), atomically resolved information can be readily obtained. However, the luminescence observed in these experiments is of extrinsic origin [16, 17]. Therefore, the first question a game-changing experiment would need to tackle is related to the feasibility of intrinsic TMD emission while preserving the atomic resolution.

This project started in 2017 as a collaboration between the team of Stéphane Berciaud, focused on the properties of 2D materials, and the team of Guillaume Schull, focused on STM-induced luminescence. The idea was to combine the expertise of both teams to investigate the origin of single-photon sources in monolayer TMDs using STML, which to this day remains unknown. Our starting point was an article published by Krane *et al.* [16] on which an attempt at obtaining intrinsic STML of a monolayer TMD was made. In the article, the observed luminescence was of extrinsic origin, suggesting that the proximity of the metallic electrode necessary to perform an STM measurement strongly quenched the luminescence of the TMD. This motivated us to design architectures that could bypass these limitations while preserving the properties of the TMDs unaffected. However, this proved to be a challenge since in all of our experiments no STML of TMDs could be achieved.

Finally, in a collaboration with the team of Eric le Moal in Paris, STML from monolayer TMDs was observed at room temperature and at air [13]. To avoid the coupling with the electrodes, they used a non-plasmonic substrate. The main limitation however remained to achieve atomic resolution simultaneously, which is not possible in these conditions.

At this point during my Ph.D., we had investigated the photophysics of TMD/graphene extensively. The natural follow-up was to address this heterostructure at the atomic scale with the STM. The hope was that graphene would act as a decoupling layer while providing an atomically flat substrate for the TMD. Moreover, the relatively small separation between the TMD and the metallic substrate would allow us to benefit from an enhancement of the EM-field provided by the STM junction (See chapter 2). In these conditions, we reported the intrinsic STML of atomically thin semiconductors with atomic resolution for the first time. In doing so, we set the basis for future investigations on near-field mechanisms that affect the excitonic dynamics in vdW heterostructures.

## 0.6 Organization of this manuscript

This manuscript is divided into five chapters:

**Chapter 1** introduces 2D materials and stresses the main properties that are relevant to our studies. In particular, a summary of TMD, graphene, and hBN properties. This is not an extensive description but a selection of the properties that are useful to follow the results presented in the manuscript.

**Chapter 2** is dedicated to the experimental methods used during this thesis. First, I will introduce the fabrication techniques. I will explain how one can get monolayers of 2D materials and the methods used to stack them into vdW heterostructures. Then, I will describe the experimental setup used for optical spectroscopies. This setup consists of a home-built confocal microscope on which we can perform PL and Raman spectroscopies with spatial resolution. To conclude, I will introduce the working principle of STM and the setup used in our experiments and how to use it to generate luminescence (STML).

**Chapter 3** is the first chapter of results. It focuses on photoluminescence and Raman studies of TMD/graphene heterostructures. I will characterize their coupling and show that one can exploit it to obtain single and narrow emission spectra from a TMD. Moreover, we will see that graphene acts as a reservoir for charges completely neutralizing the TMD. Moreover, I will present our results regarding TMD and TMD/graphene valley contrasting properties at different temperatures.

**Chapter 4** is dedicated to STML in TMDs. First, I will present a detailed review of the state-of-the-art regarding STML of TMDs. Then I will present the results obtained on $MoSe_2$/1LG studied at cryogenic temperatures. Finally, I will discuss the origin of this luminescence and explore the effect of the local environment.

**Chapter 5** concludes this manuscript and gives an outlook.

Chapter 1

# Introduction to 2D materials

In 1959 Richard Feynman gave a lecture called "There's Plenty of Room at the Bottom: An Invitation to Enter a New Field of Physics" at the annual meeting of the American Physical Society. During the lecture, Feynman emphasized what a breakthrough it would be to control matter at the atomic scale, to be able to *"arrange the atoms the way we want"*. He wondered about the problems that electronics will face when reducing the size of the circuits and about the conception of microscopes that allow us to 'see' at the smallest possible scale. He asked: *"What could we do with layered structures with just the right layers?"*. Nowadays, layered structures have been gaining attention as their range of applications grows. In particular, the transition metal dichalcogenides (TMDs) have sparked growing interest as they form a vast family with a broad range of optical and electronic properties that makes them ideal building blocks for new-generation nanodevices[31]. In this chapter, I will present the main properties of different 2D materials namely: graphene, hexagonal boron nitride and TMDs.

## 1.1 2D materials and van der Waals heterostructures

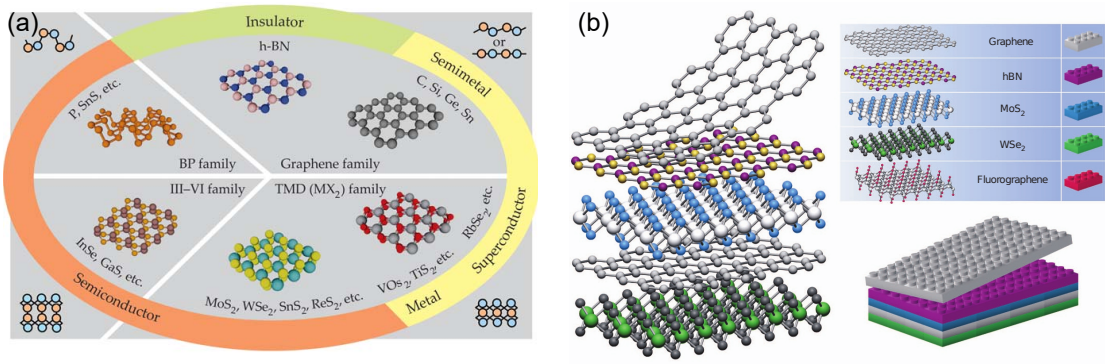


Figure 1.1: Overview of different 2D materials. It comprises graphene and its analogues. Their properties vary from insulators such as hBN, through semiconductors such as TMDs, and from semi-metals to metals. Figure adapted from [32].

As mentioned before, ever since the isolation of graphene with the scotch tape technique [1], a whole toolbox of 2D materials has appeared [32]. These 2D layers display a wide range of properties ranging from superconductors to insulators. An overview of this toolbox is shown in figure 1.1. In particular, 2D materials made from semiconducting

transition metal dichalcogenides (TMDs) quickly presented themselves as the new elemental brick for optoelectronics. Indeed, in the monolayer limit, these materials display unusually strong-light matter interactions as well as mechanical and electronic tunable properties. The discovery of monolayer TMDs together with their relatively easy isolation and inert surfaces, motivated the search for new artificial materials composed of different layered structures [3].

A van der Waals (vdW) heterostructure consists of a stacking of different 2D materials. Due to the affinity between adjacent layers, these heterostructures are characterized by atomically sharp interfaces which are ideal platforms to study proximity effects. Indeed, the interface between two adjacent 2D-materials is atomically flat and free of contamination due to the **self-cleaning** mechanism [33, 34, 35] where contaminants group together in pockets due to the smooth adaptation of the layer to the substrate as a consequence, one ends up with a patchwork of clean areas surrounded by bubbles and ripples. Figure 1.2 shows atomic force microscopy images of graphene transferred onto various crystals. In particular, we observe the self-cleaning mechanism only for interfaces involving graphene and other 2D materials.

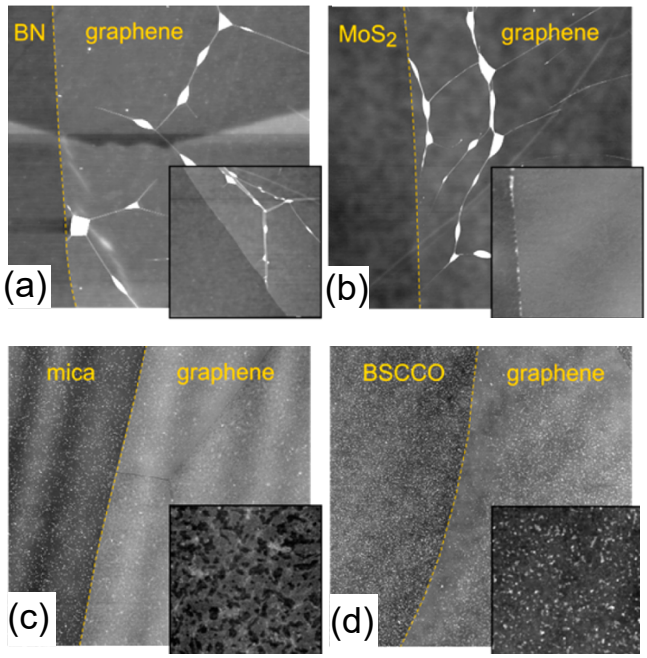


Figure 1.2: **Self-cleaning mechanism.** Atomic force microscopy images of monolayer graphene stacked onto different substrates. When graphene is stacked onto other 2D materials such as hBN (a) and $MoS_2$ (b) we observe that the contamination is concentrated in bubbles. In contrast, in other substrates such as mica (b) and BSCCO (d), the contamination is spread uniformly all over the surface. This proves that the self-cleaning mechanism is inherent to van-der-Waals heterostructures. Figure extracted from [35].

VdW heterostructures add a new dimension to the 2D-playground, since now not only do we exploit the individual properties of its components, but we can also investigate new emerging phenomena. Historically, the first vdW heterostructure was made by Dean

*et al.* [2], it consisted of a monolayer of graphene deposited onto a hexagonal boron nitride (hBN) flake. hBN is an insulator and provides a flat inert terrace for other 2D materials. In these conditions, they observe a significant increase in the electron mobility in graphene. It has been shown that by encapsulating TMD-based vdW heterostructures in hBN, one can improve their optical quality and even control their excitonic dynamics [25]. Another example is TMD/Graphene heterostructures. These have been shown to harbor efficient energy and charge transfer mechanisms which can be exploited to tailor their luminescent properties (See chapter 3). More recently, it has been shown that a slight misalignment in homojunctions can dramatically change the properties of graphene and TMDs. For instance, superconductivity has been demonstrated in twisted bi-, and trilayer graphene [4, 5]. This opened a new branch of studies and the field of **twistonics**. In the following, I will present selected properties of the 2D materials I used during my Ph.D.

## 1.2 Selected properties of 2D Materials

### 1.2.1 Graphene

Graphene is a 2D semimetal composed exclusively of carbon atoms arranged in a honeycomb lattice. Since it was first isolated in 2004 [1], graphene has sparked an important amount of research and it has become a building block for nanoelectronics. For instance, graphene is known to have remarkable conductive properties with a typical mobility of $1 \times 10^4$ cm$^2$V$^{-1}$s$^{-1}$ at room temperature and it is transparent to optical frequencies which makes it an ideal electrode [1, 36]. The remarkable properties of graphene arise from its cone-shaped dispersion relation which endows it with unique electronic properties that are better described in terms of relativistic massless particles. In this subsection, I will summarize its main properties.

#### Structure

As it was mentioned before, graphene is an allotrope of carbon in which the atoms are arranged in a honeycomb lattice structure. One has to be careful since even though all atoms are carbon, not all lattice sites are equivalent. Indeed, the honeycomb lattice can be considered as two triangular sublattices made of atoms A and B as shown in figure 1.3a. In graphene, neighboring lattice sites are separated by a distance of 1.42 Å and are connected through $\sigma$-bonds[1]. The remaining $p_z$-orbitals form $\pi$-bonds which in the crystal picture become half-filled electronic bands. Using a tight-binding model, it can be

[1]These bonds arise from the interaction between the sp$^2$-hybrid orbitals of each atom.

shown that the dispersion relation of graphene reads [37]:

$$E_{\pm}(k_x, k_y) = \pm t\sqrt{3 + 2\cos\left(\sqrt{3}k_y a\right) + 4\cos\left(\frac{\sqrt{3}}{2}k_y a\right)\cos\left(\frac{\sqrt{3}}{2}k_x a\right)} \tag{1.1}$$

Where t is the hopping constant, $\vec{k}$ is the electron wavevector and the $\pm$ sign distinguishes between the conduction and valence band respectively. From this equation, we can deduce that near the K (K') points the two bands are degenerate. If we do a Taylor expansion of the dispersion relation in the neighborhood of the K and K' points, we can show that:

$$E_{\pm} = \pm\hbar v_F |k_0| \tag{1.2}$$

In this expression, $v_F$ is the so-called Fermi velocity, and $\vec{k_0}$ is the momentum of the electron with respect to the K point, that is, $\vec{k} = \vec{K} + \vec{k_0}$. This dispersion relation is the origin of the famous Dirac cones of graphene (See figure 1.3b)[2].

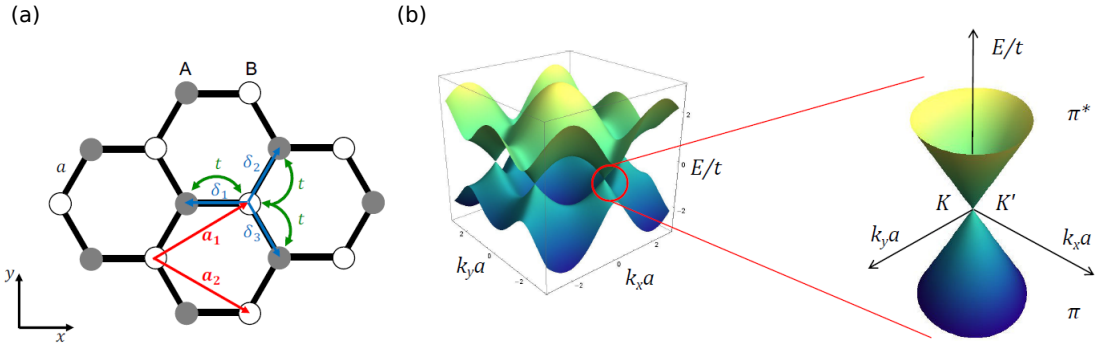


Figure 1.3: **Graphene structure.**(a) Lattice structure of graphene. This lattice can be described in terms of two triangular lattices of inequivalent atomic sites. $a_1$ and $a_2$ are the primitive vectors of the lattice. (b) Electronic dispersion relation of graphene. Zooming on the K point we can see a conic dispersion relation. Figure adapted from [38]

### Massless Dirac Fermions

Equation 1.2 resembles the dispersion relation of photons $E = \hbar ck$. The main difference between the two is that instead of the speed of light, we have $v_F$. Moreover, since the honeycomb lattice's unit cell contains two atoms, the electronic wavefunction has a 2-spinor like structure. In fact, the electronic wavefunction near K and K' satisfies Dirac equation for massless fermions and defines a robust valley-dependent chirality. This endows graphene with remarkable properties that allow the observation of phenomena such as Klein tunneling and the integer quantum Hall effect [39, 40].

[2]For relatively large values of $k_0$, *trigonal warping* occurs. This effect is the deformation of the cone shape due to higher-order terms in the Taylor expansion.

### Optical properties of graphene

Graphene can absorb light either from interband or intraband transitions depending on the doping level and spectral range. In the visible range, the main contribution to the absorption of light comes from interband transitions [36]. Moreover, the absorption coefficient "A" of graphene in the visible range is constant and does not depend on the Fermi velocity. This can be shown by estimating the ratio between incident ($P_i$) and absorbed power ($P_a$).

$$A = \frac{P_i}{P_a} \tag{1.3}$$

The incident power depends on the incident wave and it is given by $P_i = \frac{c|E|^2}{4\pi}$. In contrast, the absorbed power depends on the coupling between electrons in graphene and light $\eta_a$, and it is given by $P_a = \eta_a \hbar\omega$. $\eta_a$ represents the probability rate to jump from an initial state $|i\rangle$ in the VB to a final state $|f\rangle$ in the CB. This rate depends on the matrix element M connecting both states and it is given by Fermi Golden's rule:

$$\eta_a = \frac{2\pi}{\hbar^2}|M|^2 DoS(E) \tag{1.4}$$

In this expression, $DoS(E)$ refers to the density of states of graphene which can be estimated from equation 1.2[3]. M can be calculated from the 2D Dirac light-matter interaction Hamiltonian.[4] Using these results, the absorption coefficient can be estimated:

$$A = \pi\alpha \approx 2.3\% \tag{1.5}$$

This result has been verified experimentally and establishes graphene as a candidate for a transparent atomically thin electrode [41, 36].

## 1.2.2 Raman spectroscopy of graphene

Raman scattering occurs when a photon is inelastically scattered by a dynamic inhomogeneity, such as a vibrational state, in a crystal. Raman spectroscopy is a technique that focuses on this type of scattering. An incident photon with frequency $\nu_1$ triggers a transition to a virtual state $E^*$ and is re-emitted with frequency $\nu_2$ such that $\nu_1 \neq \nu_2$ and $E^* = \hbar|\nu_1 - \nu_2|$ (figure 1.4). The shift in frequency that the photon undergoes is called the Raman shift and it's measured in wavenumbers ($cm^{-1}$ being the most common unit of measurement). For positive shifts ($\nu_2 > \nu_1$) one says that the photon underwent a Stokes process, whereas in the opposite case ($\nu_2 < \nu_1$) it is called an anti-Stokes process.

[3] $DoS(E) = \frac{2E}{\pi(\hbar v_F)^2}$

[4] $|M|^2 = \frac{(E_0 e v_F)^2}{8\omega^2}$

To convert between wavelengths and wavenumbers of the Raman shift one can use the following relation:

$$\Delta\kappa = \left(\frac{1}{\lambda_{exc}} - \frac{1}{\lambda_{em}}\right) \tag{1.6}$$

where $\kappa$ represents the wavenumbers, $\lambda_{exc}$ is the excitation wavelength and $\lambda_{em}$ is the emitted light wavelength. A Raman spectrum is a chemical fingerprint of a material and it gives us information about its chemical structure, intrinsic strains, contamination, and impurity levels among others. To understand a typical Raman spectrum, we need first to understand how the scattering of light works in crystalline systems.

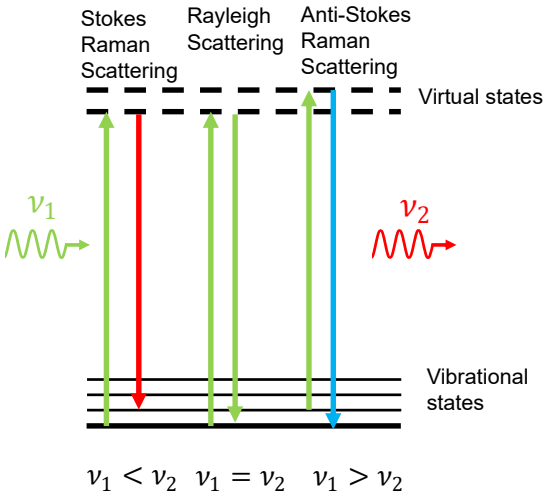


Figure 1.4: **Raman scattering.**Scheme of a scattering process in which an incident photon (Upwards arrow) of frequency $\nu_1$ induces a transition into a virtual state. Depending on the frequency $\nu_2$ of the scattered photon we can identify three possible events. If $\nu_1 < \nu_2$ the process is referred to as Stokes scattering. On the contrary, if $\nu_1 > \nu_2$ the process is called Anti-Stokes scattering. If there is no change of frequency we talk about Rayleigh scattering.

Let us consider an incident monochromatic electromagnetic wave of amplitude $\vec{E}_0$ and frequency $\omega_0$. For simplicity, let us assume that it has the following form: $\vec{E} = \vec{E}_0 cos(\omega_0 t - \vec{k}_0 \cdot \vec{r})$. Upon incidence, the electric field will induce a polarization of the crystal described by:

$$\vec{P} = \epsilon_0 \chi \vec{E} \tag{1.7}$$

In this expression, $\chi$ is the electric susceptibility and $\epsilon_0$ the vacuum permittivity. The incident wave will induce lattice vibrations which can be modeled in terms of normal modes (phonons) of the form $\vec{u} = \vec{u}_0 cos(\Omega t - \vec{q} \cdot \vec{r})$. $\vec{u}$ is the displacement vector of the atoms in the crystal, $\vec{q}$ the phonon momentum and $\Omega$ its frequency[5]. These vibrations induce a change in $\chi$. We can take this into account by doing a first-order expansion in

[5]To avoid confusion, we are going to use $\Omega$ for phonon frequencies and $\omega$ for photons.

$u$.

$$\chi = \chi_0 + \left(\frac{\partial \chi}{\partial \vec{u}}\right)_0 \cdot \vec{u} \tag{1.8}$$

Substituting this into the polarizability we obtain:

$$\vec{P} = \epsilon_0 \chi_0 \vec{E} + \frac{1}{2}\epsilon_0 \left(\frac{\partial \chi}{\partial \vec{u}}\right)_0 \cdot \vec{u}_0 \vec{E}_0 \left(cos((\Omega + \omega_0)t - (\vec{k} + \vec{k}_0) \cdot \vec{r}) + cos((\Omega - \omega_0)t - (\vec{k} - \vec{k}_0) \cdot \vec{r})\right) \tag{1.9}$$

This equation shows that $\vec{P}$ acts as a secondary source of scattering and has three main terms. The first one is called the Rayleigh scattering term and is resonant with the incident frequency. The other two modes are the aforementioned anti-Stokes and Stokes scattering. We can understand this as an induced oscillation of the dipoles in the material which behave like antennas reemiting the scattered wave. We can calculate the intensity of the emitted field [42] and show that:

$$I \propto \omega_s^4 \left| \vec{e}_s \cdot \left(\frac{\partial \chi}{\partial \vec{u}}\right) \cdot \frac{\vec{u}_0}{|\vec{u}_0|} \vec{e}_0 \right|^2 |\vec{u}_0|^2 \left|\vec{E}_0\right|^2 \tag{1.10}$$

where $\vec{e}_s$ and $\vec{e}_0$ are the unit vectors of the scattered and incident fields polarization. To keep generality, we are going to consider that $\chi$ is a tensor and we are going to define the Raman tensor as follows:

$$\mathbf{R} = \left(\frac{\partial \chi}{\partial \vec{u}}\right) \cdot \frac{\vec{u}_0}{|\vec{u}_0|} \tag{1.11}$$

From this definition, we see that the Raman tensor has the same symmetry as the corresponding phonon. This will be of importance because it tells us whether the corresponding phonon can be observed (Raman active) or not in the experimental configuration. In fact, it can be shown that if a given mode has an irreducible representation with a quadratic basis function, it is Raman active [43]. In this thesis, we are going to use Raman spectroscopy to characterize TMD/graphene heterostructures (Chapter 3). As we have seen in section 1.2.2, by studying correlations between the G- and 2D-modes of graphene, we can obtain direct information regarding doping trends and strain in this material. Therefore, this would be an important probe to monitor static charge transfer that can occur between the layers in a heterostructure.

In this thesis, Raman spectroscopy will be used to characterize TMD/graphene heterostructures (Chapter 3). In the following, we will discuss the main characteristics involving the Raman spectrum of graphene. All of the concepts developed here will be useful later to understand our results. Figure 1.5 shows a typical Raman spectrum of graphene. The spectrum is characterized by two main peaks situated at $\approx$ 1580 cm$^{-1}$ and 2675 cm$^{-1}$ (the G- and 2D-mode, respectively). In the following, we will discuss the origin of these peaks:

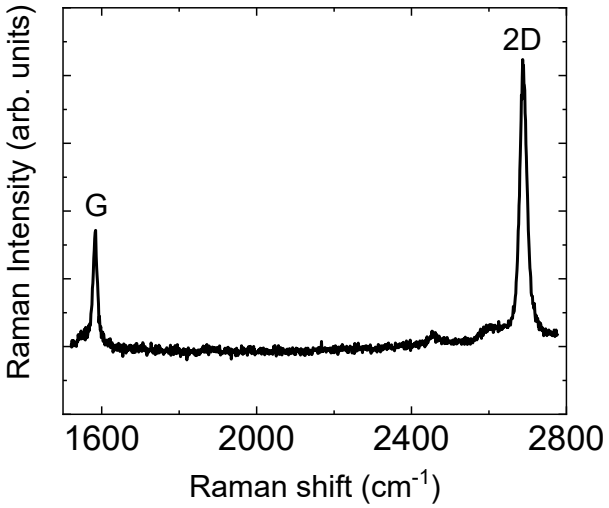


Figure 1.5: **Raman spectrum of graphene.** The spectra is characterized by two main resonances at 1580cm$^{-1}$ and 2670cm$^{-1}$ associated with the G and 2D modes of graphene. This measurement was done on a graphene layer deposited onto a $SiO_2$ substrate under cw laser illumination at a wavelenght of 532 nm.

### G-mode

Graphene has two atoms per unit cell and, in consequence, six phonon branches (see figure 1.6a). The G-mode is the only one-phonon Raman active mode in graphene. It involves a phonon in the $\Gamma$ point and it corresponds to the out-of-phase vibration of the two sublattices with respect to each other. A diagram of this process is shown in figure 1.6b. Experimentally, we can model the G mode with a Lorentzian profile [44]. By studying how the linewidth ($\Gamma_G$) and the frequency ($\omega_G$) of the G mode change with external perturbations, we can study the properties of graphene. For instance, $\Gamma_G$ and $\omega_G$ depend sensitively on doping and their evolution is deeply connected. Intuitively, the presence of electrons (holes) modifies the lattice constant due to the softening (hardening) of the carbon-carbon bonds. A change of the lattice constant translates into a modification of the phonon frequency. In reality, due to strong electron-phonon interactions in graphene, we observe a similar effect regardless of the sign of the doping (See figure 2.7). Indeed, the overall change in frequency can be understood as a sum of two terms named: adiabatic and non-adiabatic ($\Delta\omega_G^A$ and $\Delta\omega_G^{NA}$ respectively).

$$\Delta\omega_G = \Delta\omega_G^A + \Delta\omega_G^{NA} \tag{1.12}$$

The first term comes from the adiabatic adaptation of electrons to the motion of the nuclei. This term is within the Born-Oppenheimer approximation limits, and it tends to soften (harden) the carbon-carbon bonds upon electron (hole) doping. The second term arises from electron-phonon interaction and it leads to a renormalization of the G-mode phonon energy [45]. This strong coupling is a consequence of energy and momentum-

conservation near the Γ and K (K') points. Notice that at these points, the phonon frequencies change abruptly. This is known as a **Kohn anomaly** and it strongly enhances electron-phonon interactions. At finite temperatures, it has been shown that we can express these contributions as follows [45]:

$$\Delta\omega_G^A = -2.13n - 0.0360n^2 - 0.00329n^3 - 0.226|n|^{3/2} \tag{1.13}$$

$$\Delta\omega_G^{NA} = \frac{\lambda_\Gamma}{2\pi\hbar} PV \int_{-\infty}^{\infty} \frac{E^2 sgn(E)(f(E-E_F) - f(E))}{E^2 - \frac{(\hbar\omega_G^0)^2}{4}} \tag{1.14}$$

where PV is Cauchy's principal value, $\lambda_\Gamma$ is the electron-phonon coupling constant and f(E) is the Fermi-Dirac distribution. The variation of $\Gamma_G$ also arises from this coupling. Indeed, the zone-center phonons decay into virtual electron-hole pairs, increasing their lifetime. This induces a sharpening of the peak as the doping increases. Using Fermi golden's rule it is possible to show that the modification of the width is given by:

$$\Delta\Gamma_G = \frac{\lambda_\Gamma}{4}\omega_G^0 \times \left[ f(-\frac{\hbar\omega_G^0}{2} - E_F) - f(\frac{\hbar\omega_G^0}{2} - E_F) \right] \tag{1.15}$$

We can summarize the effects of both electron and hole doping as follows:

- Upshift of the G-mode's frequency.
- Sharpening of the G-mode's width.

### 2D mode

The 2D-mode arises from a resonant two phonon process connecting the K and K' points[6]. These phonons belong to the iTO branch at K (K') and have opposite momentum. Physically, they correspond to the breathing vibration of the six carbon atoms ($A_1$' symmetry) as shown in the diagram in figure 1.6c. We can consider that the process happens in 4 steps (See figure 1.6c):

1. An electron around the K point, with wavevector $\vec{k_0}$ and energy $-\hbar v_F \left|\vec{k_0} - \vec{K}\right|$ is excited into a real state with the same wavevector and energy $\hbar v_F \left|\vec{k_0} - \vec{K}\right|$ by absorbing an incident photon of frequency $\omega_0$. This creates an electron-hole pair and is a resonant process.

2. The electron then interacts with a phonon of frequency $\Omega_D$ and momentum $\vec{q}$, resulting in the electron being scattered to another real state at the K' point. This state has a momentum $\vec{k_2} = \vec{q} - \vec{k_0}$ and energy $\hbar v_F \left|\vec{k_2} - \vec{K'}\right|$. This is also a resonant process.

[6] In fact, the 2D-mode itself is an overtone of the D-mode

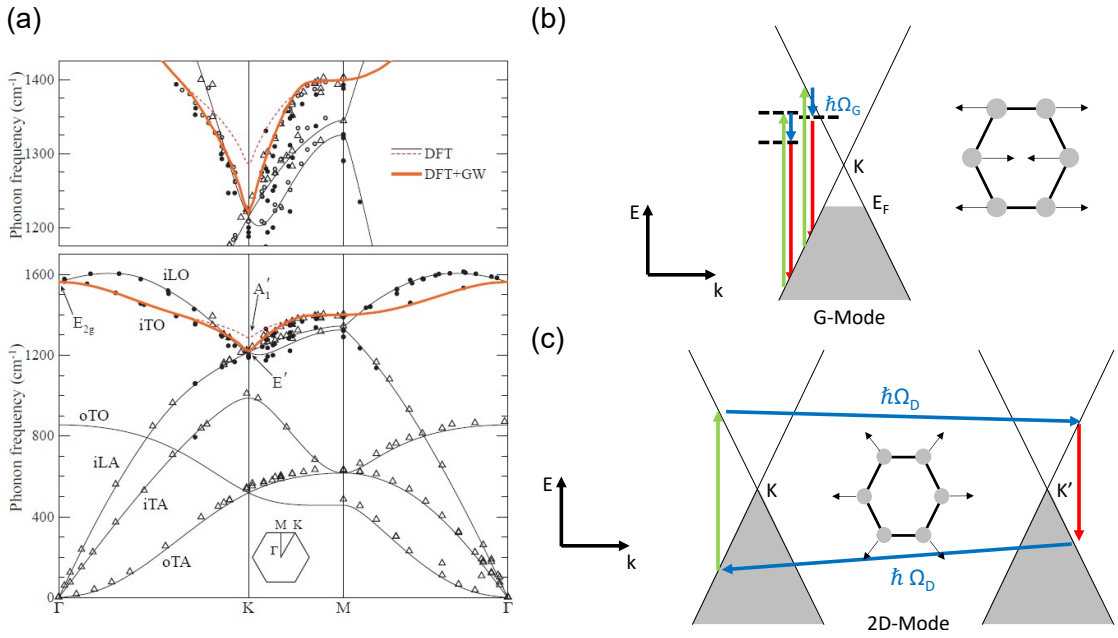


Figure 1.6: **Raman modes of graphene.**(a) Phonon dispersion of graphene. The solid lines represent theoretical calculations and the points are experimental data. We can identify six phonon branches, three acoustic (iLA, iTA, oTA) and three optical (iLO, iTO, oTO). Figure extracted from [46]. (b) 1D schematic representation of the G-mode in the energy-momentum space. The green arrows represent the absorbed photons, the blue and red ones represent the emitted phonon (of frequency $\Omega_G$) and photon, respectively. Horizontal black dashed lines represent virtual states and occupied states are shown in grey. (c) 1D representation of the fully resonant 2D-mode in the energy-momentum space. This mode involves two phonons, each with frequency $\Omega_D$ and opposite momentum. The green arrows represent the absorbed photons, and the blue and red ones represent the emitted phonon and photon, respectively.

3. Afterwards, the electron is backscattered into a virtual state at the K valley by a phonon of frequency $\Omega_D$ and momentum $-\vec{q}$.

4. The electron-hole pair then recombines and emits a photon of frequency $\omega_e = \omega_0 - 2\Omega_D$.

The resonant nature of this mode makes it depend on the energy of the incident photon[7]. In practice, one can phenomenologically describe this mode in supported graphene using a modified Lorentzian profile [47].

Experimentally, $\Gamma_{2D}$ is essentially unaffected by doping, and $\omega_{2D}$ varies weakly at moderate doping and stiffens (softens) at high hole (electron) doping. Conservation of phonon momentum $\vec{q}$ forbids the resonant decay of the 2D mode essentially 'protecting' $\Gamma_{2D}$ from doping effects. Moreover, since the phonons involved in the 2D mode are far away from the Kohn anomalies at the K points, the main contribution of the doping to

[7]Even though we have described the case on which the process is resonant with the incident photon, we can also have resonance with the scattered one. In such scenario, the first intermediate state is virtual. There is even the fully resonant case in which all states are real.

the $\omega_{2D}$ comes from the adiabatic term [48]. As for $I_{2D}$, Basko showed [47] that we can express it as follows:

$$I_{2D} \propto \left( \frac{\gamma_K}{\gamma_{e-phonon} + \gamma_D + \gamma_{ee}} \right)^2 \tag{1.16}$$

where $\gamma_{e-phonon}$ is the electron-phonon scattering rate, $\gamma_D$ is the defect scattering rate, $\gamma_{ee}$ is the electron-electron scattering rate, and $\gamma_K$ the zone-edge scattering rate. We can consider that the electron-phonon scattering can be approximated by a contribution coming from the $\Gamma$ point and a contribution coming from the $K$ point. In other words, $\gamma_{e-phonon} \approx \gamma_K + \gamma_\Gamma$. For Fermi energies lower than the incident photon energy, Basko showed that we can write [49].

$$\sqrt{\frac{I_{2D}}{I_G}} = \frac{\sqrt{\frac{I_{2D}}{I_G}}|_{E_F=0}}{\gamma_{e-phonon} + \gamma_D} (\gamma_D + \gamma_{e-phonon} + 0.06|E_F|) \tag{1.17}$$

## 1.3 Hexagonal boron nitride

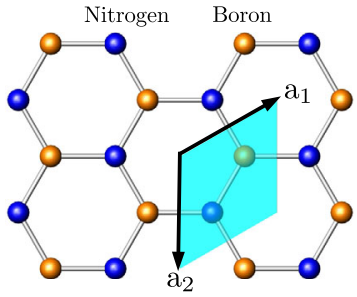


Figure 1.7: **Hexagonal boron nitride.** Lattice structure of hBN. Figure extracted from [50]

Boron nitride is a compound made of boron and nitrogen with the chemical formula BN. It exists in many different polytypes, the most stable one being hexagonal boron nitride (hBN, shown in figure 1.7). It is an insulator with a bandgap of 6 eV and it has a lattice constant of 2.5 Å [51]. Due to the flatness and relatively inert nature of hBN, it quickly presented itself as a useful substrate and protective layer for 2D materials.

### hBN as a substrate

Due to the exposed surfaces of 2D materials, they are sensitive to environmental disorder which can affect their electron mobility. To reduce this, one can, for instance, use suspended samples. However, these samples tend to be quite fragile. This sparked a search for a robust homogeneous substrate. In 2010, hBN was used as a terrace for graphene (1LG), improving its mobility by one order of magnitude with respect to $SiO_2$ supported samples [2]. These early samples were limited by the transferring techniques at the time

which lead to contamination in between the layers. Nowadays, hBN/graphene/hBN samples show ballistic transport over micron distances [52].

Scanning tunneling microscopy (STM) can be used to characterize with atomic resolution the surface roughness and charge inhomogeneity of hBN-supported samples [53, 54]. Figures 1.8a and 1.8b show STM images of hBN-supported graphene and $SiO_2$-supported graphene. It is clear that the presence of hBN induces a smoothing of the surface roughness which we can visualize with the help of a histogram of the surface profile (figure 1.8c). Using hBN as a substrate, one can diminish charge inhomogeneities which can reduce the mobility of electrons [54].

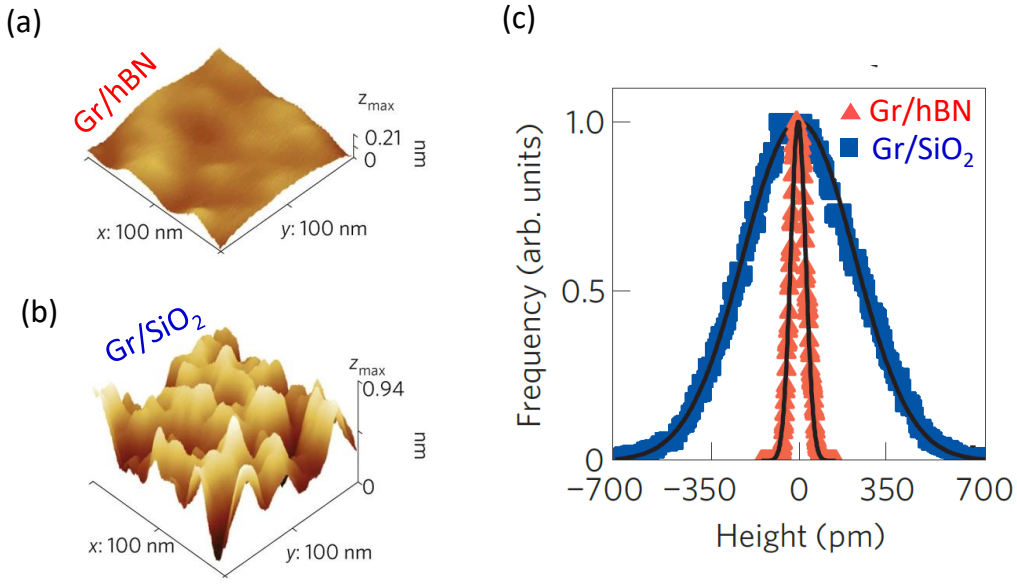


Figure 1.8: STM image of hBN- (a) and $SiO_2$-supported graphene (b). hBN provides a flatter substrate on which graphene can accomodate. (c) Histogram comparing the height variations of hBN/Gr and hBN/$SiO_2$ samples. Figure adapted from [53].

### hBN-Capping: optical quality

Even though hBN-supported samples are ideal for shielding the material from substrate disorder effects, the surface of the heterostructure remains exposed to air. We can solve this by also putting an hBN layer on top of the material and fully encapsulate it. It has been shown that with full encapsulation one can further improve the conductive properties of graphene as well the optical properties of TMDs. This translates into emission spectra with linewidths approaching the homogeneous limit (See section 1.5.2)[55]. Figure 1.9 shows an example of emission spectra of non-capped and capped TMD monolayers. The origin of these peaks is discussed in detail in section 1.7. The narrowing of the emission lines is a direct indication of the improved optical quality. Moreover, it has been shown that one can use hBN to modify the lifetime of excitons in TMDs as we will discuss in

section 1.5.2.

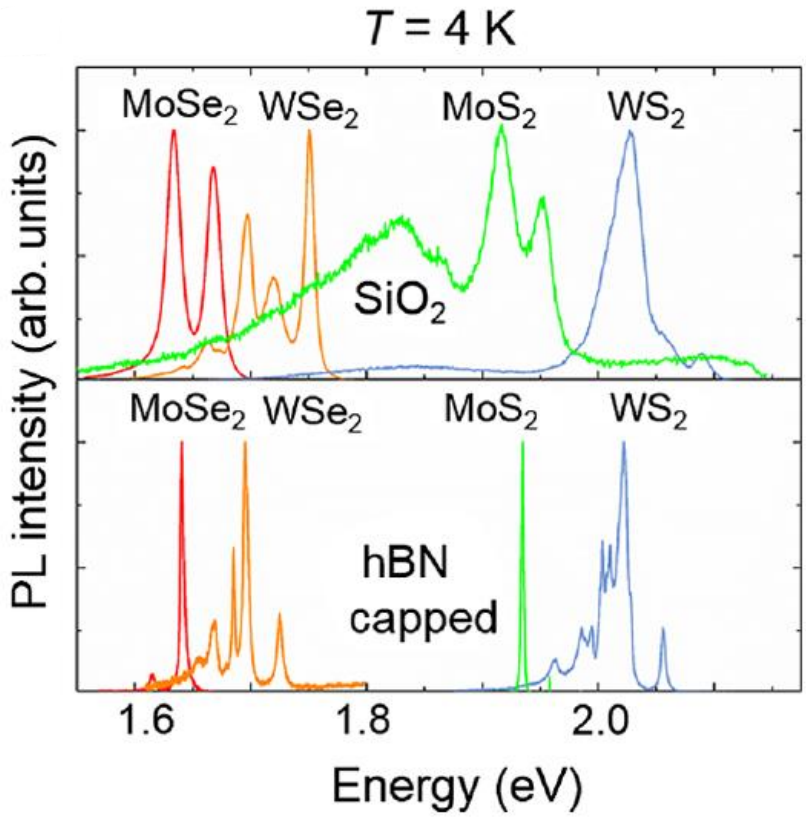


Figure 1.9: **Approaching the homogeneous limit with hBN.** Top: PL spectra of $MoSe_2$, $WSe_2$, $MoS_2$ and $WS_2$ deposited on $SiO_2$ taken at 4K. Bottom: PL spectra of hBN-capped $MoSe_2$, $WSe_2$, $MoS_2$ and $WS_2$ taken at 4K. We can see the optical quality improvement of the TMDs through the sharpening of the emission peaks. Indeed, this is a sign of a reduction of environmental disorder. Figure extracted from [55].

Furthermore, due to its inert nature, we can also use hBN as a spacer to tune interlayer coupling in vdW heterostructures without affecting the underlying physics.

## 1.4 Transition metal dichalcogenides

### 1.4.1 Crystalline structure

Transition metal dichalcogenides are a family of covalently bound layered crystals held together by Van der Waals interactions. They are composed of one atomic layer made of transition metal atoms (M) sandwiched in between two layers of chalcogen atoms (X) arranged in a trigonal prismatic structure. In this work, I used exclusively the 2Hc-polytype semiconducting TMDs[8](M=Mo, W ; X= S, Se). A scheme of this structure

[8]Unless otherwise specified I will use the TMD abbreviation to refer to 2Hc semiconducting TMDs.

is shown in figure 1.10a. Notice that due to the H2c stacking, this polytype presents a broken mirror symmetry.

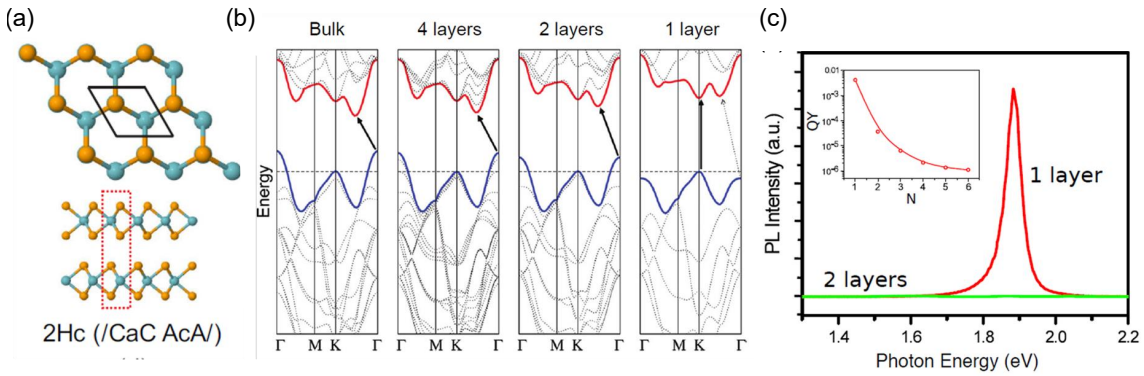


Figure 1.10: **Crystalline structure of TMDs.** (a) Top and bottom view of the 2Hc polytype. The primitive unit cell is shown with the diamond in the top view and the square box in the side view. Figure adapted from [56] (b) Calculated band structure from bulk to monolayer $MoS_2$ showing the indirect-to-direct bandgap transition at the K point. Figure adapted from [57]. The arrows show the lowest energetic transition (c) Photoluminescence spectra recorded at 300K on mono and bilayer $MoS_2$. The inset shows the quantum emission yield as a function of the number of layers. Figure adapted from [58]

### 1.4.2 Band Structure: Indirect-to-direct transition.

In 2010, it was theoretically and experimentally demonstrated that TMDs undergo an indirect-to-direct bandgap transition when thinning down from bulk to the monolayer limit (Figures 1.10b and 1.10c)[58, 57]. A signature of this transition is the large increase in photoluminescence (PL) emission signal coming from the atomically thin TMDs (figure 1.10c). This transition arises from the changes in the band structure as we approach the monolayer limit.

In the bulk crystal, the maximum of the valence band (VB) is at the Γ point, and the minimum of the conduction band (CB) is midway in between the $\Gamma - K$ direction (as shown in figure 1.10b). The proximity between adjacent chalcogen atoms affects the relative position of the bands since their orbitals overlap[9]. Meanwhile, at the K (K') point, the electronic states are strongly localized over the transition metal[10] and are composed mostly of hybrid orbitals $d_{x^2-y^2} \pm id_{xy}$ in the VB and $d_{z^2}$ in the CB [59, 60, 61]. This 'protects' the gap at the K point by shielding it from the influence of adjacent layers. The combination of these two effects results in an increase of the bandgap at Γ as N decreases until eventually, in the monolayer limit, the indirect bandgap becomes larger than the direct bandgap at K (figure 1.10b).

[9]The electronic states at the Γ point are influenced mostly by the $p_z$ orbital of the chalcogen and the

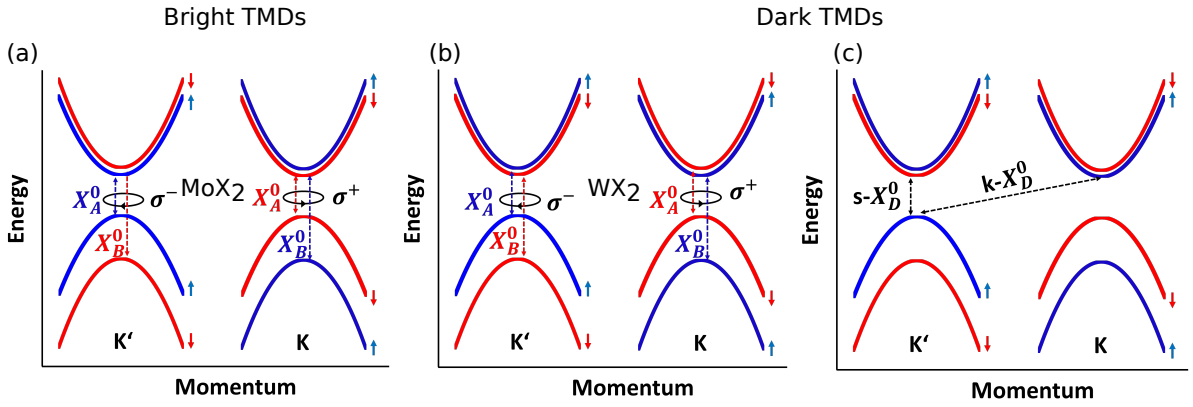


Figure 1.11: **Band structure of TMDs.** Sketch of the band structure at the K and K' valley of a monolayer TMD for (a) 'bright' ($MoSe_2$, $MoTe_2$) and (b-c) 'dark' ($WSe_2$, $WS_2$, and $MoS_2$) TMDs. The lowest spin-allowed energy transition is called the A-exciton ($X_A^0$) whereas the highest is called the B-exciton ($X_B^0$). (c) Sketch of band structure at the K and K' valleys of a dark monolayer TMD showing the spin-($s - X_D^0$) and momentum-forbidden ($k - X_D^0$) transitions.

### 1.4.3 Fine structure of TMDs: spin-orbit coupling

Due to the transition metal d-orbitals, TMDs exhibit strong spin-orbit interaction which lifts the spin-degeneracy of the bands. The magnitude and sign of the split $\Delta_{SOC}^{CB/VB}$ depend on the symmetry of the orbitals involved. For instance, $\left|\Delta_{SOC}^{VB}\right|$ varies from 160 meV (in $MoSe_2$ and $MoS_2$) up to 400 meV (in $WSe_2$ and $WS_2$), whereas for $\left|\Delta_{SOC}^{CB}\right|$ is one order of magnitude smaller [62, 63, 64, 65, 66]. More interestingly, depending on the choice of the transition metal, the sign of $\Delta_{SOC}^{CB/VB}$ can be different for the CB and the VB within the same valley. In W-based TMDs, the splitting occurs in the same direction ($\Delta_{SOC}^{CB} >$ and $\Delta_{SOC}^{VB} > 0$) and in Mo-based TMDs the opposite is true ($\Delta_{SOC}^{CB} < 0$ and $\Delta_{SOC}^{VB} > 0$). The immediate consequence is that in Mo-based TMDs, with the exception of $MoS_2$, the lowest energy transition is spin-allowed, whereas, in W-based TMDs, it is spin-forbidden. As a result, Mo-based TMDs are referred to as "bright" whereas W-based TMDs are "dark"[11]. The values of $\Delta_{SOC}^{CB/VB}$ for different TMDs are shown in table 1.1. A sketch of the band structure of bright and dark TMDs is provided in figure 1.11. We can see that the splitting of the bands happens in opposite directions for the K and K' valley and gives rise to two spin-allowed transitions per valley: $X_A^0$ and $X_B^0$ (see figure 1.11).

The last ingredient necessary to understand the fine structure of the bands comes from a symmetry argument. Due to their crystalline structure, inversion symmetry is broken in monolayer TMD. Consequently, optical selection rules become chiral, and circularly polarized light ( $\sigma^+$ and $\sigma^-$) can couple selectively to one of these transitions. This

$d_{z^2}$ orbital of the transition metal.

[10]The contribution of the chalcogens is negligible in comparison.

[11]Sometimes "dark" TMDs are referred to as "grey". The reason is that the lowest energetic transition can be excited under appropriate geometries.

valley-dependent optical selection rule effectively 'locks' the spin and valley degrees of freedom.

| System | $\mu$ ($m_0$) | $E_b$ (meV) | $E_g$ (eV) | $\Delta_{SOC}^{VB}$(meV) | $\Delta_{SOC}^{CB}$(meV) |
|---|---|---|---|---|---|
| hBN/$MoSe_2$/hBN | $0.275 \pm 0.015$ | 221 | 2.160 | 160-200 | 20 |
| hBN/$WSe_2$/hBN | $0.350 \pm 0.015$ | 231 | 1.874 | 400-500 | -36 |
| hBN/$MoS_2$/hBN | $0.175 \pm 0.007$ | 180 | 2.238 | 140-150 | -14 |
| hBN/$WS_2$/hBN | $0.2 \pm 0.01$ | 167 | 1.890 | 320-430 | -30 |

Table 1.1: Table containing different parameters for TMDs such as effective mass $\mu$, the excitonic binding energy $E_b$, the electronic bandgap $E_g$ and the VB and CB splits due to spin-orbit coupling.These values are extracted from the following articles [66, 62, 63, 64, 65, 67, 68]

### 1.4.4 Optical properties of TMDs

A semiconductor can be excited by promoting an electron from the valence band to the conduction band, leaving an empty electronic state behind. This empty electronic state behaves like a positively charged particle referred to as *hole*. Electrons and holes can bind together through the Coulomb potential. This bound electron-hole pair can be described in terms of a quasiparticle known as the **exciton**. It is essential to distinguish between the energy required to induce an interband transition (the energy required to create a *free* electron-hole pair) and the energy required to create an exciton (i.e., bound electron-hole pair). The former is referred to as the **electronic bandgap** or **free particule bandgap**, and the latter is referred to as the **optical bandgap**. The difference between the two lies in the binding energy of the exciton (see section 1.8). Furthermore, in TMDs, excitonic effects are important due to the reduced dimensionality and relatively large effective masses, as we will discuss in section 1.5. As a result, the optical properties of TMDs are entirely dominated by excitons, which, as we will see now, appear as sharp resonances in both absorption and emission spectra.

#### Optical absorption in TMDs

In section 1.4.3, we have seen that there are two allowed electronic transitions per valley. As a result, one has two absorption bands associated with these transitions denoted A-exciton ($X^0$) and B-exciton ($B_{1s}$). The $X^0$ corresponds to the lowest energy transition and $B_{1s}$ to the highest. Figure 1.12 shows a differential reflectance spectrum (see chapter 2) on which we can observe dips associated with the absorption from these quasiparticles. The resonance marked as $X^*$ originates from another excitonic species that we will discuss in section 1.7.

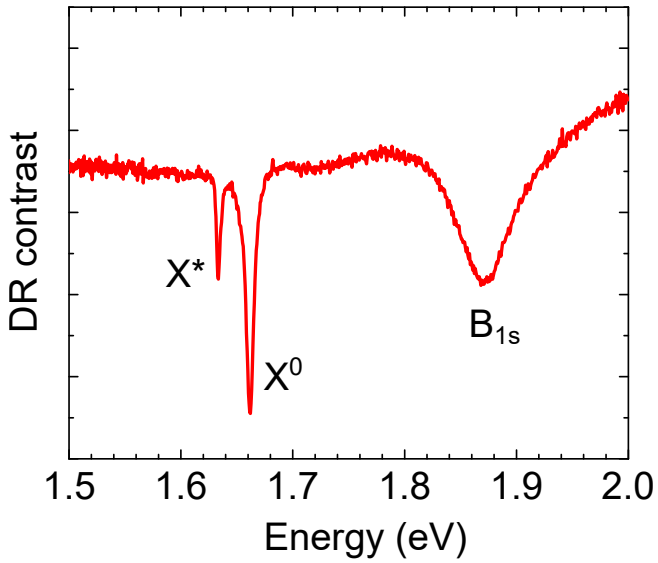


Figure 1.12: **Reflectance contrast of hBN-capped $MoSe_2$.** The neutral A-exciton (marked $X^0$) is signaled as well as the B exciton ($B_{1s}$) and a charged exciton ($X^*$).

The reflectance of the TMD contains information on the monolayer's absorption and therefore on the light-matter interaction in TMDs. This quantity is linked to the absorption coefficient and as a first approximation, it can be modeled in terms of a modified Lorentz oscillator [62, 69, 70]. However, one must be careful since this does not take into account interference effects that can modify the DR spectra. Nevertheless, the Lorentz oscillator model provides us with a simple picture to describe the underlying physics. In this approximation, excitons act as oscillating dipoles with energy $E_p$ in a medium of complex refractive index $n_b + ik_b$. As a result, the dielectric constant of the medium can be written as:

$$\epsilon(E) = (n_b + ik_b)^2 + \sum_p \frac{A_p e^{i\beta}}{E_p^2 - E^2 - i\gamma_p E} \tag{1.18}$$

Where $A_p$ is an amplitude, $\beta$ is a phase factor, and $\gamma_p$ is the damping that accounts for the width of the resonances. This is a phenomenological model that captures well the interaction between the TMD and light. The phase factor $\beta$ allows us to include the effect of additional processes that can alter the absorption profile. For instance, the interaction between excitons and a continuum of states can induce Fano-like shapes of the dielectric constant [62].

### Emission spectra of TMDs

Similar to absorption, the emission of TMDs is dominated by excitonic effects. Figure 1.13a shows room temperature photoluminescence (PL) spectra of 4 different TMDs. These spectra are characterized by one intense resonance corresponding to the radiative recombination of the A-exciton. This resonance has a linewidth given by $\sim k_B T$and is

broadened further due to the presence of inhomogeneities in the environment. At low temperatures, the PL spectra are much sharper and more complex (figure 1.9). These spectra display a manifold of transitions arising from other excitonic particles that we will discuss in section 1.7).

In PL, one uses a photon to induce an electronic transition between the VB and the CB of the TMD (see figure 1.13b). After this process has occurred, the hot carrier population rapidly relaxes through phonon emission and forms excitons in the process. These excitons can be formed either inside (cold excitons) or outside (hot excitons) the light cone. The A-exciton is the lowest energetically allowed transition and therefore defines the threshold for optical absorption and emission (and, in consequence, corresponds to the **optical bandgap**). Hot luminescence from higher-lying states can also appear in PL, but it is less intense (e.g., small shoulder in the green spectra in fig. 1.13a).

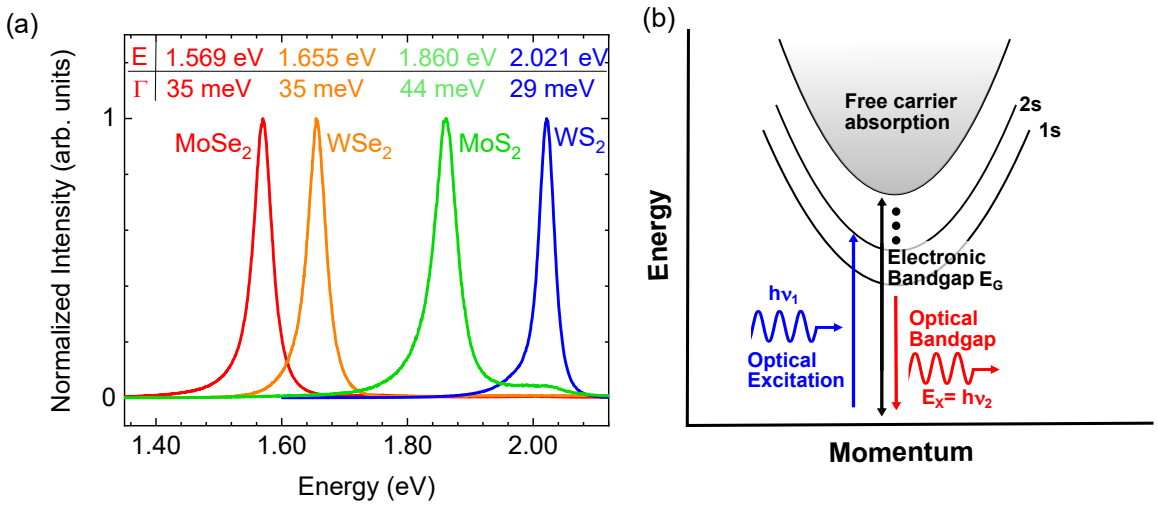


Figure 1.13: **Photoluminescence of TMDs**.(a) Typical room temperature photoluminescence spectra of hBN-capped $MoSe_2$, hBN-capped $WSe_2$, hBN-capped $MoS_2$ and $WS_2$/ITO. For each TMD, the spectra are composed of a sharp resonance corresponding to the recombination of the neutral A:1s exciton ($X^0$). The position E and FWHM ($\Gamma$) of each peak are indicated in the table on top of the spectra. (b) Scheme of the photoluminescence process in TMDs. The electronic ($E_G$) and optical bandgaps ($E_X$) of the TMD are shown in black and red, respectively. An incident photon of energy $h\nu_1$ (shown in blue) is absorbed by the TMD. Upon non-resonant excitation, excitons can be formed in highly excited states. Afterward, excitons recombine radiatively by emitting a second photon of energy $\hbar\nu_2 = E_X$ (shown in red).

### 1.4.5 Phonons in TMDs

TMD layers have three atoms per unit cell and, as a consequence, host nine different phonon modes (Figure 1.14). In contrast to graphene, no Kohn anomalies are present and as a consequence, electron-phonon interactions are weaker than in graphene. Furthermore,

due to their heavier atoms, their typical phonon frequencies are lower as well. These range from 150 $cm^{-1}$ to 500 $cm^{-1}$.

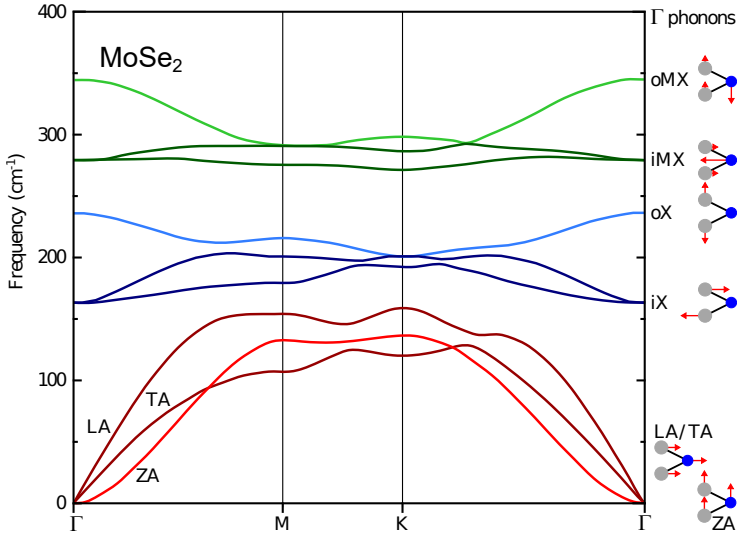


Figure 1.14: **Vibrational properties of TMDs.** Phonon dispersion relation calculated for MoSe2 monolayer. The diagrams on the right hand side of the graph represent the atomic displacement associated with each phonon mode. Figure extracted from [71] (original data from [72]).

These properties can be probed using the Raman effect as described for graphene in section 1.2.2. However, this is out of the scope of this thesis.

## 1.5 Excitons in TMDs

Strictly speaking, excitons arise from the *direct* Coulomb interaction between an electron and a hole. To understand what is meant by this, we need to look at the Coulomb interaction at small scales. Indeed, when we consider the fermionic nature of electrons, we can discriminate between two different contributions arising from the Coulomb potential. The first contribution corresponds to the classical Coulomb interaction and it is the term that defines the binding energy of the exciton. The second contribution arises from a purely quantum phenomenon: Pauli's principle. This term is dominant at short distances and takes into account the electron and hole spin as well as their valley index. This has a direct impact on the separation between different states involving bright and dark excitons and therefore defines the fine structure of the excitonic states. Let us illustrate briefly these terms using a simple example. Consider two charged particles (e.g. an electron and a hole) interacting in a vacuum. The Hamiltonian for such a system is given by:

$$H = H_a + H_b + V_C \tag{1.19}$$

In this expression $H_a$ and $H_b$ are the free-electron and free-hole Hamiltonians and $V_C$ is the Coulomb interaction. Suppose that we know the free-particle wavefunctions $|a_1\rangle$

and $|b_2\rangle$, such that $H_a |a_1\rangle = E_a |a_1\rangle$ and $H_b |b_2\rangle = E_b |b_2\rangle$. Where $E_a$ and $E_b$ are the associated eigen-energies. Then, we can construct an Ansatz to solve the Schrödinger equation for this system. To simplify things further, let us assume that we can separate $|\Psi\rangle$ in its spatial- and spin-dependent parts ($\left|\psi^{S/A}\right\rangle$ and $\left|\theta^{A/S}\right\rangle$ respectively).

$$|\Psi\rangle = \left|\psi^{S/A}\right\rangle \left|\theta^{A/S}\right\rangle \tag{1.20}$$

The superscript $S/A$ indicates the symmetry of the wavefunction (S for symmetric and A for anti-symmetric). Since the Coulomb potential does not depend on the spin of the charges we can forget momentarily about $\left|\theta^{A/S}\right\rangle$ and write:

$$\left|\psi^{S/A}\right\rangle = \frac{1}{\sqrt{2}} \left(|a(\vec{r}_1)b(\vec{r}_2)\rangle \pm |a(\vec{r}_2)b(\vec{r}_1)\rangle\right) \tag{1.21}$$

It is interesting to notice that it is the Pauli exclusion principle that imposes the symmetry of the spin-dependent part of the wavefunction even though the Coulomb potential depends only on the spatial part. From this expression we can compute the expectation values of the Coulomb potential:

$$\langle V\rangle_{S/A} = \langle a_1 b_2| V_C |a_1 b_2\rangle \pm \langle a_1 b_2| V_C |a_2 b_1\rangle \tag{1.22}$$

The first term on the right-hand side corresponds to the **direct term** ($D(\vec{r}_1, \vec{r}_2)$) and the second one to the **exchange term**($J(\vec{r}_1, \vec{r}_2)$). Let us express these terms in their integral form:

$$D(\vec{r}_1, \vec{r}_2) = \iint d^3r_1 d^3r_2 \frac{|\phi_a(\vec{r}_1)|^2 |\phi_b(\vec{r}_2)|^2}{|\vec{r}_1 - \vec{r}_2|} \tag{1.23}$$

$$J(\vec{r}_1, \vec{r}_2) = \iint d^3r_1 d^3r_2 \frac{\phi_a^*(\vec{r}_1)\phi_b^*(\vec{r}_2)\phi_a(\vec{r}_2)\phi_b(\vec{r}_1)}{|\vec{r}_1 - \vec{r}_2|} \tag{1.24}$$

From these equations, we can conclude that the exchange term becomes negligible at large distances. Indeed, this integral depends on the term $\phi_a(\vec{r}_2)\phi_b(\vec{r}_1)$ (orbital overlap of the wavefunctions) which vanishes at large separations [73].

### 1.5.1 Exciton binding energy

At first order, solving the "exciton problem" is equivalent to solving a Schrödinger equation for a hydrogen-like system. Therefore, it presents a Rydberg-like series of excited states. Indeed, using the effective mass approximation, the calculated exciton binding energy can be written as:

$$E_B^{3D}(\vec{X}) = \frac{\mu/m_0}{\epsilon^2} \frac{1}{n^2} Ry(H) = \frac{E_X}{n^2} \tag{1.25}$$

In this equation, $\mu$ is the reduced mass of the electron-hole system[12], $m_0$ is the free electron mass, $n$ is the principal quantum number, $\epsilon$ is the dielectric constant of the medium, and $R_y$ is the Rydberg constant for hydrogen. However, equation 1.25 applies for a 'bulk' semiconductor where the electron and hole can move freely. In the monolayer limit, quantum confinement becomes important, and the 3D-hydrogen model is no longer accurate. To account for the confinement, one can add a potential $V_0$ to the Hamiltonian of the system[13]. The corresponding 2D hydrogenic series can be written as[14]:

$$E_B^{2D} = \frac{E_X}{(n-1/2)^2} \tag{1.26}$$

This equation captures the effect that dimensionality plays on the Coulomb interaction. As we approach the monolayer limit, the screening of the surrounding medium decreases, and therefore the Coulomb interaction becomes stronger. Indeed, we can verify this if we combine equations 1.25 and 1.26:

$$E_X^{2D}/E_X^{3D} = \frac{n^2}{(n-1/2)^2} > 1$$

A back-of-the-envelope calculation allows us to estimate exciton binding energies in TMDs in the 500 meV range[15]. This is a substantial value compared to other more common semiconductors such as bulk GaAs or AlGaAs/GaAs quantum wells where the binding energies are 4.3 meV and 21 meV, respectively [76]. This enormous binding energy is the reason why excitons in TMDs can be observed even at room temperature. Typical values for excitonic binding energies and effective masses of TMDs are reported in table 1.1.

Despite the success of the 2D hydrogen model, experimental evidence showed that it is not enough to describe the full Rydberg series of excitonic states [77]. Figure 1.15a shows the differential reflectance contrast spectrum (see section 1.4.4) of a monolayer $WS_2$ measured at low temperature. Each resonance is a signature of an excited excitonic state. Plotting the energy position of the resonances as a function of the principal quantum number n (figure 1.15b), one can see that for small values of n, the trend does not match the expected $\frac{1}{(n-1/2)^2}$ dependence. Instead, for small n, the Coulomb potential behaves as log(r), where r is the electron-hole distance. To understand this non-hydrogenic behavior, we must look at some of the limitations of the 2D-hydrogen model:

1. We have neglected the interaction along the z-direction. The electric field permeates

[12]The latter is given by $\mu = \frac{m_e^* m_h^*}{m_e^* + m_h^*}$ where $m_e^*$ and $m_h^*$ are the electron and hole effective masses respectively.

[13]This confinement potential is usually assumed constant, and it is equal to the work function of the surface.

[14]For simplicity, we have omitted the solutions on the "z" direction. The confinement leads to an additional term on the binding energy similar to an electron trapped in a finite quantum well.

[15]The parameters taken for the calculations were $\mu = 0.25\ m_0$ and $\epsilon_{eff} = 5$ [74, 75].

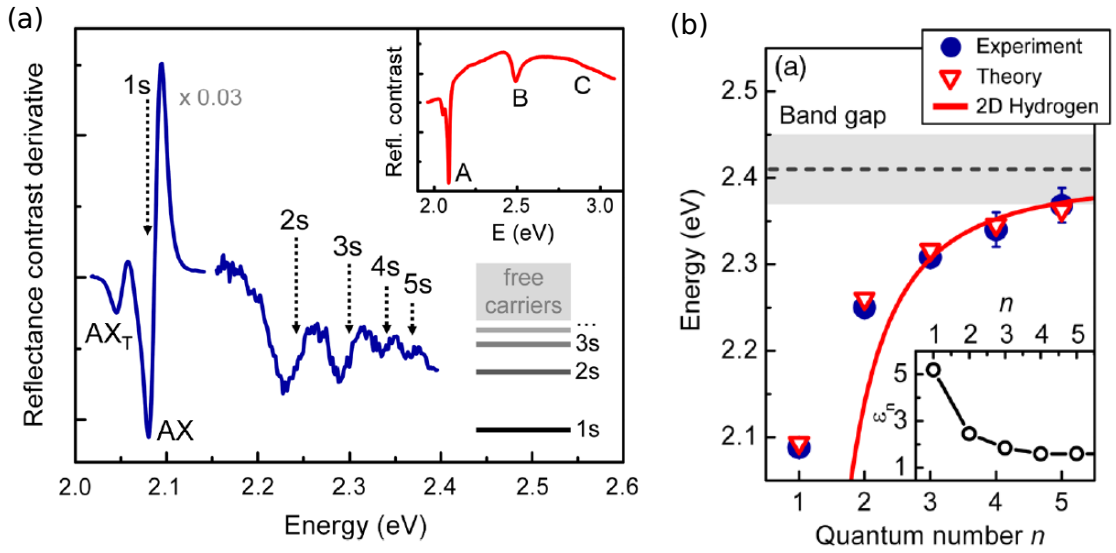


Figure 1.15: **Non-hydrogenic Rydberg series.**(a) Derivative of the reflectance contrast for monolayer $WS_2$ on $SiO_2$. The 1s A-exciton is visible as well as its corresponding Rydberg series up to the 5s state. The inset shows the full spectra and the absorption line corresponding to the B-exciton as well. (b) Experimental and theoretical values of the transition energies as a function of the quantum number. The 2D-H model is not sufficient to explain the behavior at low n. The inset shows the effective screening as a function of the quantum number n. Figures adapted from [77].

both the TMD and the region outside the monolayer (See figure 1.16a).

2. We did not take into account the different dielectric constants of the TMD and its surroundings.

In consequence, the Coulomb potential does not behave like a $\frac{1}{r}$ function. Instead, to take into account the effect of the geometry and the dielectric properties of the surroundings one can use the Rytova-Keldysh potential [77, 78]:

$$V(r) = -\frac{\pi e^2}{(1+\epsilon_s)r_0}\left[\mathbf{H}_0\left(\frac{r}{r_0}\right) - \mathbf{Y}_0\left(\frac{r}{r_0}\right)\right] \tag{1.27}$$

In this expression, $\mathbf{H}_0$ and $\mathbf{Y}_0$ are respectively the Struve and Neumann functions, r is the distance between the hole and the electron and $r_0$ is a parameter that can be understood as a screening length. In reality, $r_0$ is a crossover term between two electron-hole distance regimes. The typical value for $r_0$ varies depending on which method was used to compute it; in general, it ranges from 30 up to 80 Å[77, 74]. The "effective medium" model agrees with the observed deviations from the 2D hydrogenic series (figure 1.15b). Interestingly, one can recover the $\frac{1}{r}$ distance dependence for $r > r_0$. We can understand this in terms of an interplay between the screening and the spread of the electric field lines (See figure 1.16b). In the long-distance regime ($r > r_0$), the screening is essentially that of the surroundings, and the electron-hole pair behaves as a 2D-hydrogenic system.

In contrast, for $r < r_0$, most of the field is confined inside the TMD, and the effective screening increases.

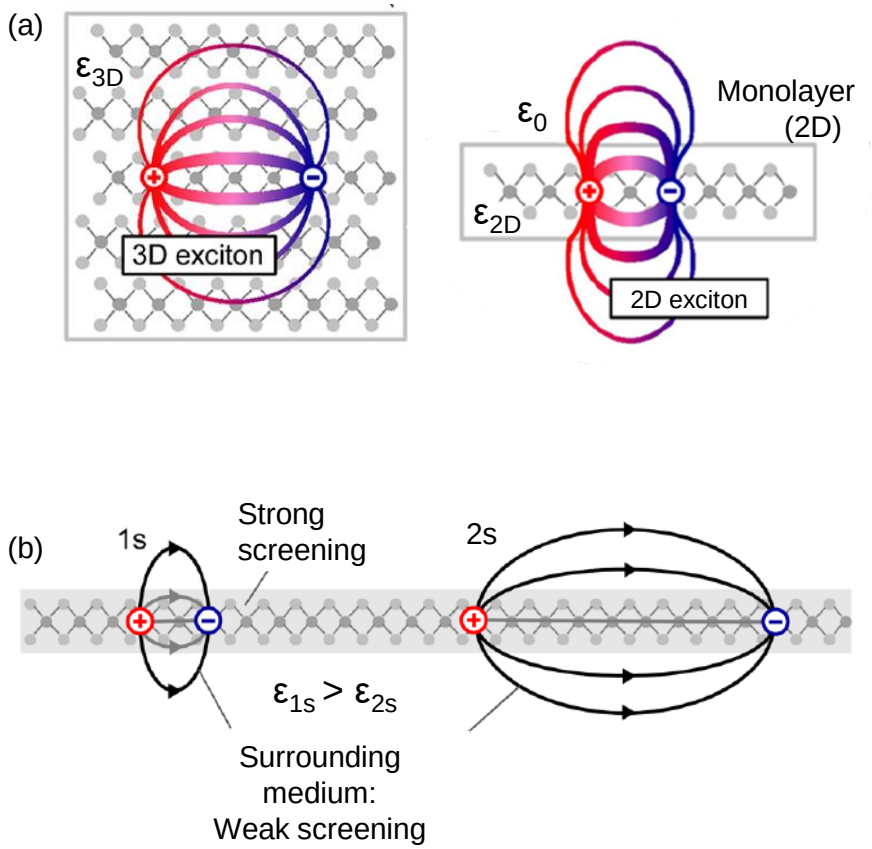


Figure 1.16: **Effective medium model.**(a) Real-space comparison between a 3D and a 2D-exciton. The 3D exciton 'feels' the full $\epsilon_{3D}$ screening, whereas the 2D excitons 'feel' the effect of the surrounding medium. (b) For larger n states, the field permeates more the weaker surrounding medium, and therefore the effective screening decreases. Figures adapted from [77]

One can go further into the formalism; some of the hypotheses should be revisited and justified further. For instance, since excitons are tightly bound, their Bohr radius is small ($\sim$ 1 nm), and in consequence, their spread on the reciprocal space is large. This means that they could be sensitive to the non-parabolicity of the bands, and the effective mass approximation is then questionable. Nevertheless, the effective medium approximation agrees quite well with the experiments and gives us an excellent simple model to understand the physics behind excitons in TMDs.

### 1.5.2 Exciton dynamics

As it moves through the crystal, an exciton interacts with its environment. This interaction gives rise to energy and momentum transfers that eventually open new exciton relaxation pathways. This process is called exciton recombination and it happens on a typical timescale $\tau_X$ which depends on both intrinsic and extrinsic factors.

### Radiative recombination

Radiative recombination is an intrinsic process that occurs when an exciton loses its energy through photon emission. This corresponds to the spontaneous decay of the exciton and it happens on a characteristic timescale $\tau_{rad}$ which depends on the coupling between the exciton and the surrounding EM field. Due to the strong Coulomb interaction in TMDs, radiative recombination occurs in ps-timescales at low temperatures [19].

### Non-radiative recombination

As its name suggests, this process occurs when the exciton loses its energy through any other mechanism that bypasses light emission. For instance, excitons can be scattered by defects in the lattice or give their energy away to phonons. These processes and their efficiencies are therefore entirely driven by extrinsic factors such as strain, temperature, and energy and charge transfer towards nearby materials. We are going to denote the characteristic timescale for non-radiative recombination as $\tau_{nr}$.

### Quantum yield

From the previous discussion, we conclude that the excitonic dynamics are determined by a competition between radiative and non-radiative recombination. We define the emission quantum yield $\eta$ as

$$\eta = \frac{\Gamma_{rad}}{\Gamma_{rad} + \Gamma_{nr}} \tag{1.28}$$

Where $\Gamma_{rad}$, $\Gamma_{nr}$ are the radiative and non-radiative recombination rates. The total rate $\Gamma = \Gamma_{rad} + \Gamma_{nr}$ is given by the inverse of the exciton lifetime.

$$\Gamma = \frac{1}{\tau_X}$$

or equivalently:

$$\frac{1}{\tau_X} = \frac{1}{\tau_{rad}} + \frac{1}{\tau_{nr}} \tag{1.29}$$

At room temperature, excitons in TMDs have lifetimes in the order of a few ns. However, at low temperatures, non-radiative processes become less efficient and radiative recombination dominates the dynamics. As a result $\tau_X$ shortens down to few ps [19]. In the following, we are going to discuss briefly both the low and room temperature regimes.

### Low temperature dynamics

Radiative decay is driven by spontaneous emission and it is a fully intrinsic process. To decay radiatively, the exciton must be able to couple to light. This coupling depends on many factors such as:

- **Occupation number of VB and CB**: The transition occurs from an occupied CB state to an unoccupied VB state.

- **The density of states of the bands**: There must be an initial electronic state and a final one. That is, $DoS(E_{CB/VB}) \neq 0$.

- **Energy conservation**: The emitted photon of energy $h\nu$ must respect energy conservation. This means that for an exciton with a center-of-mass momentum $K_{exc}$ :

$$h\nu = E_X + \frac{\hbar^2 K_{exc}^2}{2M} \tag{1.30}$$

- **Momentum conservation**: To couple to free propagating light, the center-of-mass momentum of the exciton has to match the in-plane momentum of the photon $q_{xy}$ such that:

$$q_{xy} = K_{exc} \tag{1.31}$$

  This means that there is a continuum of photon states that satisfy the condition:

$$q = \frac{\hbar\nu}{c} = \sqrt{K_{exc}^2 + q_z^2} \tag{1.32}$$

  Where q is the momentum of the emitted photon, and $q_z$ is its out-of-plane momentum component. Notice that the freedom of choice of $q_z$ gives rise to completely intrinsic recombination paths. In the ideal 3D case, momentum conservation would impose that $\vec{K}_{exc} = (K_x, K_y, K_z)$ and $\vec{q} = (q_x, q_y, q_z)$ must be equal. This is satisfied only by 1 photon mode. Moreover, as this photon propagates through the crystal, a nearby lattice site can reabsorb it, creating another exciton in the process. This everlasting emission-reabsorption process can be described in terms of a hybrid quasiparticle called **exciton-polariton** giving rise to radiative recombination rates that depend on extrinsic processes such as scattering with defects or with phonons.

We can deduce the following relation from equations 1.31 and 1.32:

$$q \geq K_{exc}$$

.

This condition defines a region on which excitons can couple to light. For optical frequencies at normal incidence, this so-called lightcone has a width of $\vec{q} = \frac{2\pi}{\lambda} \approx 10^7$ m$^{-1}$ which is much smaller than the typical size of the first Brillouin zone $\vec{k} = \frac{2\pi}{a} \approx 10^{10}$ m$^{-1}$. This means that we can consider essentially vertical transitions. To recombine radiatively, excitons residing outside of the lightcone must give away their momentum either to de-

fects or phonons. For 2D-Wannier excitons and light propagating perpendicular to the monolayer, the intrinsic radiative lifetime can be written as:

$$\tau_{rad}^{0} = \frac{1}{2\Gamma_0} = \frac{1}{2}\frac{\hbar\epsilon}{q_{xy}}\left(\frac{E_X}{e\hbar\nu_K}\right)^2 (a_B^{2D})^2 \tag{1.33}$$

Where $\epsilon$ is the dielectric constant, $a_B^{2D}$ the exciton's Bohr radius and $\nu_K$ is a parameter related to the interband matrix element of the electron's momentum[16][79]. With this in mind, there have been theoretical approaches to calculate the parameters shown in equation 1.33. For a binding energy of 500 meV, a radiative lifetime of 0.3 ps can be estimated [19]. This lifetime is shorter than the measured values which are in the 2 ps range. The disagreement between theory and experiment comes from the out-of-equilibrium nature of the initial exciton population. Indeed, as a consequence of the quasi-resonant excitation, the exciton population resides entirely within the light cone and is not in equilibrium with the lattice. Exciton-phonon interaction thermalizes such a population on a timescale that is much slower than the intrinsic recombination lifetime. As a consequence, light emission occurs prior to thermalization. This has been confirmed in time-resolved photoluminescence spectroscopy measurements (TRPL, see section 2.3.4) where $\tau_X$ can be directly accessed. Figure 1.17a shows a series of TRPL spectra recorded at different temperatures. The inset in the figure shows the extracted value for the lifetime as a function of temperature. We can see that $\tau_X$ remains constant from 4K up to 40K for monolayer $MoSe_2$. To understand why this is a signal of non-equilibrium dynamics, let us discuss the effect of temperature.

### Temperature effect on the exciton dynamics

Figure 1.17b shows a scheme of the dynamics of an out-of-equilibrium excitonic population. In general, this population should thermalize either by exciton-exciton interaction or through phonon emission. These thermalization paths can 'kick out' a fraction of the excitons from the lightcone on a timescale $\tau_{esc}$. This appears as a second longer decay time in TRPL spectra. Therefore, the experimentally measured excitonic lifetime ($\tau_X$) has two competing components: the exciton-phonon interaction and the intrinsic radiative recombination. In other words, we can consider $\frac{1}{\tau_X} = \frac{1}{\tau_{rad}^0} + \frac{1}{\tau_{esc}}$. As we ramp up the temperature, exciton-phonon interaction becomes more frequent and therefore, $\tau_{esc}$ becomes smaller. When $\tau_{esc} < \tau_{rad}^0$, temperature-driven effects become dominant and the recombination dynamics can be considered as coming from a thermalized excitonic population. This means that for intrinsic radiative times shorter than the typical exciton-phonon interaction time, $\tau_X$ is temperature independent as shown in figure 1.17a for $T \leq 40K$.

[16] Usually referred to as the Kane velocity.

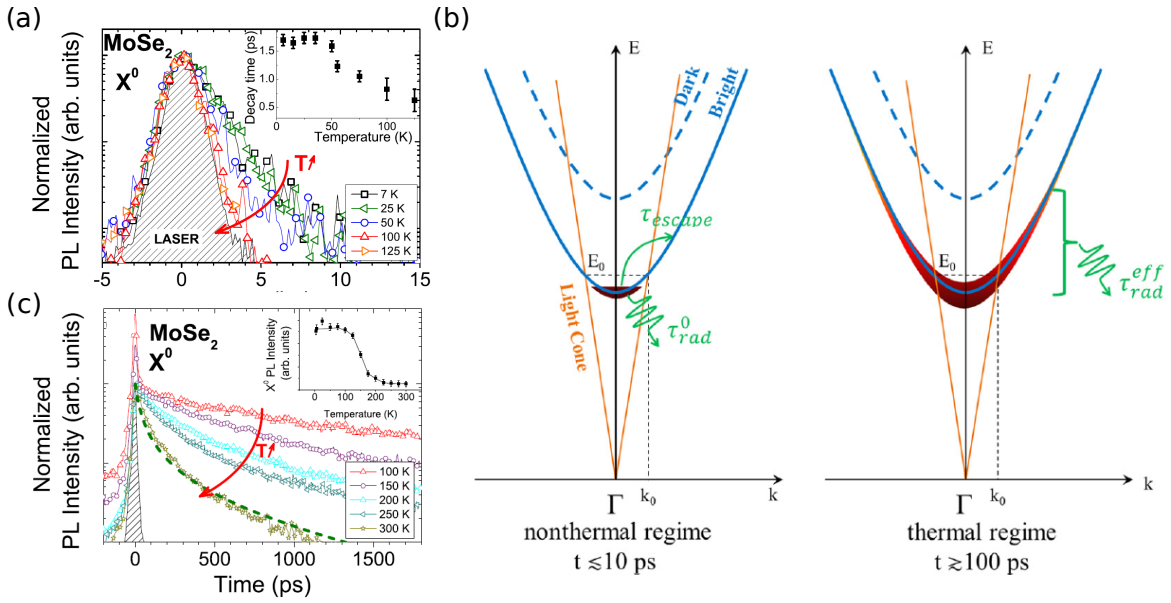


Figure 1.17: **Low temperature excitonic dynamics.**(a) TRPL spectra of $MoSe_2$ from 7K to 125K. The inset shows the evolution of the decay time as a function of T. We can see that up to 40K the lifetime remains mostly unaffected. (b) Scheme of the excitonic population before thermalization (left), at short times some of the population escapes from the light cone. At longer timescales, once the population is thermalized (right) we end up with an effective recombination lifetime which is longer than the intrinsic one. (c) TRPL spectra of $MoSe_2$ from 100K to 300K. The intensity of the excitonic emission line is shown in the inset as a function of temperature. The sharp decrease of intensity occurs because non-radiative processes are no longer negligible. Figure adapted from [19]

If we want to describe the regime for which a thermalized population can be considered, we must perform a thermal average on the exciton decay rate. It can be shown that the corresponding correction to the radiative lifetime is given by[17][79, 19]:

$$\tau_{\text{rad}}^{\text{eff}} = \frac{3}{2}\frac{k_B T}{E_0}\tau_{rad}^{0} \tag{1.34}$$

where $E_0 = (\hbar K_X)^2/(2M_X)$ is the kinetic energy of the excitons within the lightcone and T is the temperature of the lattice. $\tau_{\text{rad}}^{\text{eff}}$ represents an effective radiative lifetime and scales linearly with T. This expression is correct as long as $k_B T$ is significantly larger than the homogeneous linewidth of the exciton and its kinetic energy. The inset in figure 1.17a shows that this effective model explains the behavior of $\tau_X$ for $T \geq 50$ K. As a broad estimation, at 60 K ($k_B T \sim 5$ meV) $\tau_{\text{rad}}^{\text{eff}} \sim 1$ ns for $E_0 \leq (\hbar k_0)^2/2M \approx 13\mu$eV. Although the qualitative agreement between this model and the experiments is remarkable, we need to consider non-radiative processes. Indeed, for $T \geq 100$K, non-radiative processes become important. This translates into a sharp decrease in PL intensity as shown in the inset of figure 1.17c.

[17]Althought not included in the calculation, it is important to mention that this rate will also be affected by spin- and momentum-forbidden inter- and intra-valley scattering.

This temperature-induced quenching can be understood if we come back to equation 1.28. As temperature increases, $\tau_{\text{rad}}$ and $\tau_{\text{nr}}$ change. On one hand, $\tau_{\text{nr}}$ is (among others) given by thermally activated phonon-induced processes, and hence $\tau_{\text{nr}}$ decreases with temperature. On the other hand, the radiative lifetime is an increasing function of temperature (equation 1.34). In TMDs, the situation is made more complex since the lowest-lying exciton may be either optically bright (for $MoSe_2$ and $MoTe_2$) or dark (for $WSe_2$, $WS_2$). In the former case, an overall decrease of the luminescence quantum yield is observed as T increases [62]. In the latter case, the PL signal will be reduced at low temperatures because the dark excitonic state will be mostly populated [80]. As the temperature increases, the higher-lying bright exciton (located typically $\sim$ 30-40 meV above the dark state) is thermally populated, giving rise to an overall increase of the luminescence yield as T augments [62, 80]. The existence of a lowest-lying dark or bright state therefore has major consequences on the low-temperature emission spectra of TMDs as shown in figure 1.20.

### 1.5.3 Tuning the excitonic dynamics with hBN

In section 1.3 we saw that encapsulating a TMD with hBN led to narrow emission lines approaching the homogeneous limit. This is directly linked to the homogeneous substrate provided by hBN as well as the protection from environmental contaminants. However, the encapsulation of hBN also has a fundamental effect on the excitonic dynamics. For practical reasons, in PL spectroscopy, one uses laser excitation higher than the excitonic energy. As it was discussed before, this creates an out-of-equilibrium excitonic population that will relax rapidly through phonon emission towards excitonic states within the light cone. This relaxation time $\tau_{\text{rel}}$ depends sensitively on the environment and its homogeneity and is typically in the order of hundreds of fs. The first effect of hBN encapsulation is to provide a homogeneous environment; as a result, exciton-phonon interaction is reduced, and $\tau_{\text{rel}}$ increases up to 18 ps [25]. However, hBN encapsulation also affects the recombination dynamics. Indeed, from equation 1.15 we can see that dielectric screening modifies the radiative recombination lifetime. The higher the dielectric screening, the longer the radiative recombination time. Furthermore, there is a second effect that is also present and can dominate the intrinsic dynamics of the excitonic population. It has been shown that the encapsulation with hBN modifies the local density of optical states since hBN defines an optical cavity together with the underlying $Si/SiO_2$ substrate (Figure 1.18a). This modification gives rise to a Purcell-like effect which modifies $\tau^0_{rad}$. In fact, it modifies it in such a way that we can selectively tune $\tau^0_{rad}$ by appropriately choosing the thickness of the bottom hBN layer [25], as it is shown in figure 1.18b. Therefore, by encapsulating with hBN, we have a way to tune the dynamics of excitons in TMDs. We will exploit this effect in chapter 3.

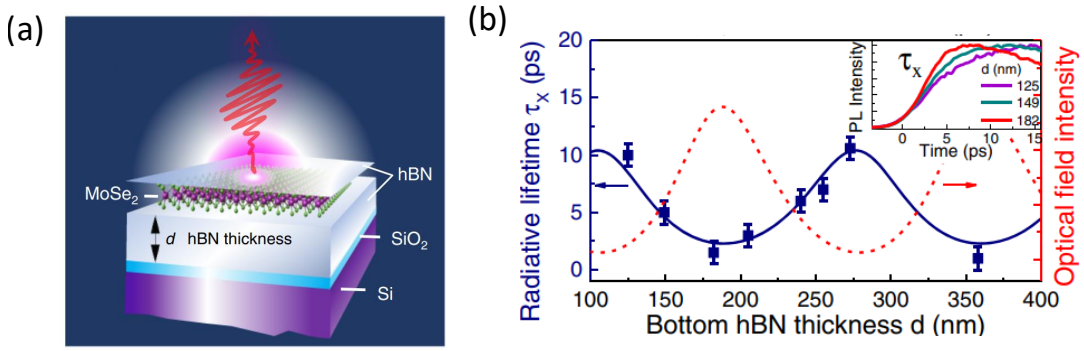


Figure 1.18: **Tunable excitonic dynamics.** (a) Scheme of the hBN-capped samples. (b) Radiative recombination lifetime as a function of the Bottom hBN thickness. We can see that by selectively choosing this thickness we can tune the value $\tau_{X^0}^{\text{rad}}$. Figure extracted from [25].

## 1.6 Spin-Valley properties

The remarkable spin-valley properties of TMDs arise from the combination of spin-orbit coupling and the lack of inversion symmetry. Indeed, these two effects cause the spin and valley degrees of freedom to lock. To understand why, let us discuss each effect separately:

1. **Spin-orbit coupling**: Spin-orbit coupling (SOC) is important in TMDs because of the d-orbitals contribution coming from the transition metal. Time-reversal symmetry imposes that the consequent band splitting occurs in opposite directions for the K and K' valleys. This can be understood by taking a look at the spin-orbit Hamiltonian.

$$H_{SO} \propto \vec{L} \cdot \vec{S} = (\vec{r} \times \hbar\vec{k}) \cdot \vec{S} \tag{1.35}$$

Where $\vec{L}$ is the orbital angular momentum, $\vec{S}$ is the spin of the carrier, $\vec{r}$ is the position and $\vec{k}$ is its wavevector. This expression explicitly shows the coupling between $\vec{k}$ and $\vec{S}$. From this, one can deduce the following relations:

$$H_{SO}(K,\uparrow) = H_{SO}(-K,\downarrow) = -H_{SO}(K,\downarrow) = -H_{SO}(-K,\uparrow) \tag{1.36}$$

Meaning that for different valleys, the split must be of opposite sign: $E(K,\uparrow) = -E(-K,\uparrow)$.

2. **Lack of inversion symmetry:** In section 1.1.2, we saw that the CB is influenced by $d_{z^2}$. This means that for the corresponding electronic states $l = 2$ and $m = 0$. In the case of the VB, we have $l = 2$ and $m = \pm 2$ instead. In a crystal with inversion symmetry, K and K' are completely equivalent. In monolayer TMDs this is not the case, meaning that the value of $m$ must be different for each valley. Since $\sigma^{\pm}$

polarized photons carry ±1 units of angular momentum, dipole-allowed transitions become chiral and therefore valley dependent.

To summarize, the consequence of the strong spin-orbit coupling is that the lowest allowed transitions in each valley have opposite spins. The consequence of the lack of inversion symmetry is that we can address one valley only with one handedness of light and not the opposite. If we combine both, it means that one can deliberately create spin-polarized excitons in one valley or the other with a suitable polarization of the incident light. This is what is called **spin-valley locking**.

### Valley polarization and valley coherence

In TMDs, spin-valley locking allows us to draw an analogy between the K and K' valley and a spin-$\frac{1}{2}$ system. Indeed, since the exciton's components can be in either valley, we can define a "pseudospin" that accounts for this. An exciton whose components are in the K valley can be labeled as having a valley pseudospin of $|+1\rangle$ whereas in the K' valley its pseudospin is $|-1\rangle$[18]. With this analogy, we can see that the binary nature of the valley pseudospin could be interesting for information storing [81]. Any application, however, is limited by the spin-polarized population lifetime and its coherence. In a device, the exciton must preserve its pseudospin at least as long as a gate operation time. Therefore, it is imperative to understand the dynamics of valley polarization. To quantify the degree of polarization, we use the following quantity:

$$\rho = \frac{I^{\mathrm{Co}}(\sigma^{\pm}) - I^{\mathrm{Cross}}(\sigma^{\pm})}{I^{\mathrm{Co}}(\sigma^{\pm}) + I^{\mathrm{Cross}}(\sigma^{\pm})} \tag{1.37}$$

Where $\rho$ is the degree of polarization and $I^{\mathrm{Co}}(\sigma^{\mu})$ and $I^{\mathrm{Cross}}(\sigma^{\mu})$ are the $\sigma^{\mu}$ ($\mu = \pm$) component of the emitted light when exciting with the same (Co) and opposite (Cross) polarizations respectively. Experimentally, we can choose to excite with linearly polarized light instead of circularly polarized. In this situation, we excite a coherent superposition of both pseudospins. Indeed, let us write linearly polarized photon states in a circularly polarized base.

$$|V\rangle = \frac{i}{\sqrt{2}}\left(\left|\sigma^{+}\right\rangle - \left|\sigma^{-}\right\rangle\right) \tag{1.38}$$

$$|H\rangle = \frac{1}{\sqrt{2}}\left(\left|\sigma^{+}\right\rangle + \left|\sigma^{-}\right\rangle\right) \tag{1.39}$$

In these expressions, $|V\rangle$ and $|H\rangle$ stand for the vertical and horizontal polarization states of light. From the expressions above, it is clear that each component will excite

[18] It is important to emphasize that the exciton is created with zero momentum. This means that the exciton itself is located at Γ.

populations with different valley pseudospin.

$$|V\rangle \xrightarrow{excites} \frac{i}{\sqrt{2}}\left(|+1\rangle - |-1\rangle\right) \tag{1.40}$$

$$|H\rangle \xrightarrow{excites} \frac{1}{\sqrt{2}}\left(|+1\rangle + |-1\rangle\right) \tag{1.41}$$

These coherent superpositions provide us with a probe for decoherence. If the emitted light remains with the same polarization as the excitation, then the valley coherence is robust. We can quantify the degree of valley coherence for a given polarization as:

$$\gamma = \frac{I^{\mathrm{Co}}(\mu) - I^{\mathrm{Cross}}(\mu)}{I^{\mathrm{Co}}(\mu) + I^{\mathrm{Co}}(\mu)} \tag{1.42}$$

Where $I_{\mu}^{\mathrm{Co}}(\mu)$ and $I_{\mu}^{\mathrm{Cross}}(\mu)$ stand for the $\mu$ polarization-component of the PL intensity $(\mu, \nu = V, H)$ under Co-polarized and Cross-polarized excitation respectively. In the ideal situation, $\gamma$ and $\rho$ should be equal to 1. However, in realistic systems, this is not the case. Decoherence and spin relaxation arise naturally from the interaction between the exciton and its environment. For example, coherence will be lost when the exciton undergoes scattering events with defects, phonons, or other excitons. These events randomize the exciton's phase and as a consequence $\gamma$ decreases.

Similarly, some of these interactions can flip the exciton pseudospin and effectively destroy the degree of valley polarization. For this process to occur, the electron and the hole must jump from one valley to the other. The mechanism behind this is still a matter of debate. The values of $\gamma$ and $\rho$, therefore, depend on the interplay between the exciton's lifetime $\tau_X$ and both the intervalley scattering time ($\tau_v$) and the decoherence time ($\tau_c$). Indeed, we can model this process using rate equations for the excitonic populations. For circularly polarized light, the intensity of emitted light in a given valley is proportional to its excitonic population $n$. Using this, we can rewrite equation 1.37 as:

$$\rho = \frac{n^{\pm} - n^{\mp}}{n^{\pm} + n^{\mp}} \tag{1.43}$$

Where $n^{+}$ ($n^{-}$) is the excitonic population in the K (K') valley. Let us suppose that we begin with $n^{+}$ in the K valley, the rate equation for the population in the K' valley reads:

$$\dot{n}^{-} = \frac{n^{+}(t)}{\tau_v} - \frac{n^{-}(t)}{\tau_v} - \frac{n^{-}(t)}{\tau_X} \tag{1.44}$$

In the stationary limit $\dot{n}^{-} = 0$ and the previous equation can be written as:

$$n^{+} = \left(\frac{\frac{1}{\tau_v} + \frac{1}{\tau_X}}{\frac{1}{\tau_v}}\right) n^{-} \tag{1.45}$$

Substituting this result into equation 1.43 we obtain:

$$\rho = \frac{1}{1 + \frac{2\tau_X}{\tau_v}} \tag{1.46}$$

This is the expression for the valley polarization as a function of the characteristic timescales of the system. If the TMD is excited slightly off-resonance, the relaxation of the hot excitons can create a finite population in the K' valley. We can take this term into account by multiplying the former expression by a value $\rho_0 < 1$.

$$\rho = \frac{\rho_0}{1 + \frac{2\tau_X}{\tau_v}} \tag{1.47}$$

In the case of coherence, we can use a similar approach to quantify it. This time, instead of defining rate equations for each valley, we are going to define rate equations for the coherent and decoherent populations. Let us assume we create a coherent population $n_c$, this population can either lose its coherence and 'feed' the decoherent population $n_d$ or recombine and emit coherent light. That means that for the decoherent population:

$$\dot{n}_d = -\frac{n_d}{\tau_X} + \frac{n_c}{\tau_c} \tag{1.48}$$

If no other dephasing mechanisms are present, then intervalley scattering is responsible for the destruction of the coherence. In other words $\tau_c = \tau_v$. This allows us to rewrite the former expression as:

$$\dot{n}_d = -\frac{n_d}{\tau_X} + \frac{n_c}{\tau_v} \tag{1.49}$$

To calculate $\gamma$, let us take a look at equation 1.42. The intensity of the detected light depends on the contribution of the coherent and decoherent populations. The decoherent part of the emitted light contains both polarizations equally (V and H), whereas the coherent part preserves the excitation polarization. That means that for co-polarized detection, the intensity consists of the coherent population and half the decoherent one, and for cross-polarized detection, it contains only half of the decoherent one. In other words:

$$I^{\text{Co}}(\mu) \propto n_c + \frac{1}{2} n_d$$

$$I^{\text{Cross}}(\mu) \propto \frac{1}{2} n_d$$

Then equation 1.42 can be reduced to:

$$\gamma = \frac{n_c}{n_c + n_d} \tag{1.50}$$

Finally, substituting the stationary solution of equation 1.48 into the former expres-

sion, we obtain:

$$\gamma = \frac{1}{1 + \frac{\tau_X}{\tau_v}} \tag{1.51}$$

If we compare equations 1.51 and 1.47, we see that coherence is more robust than the polarization. This is true only if intervalley scattering is faster than any other dephasing mechanism in the system. In addition, we must not forget that to undergo an intervalley scattering, both the electron and the hole must flip their spin. Therefore, to understand intervalley scattering we must investigate spin relaxation in TMDs. In general, for a semiconductor there are 4 main ways in which spin relaxation can occur[19]:

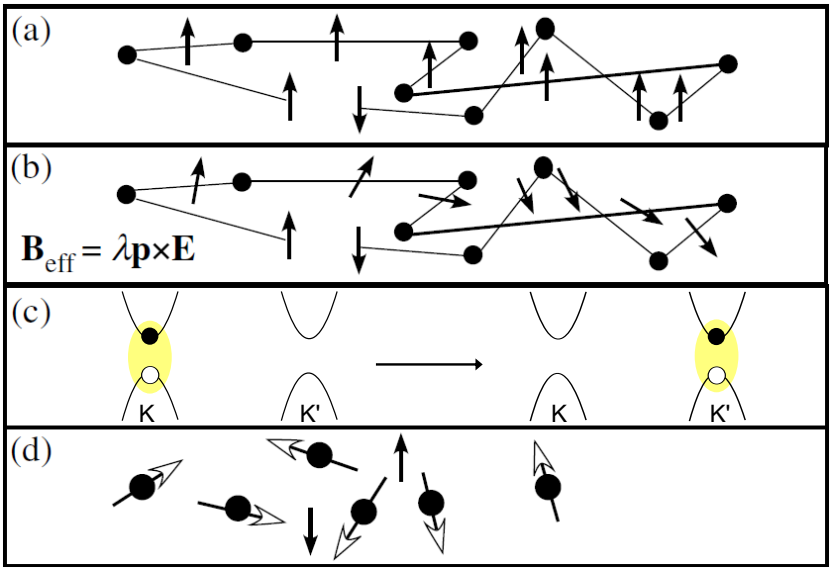


Figure 1.19: **Mechanisms of spin relaxation in semiconductors.** (a) Depiction of the Elliot-Yaffet mechanism in which successive collisions induce an admixture of spin up and spin down states. (b) Dyakonov-Perel mechanism: interaction with scattering centers can be modeled as effective magnetic fields which can induce a spin flip. (c) Exchange interaction: Both electron and hole act as a dipole and can induce the creation of an exciton with opposite pseudospin. (d)Hyperfine interaction: Spin flip caused by the interaction with the nuclei of atoms. Figures (a),(b) and (d) are extracted from [82].

1. **Elliot-Yaffet (EY)**: This process is shown on figure 1.19a. It happens when an electron scatters with impurities or with phonons. The exciton feels an electric field close to impurities that generate SOC. This interaction mixes spin-up and spin-down states making the coupling matrix element $\langle\uparrow| H_{SOC} |\downarrow\rangle \neq 0$. After several scattering events, the spin can be flipped. It happens in semiconductors with and without an inversion center but is not an efficient process. The EY mechanism induces 1 spin flip every $10^5$ collisions more or less [82]. In TMDs, due to the spin-valley locking, EY processes are not significant. Indeed, to relax the spin, the electron and the hole

[19]This part is based in reference [82]

have two options: either they undergo an intraband transition within their valley or they jump to the opposite valley in an interband transition. In the case of intravalley scattering, the hole must jump across a $\approx 100$ meV energy barrier (see table 1.1). In the case of intervalley scattering, spin-valley locking imposes that both electron and hole must simultaneously flip the spin and jump to the other valley. This means that we expect long spin relaxation times and therefore high degrees of polarization. However, this is not the case, it has been shown that the neutral exciton has a fast depolarization time. In other words, to undergo an EY process we need a sharp magnetic scatterer that increases the possibility of a spin flip [64, 83].

2. **Dyakonov-Perel (DP)**: This process is shown in figure 1.19b. It is typical of semiconductors without an inversion center. In a DP process, SOC manifests as an effective magnetic field in the medium that arises from the interaction between the charge carriers and the crystal potential $H_{soc} = \mu_B \vec{B}_{eff} \cdot \vec{\sigma}$. Where $H_{SOC}$ is the spin-orbit Hamiltonian and $\vec{\sigma} = \frac{2}{\hbar}\vec{S}$. Moreover, it can be shown that the effective magnetic field is proportional to the momentum such that: $\vec{B}_{eff} \propto \vec{p} \times \vec{E}$ [82]. Where $\vec{E}$ is the lattice electric field felt by the charge carriers. Every collision event changes $\vec{p}$, and consequently $\vec{B}_{eff}$ changes as well. This change in the precession axis can induce a spin flip. One of the major differences with respect to the EY mechanism is that the spin scattering rate is inversely proportional to the momentum scattering rate. Indeed, in the high scattering limit, the precession axis undergoes a random walk which averages to zero. This means that the scattering is effectively "fixing" the precession axis. In a way, EY mechanism is similar to *collisional broadening* whereas DP is similar to *motional narrowing*[20]. In TMDs the fluctuations of the effective magnetic field due to the DP mechanism are negligible in comparison with the valence band splitting [64].

3. **Bir-Aronov-Pikus (Exchange interaction)**: This process is shown in figure 1.19c. It is due to the Coulomb exchange interaction. The $\vec{k} \cdot \vec{p}$ interaction induces an admixture of the electronic and hole states of different valleys. This admixture couples the excitons with opposite pseudospin and therefore can be thought of as an in-plane magnetic field [84, 85]. It is important to point out that this process is not an intervalley scattering or spin-flip of individual carriers, but rather two simultaneous intraband transitions arising from the Coulomb interaction. Another way to understand this is to think of excitons as oscillating dipoles. When created, an exciton in the K valley interacts with an exciton in the K' valley and vice-versa. This interaction can result in a virtual recombination process where the exciton in the K valley is annihilated and an exciton is created in the K' valley. This mechanism is akin to energy transfer. It can be shown that the effective in-plane magnetic field

[20] which arises from motion in inhomogeneous media.

depends on the momentum of the exciton. This mechanism is the most popular candidate to explain spin-relaxation in TMDs as evidence continues to support it [59, 85, 86, 87, 88].

4. **Hyperfine interaction**: This process is shown in figure 1.19d. The spin of the electron can interact with the magnetic moment of the nuclei. In TMDs, this mechanism is suppressed partly because the overlap between the d orbitals of the hole with the nucleus is negligible [64, 83].

Even though the evidence supports the exchange interaction as the most likely explanation, the debate is not settled yet. Recent studies show that phonon- and disordered-based mechanisms can play a major, even dominant role in the spin relaxation process [89, 90, 91, 92, 93, 94, 95]. A detailed temperature-dependence study of $\rho$ and $\gamma$ could be helpful to settle this debate.

## 1.7 The zoology of excitonic particles

So far, we have described neutral excitons ($X^0$), that is, a single electron coupled to a single hole. A typical low-temperature PL spectrum of monolayer TMDs reveals that there are other lower-lying energy peaks which neutral excitons cannot account for. Figures 1.20a-d contain examples of different low-temperature photoluminescence (PL) and electroluminescence (EL) spectra of W- and Mo-based monolayers[21]. First of all, we can see a qualitative difference between the W- and the Mo-based TMDs. The PL from Mo-based TMDs is characterized by two well-defined sharp peaks: The exciton (marked $X^0$) and the charged exciton at a lower energy (marked $X^*$ or $X^{\pm}$). In contrast, the PL spectrum of W-based TMDs contains a more significant number of peaks arising from defects or other excitonic particles. This difference in PL comes from the bright vs. dark nature of the TMDs. Let us discuss some of these excitonic particles.

- **Trions**:

  All monolayers have native doping coming from the fabrication process[22]. These residual charges can be captured by a free neutral exciton and form a bound system. This three-particle system is called a **trion** ($X^*$) and can be positively ($X^+$) or negatively ($X^-$) charged. Trions can play an important, even dominant role in a monolayer's luminescence spectra and are visible for both bright and dark TMDs (see figures 1.20a-d). In state-of-the-art hBN-capped samples, singlet ($X^*_S$) and triplet trions ($X^*_T$) have been observed as well (figures 1.20b and d). Table 1.2 shows the currently reported values for the trion relative position (binding energy) with respect to $X^0$.

[21] EL is a process where excitons are created through electrical excitation.
[22] It is challenging to find a perfectly neutral sample.

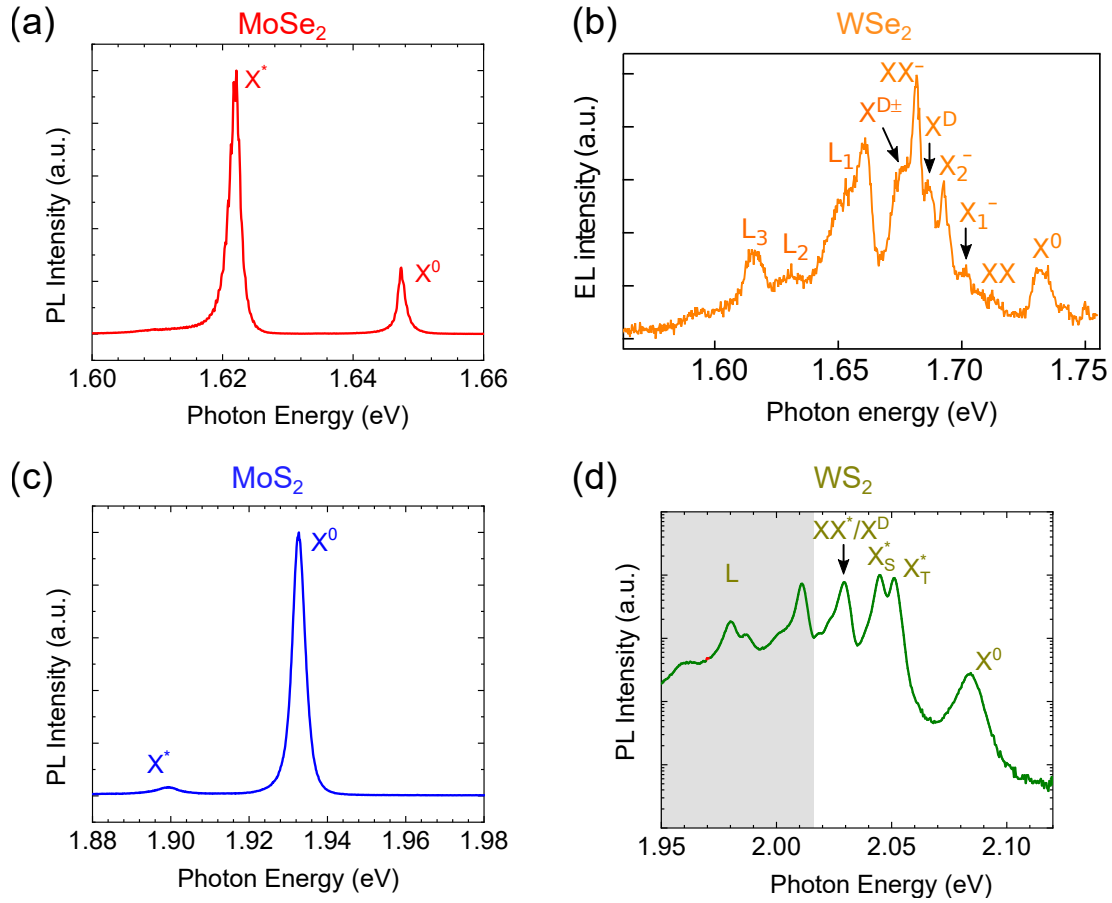


Figure 1.20: **The zoology of excitonic particles.** Photoluminescence (a,c and d) and electroluminescence (b) spectra of hBN-Capped TMDs recorded at 14 K. For each spectrum we have indicated the quasiparticle associated to each resonance. The spectrum in (b) was adapted from [96].

| System | $X^0 - X^{\pm}$ (meV) | $X^0 - X_S^-$ (meV) | $X^0 - X_T^-$ (meV) |
|---|---|---|---|
| $MoSe_2$ | 30 | – | – |
| $WSe_2$ | 21 ($X^+$) | 35-39 | 28-31 |
| $MoS_2$ | – | 27 | 37 |
| $WS_2$ | – | 35-36.6 | 30 |

Table 1.2: Currently reported values for $X^*$. This values are given in relative shift with respect to $X^0$. [96, 9, 97, 98, 99, 100, 101, 102]

- **Dark excitons**:

  Dark excitons arise from spin- or momentum-forbidden transitions. When excited out of resonance, hot excitons can create populations that cannot recombine radiatively due to conservation laws. These excitons are called **dark excitons** ($X^D$) (figures 1.20b and d). The spin-forbidden dark exciton has also a fine structure. All

intervalley excitons are momentum-forbidden for normal incidence of light. Table 1.3 shows the currently reported values for the position of the spin-forbidden dark exciton with respect to $X^0$.

| System | $X^0 - X^D$ (meV) | $X^0 - X^{D,\pm}$ (meV) |
|---|---|---|
| $MoSe_2$ | -1.4 | – |
| $WSe_2$ | 40-45 | 56.5 |
| $MoS_2$ | -14 | – |
| $WS_2$ | 46-55 | – |

Table 1.3: Currently reported values for $X^D$. These values are given in relative energy with respect to $X^0$.[96, 98, 103, 9, 100, 68]

- **Biexcitons**: If the density of excitons is high enough, they can interact with each other. The consequence of this interaction is varied. Most of the time, they undergo exciton-exciton annihilation reducing the yield of the PL. However, sometimes they can form bound states in a sort of 'excitonic molecule'. The latter has been reported in high excitation power regimes and are called **biexcitons**. Moreover, just like excitons they can be neutral ($XX$), or charged ($XX^+$,$XX^-$). Figures 1.20b and d show PL spectra of $WS_2$ and $WSe_2$ where emission from these particles can be seen. The physics of biexcitons and other exotic particles lying in the high power regime is beyond this thesis's scope. Nevertheless, it is essential to point out that they are a useful tool to understand exotic phases of matter [104, 100][23].Table 1.4 shows the currently reported values for the position of the biexcitons with respect to $X^0$.

| System | $X^0 - XX$ (meV) | $X^0 - XX^-$ (meV) | $X^0 - XX^+$ (meV) |
|---|---|---|---|
| $MoSe_2$ | 20 | 5 | 5 |
| $WSe_2$ | 17-20 | 49-52 | – |
| $WS_2$ | 19.2 | 50.4 | – |

Table 1.4: Currently reported values for the biexcitons. These values are given in relative energy with respect to $X^0$.[96, 9, 97, 98, 100]

- **Localized excitons**: The impossibility of avoiding the accidental creation of defects or residual impurities during the fabrication process is a source of localized excitons

[23]Interestingly, at even higher excitation power, the TMDs undergo a Mott transition, and the electron-hole pairs are no longer considered to form bound states. Instead, a correlated phase interpretation is more suited [105, 106, 107]

(marked as L in figures 1.20b and d). Indeed, it creates very efficient quantum traps that take away the kinetic energy of the exciton and bind it around the defect. The overall energy of the bound exciton is reduced by an amount that depends on the defect itself. Therefore, the luminescence is extrinsic by principle. Moreover, some of these defects behave as single-photon sources (SPS) [108, 30].

## 1.8 Electronic vs optical bandgap: determining the binding energy

As discussed in section 1.4.4, the **electronic bandgap** corresponds to the energy required to create a free electron-hole pair. In contrast, the **optical bandgap** represents the energy required to create an exciton. Moreover, we have seen that one can measure the optical bandgap ($E_{X^0}$) using the optical emission and absorption from the TMD. If one is able then to measure the electronic bandgap ($E_g$), one could determine the exciton binding energy using the relation:

$$E_b = E_g - E_{X^0} \tag{1.52}$$

Experimentally, the determination of the exciton binding energy can be difficult. The problem lies in the precise determination of the electronic bandgap. For instance, in PL measurements, the intense emission of the excitons and their excited states can shadow the onset of the free carrier continuum. However, one could use the Rydberg series of excitonic states to extrapolate the bandgap (see section 1.5.1). A good approach consists in using a combination of differential reflectance (DR), photoluminescence (PL), and photoluminescence excitation spectroscopy (PLE) to precisely determine the position of these excited states.

Another technique to experimentally determine the electronic bandgap is scanning tunneling spectroscopy (STS). This technique monitors the tunneling current in an STM junction as a function of the voltage applied. The idea is that by changing the voltage, we can probe the local density of electronic states (LDOS) near the bandgap and, with it, determining the onset of the lowest unoccupied CB state and the highest occupied VB state (see section 2.4.4). However, the precise determination of the band onsets in STS spectra is not straightforward. Regardless of the voltage applied, a tunneling current is always measurable, even inside the TMD gap. When the applied bias is within the gap, the TMD essentially acts as an additional tunneling barrier, and we end up probing the electronic states of the material below. Then, one complements these measurements with the optical gap measured through PL and obtains the binding energy.

Moreover, this technique is more sensitive to states with low in-plane momentum [109]. As a result, we can probe the gap at the $\Gamma$ point more easily than that at the $K$ point. Therefore, to accurately determine the bandgap, one needs to be able to explore different

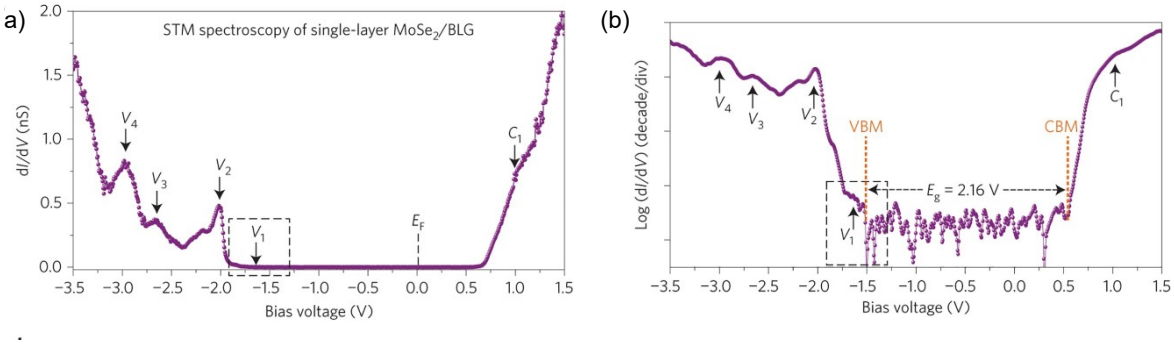


Figure 1.21: **Electronic bandgap determination.**(a) dI/dV spectra of a $MoSe_2$/BLG sample. We can see four resonances in the negative side arising from different bands being probed (b) Zoom on the dI/dV spectra showing the determination of the bandgap. Figures b-d extracted from [26]

orders of conductance within a given voltage window. To facilitate the determination of the bandgap, one can look at the gaps in logarithmic scale. Figures 1.21a and b show a dI/dV spectrum on $MoSe_2$ deposited on bilayer graphene (BLG) in linear and logarithmic scale, respectively. The onset of the conduction is difficult to estimate. It is only when we look at the spectrum in logarithmic scale that the $V_1$ feature becomes clear. This $V_1$ feature corresponds to the valence band onset at the K point. The reader can find a summary of reported values for the electronic bandgap of different TMDs in table 1.5. Unless otherwise specified, STS spectra were taken at cryogenic temperatures (5 K) and ultra-high vacuum (UHV).

### 1.8.1 Optical vs electronic measurements

Let us compare the values reported in table 1.1 and table 1.5. We can see that the estimated $E_b$ using purely optical spectroscopies give systematically smaller values than the ones estimated using a combined approach between PL and STS. Different reasons could explain this discrepancy:

#### Determination of the onset

As mentioned before, STS is weakly sensitive to states with $k_{\parallel} \neq 0$. This means that one would be weakly sensitive to the gap at the K point, which can lead to uncertainty in the determination of the band onsets.

#### Tip induced band bending

At first order, the tunneling current I can be expressed as follows (see section 2.4):

$$I \propto exp(-2\kappa z)$$

| Sample | Electronic bandgap | Fabrication method | Reference |
|---|---|---|---|
| $MoSe_2$/BLG | $2.18 \pm 0.04$ eV | MBE | [26] |
| $MoSe_2$/HOPG | $1.9 \pm 0.01$ eV @300 K | CVD | [110] |
| $MoSe_2$/HOPG | $2.15 \pm 0.06$ eV @300 K | MBE | [111] |
| $MoSe_2$/Graphene | 2.25 eV | MBE | [112] |
| $WSe_2$/HOPG | $2.08 \pm 0.01$ eV | CVD | [113] |
| $WSe_2$/HOPG | $\approx 2$ eV | CVD | [114] |
| $WSe_2$/HOPG | $2.12 \pm 0.06$ eV | CVD | [111] |
| $WSe_2$/HOPG | 2.57 eV | CVD | [115] |
| $MoS_2$/HOPG | $2.15 \pm 0.01$ eV | CVD | [113] |
| $MoS_2$/Quartz | $2.17 \pm 0.04$ eV @300K | Mechanical Exfoliation | [116] |
| $MoS_2$/HOPG | $2.15 \pm 0.06$ eV @77 K | CVD | [117] |
| $MoS_2$/Graphene | $\approx 2$ eV | CVD | [118] |
| $MoS_2$/Au(001) | $\approx 1.5$ eV @77K | CVD | [119] |
| $MoS_2$/Quartz | $2.16 \pm 0.04$ eV @300K | Mechanical Exfoliation | [120] |
| $WS_2$/quartz | $2.38 \pm 0.06$ eV @300 K | Mechanical Exfoliation | [116, 120] |
| $WS_2$/BLG | $\approx 2.5^*$ eV | CVD | [112] |
| $WS_2$/Au(001) | $\approx 2$ eV @77K | CVD | [119] |

Table 1.5: Electronic bandgap measured in different systems using STS. *Estimated from the graphs.

Where z is the tip-sample distance and $\kappa$ is a constant. In reality, $\kappa$ can depend on both the bias voltage applied and the tip-sample separation, leading to changes in the measured conductivity. Furthermore, the presence of the tip can induce a bending of the bands (called tip-induced band bending or TIBB [121, 122]), which can lead to changes in the occupation of states. For instance, a situation that might arise is that states of the semiconductor can be "pulled down" below the Fermi energy of the sample leading to a supplementary contribution to the tunneling current modifying the measured gap (figure 1.22). This has sparked a search for techniques that allows one to accurately measure the electronic bandgap of monolayer TMDs. Recently, an approach involving the acquisition of STS spectra while simultaneously varying the tip-sample distance has been gaining momentum as a suitable technique to determine the bandgap of monolayer TMDs [123, 124, 125, 126]. In this case, there will be a slight distortion of the magnitude of the features in the spectra. This is usually not a problem since we are interested in the onset of the bands, which should not change using this technique.

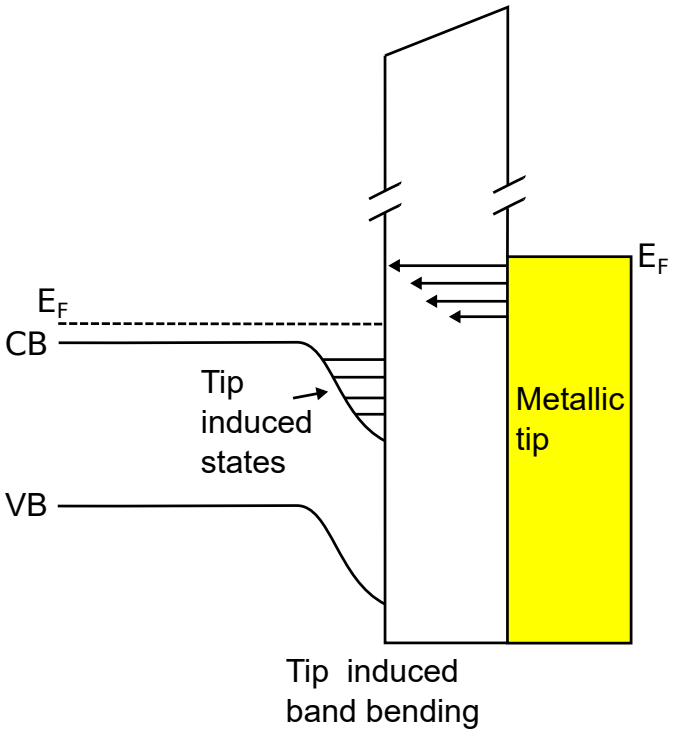


Figure 1.22: **Tip-induced band bending.** The proximity of the tip induces a deformation of the conduction and valence band of the material. This can lead to the creation of additional channels of conductance and modify the observed onset.

### PL is non-local

Usually, to determine the binding energy, one measures the optical bandgap with PL spectroscopy (See section 2.3). However, this technique is by nature diffraction-limited, and as a result, one is measuring the average optical bandgap in the TMD. STS, on the other hand, is a local measurement. As a result, one is sensitive to the local environment of the TMD. It could be helpful to measure the luminescence locally as well. STM-induced luminescence (STM-L) is a technique where one uses the tunneling current to induce the luminescence of a material with atomic resolution. This will be discussed in chapter 2.

### Sample composition

The experimental conditions required to perform an STM experiment usually involve the presence of a conductive substrate. As a result, this could lead to a renormalization of the measured bandgap.

### Nature of STS measurements

Finally, one should also discuss the physical quantity measured in STS. In principle, the charge injection may modify the measured bandgap. This has been observed in the case of single molecules, where instead of probing the gap of the molecule, one can measure

the gap of its charged state. A priori, there could be a similar phenomenon occurring in extended systems such as TMDs.

### 1.8.2 Near-field interaction in VdW heterostructures

Due to their atomically thin nature and sub-nm interlayer distances. VdW heterostructures are sensitive to phenomena that happen at the interface between the layers. These phenomena can ultimately dominate the optical and electronic properties of the heterostructure. Understanding them is of utmost importance as they can provide us with valuable information regarding near-field processes. Moreover, by better understanding the possible processes that can take place at these atomically sharp interfaces, we could exploit them to tune the properties of the heterostructure. In this section, I will briefly describe a few examples of such mechanisms.

#### Band alignment and interlayer excitons

Conventionally, when two semiconductors are put into contact, they will form depletion regions to ensure the continuity of the bands (figure 1.23a). Similarly, in semiconductor-metal junctions, the semiconductor bands will bend forming Schottky barriers at the interface (figure 1.23b). However, in the 2D limit, there is a big problem that arises from the fact that the typical size of the depletion regions is much larger than the monolayers themselves. This means that the vision of band-bending must be revisited in these systems. A more conservative approach would be to consider the new band structure as a superposition of bands instead of a mixing [127, 128] (See figure 1.23c and d). With this simple approximation, we can deduce some interesting properties of vdW heterostructures. For instance, one could think of forming a type II heterojunction from TMDs. In this case, if charge separation takes place between layers, one could end up with an electron in one monolayer and a hole in the other. This exciton is called **interlayer exciton** and it has sparked interest recently due to its robust out-of-plane dipole moment [129, 130, 131] (figure 1.23e).

#### Charge and energy transfer

Out of the different coupling mechanisms that can take place at the interface between two adjacent 2D materials, we will put our attention on charge and energy transfer (figure 1.23e). For practical reasons, I will describe these mechanisms in the context of TMD/graphene heterostructures. As an initial condition, let us consider the TMD as a two-level system that is currently in its excited state.

- **Charge transfer:**

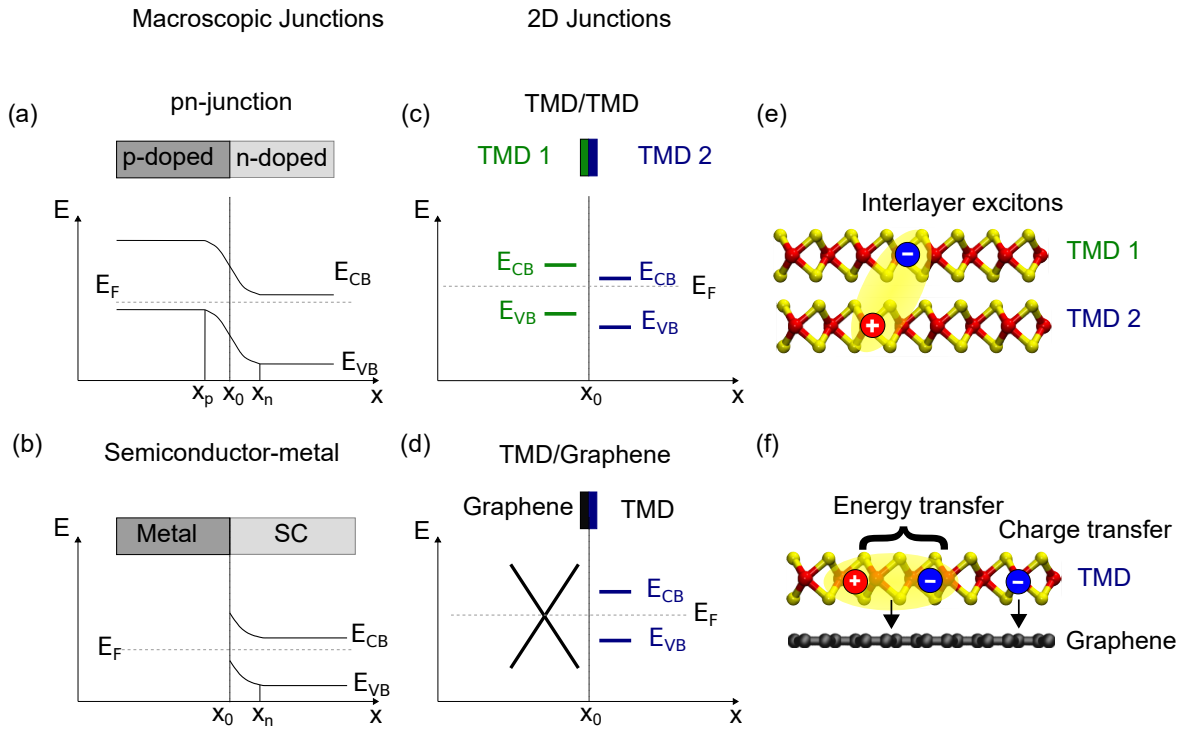


Figure 1.23: **Near field interactions in vdW heterostructures.**(a) pn-junction between two macroscopic semiconductors. At equilibrium, a band bending region is formed between the layers. (b) Semiconductor-metal macroscopic junction. Upon contact, Schottky barriers form at the interface. (c)TMD/TMD junction. Since these materials are thinner than the typical band bending region size, we must adopt a new model. We consider that the bands superpose as shown in the figure. (d) TMD/Graphene junction. In this case, no Schottky barrier is formed. Instead, we can consider the bands to remain unaltered. (e) Scheme of an interlayer exciton where an electron can be located in one layer and a hole in the other one. (f) Scheme of energy and charge transfer processes in the context of TMD/Graphene heterostructures.

As its name suggests, this occurs when an electron (hole) in the conduction(valence) band is spatially transferred towards the adjacent layer into an available state. This transfer must respect energy and momentum conservation and it will result in a quenching of the luminescence as well as a net doping in both layers. Indeed, since the TMD transfer its electron (hole) it can no longer recombine radiatively and it leaves the TMD positively (negatively) doped. This mechanism is behind the formation of interlayer excitons in TMD/TMD heterostructures. Charge transfer in TMD/graphene can occur by means of static charge transfer "in the dark" or it can be photoinduced. The latter has been reported in $MoSe_2$/graphene heterostructures and it occurs in timescales close to several minutes [8]. In this case, electrons transfer to graphene effectively leaving the TMD positively doped. This will be discussed in detail in section 3.2.

- **Energy transfer:** This mechanism occurs when instead of one charge physically transferring from one layer to the other, the whole exciton transfers its energy to an

excitonic state in the second layer. This type of energy transfer is mediated by the Coulomb interaction. If the transfer happens through dipole-dipole interaction it is called Förster energy transfer (FRET) and if it happens through charge tunneling, it is known as Dexter energy transfer (DET). FRET is a long-range mechanism that remains important up to a 10 nm separation distance. Dexter, on the other hand, has a much shorter range ($< 1$ nm) because it depends on the overlap between the excitonic wavefunctions in each layer[24]. Notice that DET resembles a charge transfer mechanism, however, in DET there is no net charge transfer.

In practice, all mechanisms can be present, and differentiating between them can be difficult since all induce a quenching of the PL signal. We are going to come back to this point in chapter 3.

## 1.9 Conclusion

In this chapter, we have introduced the main properties of atomically thin TMDs. We have discussed how one can probe and measure these properties and we have briefly discussed more complex excitonic particles. Furthermore, we have introduced two other 2D materials: graphene and hBN which are going to play an important role in our experiments. We have shown the main properties of each and discuss the mechanism that can arise when we combine them with TMDs.

#### Take home messages

The main aspects of this chapter can be summarized as follows:

- Monolayer TMDs are direct bandgap semiconductors whose optical properties are entirely governed by tightly bound excitons.
- Photoluminescence spectroscopy is a practical technique that allows us to probe excitons in TMDs. In particular, it provides us with a direct measure of the **optical bandgap** of the TMD.
- Spin- and valley-polarized excitonic populations can be created in TMDs under appropriate incident light polarization.
- At low temperatures, the luminescence from TMDs contains contributions from other more complex excitonic particles such as trions, biexcitons, spin- and momentum-forbidden dark excitons, localized excitons, and their respective fine structure.

[24]More precisely, FRET comes from the direct term of the Coulomb potential and DRET from the exchange term.

- Graphene is a 2D semimetal that when coupled with a TMD enables non-radiative decay paths for excitons.
- We can use the Raman spectrum of graphene to obtain information regarding strain and doping trends in a graphene-based heterostructure.
- Encapsulating a TMD with hBN has three effects: First, it protects the layer from external contaminations. Second, it improves the optical quality of TMDs resulting in linewidths close to the homogeneous limit. Third, it can be used to tune the radiative recombination lifetime by choosing the thickness of the substrate below.

Chapter 2

# Experimental Methods

In this chapter, I will present technical details on the experimental techniques I used during my Ph.D. The first part will focus on the sample fabrication. I will described the techniques used to isolate (section 2.1) and transfer 2D materials in order to build vdW heterostructures (section 2.2). In the second part, I will discuss the optical spectroscopy techniques that we used in our investigations of TMD/graphene (section 2.3). The third and final part is dedicated to scanning tunneling microscopy and its applications (section 2.4).

## 2.1 Sample Fabrication

In this section, I will introduce the techniques used to fabricate all samples studied in my Ph.D. All samples were fabricated in the ST-Nano clean room and the 2D lab at the IPCMS.

### 2.1.1 Mechanical Exfoliation

Mechanical exfoliation of graphene and 2D materials was popularized by Geim and Novoselov in 2004 [1]. They used the so-called "scotch tape technique" to isolate single layers of graphene starting from a bulk graphite crystal[1]. Although it seems incredible, by putting scotch tape directly onto the bulk crystal, one can cleave atomically thin layers of high quality. During this thesis, I exclusively used mechanical exfoliation to isolate mono- and few-layers of TMDs, graphene, and hBN. The steps to exfoliate monolayers with high reproducibility are summarized as follows:

1. Put the bulk crystal on a scotch tape (Fig. 2.1-1).

2. Fold the tape around the crystal and peel it off (Fig. 2.1-2).

3. Put a second scotch tape on top of the first one and apply a small pressure (Fig. 2.1-3).

[1]This technique has been used before for instance in ref. [132] but it was popularized by Geim and Novoselov.

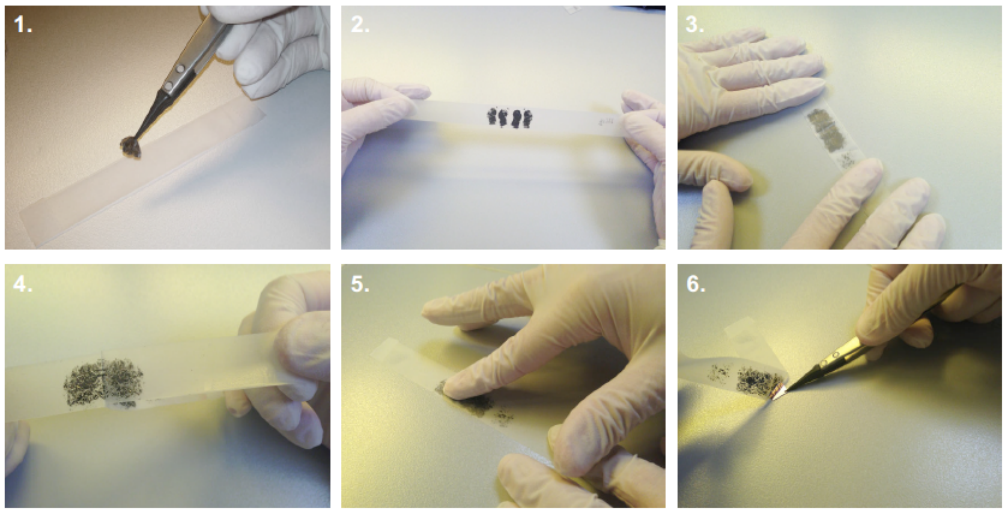


Figure 2.1: **Scheme of the exfoliation process.** (1) A bulk crystal is put onto a scotch tape. (2) The scotch tape is folded over the crystal and peeled off afterward. (3) A second scotch tape is put on top of the first one. (4) The second scotch tape is peeled off and the same procedure is repeated until transparent areas of the crystal appear. (5) The scotch tape is placed onto the target substrate. (6) Carefully peel off the scotch tape. Figure extracted from [38]

4. Gently peel off the second scotch tape. Iterate step 3 with the same tapes until transparent areas of the crystal appear (Fig. 2.1-4).

5. Stick the tape onto the target substrate and massage gently for a few minutes[2](Fig. 2.1-5).

6. Peel off slowly[3] the adhesive tape from the substrate (Fig. 2.1-6). One can also heat the substrate before peeling off the scotch tape. This has been shown to increase the average size of the exfoliated layers [133].

In my case, I used silicon substrates with a 90 nm oxide layer on top. The substrates are cleaned with acetone, ethanol, and isopropyl alcohol before exfoliation. After this, their surfaces were activated by exposing them for 20 min to an oxygen plasma. The activation step is crucial for graphene exfoliation since it increases the adhesion between graphene and $SiO_2$.

## 2.2 Transferring Techniques

Mechanical exfoliation is, by nature, a non-deterministic process. Indeed, after exfoliation, monolayers are distributed at random locations all over the substrate. This ran-

[2]You can introduce a middle step where you heat the sample to 100-120°C before exfoliation for 1 minute. This can generate large areas but the longer the time and higher the temperature the more residues from scotch tape you will have [133].

[3]In some substrates like PDMS one must quickly peel off the scotch tape.

domness limits our ability to build van der Waals heterostructures. One solution consists on exploiting viscoelastic polymers as intermediate substrates and using them to deterministically stack monolayers onto a target substrate. During my Ph.D., I used three different polymer-based methods to build van der Waals heterostructures. I will now briefly describe each one of them, their assets and their limitations.

### 2.2.1 Full dry transfer

This technique relies on a polymer called polydimethylsiloxane (PDMS) and is based on the work of Castellanos-Gomez *et al.* [134]. The idea is to exfoliate the material onto a PDMS stamp instead of the target substrate. After this, we look at the PDMS on a microscope to directly search for monolayers. Once identified through optical contrast, we can deterministically transfer the monolayer using PDMS with help of a transfer station built as a part of the Ph.D. of E. Lorchat (figure 2.2). The transfer station is composed of an optical microscope with three different large working distance objectives: 5×, 10×, and 20×. Then there are two independent movable stages. The first one is an XY stage that allows us to move the microscope with respect to the sample. The second one is an XYZ stage that allows us to move the stamp with respect to the substrate. The sample is held using a pump and is on top of a heating stage that can reach 200 ° C. Finally, the heating stage is placed on a rotational stage allowing us to control the relative orientation between the stamp and the substrate. This process can be iterated as many times as one needs with different monolayers, and one can build the heterostructure layer by layer. The main problem with this technique is that with every iteration, the risk of damaging the stack increases. It is particularly risky for complicated samples (more than four layers for instance).

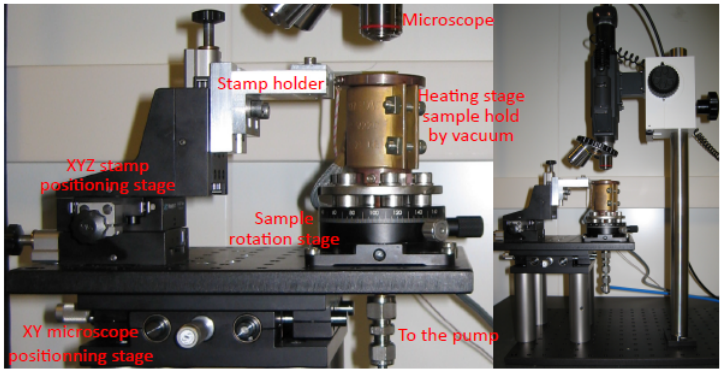


Figure 2.2: **Scheme of transfer station.** A glass slide containing the sample can be put in the XYZ movable stage. The target substrate is fixed on the heating stage by pumping underneath. An optical microscope interfaced with a camera allows us to manage the transfer. Figure extracted from [71].

### 2.2.2 PC-method

#### Preparing the stamp

This technique uses a polymer called PC (Poly bisphenol A carbonate). The idea is to directly pick up the TMDs or graphene from a substrate and then assemble the heterostructure on the polymer stamp. To do this, we need to prepare a stamp that will act as the "pick-up" layer. This stamp is composed of three layers:

- The first layer consists of a PDMS stamp on a glass slide (figure 2.3a).
- Then a layer of PC is gently put on top of the PDMS (figure 2.3b). It is recommended to heat the two to 200°C for 20 seconds to improve adhesion. In general, we need to have a smooth and clean interface between the two; otherwise, we risk breaking the heterostructure during the stacking.
- Finally, a thin hBN layer is put on top of the PC (figure 2.3c-d). The procedure to pick-up the hBN will be explained in the next subsection.

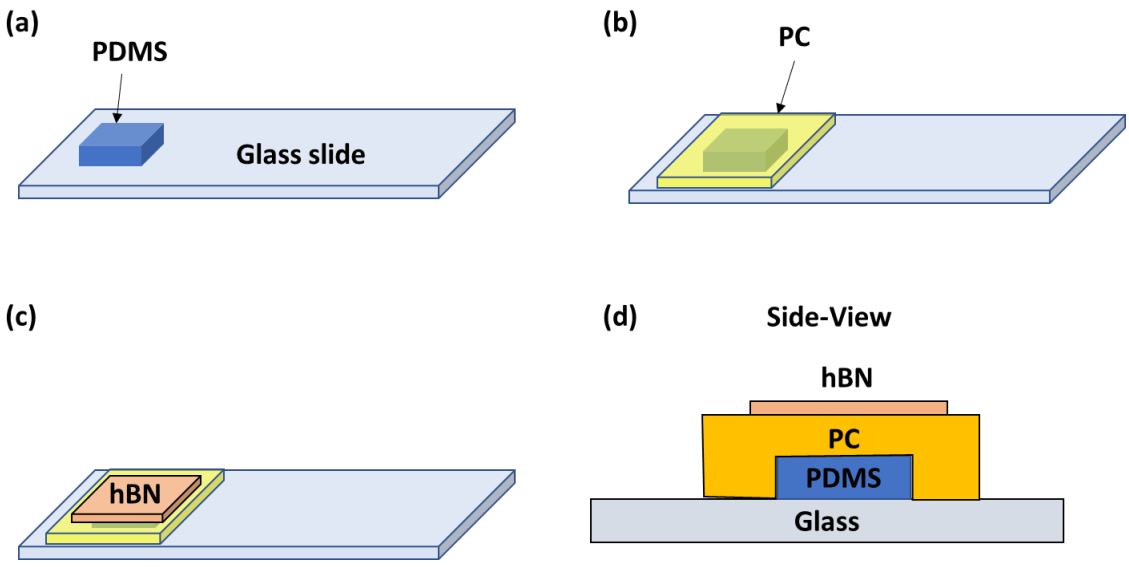


Figure 2.3: **Fabrication process of the PC stamp.**(a) Put PDMS on glass. (b)On top of the PDMS a PC thin film is deposited. (c) Finally a hBN is picked-up from a substrate. (d) Side view of the stamp.

To prepare the PC, we made a 6 % mass solution of PC in chloroform, and we left it stirring up overnight using magnetic agitators. A few drops of the solution are then poured onto a glass slide and sandwiched with a second one. Finally, we slide the glasses one relative to the other along their longest side to obtain a homogeneous film of PC covering each glass.

### Pick-up

The adhesion between PC and hBN becomes more significant than between hBN and $SiO_2$ when heated at 80°C. This allows us to pick-up the hBN layer from the substrate. The precise steps are summarized as follows:

- Identify the hBN on the silicon substrate. It is better if the hBN is thin. If the hBN is too thick, one won't be able to look through it, and assembling the heterostructure becomes challenging.
- Preheat the substrate to 40°C.
- Approach the stamp to the hBN with the positioning stage. A contact line will appear on the image. The contact line will move slowly towards the hBN as we continue to approach.
- It is essential that the contact between the PC and the hBN happens as smoothly and slowly as possible. To control this, we can increase the temperature slightly. This increase makes the polymer expand, which in turn makes the contact line advance.
- Once the stamp has fully covered the hBN, increase the temperature to 80°C.
- Slowly withdraw the stamp.

The result is a stamp composed of hBN/PC/PDMS. Now, the heterostructure can be built directly on the stamp exploiting the strong adhesion between TMDs and hBN[4]. The steps to pick-up any other layer are the same as we just described.

### Deposing

Once the heterostructure is built on the stamp, it is time to put it on the target substrate. To do this, we repeat all the steps for the pick-up except that instead of increasing the temperature to 80°C, we will increase it to 200°C. This will melt the PC on top of the target substrate, and we will finish with a heterostructure encapsulated by the molten PC. Notice that this technique allows us to make only samples with a top hBN[5].

### Cleaning

To clean the sample, we can dissolve the PC in chloroform overnight. The next day, we rinse it with ethanol and isopropyl alcohol and dry it with nitrogen. The general problem

[4]The same applies for graphene.

[5]It is possible to avoid the hBN stamp however, this will render this method difficult as TMDs and graphene adhere weakly to PC.

with this technique is that eventually, one can find some PC residues on the layers. These residues emission can shadow intrinsic signals of the monolayer's PL spectra (See chapter 3).

### 2.2.3 Mixed PC/PDMS method: "hybrid" method

Sometimes, the choice between a full dry transfer and a full PC transfer depends on the complexity and for what use the sample is being built. On the one hand, dry transfer is well adapted for quickly transferring 1L TMDs and building simple heterostructures. However, since the PDMS is in contact with every layer of the heterostructure, it can leave some contamination which can hinder the coupling between adjacent layers. Furthermore, 1L graphene transferred with PDMS is often broken and difficult to spot due to its low optical contrast. On the other hand, the PC-method is well adapted for complex samples involving a top hBN-layer. However, the risk of breaking the heterostructure or the stamp increases with every iteration. Furthermore, after the deposing stage, there is a large portion of residues remaining on the sample. The emission from these residues may shadow the spectral range of interest. One can then combine both methods to build complex samples, reducing the risk of destroying them or contaminate them.

## 2.3 Optical spectroscopies

In this thesis, we use a combination of optical excitation-based techniques to investigate vdW-heterostructures. This section is dedicated to briefly describe their working principles as well as the setup used to perform these measurements.

### 2.3.1 Setup at IPCMS

The setup used for PL, DR, and Raman spectroscopy is shown in figure 2.4a. It consists of a home-built confocal microscope in backscattering geometry. For clarity, a scheme of the experimental configuration is shown in figure 2.4b. To ensure mechanical stability, the setup is mounted on an optical table that stands on a pneumatic system. A laser is focused on the sample with the help of an objective, which in turn can be chosen between several different magnifications. In our current setup we can choose between three lasers: two continuous wave (CW) lasers with wavelengths 532 nm and 633 nm and an NKT pulsed laser with a tunable repetition rate from 2 MHz up to 78 MHz and a pulse width of 50 ps. Moreover, its emission wavelength can be tuned from 480 nm to 2400 nm. To select a particular wavelength, we use a super-K select acousto-optical filter which allows us to obtain single-line emission from 450 nm up to 1100 nm.

We can perform variable-temperature measurements in our setup. For room-temperature studies, the sample is fixed on a piezoelectric XYZ stage (200 $\mu$m $\times$ 200 $\mu$m $\times$ 200 $\mu$m) and

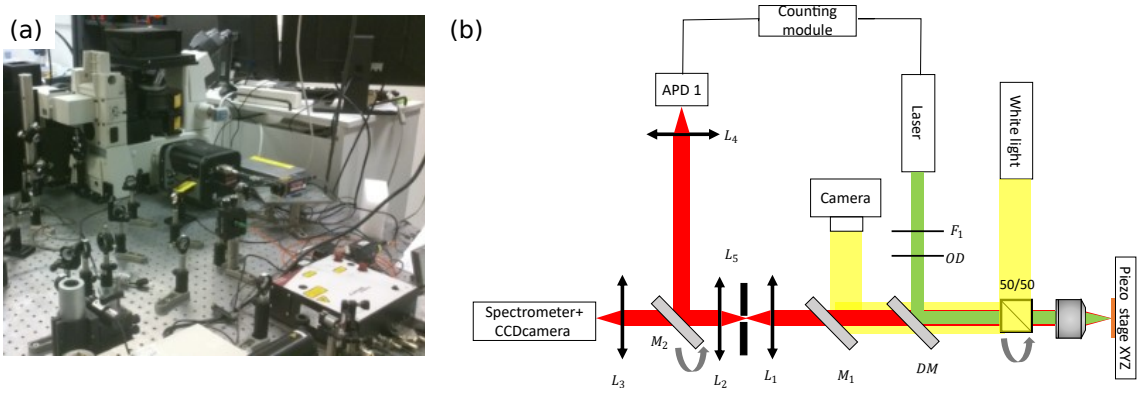


Figure 2.4: **Optical setup.** (a) Optical microscopy setup used in the IPCMS. (b) Schematics of the setup. A laser is focused on the sample with help of an objective. Then the emitted and backscattered light passes through the same objective and is later filtered with a dichroic mirror (DM) and a set of two lenses and a pinhole. This ensures the confocality of our measurement. Then the beam is redirected towards a spectrometer coupled to a CCD camera.

is moved relative to the microscope objective. For low-temperature studies, the sample is placed in a liquid helium flow optical cryostat, and measurements were performed at variable temperature. To optimize stability, the temperature is kept between 11K and 20K. The temperature is measured at a cold finger situated about a couple of centimeters away from the sample and thermally connected to it. The cryostat can be adjusted with precision relative to the optical axis of the setup and fine positioning with sub-micrometer precision is achieved by moving the objective (now mounted on the piezo-stage) relative to the cryostat. At low temperatures, the measurements were done using a $\times 50$ (NA=0.65) long working distance objective. Room temperature measurements were performed using a $\times 150$ (NA=0.95) air objective.

To control the intensity of the incident laser we use a set of optical densities (OD) as well as a half-wave plate together with a polarizing cube for fine-tuning. This is to ensure that the dynamics remain in the linear regime, i.e. avoid non-linear processes such as exciton-exciton annihilation and creation of biexcitons (See section 1.7). The emitted/scattered light (in red) is focused by the same objective and then passes through a dichroic mirror (DM figure 2.4). The beam is again filtered with two lenses and a pinhole. The main idea being that the first lens ($L_1$) will concentrate the light on the pinhole (which is conjugated with the laser spot) and a second lens ($L_2$) will collimate the beam, in order to ensure that we are recording only images originated from the particular area of the sample.

Finally, the remaining beam goes to a diffraction grating that we can choose between 150, 300, 900, 1200 and 2400 grooves/mm and a monochromator with a 500 mm focal length coupled to a liquid nitrogen cooled CCD (charge-coupled device) array; each pixel on the detector corresponds to a particular frequency and the intensity corresponds to

the number of incident photons on each pixel over a time window.

Furthermore, our setup can be adapted to make time-resolved photoluminescence (TRPL, upper branch in figure 2.4b). These measurements resemble that of the normal PL spectroscopy except that here, we used the NKT laser and we are interested in the dynamic behavior of the exciton populations. Short pulses will excite the system and then we look at its PL over time. To do this, a movable mirror ($M_2$ in figure 2.4) can be added to the detection path and we can deviate the emitted signal into a set of avalanche photodiodes (APD) that are connected with the tunable laser to a TCSPC board (PicoHarp 300) allowing us to measure the lifetime of the formed excitons. Each emitted photon has a corresponding delay time $\Delta t$ between the laser emission of the pulse $t_1$ and their arrival at the APD $t_2$. Then, a histogram is formed and by fitting a multi-exponential to this histogram, one can extract the average value of the excitation's lifetime.

### Measuring the optical bandgap

As we have seen in section 1.4.4, one can use PL and DR to measure the optical bandgap. Indeed, in both cases, the spectra are dominated by intense resonances arising from excitons. Then, one can determine the energy position of the A-exciton and, in consequence, determine the optical bandgap. In DR spectroscopy, the incident light is broadband. Instead of a photon of a given energy, one shines white light onto the heterostructures and collects the reflected light. Experimentally, a DR spectrum requires two measurements to be made. First, a reference spectrum on the bare substrate must be taken to establish a baseline of absorption. Second, a reflectance spectrum is acquired on top of the heterostructure. These two spectra are then subtracted and normalized by the baseline in the following manner:

$$\mathrm{DR} = \frac{I_{\mathrm{TMD}} - I_{\mathrm{substrate}}}{I_{\mathrm{substrate}}} \tag{2.1}$$

This expression is linked to the absorbance $\alpha$ of the layer, which in turn is proportional to $\epsilon$ (see section 1.4.4). In PL spectroscopy, the incident light is monochromatic and is used to induce an intraband transition in the TMD. Then, one collects the emitted light. One can also use PL spectroscopy to measure the optical bandgap since the A-exciton completely dominates the emission.

### Measuring the zoology of excitonic particles

In section 1.7, we showed that the low-temperature dynamics in TMDs are dominated by exciton and other excitonic particles. These particles, together with emission arising from defects, appear as prominent peaks in the PL of TMDs. In contrast, in DR, one is weakly sensitive to these particles. In fact, trions can be observed only at intermediate to

high doping. Therefore, if we want to investigate the physics of complex quasiparticles, PL spectroscopy is a valuable technique.

### Measuring excitonic Rydberg states

In section 1.5 we showed that excitons display a series of excited states associated with their band structure. If one can determine with precision the energy position of these states, one could estimate the exciton binding energy. We can access these Rydberg states using a combination of different techniques. First, one can use DR spectroscopy. Indeed, it has been shown that Rydberg states can be readily measured this way [77]. PL spectroscopy can also be used to measure Rydberg states. However, their signatures are weak, and high photon fluences are required to observe them. This implies high exciton generation resulting in PL dominated by non-linear processes.

There is a third approach involving PL at different detunings $\Delta = E_{\text{laser}} - E_{X^0}$. This is called photoluminescence excitation (PLE) spectroscopy and is a complementary technique for PL. Figure 2.5 shows a PLE spectrum of a monolayer of $WSe_2$. The spectrum represents the emission intensity of the neutral exciton as a function of the incoming photon energy. The observed peaks arise from an enhancement of the $X^0$ emission when an excited state is resonantly excited. A diagram for this process is shown to the left of the spectrum.

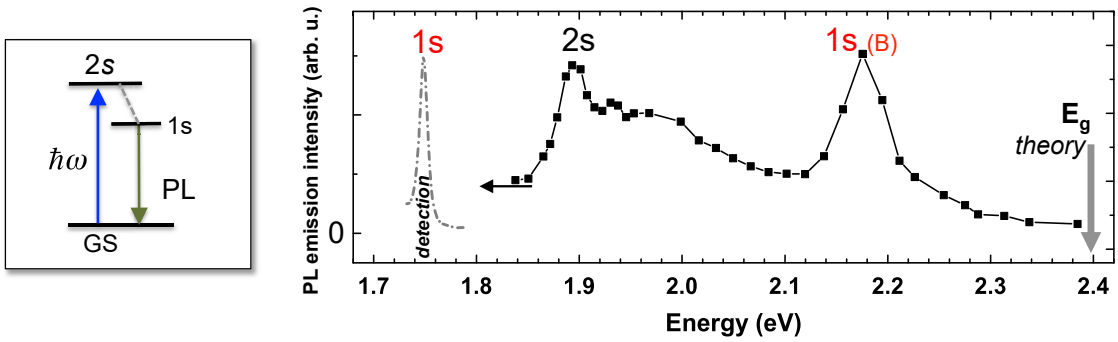


Figure 2.5: **Photoluminescence excitation.** Left: Scheme showing the resonant excitation of the 2s state. Right: $X^0$ PL Intensity as a function of the incoming photon energy. The resonances correspond to different excited states of the sample. Image adapted from [135].

In our case, we will combine DR, PL, and PLE to estimate the binding energies of the heterostructures studied in this thesis. To perform the PLE measurements, we used the NKT laser since it provides us with a tunable source. However, for each measurement, we need to filter the laser carefully. As we have mentioned before, we use an acousto-optical filter to select a particular wavelength. Even though the emission stems mainly from the selected wavelength, there are small contributions from shorter wavelengths in the output of the filter. Therefore, one needs to filter them to ensure monochromatic excitation. To

do this, we used short- and long-pass tunable filters. These filters allow the user to tune the position of the long- or short-wavelength edge by changing the relative angle between the laser and the filter. The short-pass filter ($V_1$) is used to clean the laser signal and ensure a monochromatic excitation. The long-pass filter ($V_2$) is used to filter the laser before entering the spectrometer.

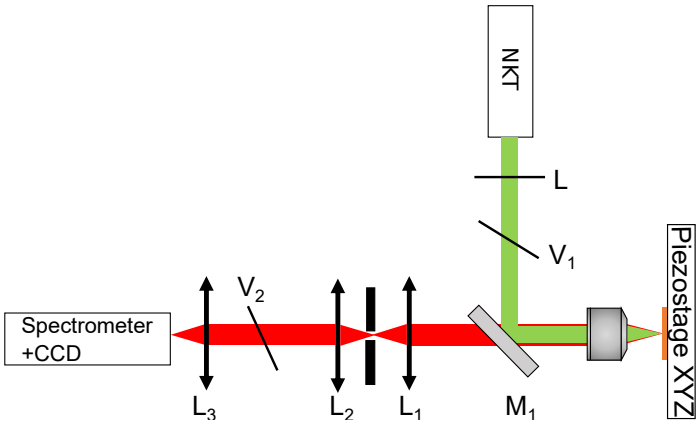


Figure 2.6: **Photoluminescence excitation setup.**

### 2.3.2 Measuring the doping and strain in vdW heterostructures

In section 1.2.2 we have introduced Raman spectroscopy as a technique that allows us to probe the vibrational properties of a material. In particular, we have discussed the case of graphene which can be characterized using the G- and the 2D-modes. In fact, one can use correlations between the linewidths and frequencies of these modes to extract universal behaviors that allow us to characterize graphene-based samples. For instance:

- $\omega_G$ **-** $\Gamma_G$ **correlation:** We can probe the doping in these samples by plotting the variations in the G-mode linewidth as a function of the variations in frequency (figure 2.7b). We can deduce this from equation (1.15).

- $\omega_G$ **-** $\omega_{2D}$ **correlation:** Figure 2.7c shows the evolution of $\omega_{2D}$ as a function of $\omega_G$. Just as before, we can see there is a clear correlation between these parameters. The slope of this correlation gives us information regarding the sign of the charge doping and even the strain on the sample. Indeed, for electron doping $\frac{\partial\Omega_{2D}}{\partial\Omega_G} = 0.2$, for hole doping $\frac{\partial\Omega_{2D}}{\partial\Omega_G} = 0.55$ and for strain $\frac{\partial\Omega_{2D}}{\partial\Omega_G} = 2.2$.

### 2.3.3 Setup for polarized PL spectroscopy

The setup can also be adapted for polarization-dependent studies. As explained in the previous chapter, we can exploit spin-valley locking to obtain information regarding depolarization and decoherence mechanisms in TMDs. Therefore, it is important to have

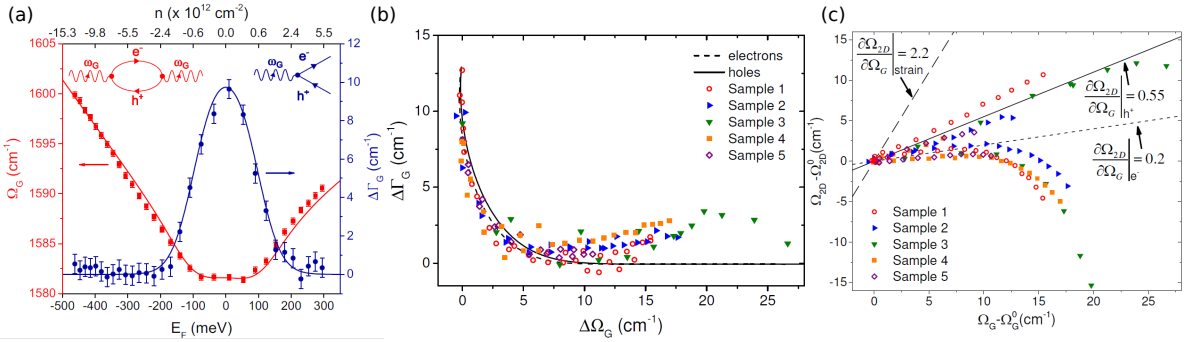


Figure 2.7: **Probing doping with graphene.** (a) G-mode frequency $\Omega_G$ (red) and relative width $\Gamma_G$ (blue) as a function of the Fermi energy. The insets show two Feynman diagrams. These diagrams show the renormalization of the phonon frequency (left) and the broadening of the phonon lifetime (right) due to its conversion into an electron-hole pair. (b) Correlation between the change in FWHM ($\Delta\Gamma$) and the change in the frequency ($\Delta\omega_G$) of the G mode. The points correspond to experimental data, the solid and dashed lines correspond to theoretical predictions for electron and hole doping, respectively. This predictions can be derived from equations (1.12) and (1.15).(c) Correlation between the G- and 2D- mode frequencies. The solid and short-dashed lines correspond to linear fits of the electron and hole doping branches. The long-dashed line corresponds to the evolution of this correlation under pure strain[136]. All figures were extracted from [38]

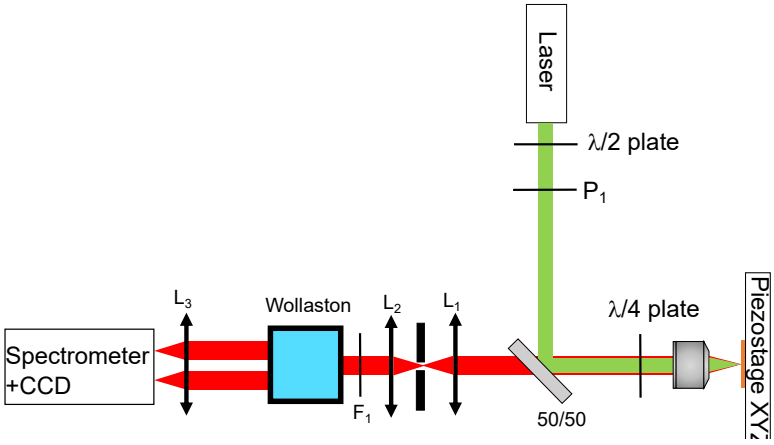


Figure 2.8: **Setup for polarization-resolved measurements.**

good control over the initial polarization of the laser. To ensure this, we use a linear polarizer and a half-wave plate in the path of the laser beam (see figure 2.8). For circularly polarized excitation, we added a quarter waveplate behind the microscope objective. This quarter-wave plate transforms the incident linear polarization into right- or left-handed polarization (See figure 2.9 a). Then the backscattered signal and the emitted one will pass through the same quarter-wave plate and will be transformed into linearly polarized light. To analyze the polarization, we used a Wollaston prism in the detection path. Due to its birefringence, this crystal splits the incident beam into two divergent beams with mutually orthogonal linear polarizations (See figure 2.9 b). In our setup, we can address individually each one of these beams.

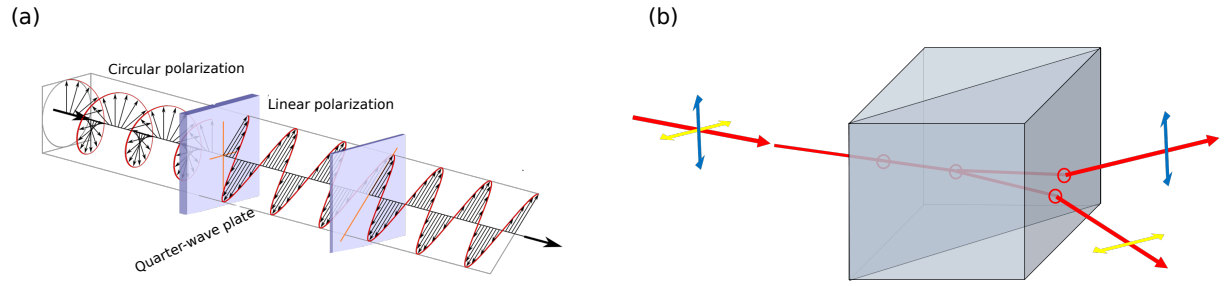


Figure 2.9: **(a)** Scheme of a quarter-wave plate transforming circularly polarized light into linear polarization. By symmetry, the inverse process is also possible. (open source image from wikimedia commons) **(b)** Wollaston prism separating the incident beam into two divergent beams with mutually orthogonal polarizations.

### 2.3.4 Time resolved photoluminescence spectroscopy (TRPL) at LCPNO

All the low-temperature TRPL measurements reported in this thesis were done in a collaboration with Cédric Rober, Delphine Lagarde, and Xavier Marie at LCPNO in Toulouse. The setup is similar to the one we used at IPCMS for PL measurement with the exception that instead of a CCD camera, the emitted signal goes into a streak camera. The latter allows us to record temporal traces of the photoluminescence signal arising from the TMDs.

The working principle of a streak camera is shown as a scheme in figure 2.10a. For simplicity, the scheme depicts the case of a monochromatic signal. When an optical signal enters the camera it gets directed towards a photocathode. Upon impact with the photocathode, electrons will be ejected in proportion to the intensity of the incident signal. These electrons are then collected and pass between two electrodes on which a time-varying voltage is applied. As a result, these electrons that arrived first to the photocathode get deflected differently than electrons that were emitted later. Finally, these deflected photoelectrons reach a fluorescent screen which is coupled to a CCD camera where a spatial distribution of the signal is obtained. The resulting image forms a "streak" of light, from which the duration and other temporal properties of the light pulse can be inferred. An example of a spectrally resolved TRPL image obtained in a streak camera is shown in figure 2.10b.

The TRPL measurements were carried out by E. Lorchat, D. Lagarde, and C. Robert. I focused on the data analysis.

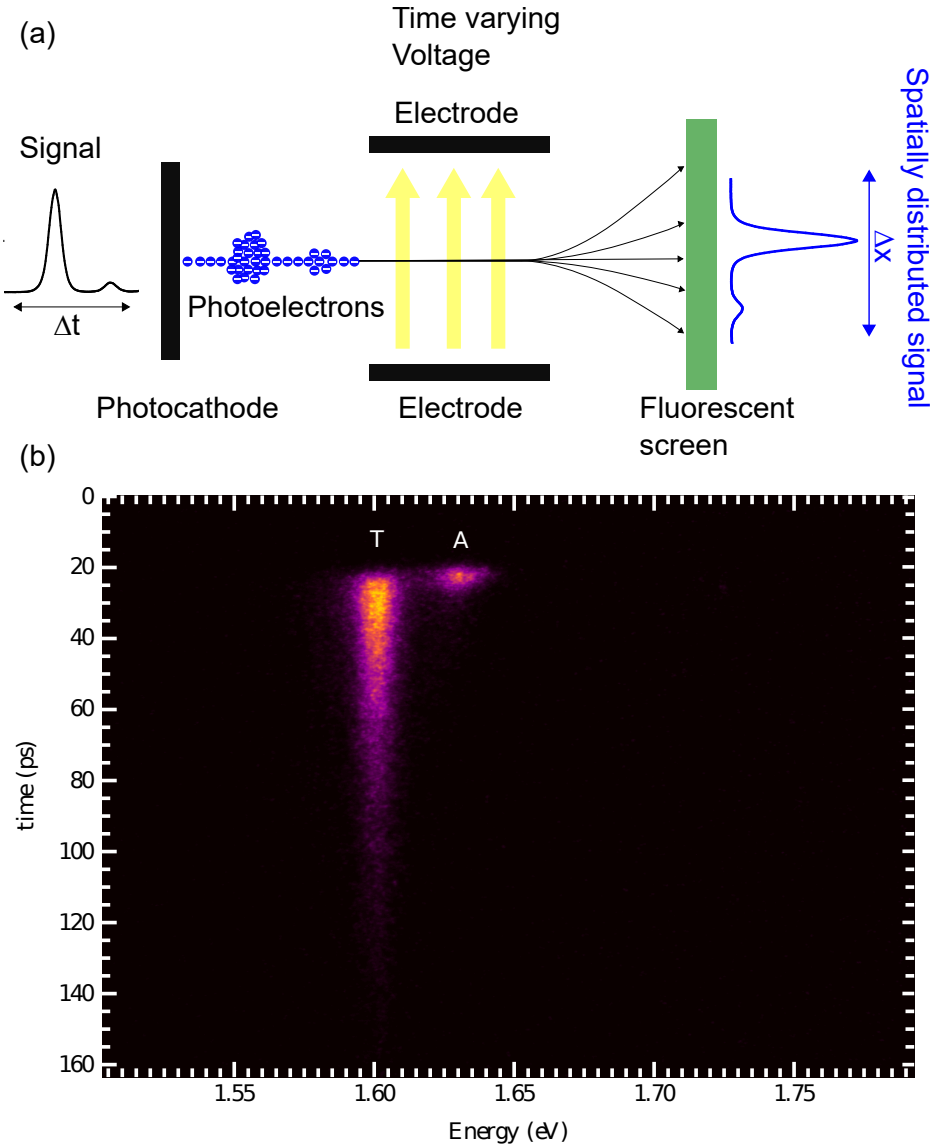


Figure 2.10: **Streak camera working principle.**(a) Scheme of the working principle of a streak camera. (b) Streak image of a monolayer $MoSe_2$ at 4 K. A and T denote the exciton and trion respectively. Figure (b) was extracted from [71]

### 2.3.5 Data acquisition and data analysis

To acquire spatial information about the homogeneity of the heterostructures, we used hyperspectral mapping. This could be done thanks to a program created by Michelangelo Romeo. He interfaced the piezo stage with the detection of the spectrometer. This allows us to do raster scans and therefore hyperspectral maps of our sample. This is extremely useful as it gives us information about the homogeneity of the emission and coupling between layers in our sample. We used Matlab routines, which I have written or adapted from previous routines, to fit[6] all the acquired spectra.

[6]We use either Lorentz, Gauss or Voigt profiles for the fit.

## 2.4 Scanning Tunneling Microscopy

To investigate TMDs at the atomic scale, we have used a scanning tunneling microscope working at low temperatures and under ultra-high vacuum (LT-UHV). In this section, I will briefly introduce the working principle of an STM as well as the information we can obtain thanks to this technique.

### 2.4.1 Working principle

Consider an electron with energy E, moving towards a potential barrier of height $W > E$ (figure 2.11). Classically, the electron would be reflected by the barrier. However, the wave-particle duality of electrons allows for non-classical behaviors. There is a non-zero probability for the electron to tunnel through the barrier. This probability depends on the barrier's thickness and height. An STM exploits this dependence to obtain sub-nanometer resolution of the system it addresses. In this section, I will present only the main results regarding the working principle of an STM. The reader can find a more detailed calculation of the results presented in this section in Appendix A.

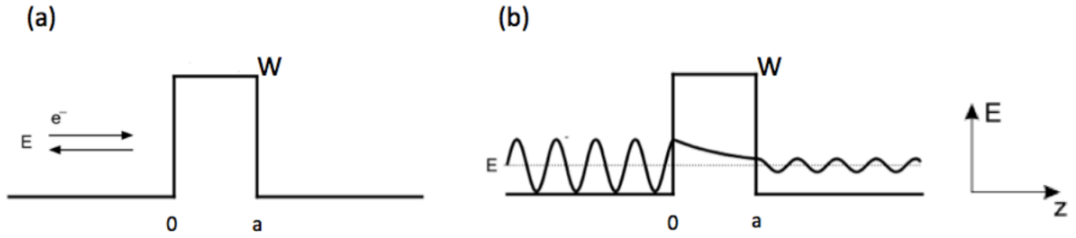


Figure 2.11: Scheme of a particle interacting with a potential barrier. **(a)** classically the particle not having enough energy to surpass the barrier would be reflected **(b)** In quantum mechanics, a non-zero contribution of the particle can exist on the other side of the barrier. This non-zero contribution is enough for the particle to have a probability to "tunnel" through the barrier.

### 2.4.2 Tunneling current

The first work regarding the calculation of a tunneling current was done by John Bardeen in 1961 [137]. This work was a follow-up of experimental results obtained in superconducting junctions presented by Giaever [138]. Bardeen's contribution set the theoretical basis for the development of the theory behind the tunneling current. In essence, he modeled the evolution of an electron in a tunneling junction. Assuming that the isolated wavefunctions of the tip and the sample were approximately orthogonal, he showed that the tunneling current is given by:

$$I = \frac{4\pi e}{\hbar} \sum_{\mu,\sigma} \delta(E_\sigma^S - E_\mu^T) |M_{\mu\sigma}|^2 (f(E_\sigma^S + eV) - f(E_\mu^T)) \tag{2.2}$$

Where $I$ is the tunneling current, $M$ is a matrix, $f$ is the Fermi-Dirac distribution and $E_\sigma^S$ ($E_\mu^T$) corresponds to the eigen-energy of the sample (tip) wavefunction in the absence of the tip (sample). This expression depends on three different terms, each one of them accounting for a different part of the tunneling process. The first term with the delta assures conservation of energy, and it is the main reason this type of tunneling is called *elastic*. The third term regarding the Fermi-Dirac distribution $f(E)$ accounts for the availability of states[7] and for the temperature. The middle term is perhaps the richer one since this term is related to the probability of transferring an electron, and it depends on the coupling between tip and sample states. Indeed, we can simplify this expression by making the relevant approximations corresponding to our measuring conditions. That is, at low temperatures and low bias, equation (2.2) can be written as:

$$I \approx \frac{4\pi}{\hbar} e^2 V \sum_{\mu,\sigma} \delta(E_\sigma^S - E_F^S - eV)\delta(E_\mu^T - E_F^T)|M_{\mu\sigma}|^2 \tag{2.3}$$

Where $E_F^{T/S}$ corresponds to the Fermi energy of the tip/sample respectively. The only unknown remaining is the tunneling matrix $M_{\mu\sigma}$. This term accounts for the electronic structure and the geometry of the tip, which makes it difficult to estimate. Tersoff and Haman did a fundamental step in this direction in 1985 [109]. They showed that if the electronic structure of the tip is approximated by an s-orbital (sphere), the matrix element can be considered as a constant[8]. This allows us to rewrite equation (2.3) as follows:

$$I = \frac{4\pi e}{\hbar}|M|^2 \int_0^{eV} dE_F \rho^S(E_F - eV)\rho^T(E_F) \tag{2.4}$$

Where $\rho$ is the local density of states. In other words, as long as the tip can be considered a sphere, we can interpret the STM current as a convolution of the density of states of the tip and the sample at a particular energy (given by the bias) and probe position. From this expression, we can see that we are sensitive to the **Local Density of States** (LDOS) of the sample.

### WKB approximation

The final element towards a more complete theory for STM is to consider the potential barrier. Indeed, the matrix element $M_{\mu\sigma} = \left\langle \psi_\mu^T \right| V_T(z) \left| \phi_\sigma^S \right\rangle$ has three main ingredients:

1. The surface electronic structure encrypted in the term $\left|\phi_\sigma^S\right\rangle$ (Can be treated exactly).
2. The tip electronic structure encrypted in the term $\left\langle \psi_\mu^T \right|$ (Tersoff-Hamann approximation [109]).

[7] you can only tunnel from an occupied to an unoccupied state

[8] This has been done under the supposition that only the outermost states of the tip overlap with the sample states, however, this is questionable. Chen proved that this is not the case, and other states should be included to fully explain corrugation in STM-images [139]

3. The shape of the potential barrier $V_T(z)$.

To take this into account, one can use the WKB (Wentzel-Kramers-Brillouin) approximation. For a slowly varying potential in space, the corresponding wavefunction should also slowly vary in space relative to the constant potential case. If we model the tunnel barrier using the WKB approximation, we obtain the following expression for the tunneling current at low temperatures:

$$I_t \propto \int_0^{eV} \rho^S(E) T(z, E, V) dE \tag{2.5}$$

$T(z, E, V)$ is the transmission coefficient that encompasses the dependence on the shape of the barrier. For a barrier with a trapezoidal shape, we can compute the following transmission coefficient:

$$T(z, E, V) \propto e^{-2z\sqrt{\frac{2m}{\hbar}(\phi - E + \frac{eV}{2})}} \tag{2.6}$$

Where $\phi$ is the average work function of the electrodes. This expression means that the transmission sensitively depends on the electron energy. The higher the energy, the higher the probability of tunneling. In the limit of low voltages, the expression 2.5 becomes:

$$I_t \propto e^{-2z\sqrt{\frac{2m}{\hbar}(\phi)}} \tag{2.7}$$

To get an idea of the effect of such coefficient, first, let us rewrite this in terms of a decay constant k: $I_t \propto e^{-kz}$ and perform a small back-of-the-envelope calculation. For silver and gold $\phi$ is typically $\sim$ 5 eV [140]. With this, we can estimate $k \approx 22.9$ nm. This means that for a variation of $\Delta z = \pm 0.1$ nm we get an order-of-magnitude change in the current. This explains the extreme sensitivity of STM.

### 2.4.3 STM imaging modes

Now that we have all the background to understand how an STM image is recorded and its physical interpretation, we can address the experimental side. In practice, the STM tip is mounted on a piezoelectric tube which can move precisely in three directions by applying three different voltages. This piezoelectric is connected to a feedback loop as sketched in figure 2.12 which regulates the tip's position relative to a given setpoint. One can make an STM image using one of the following two modes:

#### Constant Current Mode

In this mode -as its name suggests- the current is kept constant. This is ensured thanks to the aforementioned feedback loop, which makes sure that the current is kept at the given setpoint. This is done by regulating the tip-sample distance while the tip is scanning the

sample in the x and y directions. During the scan, the "z" position of the tip is being tracked and a "topographic" image can be reconstructed. However, one must remember that the STM image depends on the local density of states of the surface and depends on the voltage applied.

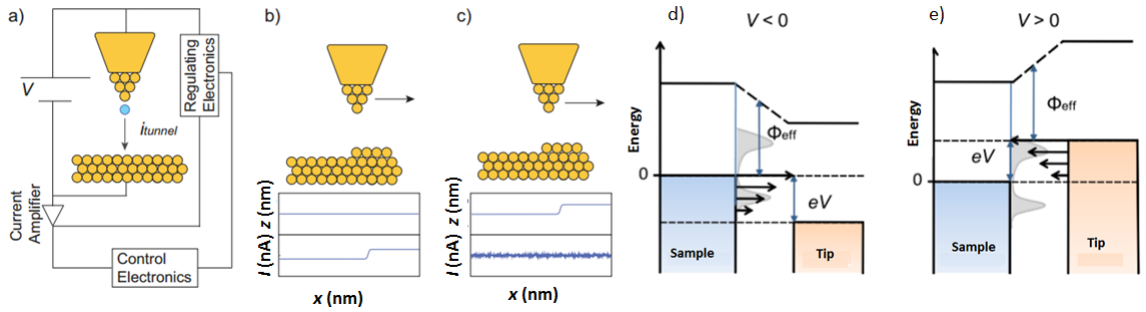


Figure 2.12: **Principle of imaging modes of an STM. (a)** Scheme of an STM circuit. **(b)** constant height imaging mode. **(c)** constant current imaging mode. **(d)** Sketch of a junction where the tip is at a lower potential than the sample. In this configuration, one is probing the occupied states of the sample. **(e)** Conversely, if the potential of the tip is higher than the potential of the sample, one probes the unoccupied states. Figures extracted from [141]

#### Constant height mode

In this mode, the tip is kept at a constant height and current variations are recorded. This mode is less used as it has the risk of crashing the tip onto the surface.

### 2.4.4 Scanning Tunneling Spectroscopy (STS)

STM goes beyond imaging. It allows us to obtain information about the electronic structure of the surface. To understand this, let us go back to the expression we derived for the tunneling current:

$$I_t(V) \propto \int_{E_F}^{E_F+eV} DoS^S(E)T(z,E,V)dE$$

we can see that the information regarding the local density of states (LDOS) is embedded in the integral. To isolate it, one possibility is to take the derivative of this expression with respect to the voltage applied:

$$\frac{dI_t}{dV} \propto DoS^S(eV)T(z,E_F+eV,V) + \int_{E_F}^{E_F+eV} dE DoS^S(E)\frac{\partial T}{\partial V}(z,E,V) \qquad (2.8)$$

Notice that the first term is directly proportional to the LDOS at the energy eV. The second term can be neglected for small voltages. The expression $\frac{dI}{dV}$ represents the conductance of the junction. This means that when an electron has a non-negligible

probability of tunneling into an available state, there will be a proportional increase in the junction's conductance. This increase appears as a peak in the dI/dV curve, indicating that a new conductive channel has been opened. This means that by scanning over a span of bias voltages, we can get direct information on energy states present in the probed window. In practice, to extract this signal, we applied a small oscillating voltage $\delta V_m(t)$ on top of the bias $V_0$. Since this voltage is small, we can express the overall change in current as follows:

$$I(V_0 + \delta V_m(t)) = I(V_0) + \delta V_m(t)\frac{dI}{dV}(V_0) + \dots \tag{2.9}$$

For simplicity, we will consider that $V_m(t) = V_m cos(\omega t)$. Equation (2.9) reads:

$$I(V_0 + \delta V_m(t)) = I(V_0) + V_m cos(\omega t)\frac{dI}{dV}(V_0) + \dots \tag{2.10}$$

Consequently, we can use a lock-in amplifier to select a particular frequency of the Taylor development of the current. This is done by exploiting the orthogonality of sinusoidal functions and it grants us access to the local density of states of the sample at the energy $eV_0$.

## 2.5 STM induced luminescence (STML)

The first observation of light coming from a tunneling junction was reported in 1976 by J. Lambe and S. McCarthy [142]. Their system consisted in a macroscopic tunneling junction composed of two metallic electrodes separated by a thin oxide layer. The luminescence was broadband and presented a cutoff at a photon energy $E_c$ that depended exclusively on the bias $V_0$ applied between the electrodes, such that $E_c = e|V_0|$ (figure 2.13a). The spectral shape changed depending on the electrodes' chemical nature and the geometry of the junction. These observations raise many questions such as **What is the physical process behind this emission? To which extent can we control this process? Can we observe such phenomenon in an STM junction?**, and if so, **What can we learn from this?** This introductory section aims at familiarizing the reader with the technique known as STM-induced luminescence (STML). Each sub-section is presented to address one of the previous questions and slowly build an understanding of the phenomena one needs to consider when investigating optical properties with an STM. Ultimately, this will create the context required to discuss our results.

### 2.5.1 The plasmonic STM-junction

Figure 2.13b shows two emission spectra originating from a metal-vacuum-metal STM junction (shown in the inset). For the moment, let us focus on the red curve. This

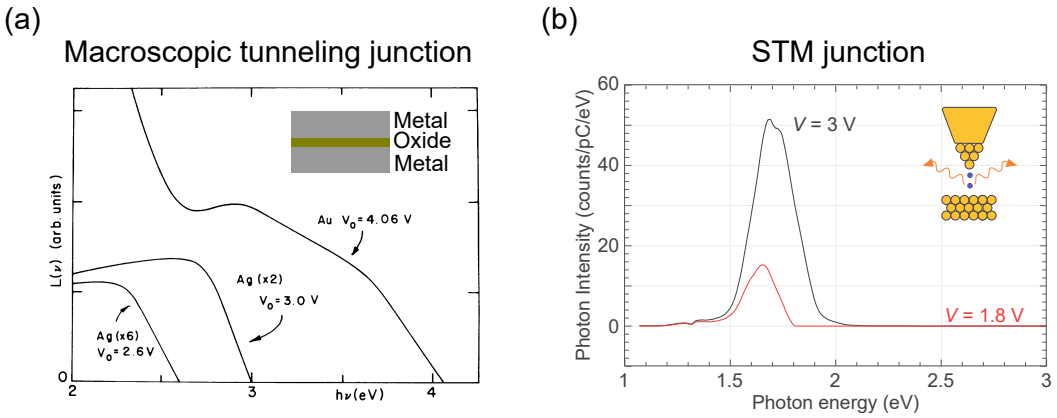


Figure 2.13: (a) Light emission spectra of an Ag and Au macroscopic tunnel junction. The spectra were recorded at 77K. Figure adapted from [142]. (b) STM-induced light emission from a gold-tip gold-sample STM junction. The two curves were taken at a bias of 3V (black) and 1.8V (red) at a current of 10 nA. Figure adapted from [141].

spectrum is characterized by a broad resonance with a cutoff at an energy of $E = 1.8$ eV. This value precisely matches the bias voltage used to acquire the spectrum. We can understand this emission in terms of an inelastic tunneling process where electrons lose their energy through photon emission (figure 2.14a). This allows us to explain most of the observed phenomenology. For instance, the maximum energy that an electron can lose is equal to the bias applied. As a result, one would expect a cutoff for photon emission precisely matching this bias. Moreover, the inelastic character of this process explains the broad nature of the spectra since one can have lower energetic transitions as well (blue arrows in figure 2.14a). However, as we will see now, these considerations alone cannot fully explain the phenomenology.

Let us come back to figure 2.13b and focus on the black curve instead. In this case, we observe no light emission above 2.1 eV. This secondary "cutoff" cannot be accounted for by inelastic tunneling alone. Instead, we need to take a step back and study the STM junction from an electromagnetic perspective. We will see that the proximity between the tip and the metallic substrate induces collective oscillations of electrons that are localized within the junction. These modes are referred to as **localized surface plasmons** (LSP) or **gap plasmons** and are essential to understand the light emission process in the tunneling junction. In the following, we are going to discuss their origin briefly.

### Bulk plasmons

Let us consider a metal subjected to an incident electromagnetic field. The incident field acts as a driving force for the free electron gas in the metal which will oscillate in response. The natural frequency for this collective oscillation is called the *plasma frequency* and can

be derived classically using Maxwell's equations:

$$\omega_p = \sqrt{\frac{ne^2}{\epsilon_0 m}} \tag{2.11}$$

In this expression, $n$ is the density of electrons, $\epsilon_0$ the vacuum permittivity and $m$ the free electron mass. In the same way, electromagnetic waves can be described in terms of photons, this collective oscillation can be described in terms of quantized quasiparticles called **plasmons** which play an important role in the optical properties of metals.

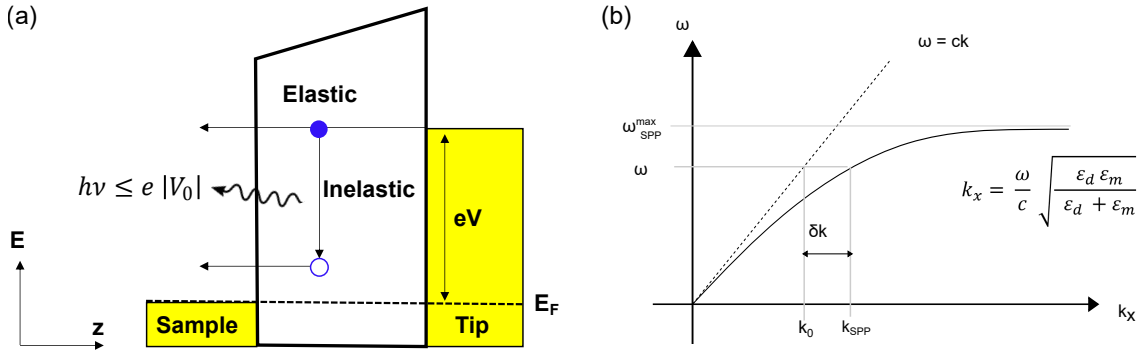


Figure 2.14: (a) Energy diagram of a biased tunneling junction. In the diagram, both elastic and inelastic are depicted as well as the photon emission arising from the inelastic tunneling. (b) Surface plasmon dispersion relation (solid line). The dashed line represents the light cone. Since the SPP dispersion lies below the light cone, momentum needs to be compensated by an amount $\delta k$ for SPPs to emit light. Figure adapted from [143]

### Surface plasmons

Strictly speaking, the previous discussion corresponded to the so-called *bulk* plasmons. These quantized collective electron oscillations about the positive ions in the bulk. However, it can be shown that if there is a change of sign in the dielectric constant across the interface between two media, surface charge oscillations can be similarly present. These are called **surface plasmons** and exist only at the interface between the two media. The charge motion associated with the surface plasmons generates decaying electromagnetic fields on both sides of the interface. Strictly speaking, the plasmon is both the charge oscillation and the EM-field. Naturally, these charge oscillations can couple with the electromagnetic far-field. For this reason, surface plasmons are also referred to as **surface plasmons polaritons** (SPP). Using Maxwell's equations, one can prove that SPP obey the following relation:

$$k_{\mathrm{SPP}} = \frac{\omega}{c}\sqrt{\frac{\epsilon_d \epsilon_m}{\epsilon_d + \epsilon_m}} \tag{2.12}$$

where $\epsilon_d$ and $\epsilon_m$ are the dielectric permitivities of the dielectric and the metal respectively. If we approximate $\epsilon_d$ to a constant and substitute $\epsilon_m(\omega)$ given by the Drude model

in the case of negligible loses ($\Gamma \approx 0$) we can write:

$$k \approx \frac{\omega}{c}\sqrt{\frac{\epsilon_d(\omega^2 - \omega_p^2)}{(\epsilon_d + 1)\omega^2 - \omega_p}} \tag{2.13}$$

Notice that when $k \to \infty$ ($\epsilon_m = -\epsilon_d$), this expression allows a maximal frequency of:

$$\omega_{SPP}^{max} = \frac{\omega_p}{1 + \epsilon_d} \tag{2.14}$$

This dispersion relation resides entirely below the light cone as shown in figure 2.14b. Therefore, **SPPs cannot couple to EM waves in free space unless momentum conservation is compensated**. This can be achieved in many ways, such as through symmetry breaking due to roughness in the surface, the use of gratings, or even interaction with tunneling electrons [144, 145]. In the case of an STM junction, the tip can provide momentum compensation as well.

### Localized surface plasmons

To fully describe the STM junction, we need to consider the tip as well. For simplicity, we can consider the tip as a metallic nanoparticle with sub-wavelength size. In this case, the charge oscillations we described before are confined to the nanoparticle's volume. These modes are called **localized surface plasmons** (LSP) and, in contrast with SPP, are not propagating modes. Indeed, the curvature of the nanoparticle exerts restoring forces on the oscillating electrons. These localized modes can be modeled as an oscillating dipole[9] which, in contrast to SPP, can radiate EM waves without the need for momentum compensation.

Having described both the tip and the surface separately, we can now discuss the effect of their proximity. As a whole, the STM junction can be modeled within the nanoparticle-on-mirror approach (NPoM). In such geometry, the SPP of the surface and the LSP of the tip hybridize, generating quasiparticles quantized in the nanogap. These modes are referred to as nanocavity plasmons (NCP), and they are known to greatly enhance the EM field intensity in the junction. NCPs can be excited by the inelastic tunneling electrons and decay through photon emission giving rise to broadband spectra.

Moreover, the shape of the spectra will be entirely dominated by the NCP eigenmodes. Therefore, if we can modify the latter, we can tailor the EM field in the junction accordingly. Since these modes form a continuum, we can understand the emission from a tunneling junction within the Fermi golden rule formalism. Indeed, Rendell *et al.* showed that if one considers the tip as a sphere, the lowest LSP-mode corresponds to a dipole located inside the junction and aligned along the tip axis [146]. Therefore, we can write:

$$\Gamma = \frac{2\pi}{\hbar^2}\left|\langle i|\,\vec{d}\,|f\rangle\right|^2 DoS_{NCP}(\Delta E)E(M)^2 \tag{2.15}$$

[9] Only in the quasi-static regime

Where $\vec{d}$ is the dipole moment associated with the inelastic transition from the state $\langle i|$ to the state $|f\rangle$, $DoS_{NCP}$ is the density of states of the NCP at an energy $\Delta E = E_i - E_f$ and $E(M)$ the spatial density of the electromagnetic field at the position M.

### 2.5.2 STML of noble metals

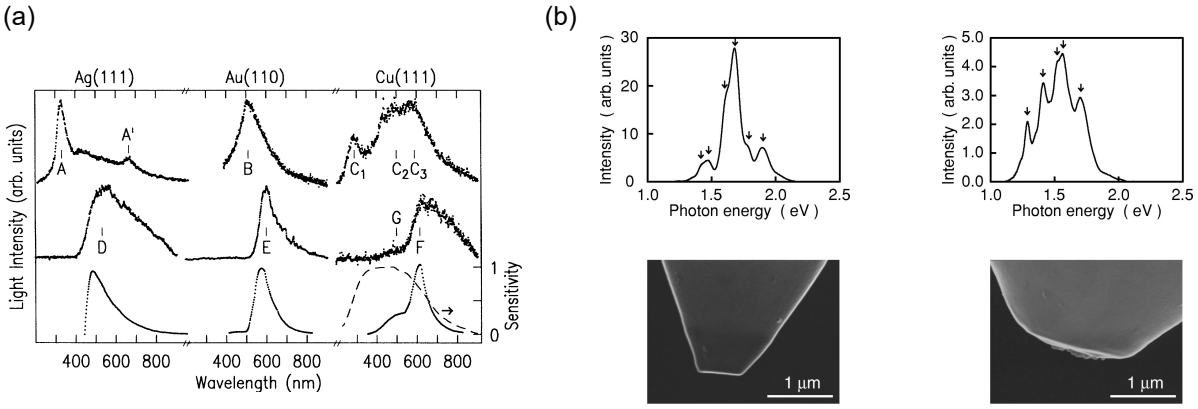


Figure 2.15: **Tuning the plasmonic response.**(a) Optical emission spectra of Ag(111), Au(110) and Cu(111) surfaces. The top row corresponds to the emission at high voltages (field emission regime). The middle row corresponds to the emission in the tunneling regime. The bottom row corresponds to the calculated spectra based on [147]. Figure adapted from [148]. (b)Optical emission from Au(111) junctions(top) obtained with different tip apex geometry (bottom).Figure extracted from [149]

We have seen that the plasmonic response of the junction strongly enhances the luminescence arising from the STM. Therefore, it is worth investigating to which degree we can control this response. The first thing one can try is changing the chemical nature of the electrodes. Indeed, the plasmonic response depends on the dielectric function of the materials involved. This was proven in the context of noble metals by Berndt *et al.* [148]. In their experiments, they investigated the emission arising from different metallic surfaces, in particular Ag(111), Au(110), and Cu(111). Figure 2.15a shows the measured (middle row) and predicted (bottom row) plasmonic responses of each junction. We can see that the emission is centered at an energy that depends on the dielectric function of the chosen metal.

Another interesting approach to tune the plasmonic response of a junction consists in modifying its geometry. This was demonstrated by Meguro *et al.* in 2002 in Au(111) junctions [149]. Figure 2.15b shows two optical spectra obtained in such junctions with different tip shapes. The corresponding shape of each tip is shown below each spectrum. We can see that the main peak is composed of secondary resonances, which are directly linked to the shape of the tip apex. This means that we can change the EM response of the STM junction to a certain degree by modifying the latter.

### 2.5.3 STML on single molecules: the decoupling problem

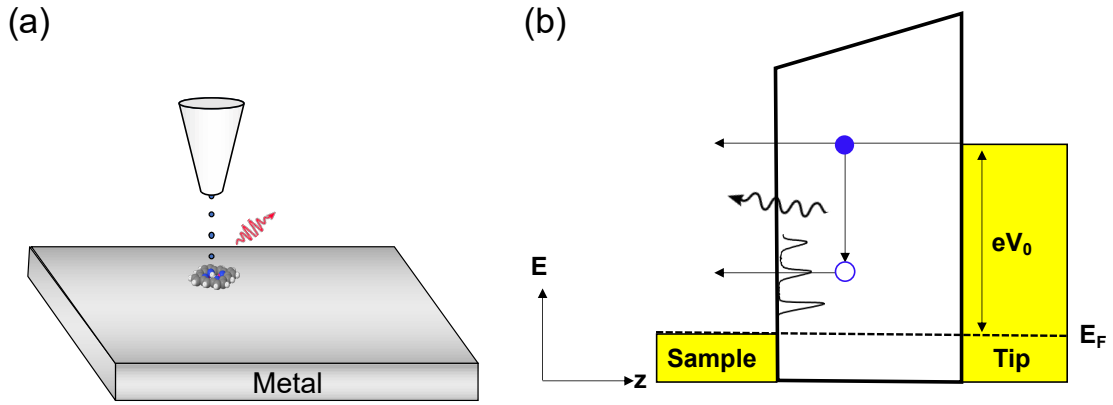


Figure 2.16: **STML on single molecules.**(a) Scheme of a molecule deposited on top of a metallic surface. (b) Energy diagram of a biased STM junction with a molecule in contact with the sample electrode. The resonances shown in the figure represent molecular states onto which electrons can inelastically tunnel.

One of the most promising aspects of STML is the sub-nm resolution it can provide. Indeed, in STML, the excitation resolution is defined by the tunneling current. This aspect sparked many investigations in the context of single-molecule fluorescence. In the early experiments, the idea was to evaporate molecules directly on a metallic surface and then use the STM to excite them (figure 2.16a). The expectation was that inelastic transitions could induce the fluorescence of the molecule. However, this proved to be more challenging than expected. Indeed, instead of a sharp emission arising from intrinsic processes, a broad emission more akin to plasmons was observed. These spectra were different from the ones obtained on the bare metallic surface but remained plasmonic in nature. We can understand this difference by taking into account inelastic transitions towards molecular states [150, 151, 152]. Figure 2.16b shows an energy diagram of such process. In this example, the molecular levels act as channels into which electrons can inelastically tunnel. This results in a molecule-induced modification of the plasmonic response of the junction. Nevertheless, this is not intrinsic in nature. The proximity between the molecule and the metal opens efficient non-radiative decay paths resulting in a complete quenching of the molecule's fluorescence similar to the case of TMD and graphene discussed in chapter 3.

A breakthrough came in 2016 when the intrinsic luminescence of molecules was demonstrated in two different configurations. The first one consisted in suspending the molecule in the junction using molecular wires. This configuration is shown in the top panel of figure 2.17a. In this geometry, one can precisely control the distance between the molecule and the surface and, therefore, the coupling. This was demonstrated experimentally by M. Chong *et al.* in porphyrin molecules suspended by oligothiophene wires [153]. STML spectra of this system for different molecule-surface separations are shown in the bottom

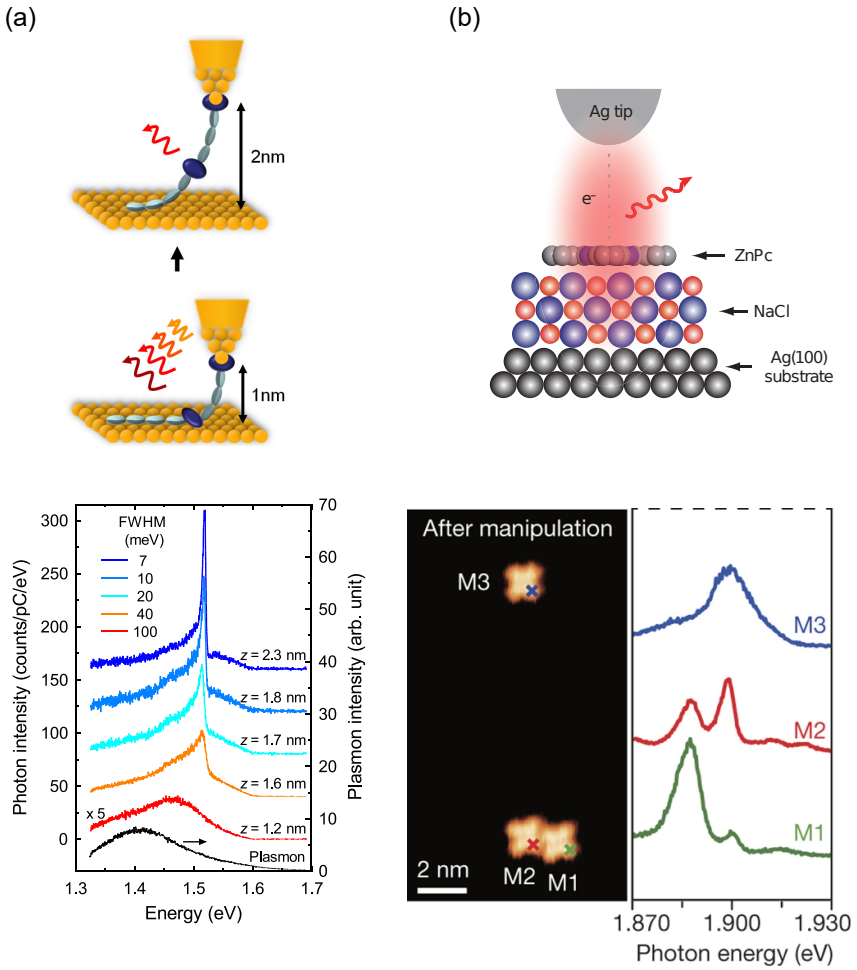


Figure 2.17: **Decoupling strategies.**(a)Top: Scheme showing the suspended molecule configuration. A molecular wire is used to suspend an emitter and precisely decouple it from the substrate. Bottom: STML spectra from the suspended emitter. The spectra were acquired at different tip-sample distances indicated next to each spectrum. Sharp emission (7 meV) arising from the intrinsic process can be observed at large separations. Figure extracted from [153]. (b)Top: Scheme showing a ZnPc molecule being decoupled from the Ag(100) substrate by a NaCl layer. Bottom: STM images (left) and STML spectra (right) recorded on the positions indicated in the figure. The emission corresponds to the fluorescence of the molecule and the dimer. Figure adapted from [154].

panel of figure 2.17a. We can observe that once the molecule is sufficiently far from the substrate, narrow (7 meV) emission arising from intrinsic processes in the molecule is obtained. The main constrain of this strategy is the lack of spatial resolution inherent to the suspension. The same year, Zhang *et al.* proposed a new approach involving NaCl as a decoupling layer between the molecule and the metal[10] [154] similar to early works by Qiu *et al.* in which they used oxides as decoupler [155]. This configuration is shown in the top panel of figure 2.17b. They investigated Zinc-phthalocyanine molecules (ZnPc) deposited on an Ag(100) substrate. In this configuration, one retains the spatial resolution

[10]NaCl provides a relatively inert substrate for the molecule similar to the use of hBN. See chapter 3

of the STML approach that allows probing fluorescence characteristics with sub-molecular resolution. STML spectra obtained in such configuration are shown in figure 2.17b (bottom panel). The spectra were recorded on top of a single ZnPC molecule and a nearby dimer. This is direct proof that one can perform single-molecule spectroscopy with atomic resolution.

### 2.5.4 STML on semiconductors

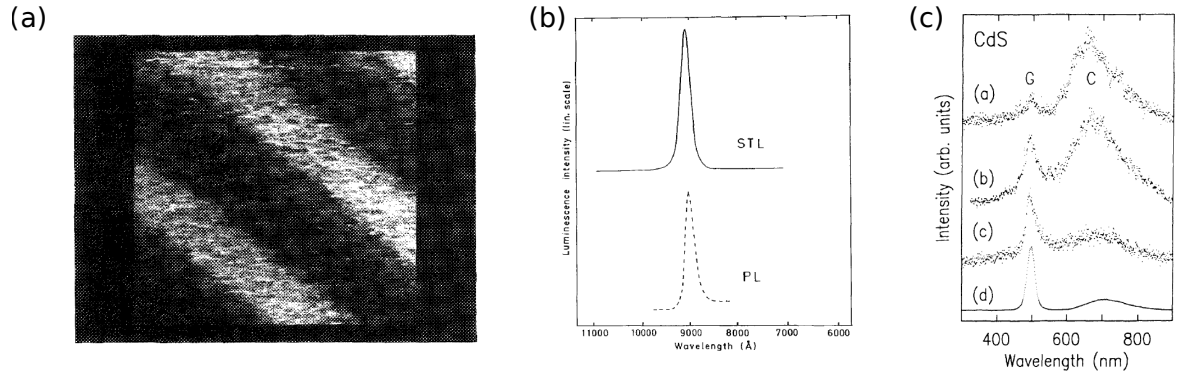


Figure 2.18: (a)Photonmap of a quantum well taken at -4V and 1 nA. The luminescent area corresponds to GaAs luminescence [156].(b) STM-F and PL spectra of GaAs/AlGaAs at 200K. The parameters for the STM-F acquisition were -1.6V and 1 $\mu$A. [157] (c) STM-F spectra of CdS(1120) at room temperature. The parameters for aquisition were -7 V and 10 nA for the spectra (a), (b) and (d). The spectra (c) was taken at 10 V. [158]

STML was also investigated in the context of extended systems such as semiconductor surfaces. The idea is similar to that of single molecules, but instead of molecular levels, the semiconductor has bands. These measurements were pioneered by the works of Gimzewski *et al.* [159], and Alvarado *et al.* [156] at the end of the 80s. In these early experiments, the authors pointed at inelastic tunneling towards the band edges as the origin of the luminescence. Interestingly, they were able to measure highly resolved photon maps on individual quantum wells in GaAs/AlGaAs heterostructures (figure 2.18a).

The first spectrally resolved intrinsic STML spectra of semiconductors were obtained in 1992 by Montelius *et al.* on InP at low temperatures[157], and by Berndt *et al.* on CdS at room temperature [158]. These spectra are shown in figures 2.18b and c, respectively. The intrinsic nature of the spectra was demonstrated by comparing them with reference PL spectra of the same samples. From their observations, they concluded that the luminescence steamed from charge carrier injection into the bands and impact ionization of hot carriers with excitons.

### 2.5.5 Summary

We can summarize the main key points of this discussion as follows

- An STM junction presents localized EM-modes that can strongly enhance the EM field inside the junction when noble metals are used.

- These plasmonic modes can be excited by inelastic tunneling electrons resulting in broadband optical emission.

- The plasmonic response of the junction depends on the tip geometry and the chemical nature of the electrodes.

- The proximity of a plasmonic structure to an emitter can quench its intrinsic emission. This motivates the realization of different strategies to decouple the emitter from the electrodes.

- Intrinsic STML emission has been demonstrated in the context of single molecules and bulk semiconductor surfaces.

### 2.5.6 Our setup

I used a commercial low-temperature STM produced by Unisoku Co., Ltd (figure 2.19). The cryogenic system is composed of one cryostat that can be filled with liquid nitrogen ($LN_2$) or liquid helium (LHe), depending on the temperature range we want to work with. This STM has an approximate standing time of 48 hours at 6 K. The STM-head is in thermal contact with the cryostat, which allows us to cool down to 6 K[11]. Thanks to an ionic pump, the STM is kept in UHV conditions ($P \approx 10^{-11}$mbar). External vibrations are minimized thanks to two damping systems in place. The first one allows us to decouple the STM-head from the rest of the chamber by suspending it through springs and magnetic dampers. The second one involves suspending the whole STM chamber with pneumatic feet. Thanks to this, we can isolate efficiently the STM from vibrations in the building.

The STM chamber is connected to a preparation chamber which is also kept under ultra-high vacuum. This chamber is used to prepare the samples and the tips used in the measurements. It is equipped with an ion gun and a sample stage on which we can do thermal annealing. Although I did not use it for my experiments, the preparation chamber is also equipped with an evaporator that allows one to sublimate molecules. To introduce samples and tips in the STM, we use a load-lock that is connected to the preparation chamber by a gate valve. Before opening the valve, a preliminary vacuum is done in the load lock.

[11]This system can descend to 1K by pumping on the cryostat.

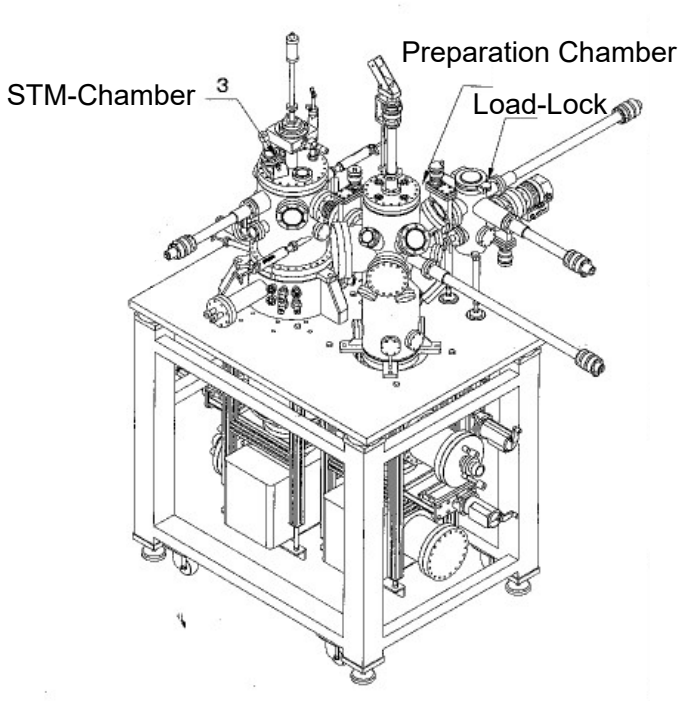


Figure 2.19: **Scheme of the unisoku STM.** Source: Unisoku

#### Tip preparation

Two kinds of tips were used for all STM studies done during this work: Ag and W tips. W tips were prepared from a 0.25mm thick wire. The wires were etched in a NaOH solution as described in [160]. After etching, the tips are annealed and argon sputtered. In the case of Ag tips, instead of NaOH, a 1:4 solution of $HClO_4$ and ethanol was used. After etching, the tips are only argon sputtered.

The sputtering is done to further clean and sharpen the tip. In the case of the W tip, one must indent it on a metallic surface. The idea is to cover the tip with the metal and optimize its plasmonic properties (See section 2.5.2).

### 2.5.7 Light detection in our setup

During my Ph.D., I participated in designing and preparing the optical table for the Unisoku STM. A scheme of this setup is shown in figure 2.20. The setup is mounted on a platform attached to the STM. The emitted light (in red) is collected using two lenses (L1 and L2) inside the STM chamber. The collimated beams go to two different paths leading to two different kinds of measurements. The lower path is used for STML and in-situ PL. For STML, the collimated beam is aligned on an optical fiber using a set of mirrors and lenses. If needed, a linear polarizer (P1) can be added to the setup.

For the PL, a 532 nm continuous wave laser (green) is used. To control the power, a series of optical elements composed of a half-wave plate (l/2), a linear polarizer (P2), and

a second half-wave plate is used. Indeed, the laser is already polarized, and we can use the first l/2 to turn this polarization. Then, the polarizer at P2 is fixed such that only light propagating perpendicular to the table is transmitted. By rotating the first plate, we can continuously modulate the power of the laser. The second half-wave plate is in place in case one wants to turn the incident polarization. After this, the laser is shone onto the junction using a dichroic mirror (DM 532). To avoid laser backscattering, we added a notch filter in front of the optical fiber.

The upper path is used for time-correlated measurements. After emission, the signal can be split using a 50/50 beam-splitter cube. The new paths are aligned to a set of avalanche photodiodes (APD). We have adapted the setup to measure in the Hanbury-Brown and Twiss configuration [161]. This part of the setup was not used during my Ph.D.

### 2.5.8 Detection efficiency

The in-situ collection system consists in a lens (diameter= 20 mm, focal distance= 11 mm) fixed at an angle of 35 degrees with respect to the sample. The collected light then depends on the solid angle covered by the lens which can be estimated using:

$$\Omega = 2\pi(1 - \cos(\arctan(d/2f))) \approx 1.63 \text{ sr} \tag{2.16}$$

Supposing light is emitted isotropically in the upper hemisphere of the sample, this would imply that the lens collects $\Omega/2\pi \approx 26$ % of the emitted light. However, this value must be adapted to the directional emission of the tunneling junction. Indeed, it has been shown that the emission intensity from metallic junctions has a maximum at 30°. To correct for this, let us suppose that all the emission occurs in a spherical segment at 30° with a height equal to the lens diameter. Using this, we estimate an upper limit for the collection efficiency of the lens at 38 %.

The emitted light then travels through the UHV windows (whose transmission in the IR and visible is $\sim 90\%$) and the optical path shown in figure 2.20. In optimal conditions, the transmission between the lens and the optical fiber can reach up to 90%. In the best-case scenario, we estimate that around 50% of the photons collected by the in-situ lens arrive at the spectrometer. Therefore, we can calculate an overall detection efficiency between 13% and 19%.

#### Spectral analysis

We used a Princeton SCT-320 spectrometer coupled with a Pylon 400BR eXcelon CCD camera. After the signal is collected with the optical fiber, the beam goes to a diffraction grating that we can choose between 150 gr/mm, 300 gr/mm, and 1200 gr/mm. Each pixel

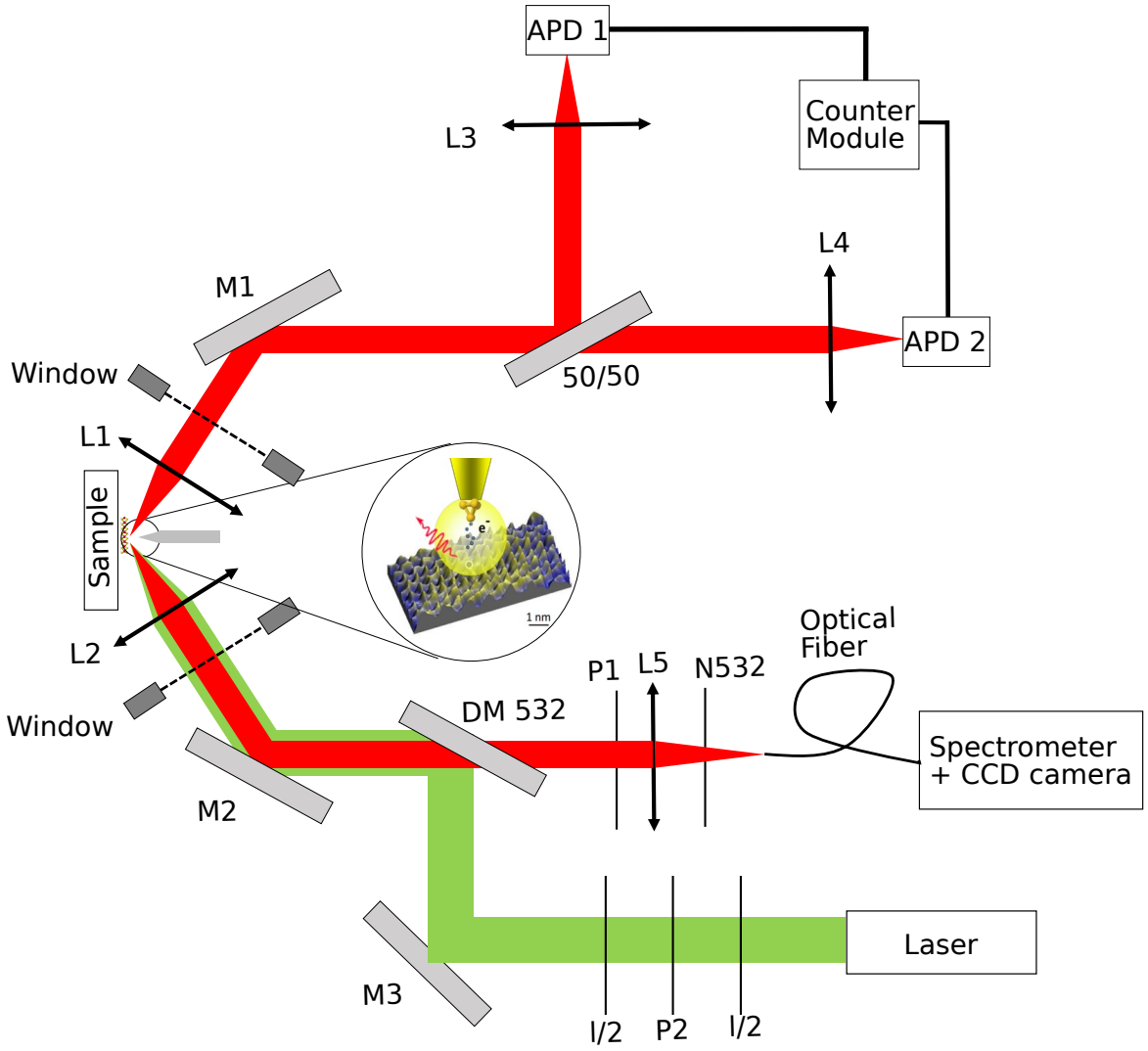


Figure 2.20: Scheme of the STM optical table. The emitted light is divided into two paths. The upper path is used for time-correlated measurements. The lower path is used for STM-F and in-situ PL spectroscopy. A series of halfwave plates and polarizers allow us to control the power of the incident laser and a dichroic mirror is used to filter the laser. The emitted light deviates to an optical fiber coupled to a CCD camera.

on the detector corresponds to a particular frequency and the intensity is related to the number of incident photons on each pixel.

Chapter 3

# Tailoring the luminescence of monolayer TMDs with graphene

## 3.1 Motivation

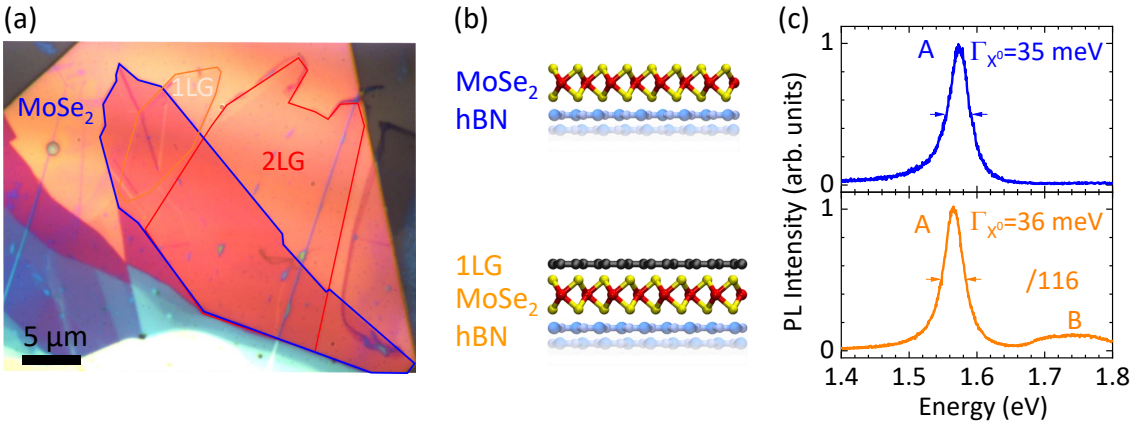


Figure 3.1: **hBN-supported $MoSe_2$/1LG sample.** (a)Optical microscopy image of a hBN/$MoSe_2$/1-2LG sample. (b) Lateral view of the sample. (c) Room temperature PL spectra of hBN/$MoSe_2$ (top) and hBN/$MoSe_2$/1LG (bottom). The FWHM of the peaks is indicated in the figure. Spectra recorded with a 532 nm cw-laser with an intensity of 1 $\mu W/\mu m^2$.

In chapter 1, we have mentioned the different phenomena that can arise at the interface between the layers in a van der Waals heterostructure. These phenomena ultimately influence or even define the optical and electronic properties of a heterostructure-based device. Therefore, it is essential not only to identify them but also to control them to a certain degree. A monolayer TMD stacked onto graphene is an example of a heterostructure whose properties are dominated by near-field coupling mechanisms at the interface. Let us look at the graphene/$MoSe_2$/hBN heterostructure shown in Figure 3.1a. This sample was fabricated using the method introduced in section 2.1. The highlighted areas correspond to a monolayer graphene (1LG, highlighted in orange), a bilayer of graphene (2LG, highlighted in red), and a monolayer of $MoSe_2$ (shown in blue). A scheme showing a lateral view of the heterostructure is shown in figure 3.1b. Two PL spectra characteristic from the 1LG/$MoSe_2$/hBN (orange) and $MoSe_2$/hBN (blue) areas are shown in figure

3.1. The spectra are composed of a resonance corresponding to the recombination of the neutral exciton and are normalized to the maximum of the exciton emission. A scaling factor between the two is shown next to the orange spectrum. We observe a two-orders of magnitude reduction of the PL signal coming from the TMD/1LG heterostructure with respect to the bare TMD. This suggests a shortening of the excitonic lifetime due to non-radiative decay paths towards graphene as it was shown in reference [8]. Since excitons in TMDs display ns-lifetimes at room temperature, non-radiative decay must happen in much shorter times. In fact, it has been shown that the exciton lifetime in TMD/graphene is of the order of few ps [8, 162]. The exact mechanism through which the non-radiative decay occurs is to this day a matter of debate. The principal difficulty is that different processes can lead to the observed quenching (see section 3.2). Therefore, to obtain insights on the photophysics of TMD/1LG, one cannot rely exclusively on PL spectroscopy. Instead, to investigate the microscopic origin of this coupling we need to complement PL with other techniques such as DR, Raman spectroscopy, TRPL, PLE which provide useful information regarding doping trends and excitonic dynamics.

Among the different mechanisms that can arise at the interface between TMD and 1LG, let us start our discussion with electron redistribution. As mentioned in section 3.2, TMD/1LG cannot be understood in the same terms as a macroscopic semiconductor/metal junction. In the latter, Schottky barriers form at the interface. However, both graphene and the monolayer TMD are smaller than the typical band bending region. Therefore we need to reconsider our approach. For simplicity, let us suppose that the bands remain unchanged and instead undergo rigid shifts. In this scenario, just as for macroscopic junctions, electron redistribution can occur through charge tunneling upon contact (figure 3.2). This is called **static charge transfer** and it depends on the relative band offset between the TMD and graphene. This process happens entirely in absence of photo-excitation and leads to a charge redistribution between the layers. In the case of photo-excited carriers and excitons, energy and charge transfer processes are the main coupling mechanisms. Energy transfer can occur either through Förster energy transfer or through Dexter energy transfer (as mentioned in section 3.2 ). Charge transfer occurs when the electron and the hole have different tunneling probabilities towards graphene. If this difference is big enough, there will be a time on which the heterostructure is in a charge-separated state. This state can be short ($\sim$ 1 ps) or long-lived ($>>$ 1 ps). In the case of long-lived charged separated states, this could lead to photodoping which can have an intrinsic (through charge tunneling) or extrinsic origin (adsorbates, residual doping, etc... ). Needless to say, a device would benefit from such effect since one can enhance the photoconductivity of this heterostructure by harvesting the charges from graphene before relaxation takes place. Our studies regarding these points will revolve around the following questions:

- What is the impact of electron redistribution (static charge transfer) in TMD/Graphene

heterostructures?

- How can we understand photodoping in these heterostructures?

An interesting situation might arise at low temperatures where the radiative lifetime of excitons in TMDs reduces down to few ps [19]. This means that there will be a competition between radiative decay and non-radiative decay towards graphene. We will discuss the experimental realization of this concept in detail in section 3.3 and we will see that one can obtain single- and narrow-line emission spectra from TMDs. In that case, we would need to answer the following questions:

- What is the origin of this filtering effect?
- What is the underlying dynamics at low temperatures?

In this chapter, I will discuss the physics of TMD/1LG heterostructures. In section 3.2, I will discuss with more detail the previously mentioned near-field coupling mechanisms and the extent of their effects in the optical properties of the heterostructure. In section 3.3, I will address the filtering of the PL at low temperatures. Section 3.4, is dedicated to giving microscopic insights on low-temperature excitonic dynamics. Finally, in section 3.6, I will conclude the chapter and give some perspectives. The results presented in this chapter resulted in two publications on which I was co-author [9] and first author [10].

## 3.2 Near field mechanisms in TMD/graphene

In this section, I will discuss the aforementioned interlayer coupling mechanisms.

### 3.2.1 Static charge transfer

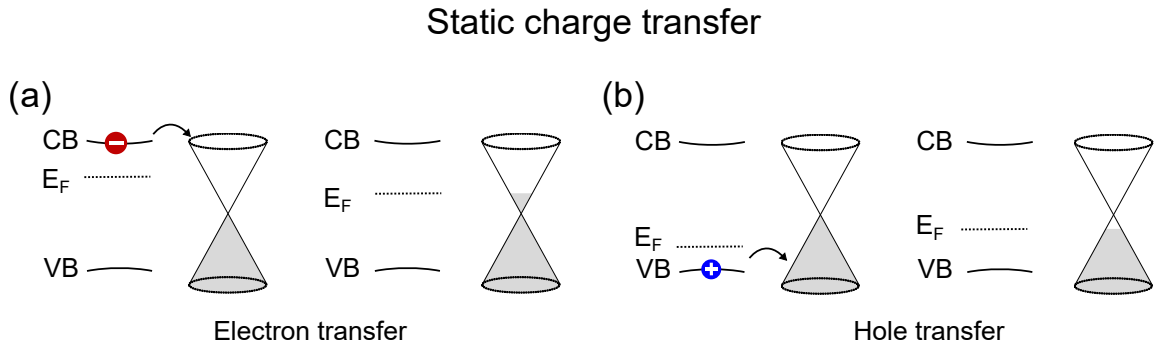


Figure 3.2: **Static charge transfer process.** Scheme illustrating electron redistribution in TMD/1LG heterostructures. Depending on the relative offset between the bands and the Fermi levels, charge tunneling can occur upon contact. This process is illustrated for electrons (a) and holes (b).

Static charge transfer occurs when charges tunnel from one layer to the other. This process happens in absence of photoexcitation and it depends on the band offset and the Fermi level alignment between the TMD and graphene. In essence, graphene is a broadband acceptor with a Fermi level located within the gap of TMDs. As a result, electron redistribution can happen as long as graphene is not heavily doped (typically for values of $|E|_F < 200 - 300$ meV). Figure 3.2 shows a scheme illustrating this process. Although this process happens in the dark, one can single out hints of charge transfer using PL and Raman spectroscopies using the lowest possible powers to avoid photo-induced effects. One example is the appearance of charged excitons. TMDs are known to display residual doping arising from the fabrication process. In fact, it is challenging to obtain perfectly neutral samples. Neutral areas can be found, but are reduced to localized spots which are far from being reproducible. As a consequence, trions can be formed due to the interaction between $X^0$ and native dopants. At room temperature, the luminescence spectra of TMDs contain contributions arising from the radiative recombination of trions[1]. This is possible because their binding energy varies from 30-40 meV depending on the material (see table 1.2), which is is comparable to $k_BT \sim 25$ meV. As a result, we can use this contribution to indirectly obtain information regarding the doping of the TMD layer. Figure 3.3 shows room temperature PL spectra of TMD and TMD/1LG heterostructures. In the former, trion recombination appears as a shoulder located 30 meV below the neutral exciton. In contrast, in TMD/1LG, we observe no such shoulder,

[1]It is difficult to conclude whether $X^*$ is positively ($X^+$) or negatively ($X^-$) charged only by using PL, especially at room temperature.

which suggests a vanishingly small doping. Similar observations have been reported in $WS_2$/1LG heterostructures by Hill *et al.* [163]. This is promising since it could provide a deterministic way of obtaining quasineutral or even completely neutral samples. We are going to come back to this point in section 3.3.6.

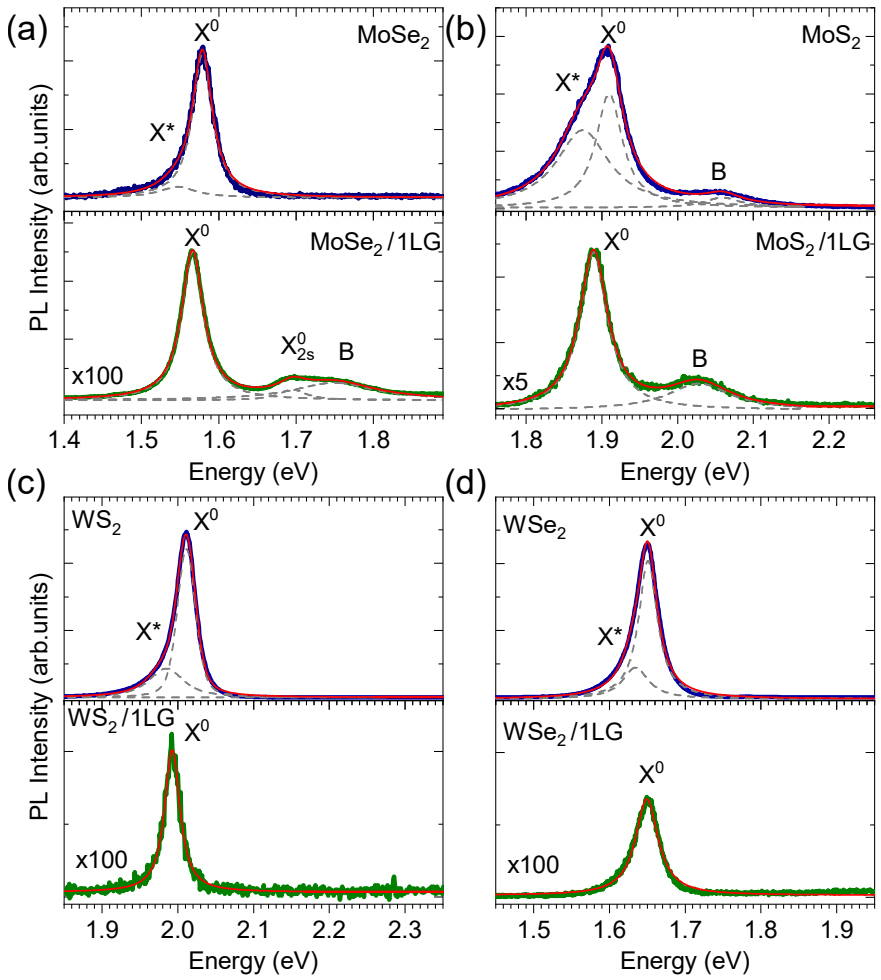


Figure 3.3: **Signs of neutralization at room temperature.** PL spectra at room temperature of (a) $MoSe_2$ (top), $MoSe_2$/1LG (bottom),(b) $MoS_2$ (top), $MoS_2$/1LG (bottom),(c) $WS_2$ (top), $WS_2$/1LG (bottom),(d) $WSe_2$ (top), $We_2$/1LG (bottom). The spectra are fitted with double lorentzians. The spectra were recorded under cw-excitation at 532 nm and under a photon flux of $10^{21}$ $cm^{-2}$.

However, as this happens "in the dark" upon contacting the layers, charge redistribution can not account for the reduction of the excitonic lifetime.

### 3.2.2 Charge transfer and photodoping

Photo-induced charge transfer or **photodoping** occurs when charge carriers tunnel from the TMD to graphene upon illumination or vice-versa. This process can have an intrinsic origin (through a long-lived charge separation state) or an extrinsic origin (due to adsorbates, surface traps, or defects). In the former, photoexcited carriers rapidly tunnel from

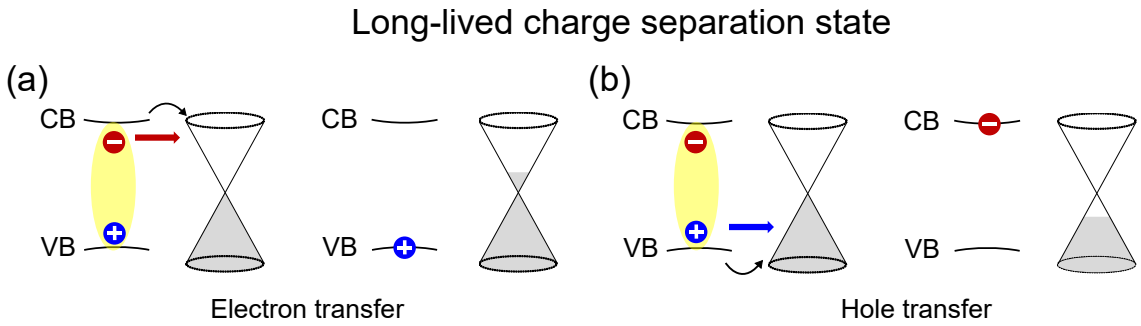


Figure 3.4: **Photoinduced charge transfer.** Scheme illustrating electron (a) and hole (b) transfer upon photoexcitation.

the TMD towards graphene and reside in graphene as long as the illumination is on. The sign of the carriers depends on the relative position between the bands and the Fermi level in graphene (figures 3.4a and b). Ultimately, this results in a charge-separated state on which both the graphene and the TMD are doped with opposite signs. Experimentally, photoinduced charge transfer can be probed by monitoring the doping level of graphene as a function of the incident photon flux. One of the first works reporting on this process was done by Zhang *et al.* [164]. In this article, they focused on a $MoS_2$/1LG heterostructure and used the charge neutrality point (CNP) of graphene as a probe, and determined that electrons are being transferred towards graphene. Nevertheless, there is no consensus on how long the lifetime of this charged state is.

Extrinsic photodoping has been demonstrated in $SiO_2$-supported TMD/1LG heterostructures [8]. This was a part of a study performed by two former Ph.D. students in my group. In their work, they used a combined approach of PL and Raman spectroscopies and compared 5 different $MoSe_2$/1LG/$SiO_2$ samples in a vacuum and at air. They observed that:

- At air, the Fermi energy of graphene in the heterostructure increases with the incident photon flux ($\phi$) up to a saturation value close to $\sim$ 300 meV.
- In a vacuum, the same saturation occurs but one can achieve at any given incident photon flux. This happens slowly in timescales in the order of minutes.

This suggests the suppression of a charge leaking channel in air. Indeed, contaminants present in the surrounding air can be adsorbed on the surface of the TMD and act as a trap for excitons. In vacuum, an important proportion of contaminants is desorbed and one recovers the intrinsic situation where the transferred carriers remain in graphene as long as the laser is on. In contrast, in ambient air, the carriers can escape the graphene layer due to the desorption process. Their work proves that photo-doping can occur in these samples, however, it has little to no effect on the excitonic dynamics. Therefore, photo-induced charge transfer alone can not be behind the observed PL quenching in TMD/1LG. This is

further supported by a recent work done in collaboration with La Sapienza in Rome (T. Scopigno's team). In this study, time-resolved Raman scattering spectroscopy is employed to demonstrate that no net charge transfer is observed in WS2/1LG after  3 ps. In other words, if charge separation is at play, this study provides an upper bound of  3 ps for the lifetime of the charge-separated state [162].

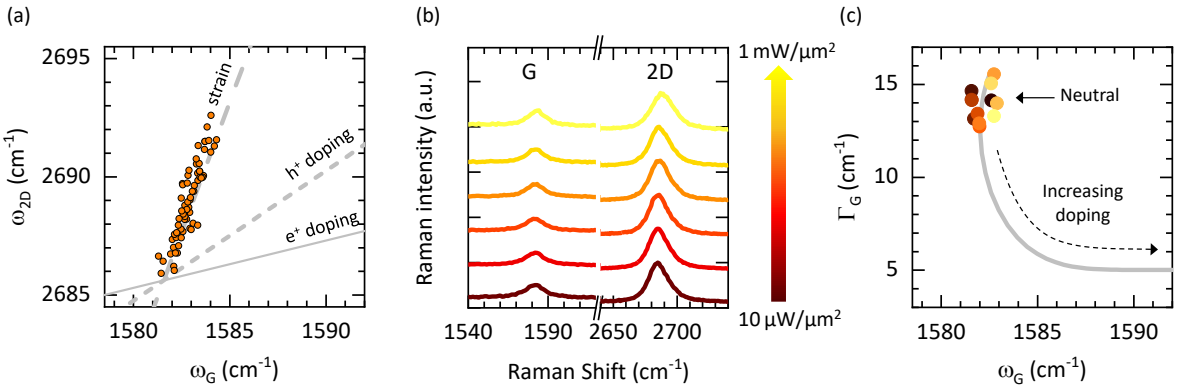


Figure 3.5: **Photodoping.**(a) Correlation between $\omega_{2D}$ and $\omega_G$ extracted from a Raman map of the sample in figure 3.1. The slope suggest native strain in the heterostructure [165, 136].(b) Selected Raman spectra with different incident photon fluxes. The color code corresponds to the explored incident flux range.(c) Correlation between $\Gamma_G$ and $\omega_G$ indicating low doping. The points are extracted from the spectra shown in (b) and are color-coded accordingly. All spectra were acquired under cw excitation at 532 nm and in vacuum.

Even though these processes are not behind the observed quenching, they can hamper our access to intrinsic features. We can suppress this effect by studying the sample in vacuum, however, there could be a similar effect arising from trapped charges in the underlying substrates [166, 8, 167]. A workaround to this problem is to use inert substrates that are less prone to dope the monolayer upon illumination. This is the case for the sample shown in figure 3.1. The sample consists of a thick ( 100 nm) hBN flake on which we transferred a $MoSe_2$/1LG heterostructure. To probe the doping, we used Raman spectroscopy as in reference [8], and focused on the G- and 2D-mode of graphene (See section 1.2.2). As discussed in chapter 1, the presence of doping leads to a renormalization of the Kohn anomaly at the $\Gamma$ point. This induces an upshift of the G-mode frequency ($\omega_G$) and a narrowing of its width ($\Gamma_G$). The 2D mode is expected to change similarly, although the effect is much less pronounced. Then from the correlation between $\omega_G$ and $\omega_{2D}$ as well as between $\Gamma_G$ and $\omega_G$, we can extract information on possible doping arising from the substrate. Figure 3.5a shows the correlation between $\omega_{2D}$ and $\omega_G$ extracted from a hyperspectral Raman map of the sample. We observe a linear correlation with a slope equal to 2.2. From this value, we can deduce that the sample is subject to native compressive strain [165, 136], probably originated during the fabrication process. No contributions coming from residual doping are observable in this curve.

Figure 3.5b shows a series of Raman spectra with increasing incident power. For this data set, the power was varied from 10 $\mu$W/$\mu$m$^2$ up to 1mW/$\mu$m$^2$. We extracted $\omega_G$ and $\Gamma_G$ from these spectra and plotted their correlation in figure 3.5c. We observe that the G-mode remains at a value equal to $1582.2 \pm 0.5$ cm$^{-1}$. $\Gamma_G$ also remains constant around $\approx 14 \pm 1$ cm$^{-1}$. These values are matching a scenario on which we have quasi-neutral graphene with at most $10^{11}$cm$^{-2}$[168]. Therefore, we can safely conclude that there is no photodoping in this architecture. This proves that hBN not only provides a substrate that improves the optical quality of TMD samples but also provides a good sample to get rid of the photodoping.

### 3.2.3 Energy transfer

Energy transfer in TMD/1LG stems from the near field Coulomb interaction between carriers in both layers. Formally, it can happen in two ways: either through dipole-dipole interaction (Förster Energy transfer or FRET [169]) or through charge tunneling (Dexter energy transfer or DET [170]) as shown in figures 3.6a and b. In both cases, no net charge is flowing between the layers.

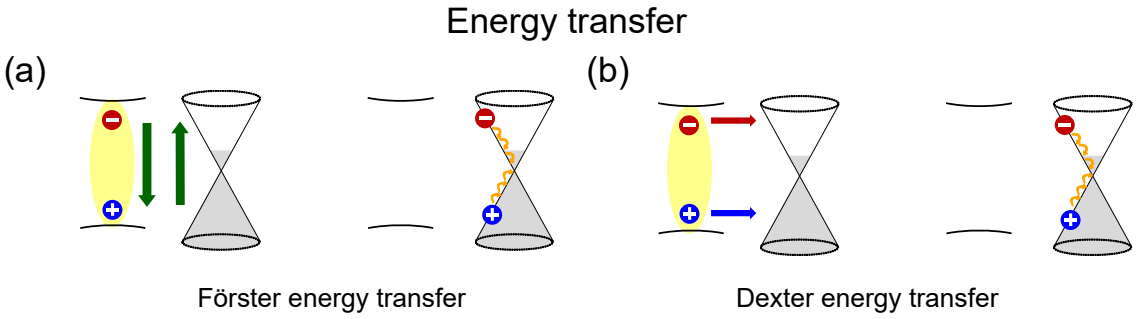


Figure 3.6: **Energy transfer mechanism.** Scheme illustrating the energy transfer process. (a) FRET process in which an exciton in the TMD transfer its energy to graphene through dipole-dipole interaction (b) DET process in which an exciton in the TMD tunnels into graphene. Both processes end up in the same final state.

Notice that both processes end up in the same final state: an electron-hole pair in graphene. However, the underlying physics is quite different. For instance, FRET is a long-range process that depends on the spectral overlap between the emitter and the acceptor. Furthermore, it is a process that becomes more efficient with increasing volume and dimensionality of the species involved [169, 145]. Since excitons in TMDs and graphene have dipoles aligned in-plane, FRET can play an important role in the heterostructure. On the other hand, DET is a short-range mechanism that depends on the overlap between the orbitals of adjacent layers. As such, this mechanism decays exponentially with distance and becomes negligible at distances larger than $\sim 1$ nm. Therefore, to differentiate between them, one could investigate situations in which DET can be ne-

glected. For instance, by separating the TMD and graphene by more than 1 nm and study the PL quenching. Altogether, energy transfer either through DET or FRET is currently the main candidate to explain the PL quenching observed in TMD/1LG [8, 162].

### 3.2.4 Short-lived charge-separated state.

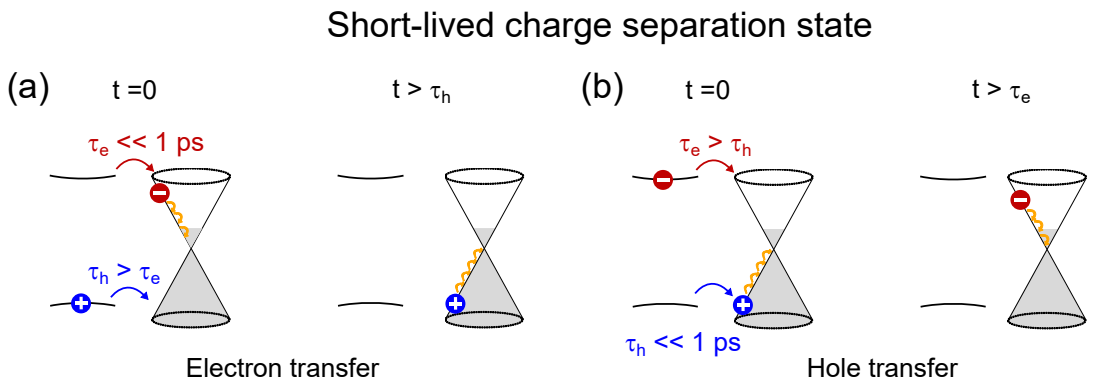


Figure 3.7: **Short-lived charge-separated state.** This process occurs when electrons and holes have different tunneling probabilities to graphene. As a result, a charged separated state can be formed. Moments after the initial excitation one of the carriers instantly transfers into graphene leaving the other one behind. After a timescale $\tau_2$ the remaining carrier tunnels into graphene resulting in non-radiative decay of the initial exciton. This process is shown in (a) for electrons and in (b) for holes. Eventually, after a few ps, the system ends up in the same final state as in the case of Förster or Dexter energy transfer.

Recently, a new scenario has been proposed. In this scenario, electrons and holes have different tunneling probabilities to graphene resulting in a short-lived charged separated state (as shown in figure 3.7). This has been demonstrated recently in a $WS_2$/1LG heterostructure [18]. In this case, after the exciton is created, the hole tunnels into graphene practically instantaneously while the electron remains in the CB for at least 1 ps. In the transient state, the monolayer is negatively charged, and graphene is correspondingly positively charged. Evidence of this transient state was obtained through time- and angle-resolved photoemission spectroscopy (tr-ARPES). Notice that this process is equivalent to charge transfer for short times (t $<$ 1 ps). However, once the electron tunnels to graphene, the net charge transfer is zero. An important point in this article [18] are the experimental conditions with which the transient state was observed. They used photons with an energy of 2 eV and a fluence of $2\text{mJcm}^{-2}$. This corresponds to an exciton density of $\sim 10^{14}$ $\text{cm}^{-2}$ which is three orders of magnitude above the typical exciton densities we create in our experiments. Moreover, this also means these experiments are carried out in the non-linear regime. Overall, this mechanism is efficient for unbound electrons and holes. We could imagine a scenario in which energy transfer (either through FRET or DET) dominates at low photon fluxes a near resonance, whereas charge separation dominates at high excitonic density regimes and for excitation well above the bandgap.

## 3.3 Filtering the luminescence of TMDs with graphene

So far, we have discussed all interlayer coupling mechanisms that can be relevant in TMD/1LG heterostructures. Among these, only energy transfer processes such as FRET, DET, or short-lived charge-separated states can explain the observed PL quenching at room temperature. However, a detailed investigation of the excitonic dynamics can be complex since non-radiative processes are non-negligible at room temperature. This motivates us the investigate TMD/1LG at cryogenic temperatures where the excitonic lifetime is reduced to few ps [19] and determined only by radiative recombination (section 1.5.2). The shortening of $\tau_{X^0}$ is advantageous since it hinders the accumulation of excitons in the light cone, which prevents them from interacting with each other[2]. This presents an interesting situation because in these conditions radiative recombination occurs in the same timescale as the energy transfer to graphene. We will see that this has fundamental consequences in the low-temperature PL spectra of TMDs and leads to a filtering effect where only luminescence from the neutral exciton is observed. In the following, I will present a combined approach involving PL, DR, TRPL, and PLE spectroscopies on which we investigated the properties of TMD/1LG at low temperatures. These results culminated in the following publications [9] and [10].

### 3.3.1 Phenomenology

Figure 3.8 shows typical PL spectra of hBN-capped $MoSe_2$, $WSe_2$, $MoS_2$ and $WS_2$ (upper panel) and hBN-capped TMDs/1LG of the same TMDs (lower panel). All spectra are normalized and the scaling factors between the $X^0$-line in the TMDs and the single peak in TMD/1LG spectra are shown next to the $X^0$-line in the upper panel. In the bare TMD, the spectra are composed of two or more peaks arising from the recombination of different excitonic particles as explained in section 1.7. As expected, bright TMDs ($MoSe_2$, $MoS_2$) display spectra composed of two peaks which we attribute to the neutral exciton $X^0$ (marked with an asterisk) and the trion $X^*$ situated at lower energy. Dark TMDs ($WSe_2$ and $WS_2$), on the other hand, display the same two peaks together with a manifold of other lower energy resonances arising from other excitonic species such as dark excitons, biexcitons, localized excitons, among others (see section 1.7). A tentative assignment of these transitions is shown in Figure 3.9. This assignment was done based on recent reports [100, 99, 101, 103]. Interestingly, in the case of $WS_2$, we can resolve the fine structure of the trion arising from singlet and triplet states ($X^*_{S/T}$).

In the lower panel, the spectra are strikingly different. Instead of a manifold of peaks, we observe single and narrow emission lines for all TMDs coupled with graphene. This is striking since even complex spectra such as the one of $WSe_2$ and $WS_2$ lack these low energy

[2]It is important to point out that this holds as long as one investigates the dynamics at low incident photon fluxes where Auger-recombination cannot occur. i.e. we can neglect exciton-exciton interaction.

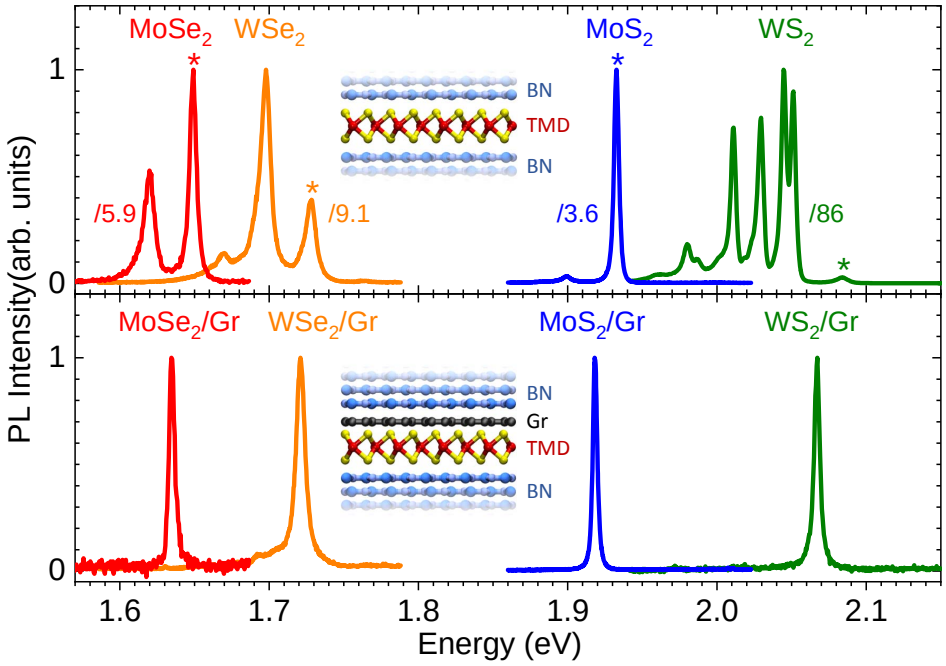


Figure 3.8: **Filtering the luminescence of TMDs at 15 K.** Top: PL spectra of hBN-capped $MoSe_2$, $WSe_2$, $MoS_2$ and $WS_2$. Bottom: PL spectra of hBN-capped $MoSe_2$/1LG, $WSe_2$/1LG, $MoS_2$/1LG and $WS_2$/1LG. The spectra are normalized to the maximum of emission and the scaling factor between the TMD and TMD/1LG counterpart is shown in the top panel for each spectra. The resonance corresponding to $X^0$ is marked with an asterisk. All spectra were recorded at 15 K under cw-laser excitation at 2.33 eV ($MoSe_2$, $WS_2$, $MoS_2$) and 1.96 eV ($WSe_2$).

contributions. This is shown in semi-logarithmic scale in figure 3.9. For instance, we can see that there is no sign of the dark exciton $X^D$ in both $WS_2$ and $WSe_2$, even though there is a small remnant of the $X^*$ in the former probably due to a partial decoupling between the layers. Nevertheless, our observations remain qualitatively the same for all TMD/1LG heterostructures: single- and narrow-line emission spectra. Furthermore, for all TMD/1LG heterostructures, the single-line appears redshifted with respect to the $X^0$-line in the bare TMD by about 10 meV. Furthermore, these lines exhibit Lorentzian profiles with widths in the order of $\sim$ 5 meV suggesting a reduction of dephasing. The energy and width of these peaks are obtained through a Lorentzian fit and are reported in table 3.1.

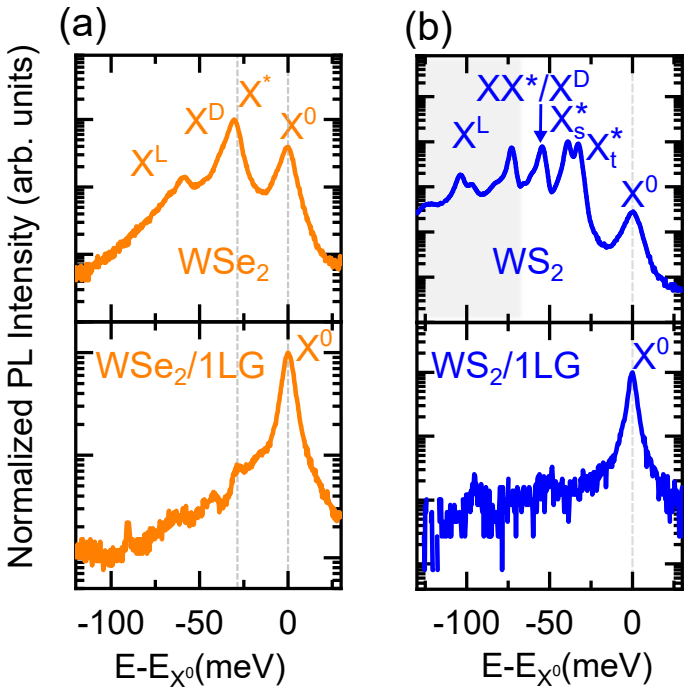


Figure 3.9: **Characterizaton of PL spectra of dark TMDs.** Low temperature PL spectra of hBN-Capped $WSe_2$ (a) and $WS_2$ (b)samples. The spectra are characterized by many peaks arising from $X^0$ and $X^*$ as well as dark excitons($X^D$), biexcitons($XX$) and localized excitons ($X^L$).The spectra were recorded at 15 K, in the linear regime and using cw-laser excitation at 2.33 eV ($WS_2$) and 1.96 eV ($WSe_2$).

### 3.3.2 Identifying $X^0$

For simplicity, let us continue our discussion by focusing on $MoSe_2$. In order to identify the origin of this single-line emission, we measured both the PL and DR spectra of the sample. Figures 3.10a and b show the DR (top) and PL (bottom) spectra from hBN-capped $MoSe_2$ and hBN-capped $MoSe_2$/1LG areas.

Just as before, in the bare TMD, both spectra display two resonances associated with $X^0$ and $X^*$ (marked with the gray dashed lines). In contrast, we observe only one intense resonance in TMD/1LG in both DR and PL. This suggests that the resonance in TMD/1LG might arise from a screened $X^0$. The redshift could be understood in terms of dielectric screening due to the presence of graphene [20]. To further prove our hypothesis that the single-line character of the TMD/1LG spectrum arises from $X^0$, we studied the PL as a function of temperature (T). Figure 3.11 shows the emission energy of the main peak obtained from this sample as a function of temperature. We can see that the emission energy in TMD/1LG is systematically located between the $X^0$ and $X^*$ lines in the bare TMD. Therefore, we can safely assign the single-emission line in TMD/1LG to the recombination of $X^0$.

From this observation, we can conclude that no $X^*$ emission is observed in the het-

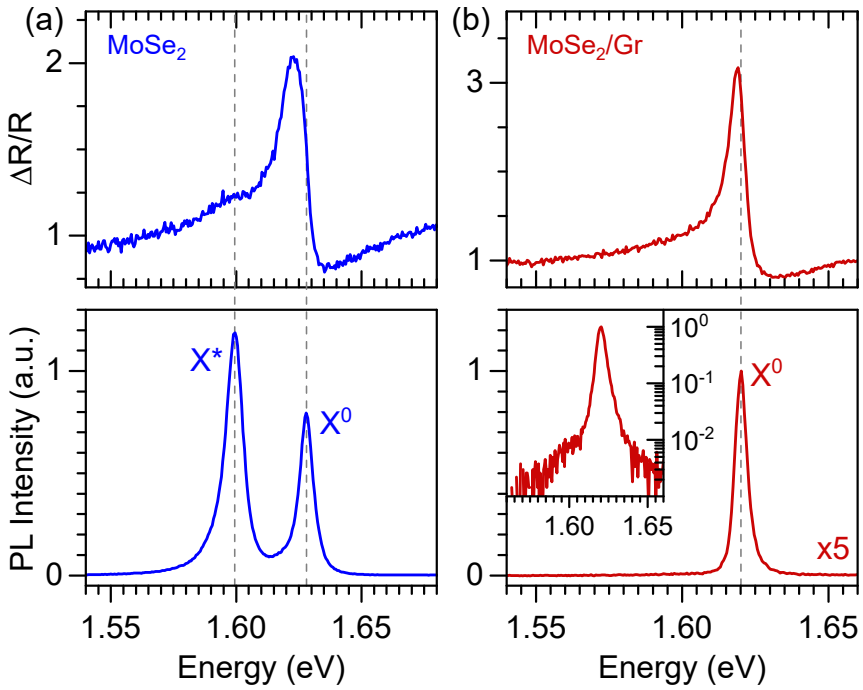


Figure 3.10: **Identifying $X^0$.** DR (top) and PL (bottom) spectra of hBN-capped $MoSe_2$ (a) and $MoSe_2$/1LG (b). The spectra were acquired at a temperature of 4 K, in the linear regime using cw-laser excitation at 2.33 eV.

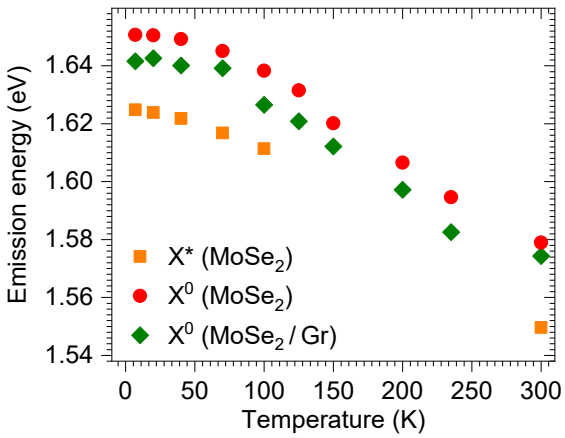


Figure 3.11: **Temperature dependent PL spectroscopy on a hBN-capped $MoSe_2$/1LG sample.** Temperature dependent peak energy of the $MoSe_2$ exciton ($X^0$) and trion ($X^*$) emission lines. All data were recorded in the linear regime using cw-laser excitation at 2.33 eV.

erostructure and that the emission stems from a screened $X^0$.

### 3.3.3 Quenching factors

Now that we have identified the origin of the single-emission line. Let us comment on two different quenching factors which will be useful to understand our measurements. First, let us define the exciton quenching factor $Q_{X^0}$ in terms of the integrated intensity of the

$X^0$ in $MoSe_2$ ($I_{X^0}$) and $MoSe_2$/1LG ($I'_{X^0}$) such that:

$$Q_{X^0} = \frac{I_{X^0}}{I'_{X^0}}$$

By monitoring this value, we can obtain information regarding the energy transfer from the cold exciton population towards graphene. The values of $Q_{X^0}$ found for the samples shown in figure 3.8 are shown in table 3.1. We observe moderate quenching factors close to one order of magnitude. This reduction with respect to the two orders of magnitude quenching observed at room temperature is not surprising. It is a direct consequence of the shortening of the radiative lifetime at low temperatures.

The second quenching factor that will be useful is the total quenching factor $Q_{\text{tot}}$. This value relates the total integrated intensity in the bare TMD spectra with the integrated intensity of the exciton in the TMD/1LG such that:

$$Q_{\text{tot}} = \frac{I_{\text{tot}}}{I'_{X^0}}$$

$Q_{\text{tot}}$ gives us information about the dynamics of the hot excitonic population created moments after excitation (figure 3.17). In the TMD, hot excitons can undergo relaxation resulting in the formation of different excitonic species. In contrast, in TMD/1LG, hot excitons can only form neutral excitons. The calculated $Q_{\text{tot}}$ for the samples in figure 3.8 are shown in table 3.1. As we can see, these values are larger than $Q_{X^0}$ suggesting an additional non-radiative decay path involving hot exciton transfer to graphene.

| | $E_{\text{X}^0}$ (eV) | $\Gamma_{\text{X}^0}$ (meV) | $Q_{\text{X}^0}$ | $Q_{\text{tot}}$ |
|---|---|---|---|---|
| $MoS_2$ | 1.933 | 4.0 | 3.9 | 4.3 |
| $MoS_2$/1LG | 1.918 | 3.5 | | |
| $MoSe_2$ | 1.649 | 5.6 | 7.1 | 13.6 |
| $MoSe_2$/1LG | 1.635 | 4.4 | | |
| $WS_2$ | 2.084 | 9.7 | 3.0 | 227 |
| $WS_2$/1LG | 2.067 | 4.3 | | |
| $WSe_2$ | 1.728 | 8.7 | 3.7 | 21 |
| $WSe_2$/1LG | 1.721 | 7.2 | | |

Table 3.1: **Emission characteristics for the samples shown in Fig. 3.8** Peak emission energy ($E_{\text{X}^0}$), full width at half maximum ($\Gamma_{\text{X}^0}$) of the $X^0$ emission line for the PL spectra of the four hBN-capped samples discussed in Fig.3.8. The data were extracted from Lorentzian fits for hBN-capped samples and graphene/$MoSe_2$ and from Voigt fit for hBN-capped $MoSe_2$.

### 3.3.4 Spatial homogeneity

To verify the robustness of our results, we repeated the same measurements on another sample. In particular, we focused on the 1LG/$MoSe_2$/hBN sample shown in figure 3.1a. PL spectra of the $MoSe_2$/hBN (blue), 1LG/$MoSe_2$/hBN (orange) and 2LG/$MoSe_2$/hBN (red) areas are shown in figure 3.12a. The spots on which the measurements were done are indicated in the PL intensity map in figure 3.12b. Just as before, we confirm the single line character of the spectra and the narrowing of the $X^0$ line. This indicates that one graphene layer is enough to reduce dephasing in TMDs. Moreover, thanks to a hyperspectral mapping of the sample, we could verify these observations everywhere in the heterostructure. Figures 3.12c-g show a hyperspectral map study of these peaks. Averaging over these maps, we deduce that in the reference $X^0$ and $X^*$ are situated at $1.645 \pm 0.002$ eV and $1.616 \pm 0.003$ eV, respectively. In the heterostructures we observe $1.636 \pm 0.002$ eV and $1.633 \pm 0.003$ eV for hBN/$MoSe_2$/1LG and hBN/$MoSe_2$/2LG respectively.

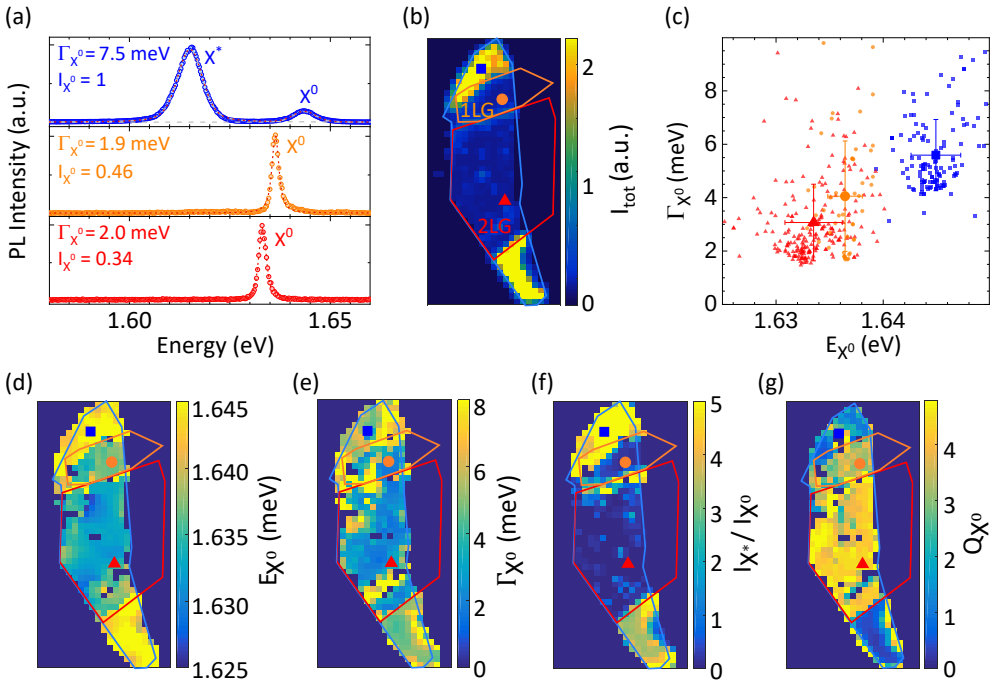


Figure 3.12: **Low temperature characterization.** (a) PL spectra of $MoSe_2$/hBN (top), 1LG/$MoSe_2$/hBN (middle), 2LG/$MoSe_2$/hBN (bottom) taken on the spots shown in (b). The intensity $I_{X^0}$ and FWHM $\Gamma_{X^0}$ of each spectra are shown in the figure. (b) PL Intensity map of the sample. The blue, orange and red countours in figures (b) and (d-g) mark the different regions of the sample.(c) Correlation between $\Gamma_{X^0}$ and $E_{X^0}$ extracted from hyperspectral maps of the sample. The average values and standard deviations of each set of points is shown in the figure with the same color code. Neutral exciton emission (b) energy $E_{X^0}$ and (d) FWHM maps.(e) Map of the intensity ratio between $X^0$ and $X^*$. (g) $Q_{X^0}$ map. The data was recorded at 14 K, using cw-laser excitation at 633 nm and under a laser intensity close to 100 $\mu W/\mu m^2$.

Furthermore, we confirm that the narrowing effect is linked to the presence of graphene. Indeed, the FWHM ($\Gamma_{X^0}$) is reduced from 7.5 meV in the bare TMD, down to 1.9 meV and 2 meV in 1LG and 2LG respectively. In well-coupled areas, $\Gamma_{X^0}$ can get as low as 1.6 meV which is the narrowest peak I have observed so far. This value is not far from the homogeneous linewidth ($\sim 300$ $\mu$eV) and is comparable to the ones reported in fully hBN-capped samples (table 3.1 and references [55, 25]). We conclude that graphene alone is enough to reduce inhomogeneous broadening without the need for a top hBN layer. This is further verified through a statistical analysis of the emission spectra all over the sample (figure 3.12c). From this spatial analysis, we can also conclude that the second layer of graphene further improves the encapsulation effect. We observe a moderate quenching factor from both the $MoSe_2$/1LG and $MoSe_2$/2LG corresponding to $Q_{X^0} = 3 \pm 1$ and $Q_{X^0} = 4 \pm 1$ respectively. This is in agreement with what we have observed in the fully hBN-capped samples in the previous section.

### 3.3.5 Summary of observations

So far we have seen that the coupling with graphene results in:

- Relatively small quenching of the $X^0$-emission at low temperatures.
- Narrowing of the $X^0$-line.
- No $X^*$ signatures in PL.
- No peaks arising from other excitonic particles can be observed either.

We have already discussed some of these phenomena. For instance, the small reduction of the quenching factor arises from the shortening of the excitonic lifetime at low temperatures. Similarly, the narrowing stems from the encapsulating effect that graphene provides. However, we have yet to understand the remaining ones. In the following, we are going to address these observations.

### 3.3.6 Neutralization of the TMD

In section 3.2 we have seen that the trion is a good probe for doping in the heterostructure. Indeed, at low incident fluxes, trions form when excitons interact with native dopants. Therefore, the absence of the $X^*$ could indicate a reduction of doping due to electron redistribution. However, to support this, we must rule out alternative scenarios that could account for the observed behavior. In total, three scenarios could explain this trion absence (figures 3.8 and 3.10) in the heterostructure:

1. **The TMD is doped and graphene quenches trion emission.**

In this scenario, the energy transfer towards graphene is more efficient than the radiative decay of $X^*$. However, our observations (figure 3.10) allow us to put a lower bound for the trion quenching factor defined as:

$$Q_{X^*} = \frac{I_{X^*}}{I'_{X^*}} \sim 10^2 - 10^3$$

This implies a reduction of the trion lifetime down to $\sim$ 100 fs while the $X^0$ remains with a $\sim$ ps lifetime. This value is extremely short for such quasiparticles. This is further supported by the absence of the $X^*$ resonance in the DR spectrum which suggests trions are not being efficiently formed. These observations allow us to safely rule out scenario 1.

2. **The TMD is doped and graphene quenches trion formation.**

   In this scenario, hot excitons are transferred to graphene before they can from trions. Indeed, in TMDs, non-resonant excitation results in the creation of an out-of-equilibrium excitonic population. This population rapidly relaxes towards the band edges and ends up outside of the light cone [21]. Afterwards, these so-called 'hot excitons' relax back to the light cone through phonon emission resulting in exciton and trion formation. However, it is known that $X^0$ and $X^*$ form in the same timescale [19]. This means that we should observe a similar quenching factor for both species, which is clearly not compatible with our results. Therefore, we can safely rule out scenario 2 as well.

3. **The TMD is neutralized by graphene.**

   The only possibility remaining and the most likely to be correct is the third one. Here, graphene acts as a reservoir for electrons and holes and completely neutralizes the TMD through static charge transfer. This charge transfer happens without the need for photoexcitation and will increase the Fermi energy of graphene slightly. We expect this neutralization effect to occur for all TMDs, regardless of their bright or dark nature. This is consistent with our observations in figure 3.3.

### 3.3.7 Filtering of long-lived excitonic species

The neutralization inhibits the formation of charged species. However, as we discussed in section 1.7, dark TMDs exhibit supplementary peaks arising from quasiparticles that are not necessarily charged. Therefore their absence in the PL spectra cannot be explained as a consequence of neutralization. Nevertheless, all of the aforementioned excitonic species have characteristic lifetimes in the order of 100 ps, which are much longer than the ps-energy transfer to graphene [19, 22, 23, 24]. In consequence, the decay path of these species is predominantly non-radiative.

### 3.3.8 Photostability

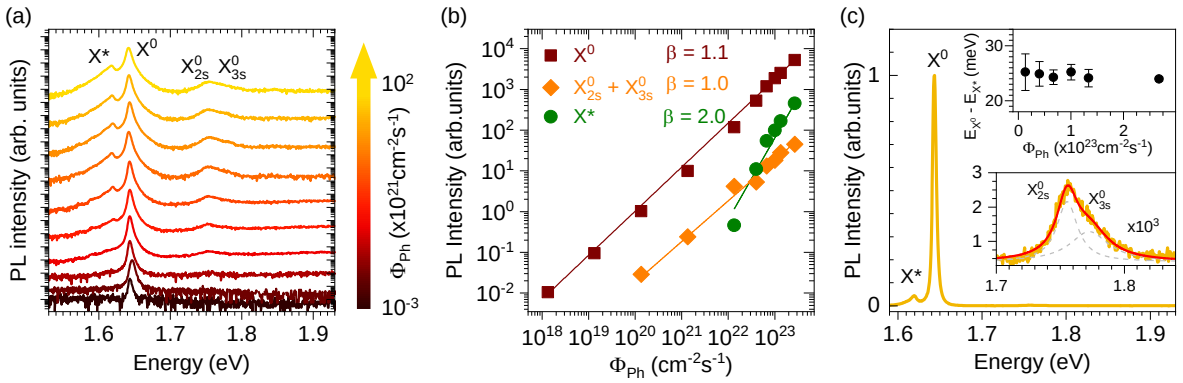


Figure 3.13: **Photostability of $MoSe_2$/1LG heterostructure.** (a) PL spectra of $MoSe_2$/1LG taken at increasing photon fluxes. Luminescence arising from $X^0$ and its excited states, $X^0_{2s}$ and $X^0_{3s}$, is observed. At high powers, a photogenerated trion $X^*$ appears 25 meV below the $X^0$ line. (b) PL Intensity of the different excitonic species shown in (a). For the exciton and its excited state, a linear dependence is observed. $X^*$ on the other hand evolves quadratically, which is consistent with photogeneration due to Auger processes.(c) PL spectra taken on $MoSe_2$/1LG under cw-laser of energy 2.33 eV at a incident photon flux of $\phi = 3 \times 10^{23}\text{cm}^{-2}s^{-1}$ and at 14 K. The upper inset shows the trion binding energy as a function of the photon flux. The lower inset shows a zoom on the excited states. Figure extracted from [9]

It is clear that TMD/1LG offers an interesting platform to tune the luminescence of a TMD. Indeed, we have seen that the coupling between these two leads to:

- Filtering of long-lived excitonic species due to energy transfer towards graphene.
- Neutralization of the TMD due to static charge transfer.
- Narrowing of the emission features due to the encapsulation provided by graphene. This is true even in absence of a top hBN layer.

To further investigate the benefits of this heterostructure, we studied the PL of this heterostructure at different incident photon fluxes. A series of spectra acquired at different incident powers is shown in figure 3.13a. At increasing photon flux, we observe two new features emerge in the PL emission. The first one is blueshifted by 120 meV with respect to $X^0$. We assign it to the hot-luminescence of the 2s- and 3s-excitonic states ($X^0_{2s}$ and $X^0_{3s}$ respectively). The energy position of these states will be useful to estimate the excitonic binding energy as we will see in section 3.3.9. The second one is redshifted by $25 \pm 2$ meV with respect to $X^0$. To investigate the origin of this feature (marked $X*$), we plotted the PL intensity of each peak as a function of the incident photon flux. This is shown in figure 3.13b. We observe a quadratic dependence which could be consistent with biexcitons ($XX^0$). However, $XX^0$ in $MoSe_2$ monolayers have binding energies of $\leq 20$

meV, which is lower than the value of the $X^*$ peak [97]. Moreover, the $XX^0$ binding energy should be even lower in $MoSe_2$/1LG due to dielectric screening. Therefore, we assign the redshifted feature to a screened photogenerated trion. Indeed, at high incident photon fluxes, exciton-exciton interaction becomes non-negligible due to the increased excitonic density. Their subsequent annihilation can generate free carriers, which then form trions upon photon absorption. This process would also produce the quadratic dependence we observe. Surprisingly, we observe a linear dependence for $X^0$ and its excited states in all the explored power range. This means that even at high photon fluxes, the TMD/1LG remains in the linear regime. As a reference, figure 3.13c shows a PL spectrum taken on $MoSe_2$/1LG under an incident photon flux $\phi = 3 \times 10^{23} \mathrm{cm}^{-2} s^{-1}$. This value corresponds to 1 mW/$\mu$m$^2$. Assuming an absorptance of 10% [171] and an excitonic lifetime of 2 ps [19]. We can estimate the generated excitonic density as follows:

$$n = \phi \times \tau \times 0.1 \approx 6 \times 10^{10} \mathrm{cm}^{-2} \tag{3.1}$$

This excitonic density is in the intermediate regime where the typical exciton-exciton distance is between 10 and 100 $a_B$.

### 3.3.9 Screening and binding energy

The presence of graphene induces a screening in the heterostructure, as evidenced through the $\sim$ 10 meV redshift observed for the $X^0$ line. This screening is interesting per se and as we will see later, it will play an important role in shaping the excitonic dynamics through the modification of the excitonic binding energy [20]. Using the Rydberg series of excitonic states, we can estimate the reduction of the binding energy due to the presence of graphene. If we assume that changes in $\Delta_{1s\text{-}2s}$ are proportional to changes in $E_b$, we can write:

$$\frac{E_b}{E_b'} = \frac{\Delta_{1s-2s}}{\Delta_{1s-2s}'} \tag{3.2}$$

where the superscript ' relates to the presence of graphene. We did this for 4 samples namely:

- hBN-supported $MoSe_2$/1LG.
- hBN-capped $MoSe_2$/1LG deposited on quartz.
- hBN-capped $MoSe_2$/1LG deposited on $SiO_2$/Si.
- hBN-capped $MoS_2$/1LG.

To measure $\Delta_{1s\text{-}2s}$, we used a combination of PL and DR spectroscopies as described in section 2.3.

### hBN-supported $MoSe_2$/1LG

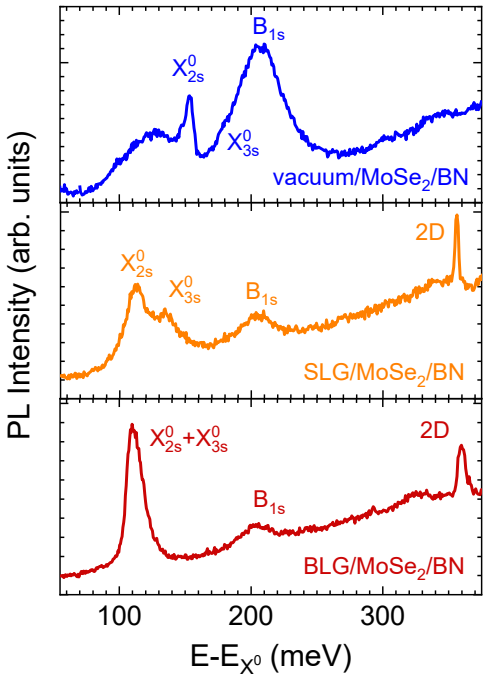


Figure 3.14: **Dielectric screening and reduced binding energy in hBN-supported $MoSe_2$/1LG**. Hot photoluminescence of the 2s and 3s states of the A-exciton and the 1s-state of the B-exciton in the sample shown in figure 3.1a. The spectra were recorded at T = 15 K with a laser photon energy of 2.33 eV. We can also observe the Raman 2D-mode of graphene around 370 meV above the $X^0$-line.

Figure 3.14 shows PL spectra of the hBN-supported $MoSe_2$, $MoSe_2$/1LG and $MoSe_2$/2LG areas. The peaks we observe arise from hot luminescence of the $X^0_{2s}$, $X^0_{3s}$ and $B_{1s}$. We measured $\Delta^{1LG}_{1s-2s} \approx 113$ meV and $\Delta^{1LG}_{1s-3s} \approx 135$ meV in 1LG/$MoSe_2$/hBN. In the case of 2LG/$MoSe_2$/hBN $\Delta^{2LG}_{1s-2s} \approx 109$ meV and in the case of the bare $MoSe_2$ reference we observe $\Delta_{1s-2s} \approx 153$ meV. Using our measurements and the value for $E_b$ reported in reference [66] for hBN-capped $MoSe_2$, we can estimate the following binding energies $E_b \approx 210$ meV, $E_b^{1\mathrm{LG}} \approx 155$ meV and $E_b^{2\mathrm{LG}} \approx 150$ meV respectively. these values are reported in table 3.2.

### hBN-capped $MoSe_2$/1LG on quartz

From our measurements in figure 3.13, we can extract the values $\Delta_{1s-2s} = 110$ meV and $\Delta_{1s-3s} = 127$ meV in $MoSe_2$/1LG. Using the same procedure as for the hBN-supported sample, we estimate a binding energy $E_b^{1\mathrm{LG}} \approx 150$ meV. This value is reported in table 3.2.

### hBN-capped $MoSe_2$/1LG on $SiO_2$/Si

Figure 3.15 shows a series of PL and DR measurements on the three areas of the heterostructure shown in figure 3.20. In every spectra, the 2s-state is indicated by a dashed gray lines. We observe $\Delta_{1s\text{-}2s} \approx 173$ meV, $\Delta^{1LG}_{1s\text{-}2s} \approx 109$ meV and $\Delta^{2LG}_{1s\text{-}2s} \approx 110$ meV for hBN-Capped $MoSe_2$, $MoSe_2$/1LG and $MoSe_2$/2LG respectively. From this, we estimate $E_b \approx 237$ meV, $E_b^{1LG} \approx 150$ meV and $E_b^{2LG} \approx 151$ meV respectively. These values are reported in table 3.2.

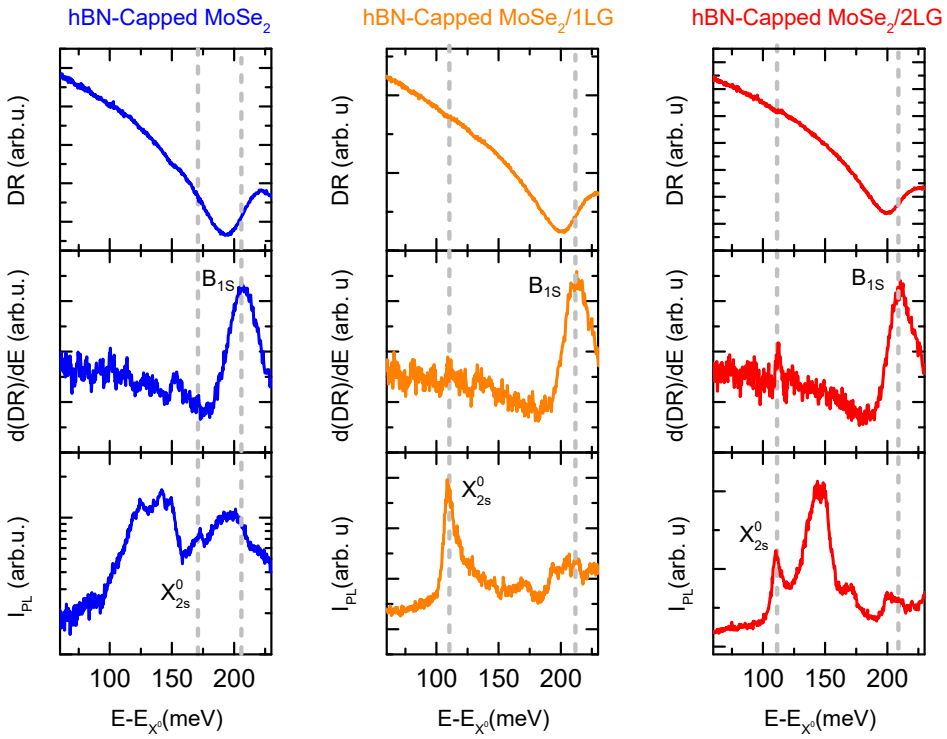


Figure 3.15: **Dielectric screening and reduced binding energy in hBN-capped $MoSe_2$/1LG** From top to bottom: DR, d(DR)/dE and $I_{PL}$ spectra of hBN-capped $MoSe_2$ (blue), hBN-capped $MoSe_2$/1LG (orange) and hBN-capped $MoSe_2$/2LG (red). PL Spectra recorded at 14K under cw excitation at 633 nm and 100 $\mu W/\mu m^2$.

### hBN-capped $MoS_2$/1LG

Figure 3.16 shows a series of PL and DR measurements on the hBN-capped $MoS_2$/1LG sample from figure 3.8. From these figures we find $\Delta_{1s-2s} \approx 171$ meV and $\Delta'_{1s-2s} \approx 136$ meV, which together with reference [66] allows us to estimate $E'_b \approx 176$ meV.

### Partial conclusion

Table 3.2 contains all of the previously mentioned values for the excitonic binding energy. In all cases, we observe a similar reduction of the binding energy. Indeed, the presence of one graphene layer reduces the binding energy by $\sim 30\%$. From our measurements, we can conclude that:

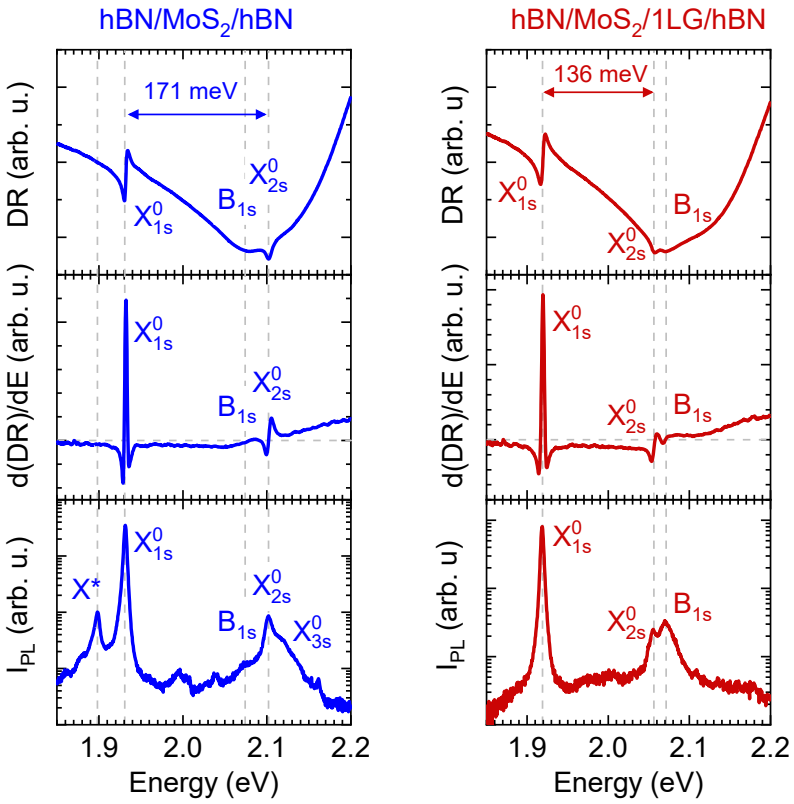


Figure 3.16: **Binding energy in $MoS_2$/1LG.** PL and DR recorded at 14 K on a hBN-capped $MoS_2$/1LG sample. The left panel and blue traces correspond to the measurements done in hBN-capped $MoS_2$. The right panel and red traces correspond to the measurements on hBN-capped $MoS_2$/1LG. All relevant excitonic species are marked by the dashed lines. The PL spectra were acquired under cw excitation at 2.33 eV. Figure extracted from [9]

- The dielectric screening in TMD/1LG heterostructures arises exclusively from graphene and the effect of the top hBN layer is negligible.
- A second layer of graphene does not change the screening appreciably.

| System | $\Delta_{1s-2s}$ (meV) | $\Delta_{1s-3s}$ (meV) | $E_b$ (meV) |
|---|---|---|---|
| $MoSe_2$/hBN (Fig. 3.14) | $153 \pm 2$ | $180 \pm 5$ | $\approx 210$ |
| 1LG/$MoSe_2$/hBN (Fig. 3.14) | $113 \pm 2$ | $135 \pm 5$ | $\approx 155$ |
| 2LG/$MoSe_2$/hBN (Fig. 3.14) | $109 \pm 2$ | – | $\approx 150$ |
| hBN/$MoSe_2$/hBN (Ref. [66]) | $168 \pm 2$ | – | $231 \pm 3$ |
| hBN/1LG/$MoSe_2$/hBN/Quartz (Fig. 3.13) | $110 \pm 2$ | $127 \pm 4$ | $\approx 150$ |
| hBN/$MoSe_2$/hBN (Fig. 3.15) | $173 \pm 2$ | – | $\approx 237$ |
| hBN/1LG/$MoSe_2$/hBN/$SiO_2$ (Fig. 3.15) | $109 \pm 2$ | – | $\approx 150$ |
| hBN/2LG/$MoSe_2$/hBN/$SiO_2$ (Fig. 3.15) | $110 \pm 2$ | – | $\approx 151$ |
| hBN/$MoS_2$/hBN (Fig. 3.16) | $171 \pm 2$ | $195 \pm 5$ | $\approx 221$ |
| hBN/1LG/$MoS_2$/hBN (Fig. 3.16) | $136 \pm 2$ | — | $\approx 176$ |

Table 3.2: Estimated binding energies for hBN-capped $MoSe_2$, $MoSe_2$/1LG, $MoS_2$ and $MoS_2$/1LG.

## 3.4 Low temperature exciton dynamics in TMD/1LG

### 3.4.1 A three level system

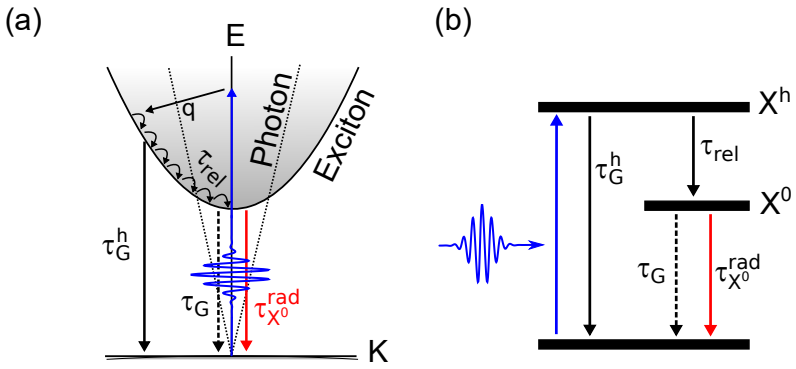


Figure 3.17: **Exciton dynamics.** (a) Scheme showing the processes that we are considering in our experiment. The blue arrow corresponds to the photogeneration of a hot excitonic population which rapidly relaxes towards the band edges outside the light cone through phonon emission (represented by the diagonal black arrow). The letter q accounts for the phonon momentum. This population undergoes relaxation through phonon emission (curved arrows) or energy transfer to graphene (solid black arrow). After relaxation towards the light cone, the excitonic population decays either radiatively (red arrow) or non-radiatively by transferring its energy to graphene (dashed black arrow). (b) Three level system to model the situation described in (a).

To study the excitonic dynamics, we performed time-resolved PL measurements (TRPL) at LCPNO Toulouse in collaboration with Cédric Robert, Delphine Lagarde, and Xavier Marie. The ps-timescales of these phenomena require a setup with higher temporal res-

olution than we can achieve in ours. To carry these measurements, they used a streak camera whose working principle is described in section 2.3.4. To facilitate the analysis, we will use a toy model consisting of a three-level system composed of a hot exciton level ($X^h$) corresponding to the exciton population outside of the light cone, a cold exciton level ($X^0$) corresponding to the excitons that can recombine radiatively and a ground state. This model is shown in figure 3.17. The arrows indicate the different processes that can take place in the sample with their characteristic timescales. For instance, the hot exciton population has two ways of decaying: either through $X^0$ formation or decaying non-radiatively towards graphene. The first process happens on a characteristic relaxation time $\tau_{rel}$ that depends on the environment. The second process is the already mentioned energy transfer to graphene, which a priori can affect excitons outside the light cone as well. We associated a typical time $\tau_G^h$ to this process. Similarly, the exciton population can decay either by transferring energy to graphene (on a timescale $\tau_G$) or radiatively ($\tau_{X^0}^{rad}$). With this in mind, we can write the rate equation for the populations n of the $X^0$ level:

$$\dot{n}_{X^0} = \left(\frac{1}{\tau_{rel}}\right) n_{X^h} - \left(\frac{1}{\tau_G^0} + \frac{1}{\tau_{X^0}^{\text{rad}}}\right) n_{X^0} \tag{3.3}$$

$$\begin{cases} \dot{n}_{X^h} = -\left(\frac{1}{\tau_{\text{rel}}}\right) n_{X^h} \\ \dot{n}_{X^0} = \left(\frac{1}{\tau_{\text{rel}}}\right) n_{X^h} - \left(\frac{1}{\tau_G^0} + \frac{1}{\tau_{X^0}^{\text{rad}}}\right) n_{X^0} \end{cases} . \tag{3.4}$$

The intensity of the PL is $I_{X^0} \propto n_{X^0}(t)$, therefore we can write:

$$I_{X^0}(t) \propto \frac{n_{X^h}(0)}{\tau_{rel} - \tau_{X^0}} \left(e^{-t/\tau_{\text{rel}}} - e^{-t/\tau_{X^0}}\right) \tag{3.5}$$

Where $\tau_{X^0} = ((\tau_G)^{-1} + (\tau_{X^0}^{\text{rad}})^{-1})^{-1}$. This curve can be fitted to the experimental data[3] in order to deduce $\tau_{X^0}$ and $\tau_{\text{rel}}$. One should be careful when assigning the rising and decay time acquired in the experimental results to physical quantities. For instance, if $\tau_{\text{rel}} > \tau_{X^0}^{\text{rad}}$, the rise time would correspond to the exciton lifetime and the decay to the relaxation time.

### 3.4.2 TRPL measurements on hBN-capped $MoSe_2$/1LG on quartz

Figure 3.18a shows PL spectra of a hBN $MoSe_2$/1LG sample deposited onto a transparent quartz substrate. The spectra are normalized so that the $X^0$ line corresponds to an intensity of 1 in both cases. The scaling factor is indicated in blue. TRPL measurements on this heterostructure are shown in figures 3.18b-d. To avoid the influence from higher-lying excitonic states, we use laser excitation with an energy of 1.73 eV which is below the

[3] A convolution with the instrument response function (IRF) is required beforehand.

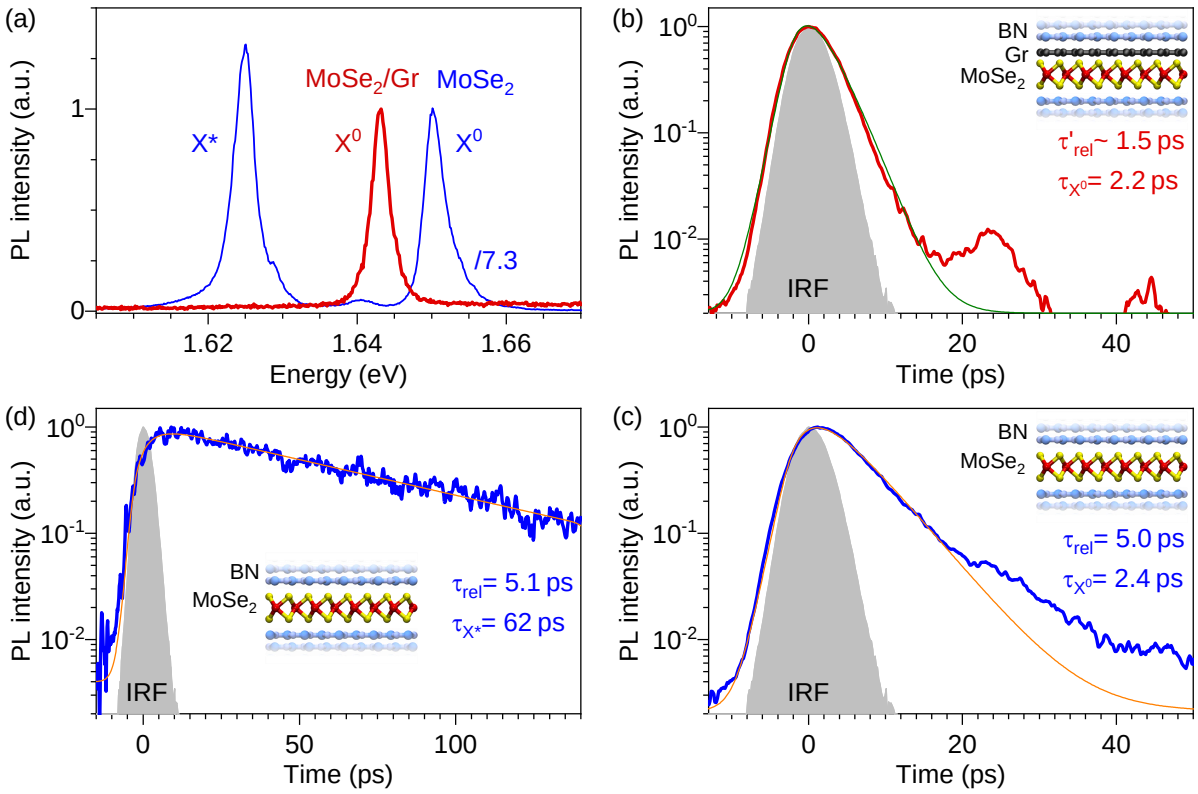


Figure 3.18: **TRPL spectra hBN-capped samples.** (a) PL spectra of hBN-capped $MoSe_2$/1LG (red) and hBN-capped $MoSe_2$ (blue). The spectra are normalized to the $X^0$ line and the scaling factor between the spectra is shown in the figure. TRPL of the neutral exciton $X^0$ for $MoSe_2$ and $MoSe_2$/1LG are shown in figures (b) and (c) respectively. (d) TRPL of the $X^*$. All spectra were recorded under pulsed excitation at 1.73 eV and at 7 K.

2s-state (figure 3.13). In $MoSe_2$/1LG, we observe a short rise time $\sim$ 1.5 ps and a decay time of 2.2 ps. We associate the former to a shortened relaxation time and the latter to $\tau_{X^0}$. In the $MoSe_2$ reference, we observe a PL rise time of 2.4 ps and a PL decay time of 5 ps for $X^0$. For $X^*$ we observe a much longer decay time of 62 ps and a rise time of 5.1 ps. Since $X^0$ and $X^*$ are known to form in the same timescale, we assign the 5.1 ps time to $\tau_{\text{rel}}$. All of these values are reported in table 3.3. Let us focus on two of these observations, namely:

- The mismatch between $\tau_{\text{rel}}$ in hBN-capped TMD and hBN-capped TMD/1LG

  We observe a shortening from 5 ps in the bare TMD down to $\leq$ 1.5 ps in TMD/1LG. This suggests that hot excitons ($X^h$) are being efficiently transferred from the TMD towards graphene reducing the effective relaxation time (see figure 3.17). Furthermore, this could explain the quenching factors $Q_{X^0}$ and $Q_{\text{tot}}$ we observe. Indeed, in bare $MoSe_2$, the $X^h$ population will form $X^0$, $X^*$ and localized excitons. However, in $MoSe_2$/1LG, no $X^*$ can be formed as a consequence of the neutralization effect. Consequently, we would expect a larger population of $X^0$ and localized emitters

to be formed. This hypothesis holds as long as hot exciton transfer to graphene can be neglected. If $\tau_{rel}$ is larger than the typical transfer time to graphene. Then part of the hot excitonic population will transfer its energy resulting in a quenching of exciton formation. This points towards a momentum-dependent energy transfer which is compatible with a FRET scenario [172].

- The similar excitonic lifetimes in both areas.

  We observe that $\tau_{X^0}$ does not change in presence of graphene. Intuitively, one could think that radiative recombination completely dominates the dynamics ($\tau_G \gg \tau_{X^0}^{rad}$.) and therefore $\tau_G$ can be neglected. However, this observation could also be a consequence of the dielectric screening provided by graphene. Indeed, in presence of graphene, the exciton binding energy is expected to decrease. This leads to an increase of the exciton radiative recombination lifetime $\tau_{X^0}^{rad}$ since (see section 1.5):

$$\tau_{X^0}^{rad} \propto \frac{1}{E_b^2}$$

  Therefore, we might be in a situation in which $\tau_G$ is in the same order of magnitude as $\tau_{X^0}^{rad}$. Then, the similar measured lifetimes result from a compensation between dielectric screening and energy transfer to graphene. Furthermore, we can not rule out the possibility of a slight contribution from non-radiative decay in the bare TMD. It is particularly challenging to find a good TMD "reference" that is close to pristine conditions. As a consequence, we are unable to tell which of these situations is the correct one. The problem lies in the already short radiative recombination time we observe in the bare TMD.

### 3.4.3 TRPL measurements on hBN-capped $MoSe_2$/1LG on $SiO_2$

A way to circumvent the aforementioned issue is to engineer our samples such that $\tau_{X^0}^{\mathrm{rad}}$ is as long as possible. This can be done by appropriately choosing the bottom hBN-thickness in $SiO_2$-supported samples. Indeed, as discussed in section 1.5.3, the radiative decay rate can be tuned through a Purcell-like effect by means of an optical cavity defined by the hBN/$SiO_2$/Si geometry. Then, by choosing the bottom hBN thickness, we can control the EM modes in the cavity [25]. The sample we have discussed so far is deposited onto a quartz substrate and therefore practically unaffected by the cavity effect. Figure 3.19a shows an optical image of an hBN-Capped $MoSe_2$/1LG sample deposited onto a $SiO_2$/Si substrate. The sample was made with a $\sim$ 110 nm-thick bottom hBN in order to maximize the excitonic radiative lifetime as shown in reference [25].

Figure 3.19b shows three PL spectra representative of each area of the heterostructure. In hBN-capped $MoSe_2$ we observe two features located at $1.642 \pm 0.001$ eV and $1.615 \pm$

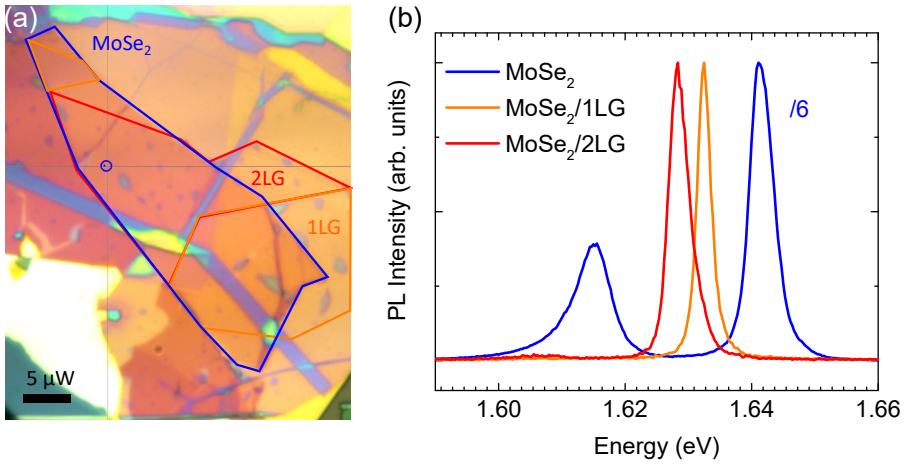


Figure 3.19: **Low-temperature PL of $SiO_2$ supported hBN-capped $MoSe_2$/1LG**(a) Optical microscopy image of a hBN-capped $MoSe_2$, $MoSe_2$/1LG and $MoSe_2$/2LG.(b) PL spectra corresponding to the main three areas of the heterostructure. The spectra were recorded at 14 K, using cw-laser excitation at 1.96 eV and under a laser intensity close to $100\mu W/\mu m^2$.

0.003 eV corresponding to $X^0$ and $X^*$ respectively. We confirm the coupling between the TMD and the graphene layers since we recover the expected filtering effect in both hBN-capped $MoSe_2$/1LG and hBN-capped $MoSe_2$/2LG areas. The $X^0$ resonance is located at $1.633 \pm 0.1$ eV for the former and $1.628 \pm 0.1$ eV for the latter.

TRPL spectra of the neutral exciton emission in each area are shown in figure 3.20. All spectra were recorded at 14 K and with a laser energy of 1.72 eV which is below the $X^0_{2s}$ state. As mentioned before, this is done to avoid modification in the dynamics related to highly lying excitonic states. In the reference, shown in figure 3.20a, we observe a rise time of $11 \pm 8$ ps and a similar decay time. We assign these values to $\tau_{\text{rel}}$, and $\tau_{X^0}$. The large uncertainty we observe is due to the similar $\tau_{\text{rel}}$ and $\tau_{X^0}$. Indeed, if we look at equation (3.5), we can notice that when $\tau_{\text{rel}} \to \tau_{X^0}$, the function approaches $\frac{0}{0}$. Therefore, the fitting becomes challenging and there are multiple combinations of parameters that may work as well. We find that the best fit occurs when both times are equal to 11 ps. Notice that this value of $\tau_{X^0}$ is 5 times larger than the one observed in the previous sample. This is a direct confirmation that the excitons are at a node of the EM field of the cavity. In contrast, for both $MoSe_2$/1LG and $MoSe_2$/2LG, we observe much smaller rise and decay times. Since the effect of the cavity is to modify radiative recombination, we do not expect a change in the formation dynamics. In other words, we associate the rise time to the modified relaxation time in graphene, and the decay time corresponds to $\tau'_{X^0}$. All these values are reported in table 3.3. Quantitatively, we measured $\tau'_{rel} < 1$ ps, which is below the resolution we can achieve, and $\tau'_{X^0} = 2.3 \pm 0.2$ ps in $MoSe_2$/1LG. Remarkably, we measured a slightly shorter lifetime $\tau'_{X^0} = 1.75 \pm 0.1$ ps in $MoSe_2$/2LG. As a reference, PL spectra taken in the same spots as the TRPL measurements are shown in figure 3.20d. All

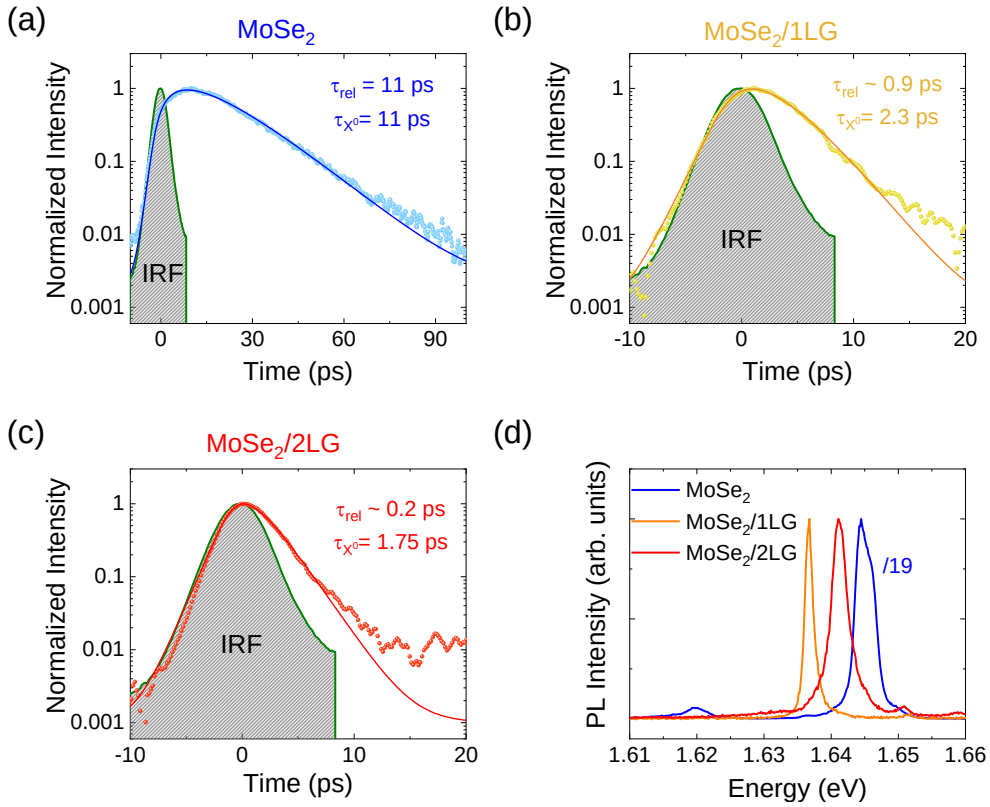


Figure 3.20: **Low temperature dynamics.** TRPL of the neutral exciton emission in $MoSe_2$ (a) $MoSe_2$/1LG (b) and $MoSe_2$/2LG (c). (d) PL spectra of $X^0$ in $MoSe_2$, $MoSe_2$/1LG and $MoSe_2$/2LG. All spectra were recorded at 14K and with a pulsed laser at 722 nm in the linear regime.

spectra are normalized to the $X^0$-line intensity and the scaling factor between the spectra is shown in blue. We note the same scaling factor for both $MoSe_2$/1LG and MoSe2/2LG. Let us first focus on the reduction of the relaxation time. From our three level system model, we can estimate a bound for hot exciton transfer time of $\tau_G^h < 1$ ps. However, this value must be taken with care as we are too close to the resolution of our setup and therefore the measured rise time is questionable. What is clear from this measurement is that $X^h$ transfer is a highly efficient mechanism that entirely dominates hot-exciton dynamics. We are going to come back to this point in section 3.4.6.

Now, let us focus on the excitonic lifetimes. The reduction from $11 \pm 8$ ps in the bare TMD down to $\sim 2$ ps in the heterostructure, indicates that the dynamics is dominated by the energy transfer from the TMD to graphene. This is consistent with the higher exciton quenching factor observed in the PL with respect to the sample studied in figure 3.18. Indeed, we measure $Q_{X^0}^{\mathrm{1LG}} = 19 \pm 7$ and $Q_{X^0}^{\mathrm{2LG}} = 15 \pm 4$ for $MoSe_2$/1LG and $MoSe_2$/2LG respectively. Similarly, we measured $Q_{\mathrm{tot}}^{\mathrm{1LG}} = 37 \pm 12$ and $Q_{\mathrm{tot}}^{\mathrm{2LG}} = 28 \pm 9$.

**Limits of interpretation**

The assignment of the rise and decay time in the case of $MoSe_2$/1LG and $MoSe_2$/2LG could be questioned. Indeed, in the bare TMD, there are no such problems since one can always compare with the rise time of $X^*$ and from there identify $\tau_{X^0}$. In the heterostructures no $X^*$ are formed and therefore this comparison can not be made. This means that a priori we could be in a situation where the rise time in figure 3.20 corresponds to $\tau_{X^0}$ and the decay time to $\tau_{rel}$. Furthermore, we are not able to resolve the rise time fully as we are limited by the resolution of our setup. This calls for further measurements focusing on the fs domain in order to get insights on this timescale.

### 3.4.4 Estimating the transfer time to graphene

So far, we have measured the excitonic lifetimes in the three areas of the sample (see table 3.3) and we have estimated the modification of the binding energy due to the presence of graphene. To estimate the transfer time to graphene, we need to estimate $\tau_{X^0}^{\text{rad}}$. To do so, we are going to exploit the relation between the radiative recombination lifetime and the binding energy which allow us to write:

$$\frac{\tau_{X^0}^{rad}}{\tau_0^{rad}} \propto \left(\frac{E_b}{E_b'}\right)^2 \tag{3.6}$$

Where $\tau_0^{rad}$ corresponds to the exciton radiative recombination time in the bare TMD reference, $\tau_{X^0}^{rad}$ is the exciton radiative recombination time in TMD/1LG and $E_b$ and $E_b'$ are the respective binding energies. The change in notation is done to avoid confusion. There might be a contribution from the photonic density of states provided by the graphene layer. This could induce also an increase in $\tau_{X^0}^{\text{rad}}$. However, as shown in reference [25], the inclusion of an atomically thin layer in multi-layered heterostructures has a negligible effect on the local field enhancement. In other words, we can suppose that the change in the radiative lifetime arises exclusively from the screening of Coulomb interactions. Finally, we can plug the values obtained in the previous section into the relation (3.6) and deduce the modified radiative recombination time due to graphene

$$\tau_{X^0}^{\text{rad}} \approx 26 \text{ ps}$$

and since

$$\frac{1}{\tau_{X^0}'} = \frac{1}{\tau_{X^0}^{rad}} + \frac{1}{\tau_G} \tag{3.7}$$

We can give a conservative estimation on the energy transfer time to graphene and bilayer graphene equal to $\tau_{1LG} \approx 2.5$ ps and $\tau_{2LG} \approx 1.9$ ps respectively. This result suggests that the transfer towards the 2LG is more efficient than towards the 1LG. We

repeated the same calculation for the sample in section 3.4.2 and obtained similar values, albeit a bit larger (see table 3.3).

| | Substrate | $\tau_{X^0}$ (ps) | $\tau_{\text{rel}}$ (ps) | $\tau_{X^0}^{\text{rad}}$ (ps) | $\tau_{\text{G}}$ (ps) |
|---|---|---|---|---|---|
| hBN/$MoSe_2$/hBN | Quartz | 2.4 | 5.1 | 2.4 | – |
| hBN/$MoSe_2$/1LG/hBN | | 2.2 | $\leq 1.5$ | 5.7 | 3.6 |
| hBN/$MoSe_2$ | hBN$^\star$ | 11 | 11 | 11 | – |
| hBN/$MoSe_2$/1LG | | 2.3 | $< 1$ | 26 | 2.5 |
| hBN/$MoSe_2$/2LG | | 1.75 | $< 1$ | 26 | 1.9 |

Table 3.3: TRPL parameters extracted from figures 3.18 and 3.20 and estimated transfer times.

### 3.4.5 Exciton emission yield

Now that we have estimated the transfer time to graphene, we can estimate the expected yield and compare it to the $Q_{X^0}$ value we observe. We first define the total emission yield as:

$$\eta_{tot} = \frac{N_{\text{em}}}{N_{\text{abs}}} \tag{3.8}$$

Where $N_{\text{em}}$ and $N_{\text{abs}}$ are the number of emitted and absorbed photons respectively. We can then rewrite this expression as follows:

$$\eta_{\text{tot}} = \eta_{X^0} \frac{N_{X^0}}{N_{\text{abs}}}$$

with $N_{X^0}$ the number of cold excitons $X^0$ and $\eta_{X^0} = N_{\text{em}}/N_{X^0}$ the exciton emission yield. Experimentally, due to the limited collection efficiency in our cryogenic setup and the uncertainty in the sample absorptance, it is challenging to measure $\eta_{tot}$ at low temperatures. However, we could estimate the exciton yield $\eta_{X^0}$:

$$\eta_{X^0} = \frac{\frac{1}{\tau_{X^0}^{\text{rad}}}}{\frac{1}{\tau_{X^0}^{\text{rad}}} + \frac{1}{\tau_{\text{G}}}} \tag{3.9}$$

In section 1.5.2, we saw that at low temperatures, exciton decay in TMDs is purely radiative. Therefore $\eta_{X^0}^{TMD} \sim 100\%$ in bare $MoSe_2$. Now, using the values reported in table 3.3, we can estimate the yield for the samples in quartz and in $SiO_2$. Table 3.4 contains all of the estimated $\eta_{X^0}$ as well as the measured quenching factors.

We observe yields ranging from 6 % in the $SiO_2$ supported sample up to 50 % in the quartz-supported sample. This contrast in values does not come as a surprise since

| | Substrate | $\eta_{X^0}$ | $Q_{X^0}$ | $Q_{\text{tot}}$ |
|---|---|---|---|---|
| hBN/$MoSe_2$/1LG/hBN | Quartz | 50 % | 7.1 | 20 |
| hBN/$MoSe_2$/1LG | hBN$^\star$ | 8 % | 19 | 37 |
| $MoSe_2$/2LG | hBN$^\star$ | 6 % | 15 | 28 |

Table 3.4: Estimated yields for hBN-capped $MoSe_2$/1LG deposited on quartz and on hBN. The $\star$ symbol indicates that the substrate is composed of a bottom 110nm-thick hBN flake, deposited onto an $SiO_2$/Si substrate.

the former was designed to be maximally affected by the energy transfer to graphene and therefore display low emission yields. Interestingly, in both cases, there is a discrepancy between $\eta_{X^0}$ and $Q_{X^0}$. We observe quenching factors compatible with much lower yields. We conclude that a significant part of the observed quenching arises from the energy transfer from the hot exciton population towards graphene, which affects exciton formation.

### 3.4.6 Investigations on hot exciton transfer

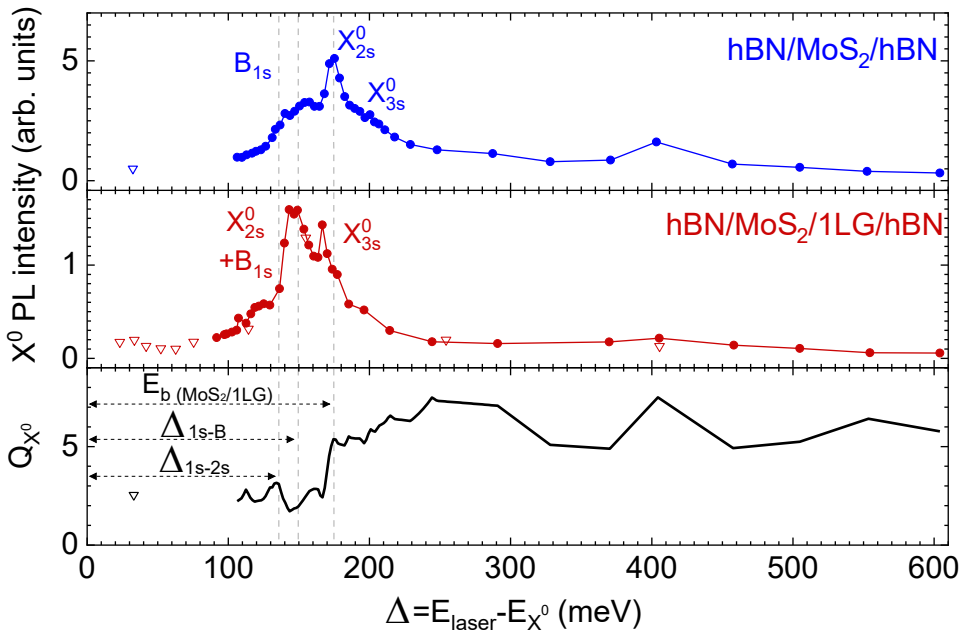


Figure 3.21: **PLE measurements on hBN-capped $MoS_2$/1LG.** Integrated PL intensity of the $X^0$ line as a function of the detuning $\Delta$ between the laser energy and the $X^0$ line in hBN-capped $MoS_2$ (top) and hBN-capped $MoS_2$/1LG (middle). The bottom panel shows $Q_{X^0}$ as a function of the detuning. All data was recorded at 15 K.

Let us finish this section by discussing the hot exciton transfer that we have observed in our measurements. Previously, we have seen that $Q_{X^0}$ contains a contribution not only

from the energy transfer of $X^0$ to graphene but also from $X^h$ through quenching of exciton formation. We can get more insights into this process using photoluminescence excitation spectroscopy (PLE). By exciting at different detunings ($\Delta$), we can expect to create a larger $X^h$ population. As a result, if there is any transfer from $X^h$ towards graphene, we should observe a change in $Q_{X^0}$. We decided to focus on the hBN-capped $MoS_2$/1LG sample used in section 3.3. The advantage of this sample is the almost negligible contribution to the PL of the $X^*$ feature. This allows us to focus only on the $X^0$ dynamics. Our PLE measurements on this sample are shown in figure 3.21. We are able to explore a wide range of values, starting at $\Delta \sim 30$ meV (below $X^0_{2s}$) up to $\Delta \sim 600$ meV (above the free carrier continuum). In the top and middle panel, we can identify resonances in the PLE spectra arising from $X^0_{2s}$, $X^0_{3s}$ and $B_{1s}$.

Let us now focus on the bottom panel of figure 3.16. We observe that $Q_{X^0} \sim 3 \pm 1$ from 33 meV up to 100 meV. This is consistent with the results presented in [25] where no change in the dynamics is observed for $\Delta < \Delta_{1s-2s}$. However, once we reach $\Delta \approx 175$ meV, we observe an increase in $Q_{X^0}$ to around $\sim$ 5-7. This increase occurs at an excitation energy that matches the onset of the $X^0_{2s}$ state in the reference, as well as the excitonic binding energy in $MoSe_2$/1LG. At higher detunings, $Q_{X^0}$ does not vary substantially even at $\Delta \sim 600$ meV. This suggests that higher-lying excitons such as the B-exciton and others transfer more efficiently to graphene than $X^0_{1s}$.

## 3.5 Valley contrast in TMD/1LG

Let us finish our discussion by looking at the valley properties of TMD/1LG heterostructures. These samples have been shown to be chiral emitters with robust degrees of valley polarization ($\rho$) and coherence ($\gamma$) up to room temperature. This is due to the coupling with graphene which allows excitons to recombine before undergoing intervalley scattering and dephasing [173, 174]. Furthermore, we have seen that graphene acts as a capping layer reducing disorder and spatial inhomogeneities. This contributes further to the preservation of the valley coherence which explains recent results in which $\gamma$ as large as 20% has been observed in $WS_2$/1LG at room temperature [173]. In our case, we studied the valley properties of the sample shown in figure 3.1. Figure 3.22 shows polarization-resolved PL spectra recorded using a circular and a linear polarization as described in section 2.3 and with an excitation 60 meV above the $X^0$ resonance. For the $X^0$ emission line, we measured $\rho = 0\%$, $4 \pm 4$ % and $13 \pm 3$ % and $\gamma = 0\%$, $10 \pm 4$ % and $15 \pm 4$ % for hBN-supported MoSe2, MoSe2/1LG and MoSe2/2LG, respectively. These values are reported in table 3.5

The negligible contrast in the reference does not come as a surprise. Similar result have been reported for $MoSe_2$ monolayers [175]. This is an indication that intervalley scattering occurs in a much faster timescale than the $\sim$ 2 ps excitonic lifetime in $MoSe_2$. Moreover, in our case, the bottom hBN has a thickness close to $\sim$ 110 nm which means

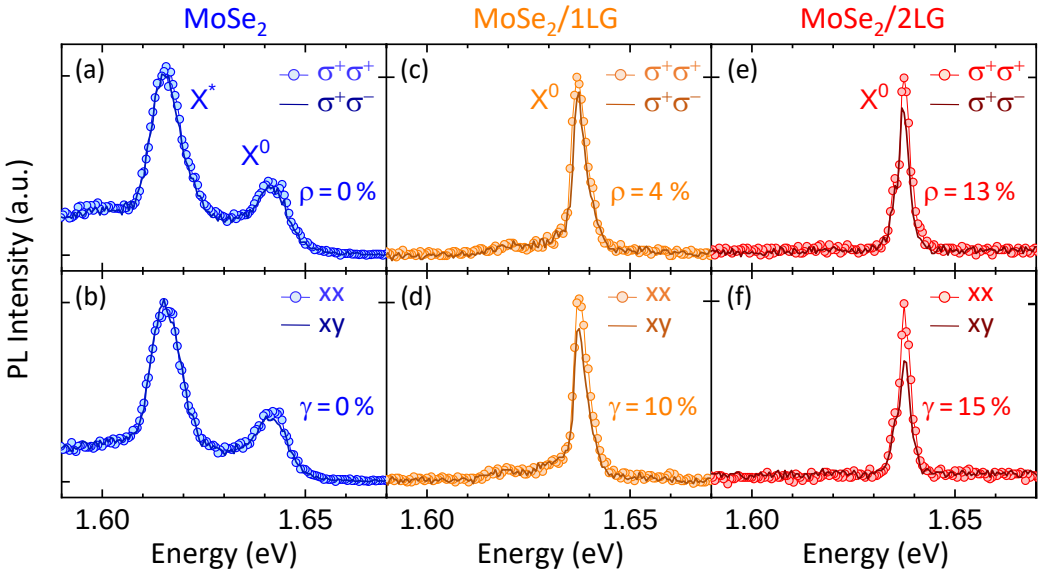


Figure 3.22: **Low temperature valley contrast properties of TMD/1LG.** Low temperature (9 K) polarization-resolved PL spectra of hBN-capped $MoSe_2$ (a,b), $MoSe_2$/1LG (c,d) and $MoSe_2$/2LG (e,f) done in the sample shown in figure 3.1. All measurements were done at 9 K and under cw-laser excitation 60 meV above the $X^0$ line. The laser intensity corresponds to 50 $\mu W/\mu m^2$ and we have verified that these measurements are done in the linear regime. The corresponding degrees of polarization ($\rho$) and coherence ($\gamma$) are indicated in each panel. We have normalized all spectra for clarity and the corresponding quenching factors are $Q_X^0 = 1.8 \pm 0.1$ and $Q_X^0 = 2.0 \pm 0.1$ for MoSe2/1LG and $MoSe_2$/2LG respectively.

| System | $\rho$ | $\gamma$ |
|---|---|---|
| $MoSe_2$/hBN | 0% | 0% |
| 1LG/$MoSe_2$/hBN | $4 \pm 4$ % | $10 \pm 4$ % |
| 2LG/$MoS_2$/hBN | $13 \pm 3$ % | $15 \pm 4$ % |

Table 3.5: Degrees of polarization ($\rho$) and coherence ($\gamma$) extracted from figure 3.22.

$\tau_{X^0}^{rad}$ should be close to 10 ps. As a result, we expect negligible degrees of polarization and coherence in the bare TMD and slightly larger values in $MoSe_2$/1LG [9, 25]. Furthermore, we observe the effect of graphene encapsulation in the higher degree of coherence with respect to the polarization.

## 3.6 Conclusion

In this chapter, we investigated the interaction between a monolayer TMD and graphene. Our investigations started with a ubiquitous observation: the massive PL quenching of TMDs by graphene at room temperature. This indicates a reduction of the excitonic lifetime in TMD/1LG from a few ns down to ps-timescales. To understand this, we presented

several mechanisms that can arise at the interface between the layers and discussed their effect on the heterostructure. We can summarize as follows:

- Electron redistribution occurs upon contacting the layers. This results in the neutralization of the TMD by graphene which acts as a reservoir for charges. This process depends on the relative band offsets and the Fermi level alignment between the layers.
- We divided the remaining mechanisms into two categories: charge and energy transfer where the main parameter to differentiate between the two was the presence of a **net** charge flux between the layers.
- We have seen that photodoping in TMD/1LG has an extrinsic origin and one can suppress it by studying samples in a vacuum and using hBN as a substrate. Furthermore, this process is extremely slow compared with the excitonic lifetime. Therefore, charge transfer alone can not explain the observed quenching of the luminescence.
- Finally we discussed energy transfer processes as the most likely mechanisms to explain interlayer coupling in TMD/1LG. This can happen in three ways: Through FRET, DET, or possibly by means of a short-lived ($\sim$ 1 ps) charge-separated state.

However, since all energy transfer processes happen in the same timescales, this calls for an in-depth study of the excitonic dynamics. To this end, We decided to investigate TMD/1LG heterostructures at low temperatures using a combined approach of PL, TRPL, DR, and Raman spectroscopies. In these conditions, we showed that the coupling with graphene results in two major effects:

- Graphene completely neutralizes the TMD monolayer through static charge transfer resulting in the absence of charged species in the PL spectra.
- The energy transfer process efficiently quenches the luminescence of long-lived excitonic species such as dark excitons, biexcitons, localized excitons, etc.

As a result, the low temperature PL spectra are composed of a single and narrow emission line arising from the recombination of a screened $X^0$. Furthermore, we showed that this single- and narrow-line character remains even in absence of a top hBN-layer showcasing the encapsulating properties of graphene. Our results suggest that one can improve these values further by increasing the number of graphene capping layers. This is promising, especially for optoelectronic devices since the absence of a top hBN layer allows one to directly contact the graphene electrode for photodetectors, as well as for studies involving scanning tunneling microscopy, as we will see in the next chapter.

We then investigated more in detail the low temperature dynamics of our samples. In particular, we observed that the quenching of the $X^0$ luminescence in TMD/1LG

originates from the energy transfer from both cold- and hot-excitons to graphene. The mechanisms behind the hot-exciton transfer remain to be determined. This is interesting as it gives us clues into the coupling mechanism. We can summarize some of our observations as follows:

- The coupling mechanism is efficient for hot-excitons with finite momentum outside of the light cone.
- The mechanism affects excitonic species with out-of-plane dipoles (dark excitons).
- The coupling mechanism weakly depends on the number of graphene layers.

The first point is consistent with a FRET scenario since this mechanism becomes more efficient for large momentum excitons [172, 176]. However, the absence of dark excitons would be better explained by a DET process since FRET is inefficient for an out-of-plane dipole coupled to an in-plane dipole (in graphene). Finally, the third point is more of a preliminary observation. Indeed, we have observed this effect in monolayer and bilayer of graphene which could be compatible with both FRET and DET. However, concluding on their relative efficiencies remains an open question.

Two experiments could be helpful to settle this discussion. The first one consists in studying the distance-dependent behavior of the energy transfer. As mentioned in section 3.2.3, FRET and DET are expected to display different distance-dependent properties. In particular, DET is negligible for distances larger than 1 nm. One could think of using hBN as a spacer to separate the layers. However, the fabrication process of such a sample is quite challenging since the thin hBN-layers display low optical contrast. The second possibility consists of investigating the energy transfer with an increasing number of graphene layers. Using a similar reasoning, charge tunneling should become more efficient by increasing the number of layers. However, it should quickly saturate when no tunneling into deeper layers is possible. FRET on the other hand should continue to increase with increasing number of layers. We have shown that TMD/1LG offers an ideal playground to investigate and tailor the near-field coupling between layers in a vdW heterostructure with the sub-nm control given by the van-der-Waals gap that separates the layers. Generally speaking, we would like to understand the physical processes that give rise to the PL quenching at low temperatures. The main limitation is the absence of good TMD references. As a result, we cannot rule out the effect of other non-radiative processes linked to microscopic inhomogeneities. These processes can play an important role in the exciton formation process which can not be probed effectively using optical spectroscopies. This motivates the use of techniques that allow us to investigate the optical properties of vdW heterostructures beyond the diffraction limit.

Chapter 4

# STM-induced luminescence of atomically thin semiconductors

## 4.1 Motivation

In the previous chapter, we have seen that one can tailor the luminescence of TMDs by exploiting their interaction with a nearby graphene layer. As a result, the emission from these heterostructures is exclusively dominated by the neutral exciton. This filtering effect sensitively depends on the sub-nm van der Waals gap that separates the layers providing us with *out-of-plane* atomic control of the luminescence. However, the diffraction-limited nature of the excitation limits investigations with *in-plane* resolution. For instance, we can not investigate the impact of the local inhomogeneities such as defects or adsorbates on the excitonic luminescence at the nanoscale. Besides, some of these inhomogeneities are candidates for single-photon sources in TMDs. One could also wonder about the impact on the exciton dynamics of emerging moiré patterns in heterostructures. Going further, it could be interesting to engineer the substrate or even use nanoscopic adsorbates such as metallic clusters to enhance the luminescence of a material. To overcome the limitations related to diffraction-limited techniques, we can use an STM as both a probe and a means of excitation. Indeed, STM-induced luminescence (STML) allows probing optical properties with the resolution provided by the STM. While a few seminal works have reported STML data on monolayers TMDs (see section 4.2), the excitonic properties of TMD and VdW heterostructures remain to be explored in experiments combining high spectral (sub meV) and spatial (sub-atomic) resolutions. Below we list some of the questions related to the atomic-scale excitonic properties of TMDs that one would like to address:

- How does STM-induced luminescence depends on the electronic band structure of different TMDs? How will different excitonic species be excited in these conditions and how would their emission properties vary spatially at the nanoscale?

- How does the local electronic bandgap measured by STM compare with the local optical bandgap measured by STML? What does this tell us about the excitonic binding energy?

- How would local STML measurements compare with diffraction-limited PL measurements?
- What is the impact of the TMD/2DM interface (2DM = Gr, hBN, TMD) on the local emission properties of the different excitonic species (exciton, trions...)? Can this interface be addressed with atomic-scale precision measuring simultaneously STM and STML?
- Can we probe interlayer excitons and how would that be affected by atomic-scale inhomogeneities such as moiré patterns?
- What is the atomic-scale nature of SPS associated with defects?

In this chapter, I will present our results regarding the first observation of intrinsic luminescence of vdW heterostructures within an LT-UHV STM junction. The chapter is divided into 4 main sections. In the first section, I will introduce the current state of the art in STML on TMDs. In the second section, I will describe the sample we chose for our investigations. The third section focuses on the STML properties of our sample. Finally, in the last section, I will summarize our observations and conclude.

## 4.2 STML on TMDs

In this section, I will present the state of the art regarding the STML of monolayer TMDs. This is a relatively new field that started around 2016. Apart from the work discussed in section 4.2.1, none of these works were published when I started my Ph.D.

### 4.2.1 LT-STM of $MoS_2$/Au(111): Influence of nanopits

The first attempt to obtain intrinsic STML of monolayer TMDs was made by Krane *et al* in 2016 [16]. Their sample consisted of a monolayer of $MoS_2$ that was evaporated in-situ onto an Au(111) substrate. They studied this system at 4K and under UHV conditions. To decouple the TMD monolayer, they relied on nanopits corresponding to the removal of one layer of gold atoms that were present in the Au surface (figure 4.1a). In these pits, the TMD monolayer is no longer in contact with the surface. In this configuration, one can hope that the TMD is sufficiently decoupled so that intrinsic STML can be obtained. Atomically resolved STM and AFM images of the suspended layer can be seen in figures 4.1b and c. Figure 4.1d shows three STML spectra taken on bare Au (dashed green line), $MoS_2$/Au (solid blue line), and suspended $MoS_2$ (solid black line). The spectrally broad nature ($\sim$ 100 meV) of the spectra suggests an extrinsic (i.e. plasmonic) origin of the emission. This is also the conclusion of the authors, who associate the emission with the inelastic tunneling of electrons from the band edge of the TMD towards the unoccupied

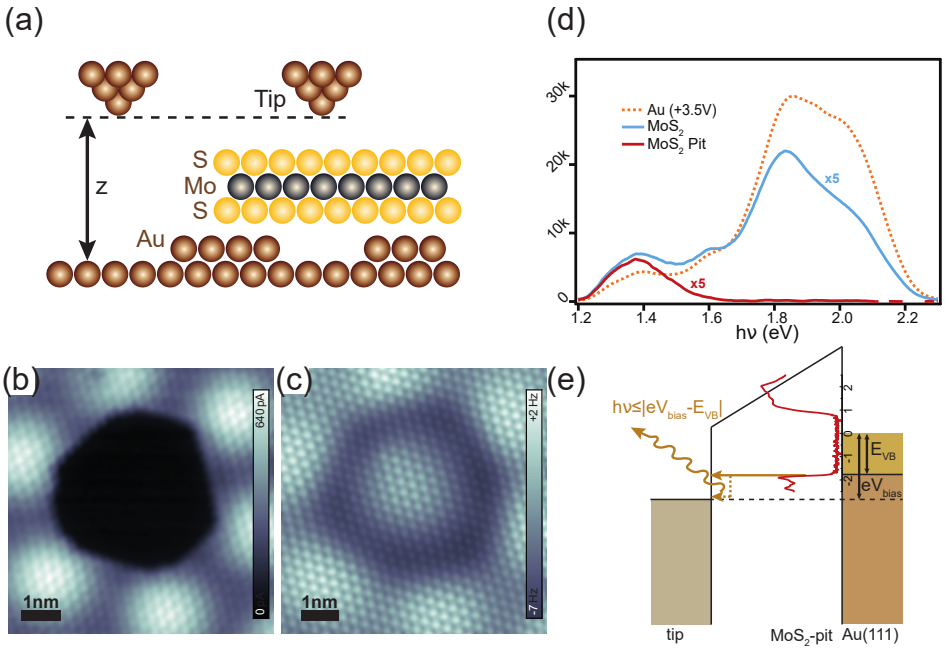


Figure 4.1: **Suspended $MoS_2$**(a) Scheme of the configuration. The figure shows a monolayer of $MoS_2$ suspended on top of an Au(111) nanopit. Atomically resolved STM and AFM images on the nanopit are shown in figures (b) and (C). (d) STML spectra obtained in three different locations. The dashed green line corresponds to the plasmonic response of the bare Au(111) surface. The blue curve corresponds to the luminescence arising from the supported monolayer. The red curve corresponds to the STML spectra obtained on top of the nanopit. The spectra on the monolayer were acquired at a bias voltage of -3.5 V. (e) Energy diagram of the emission mechanism. At negative bias, electrons tunnel inelastically from the VBM towards the tip. This results in broad emission with an energy $E \leq |eV_{bias} - E_{VBM}|$. Figures adapted from [16].

states of the tip. This process is shown in figure 4.1e. The absence of intrinsic features (i.e., sharp spectral lines associated with the excitonic TMD emission) suggests that the monolayer is not decoupled enough from the substrate.

### 4.2.2 RT-STM on $MoSe_2$: Non-plasmonic substrates.

Three years later, Pommier *et al.* made a significant breakthrough by demonstrating STML of monolayer $MoSe_2$ at room temperature [13]. These results were part of a collaboration between the group of Eric Le Moal at ISMO (Orsay) and our group in which I was directly involved. The idea was to avoid plasmon-related phenomena altogether by transferring the layer onto an indium-tin-oxide (ITO) coated glass and by using non-plasmonic W-tips. Indeed, ITO is a transparent conductive oxide widely used as an electrode for optoelectronic applications [177]. The monolayers were exfoliated on PDMS and then transferred on top of the ITO-coated glass. Moreover, in their setup, they can collect light with the help of a high NA (1.49) immersion objective (as in figure 4.2a).

Figure 4.2b shows an optical image of the monolayer. In the image, we can identify

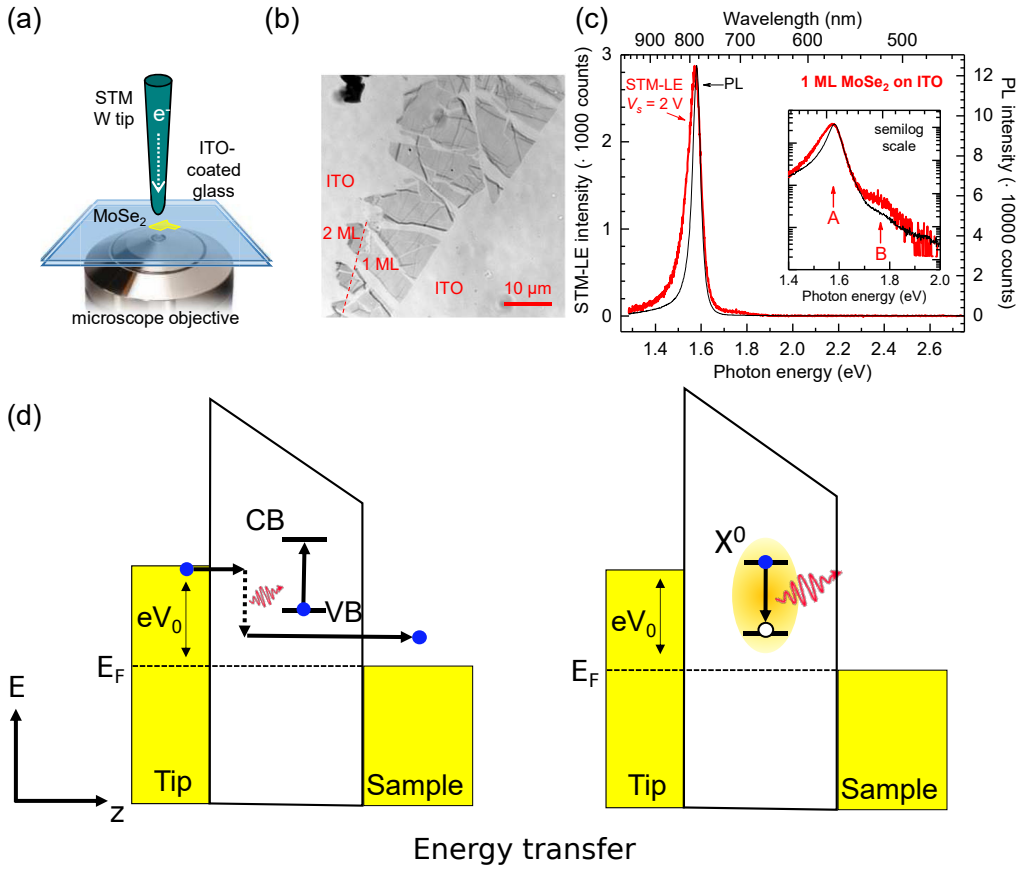


Figure 4.2: (a) Scheme of the experimental setup. The monolayer of $MoSe_2$ is deposited onto a transparent ITO-coated glass slide. (b) Optical microscopy image of the monolayer. (c)PL and STML spectra acquired on the 1L $MoSe_2$/ITO. The PL measurements were done with a laser of wavelength 465.8nm. The STML spectrum was acquired under a bias of 2V and a current setpoint of 10 nA. The inset shows the same spectrum on logarithmic scale. We can identify a small contribution arising from the B-exciton recombination. (d) Scheme of the energy transfer mechanism. Electrons tunnel inelastically from one electrode towards the other (left). During the tunneling process, the energy loss by the electrons can induce the creation of excitons that then recombine radiatively (right). Figures a-c were extracted from [13].

several cracks and folds on the layer. These are a direct consequence of the fabrication process. Figure 4.2c shows an STML and a PL spectrum measured on the monolayer. The striking resemblance between the two indicates an intrinsic origin of the luminescence. More surprisingly, hot-luminescence arising from the B-exciton can be observed as well (inset in figure 4.2c). A detailed investigation of the luminescence is interpreted in the way that the formation of excitons stems from energy transfer from the tunneling electrons. A signature of such mechanism is the voltage onset of the emission that matches the optical bandgap of $MoSe_2$. From this observation, we can draw a picture of the exciton formation process. The tunneling electrons can be modeled as an oscillating dipole aligned along the tip-sample axis. As a result, there is a non-negligible probability that they can couple through dipole-dipole interaction with excitons in the TMD. A scheme of this process is

shown in figure 4.2d. However, there were some limitations related to the measurement itself. First, the experimental conditions (room temperature and air) yielded a limited spatial resolution on the order of 10 to 20 nm. Second, the parameters used to acquire the spectra resulted in the partial destruction of the underlying layer. These limitations must be overcome to address TMDs with atomic resolution.

### 4.2.3 RT STM on TMD/Au: decoupling with $H_2O$

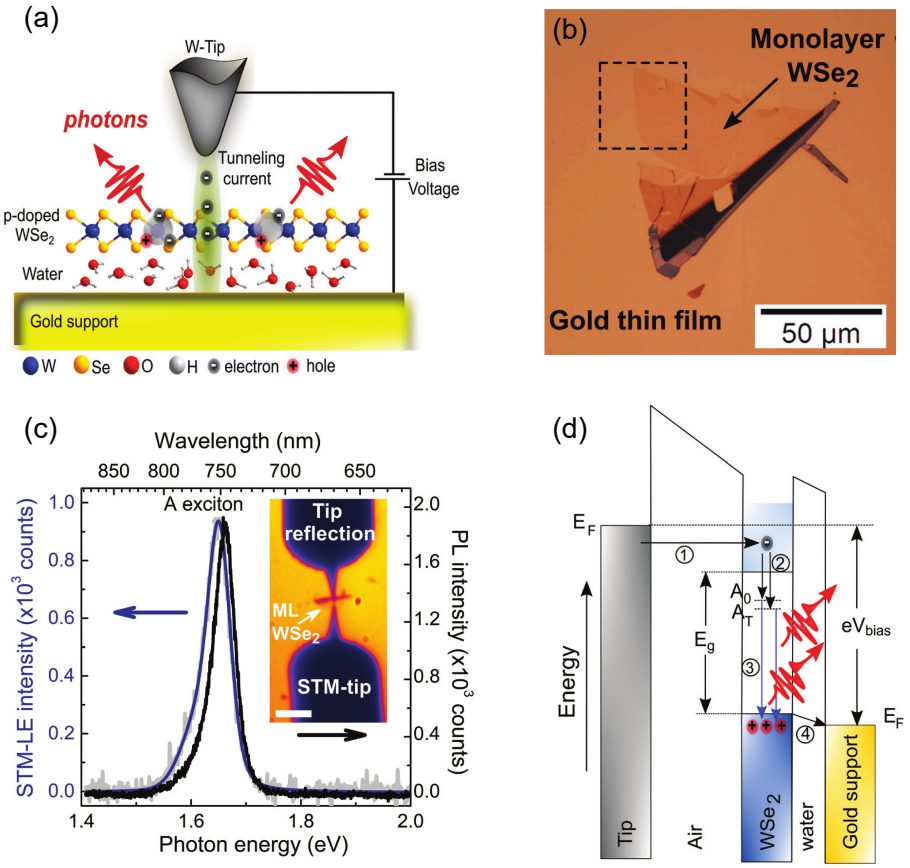


Figure 4.3: **Decoupling with water.**(a)Scheme of the configuration. A monolayer of $WSe_2$ is deposited on top of a gold substrate. The transfer process results in a water layer that is present at the interface. (b)Optical microscopy image of the monolayer. (c) STML (blue) and PL (black) spectra acquired on the monolayer. The inset contains an optical image of the experimental configuration. It shows the monolayer, the tip, and the reflection of the tip in the substrate. The acquisition parameters for the STML were 4 V and 25 nA. The PL spectra were recorded under CW excitation at 532 nm. The tip was retracted during these measurements. (d) Energy diagram of the emission mechanism. The luminescence is attributed to the injection of electrons from the tip into the conduction band. Afterward, exciton formation occurred when the injected carriers bind with native dopants in the TMD. Figures adapted from [14].

The following year, R. Peña *et al.*[14] at the University of Campinas in Brazil, demon-

strated STML of exfoliated monolayer $WSe_2$ deposited onto an Au surface. Although similar to the configuration of Krane, the ex-situ nature of the fabrication process leads to contaminant layers between the TMD and the metal. Among these contaminants, the most common one is water [178]. One can exploit this to decouple the TMD from the gold. A scheme of the configuration and an optical image are shown in figures 4.3a and b, respectively. Under positive bias, the authors observed STML closely resembling the PL of the monolayer. A comparison between the acquired STML and PL spectra is shown in figure 4.3c. The slight redshift of the STML with respect to the PL is attributed to nanoscale inhomogeneities in the substrate. Moreover, they observed that:

- The emission was unipolar. No luminescence at negative bias is observed.
- The onset of the luminescence occurs at voltages larger than the measured electronic bandgap.
- The TMD is p-doped. This means electron injection could result in exciton formation.

These observations are consistent with a scenario in which electrons are being injected into the conduction band of the TMD and subsequently form excitons. Indeed, the p-doped nature of the sample together with the polarity dependence are a strong indication that electron injection could result in exciton formation. Moreover, to inject charge carriers, a partial alignment between the bands and the Fermi level of the electrodes is required. As a result, this mechanism is expected to become efficient at bias larger than the electronic bandgap. A scheme of this process is shown in figure 4.3d. Importantly, the authors pointed out that in UHV conditions the water layer would not be present, and therefore, the TMD luminescence would be quenched by gold.

Similar observations were reported for CVD grown monolayer $MoSe_2$ on $SiO_2$ by Pechou *et al.* [15]. These layers were subsequently transferred onto a patterned Au array in order to enhance the STML yield. In this configuration, they observed an important increase in STML signal coming from $MoSe_2$. This establishes surface engineering as a viable strategy to improve the emission of TMDs. Similar to Peña, charge injection is the most likely explanation for the origin of the luminescence. Nevertheless, there are some limitations related to these configurations. First, just as in the case of Pommier *et al.*, the experimental conditions of the experiment meant the loss of atomic resolution. Second, the parameters used to record the luminescence were either partially destroying the layer or evacuating the water below, resulting in quenching of the STML.

### 4.2.4 LT-STM on $WS_2$/2LG/SiC(111)

Another result was reported later in 2020 by B. Schuler *et al.* [17]. In this work, they were interested in the luminescence of defects embedded in a $WS_2$/2LG heterostructure

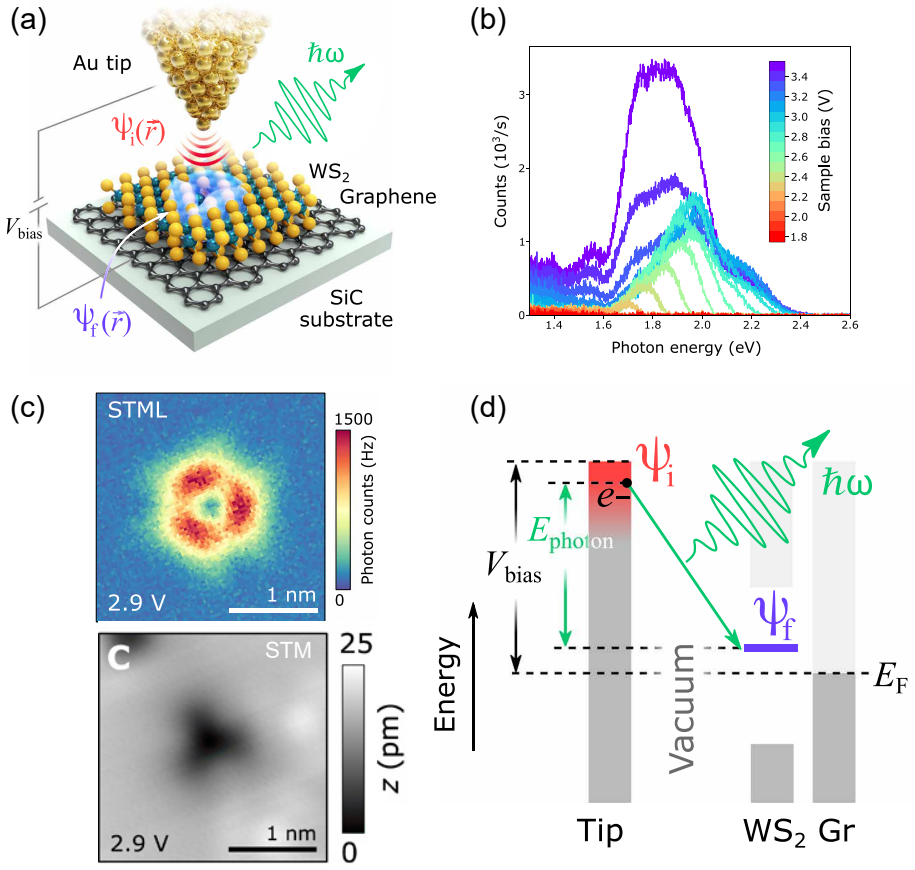


Figure 4.4: **$WS_2$/2LG/SiC**(a) Scheme of the configuration showing a monolayer of $WS_2$ on top of a 2LG.(b)STML spectra recorded at different bias voltages on top of a defect native to $WS_2$/2LG. (c)Top: Photon map recorded on top of a S-vacancy defect acquired at 2.9 V and 20 nA. Bottom: STM-image simultaneously acquired during the photon map.(d) Energy diagram of the emission mechanism. Electrons inelastically tunnel into the defect state giving rise to the observed broad emission. Figure adapted from [17].

synthesized on an SiC substrate. These measurements were carried out at 6 K and in UHV conditions. The idea was to avoid metallic substrates using 2LG instead. A graphic representation of the sample is shown in figure 4.4a. A series of STML spectra recorded at different biases on top of a defect is shown in figure 4.4b. The spectra are characterized by broad emission suggesting an extrinsic origin of the luminescence. However, even though the emission is extrinsic, it strongly depends on the presence of defects. Figure 4.4c shows an atomically resolved photon map of the emission arising from the defect below (top) as well as an STM-image (bottom) acquired simultaneously. In this case, the emission is assigned to the inelastic tunneling of electrons towards the defect state. This mechanism (fig 4.4d) is somehow similar to the one reported by Krane *et al.*, (figure 4.1e). The absence of intrinsic luminescence, in this case, may have different origins:

- Energy transfer towards graphene suggesting a very tight coupling between the layers.

- Absence of a plasmonic substrate that is expected to enhance the emission.
- Epitaxial heterostructures lead to efficient coupling between the layers and the substrate which could lead to a quenching of the luminescence.

### 4.2.5 Summary

We have discussed different approaches aimed at the same goal: the investigation of intrinsic luminescence of TMDs with atomic resolution. These observations are summarized in table 4.1. In-vaccuo techniques performed at low temperatures provide clean interfaces on which atomic resolution can be readily obtained. However, the very same clean interface seems to result in the quenching of the intrinsic emission of the TMD. In contrast, ex-situ techniques performed at room temperature seem to benefit from contaminants (e.g., water) acting as decoupling layers, and as a result, luminescence arising from excitons can be observed at room temperature. Furthermore, room temperature approaches benefit from the use of larger N.A. optics which increases the collection efficiency substantially in contrast to low temperature setups. However, no atomic resolution is observed, and the parameters required to excite the layers can result in the partial destruction of the TMD.

| Sample | Experimental conditions | Emission | Atomic resolution | Emission Mechanism | Ref. |
|---|---|---|---|---|---|
| $MoS_2$/Au(111) | 4K and UHV | Extrinsic | Yes | Plasmonic emission. | [16] |
| $WS_2$/2LG/SiC | 4K and UHV | Extrinsic | Yes | Plasmonic emission. | [17] |
| $MoSe_2$/ITO | 300K and air | Intrinsic | No | Energy transfer. | [13] |
| $WSe_2$/Au | 300K and air | Intrinsic | No | Charge injection. | [14] |
| $MoSe_2$/Au | 300 K and air | Intrinsic | No | Charge injection. | [15] |

Table 4.1: Summary of STML results on different TMDs.

Therefore, to address the excitonic properties of TMD and VdW heterostructures with simultaneous high spectral (sub meV) and spatial (sub-atomic) resolutions, one would need a strategy that is compatible with low-temperature measurements and that sufficiently decouples the layer so we can observe intrinsic luminescence.

#### Comment on emission mechanisms

In the experiments performed by Pommier (section 4.2.2) and Peña (section 4.2.3), different excitation mechanisms were considered. In the former, energy transfer from the tunneling electrons to the TMDs resulted in exciton formation. In the latter, charge injection into the conduction band was the culprit. The assignation of the TMD luminescence to a given mechanism is based on the experimental parameters required to generate the

emission. Each one of these mechanisms requires a different set of conditions which we can use to identify them. For instance, energy transfer requires that the applied bias $V_0$ is at least as large as the optical bandgap ($E_{X^0}$) of the TMD. In other words:

$$e|V_0| \geq E_{X^0} \tag{4.1}$$

Notice that this condition is true for either polarity. On the other hand, charge injection requires at least an alignment between the Fermi level of one electrode and the conduction or valence band of the TMD. As a consequence, a direct link between the luminescence and the dI/dV spectra is expected. Furthermore, the luminescence threshold in a charge injection mechanism should depend on the polarity of the applied bias.

## 4.3 Results

This section contains results on the intrinsic luminescence of TMDs investigated with a low-temperature STM. This was achieved after a long effort over the course of my Ph.D. as the required experimental conditions were difficult to identify.

## 4.4 The sample

All experiments in this chapter have been carried out on a sample made of monolayer $MoSe_2$ stacked onto FLG ($< 4$ layers) using the dry transfer method (see section 2.2). This heterostructure was then deposited onto a commercial thin Au(111) film grown on mica produced by Phasis Sàrl. An optical image of the sample and a scheme are shown in figures 4.5a and b, respectively. In this configuration, the graphene layers may act as a decoupling element, preventing quenching of the TMD by the Gold substrate while simultaneously providing a smooth interface. We might hope, however, to have a lower coupling than in the case of epitaxial heterostructures. Meanwhile, the short distance ($\sim$ 1 nm for 3LG-supported $MoSe_2$) may preserve some of the plasmonic enhancement provided by the gold substrate. For the same reason, silver tips were used for these experiments. Eventually, this configuration allows us to explore the electroluminescence properties of the TMD/1LG-FLG heterostructure under UHV and at low temperature (i.e. potentially with atomic-scale precision). Furthermore, as we used the same $MoSe_2$/1LG heterostructure, our STML data could be discussed in the frame of the results obtained in the previous chapter by optically averaging methods.

The sample shown in figure 4.5 was integrated into an STM-compatible sample holder, which allows us to contact the substrate from two sides. The final configuration of the sample is shown in figure 4.5c. To confirm the monolayer nature of the TMD, we used PL spectroscopy. Figure 4.5d shows a selection of PL spectra taken on different points of the

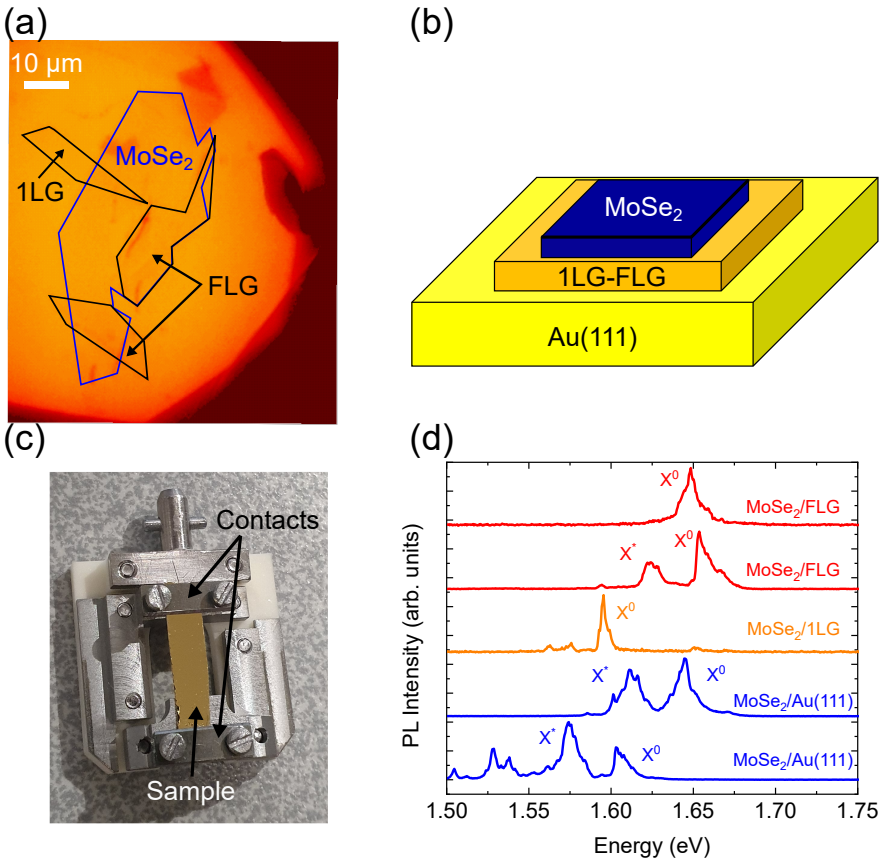


Figure 4.5: **Characterization of the sample.**(a)Optical microscopy image of a monolayer $MoSe_2$/FLG deposited onto a Au(111) film on mica.(b)Graphical representation of the sample architecture.(c) Image of the sample holder. (d) Normalized PL spectra acquired in different regions of the sample. For each spectra the $X^0$ and $X^*$ are signaled. The PL measurements were done under cw excitation at 532 nm under a laser power of 60 $\mu$W/$\mu$m$^2$ and at 14 K.

sample and recorded under CW excitation at 532 nm and 14 K. For the $MoSe_2$/Au(111) region, the PL is characterized by two relatively broad ($\sim$ 13 meV) resonances that we assign to $X^0$ and $X^*$ (blue spectra).

Variations of up to 60 meV in the position of $X^0$ are observed all over the sample, as well as a manifold of supplementary peaks at lower energies. We assign this complex spectral emission to the inhomogeneous interface between the heterostructure and the underlying Au substrate, which significantly modifies the local environment felt by the excitons. The influence of the substrate in the PL can be observed even in $MoSe_2$/1LG (orange). However, in $MoSe_2$/FLG (red), the effect is reduced probably due to a higher decoupling provided by the FLG. Overall, this data suggests that our sample is subject to inhomogeneities that strongly impact the width and the energy of the emission lines, and that cannot be addressed by diffraction-limited approaches.

After this PL characterization, the sample is rapidly introduced in the preparation chamber and annealed for a whole day at 200°C and under UHV conditions. This is done

to ensure the removal of surface contaminants, including water.

### 4.4.1 Surface Morphology

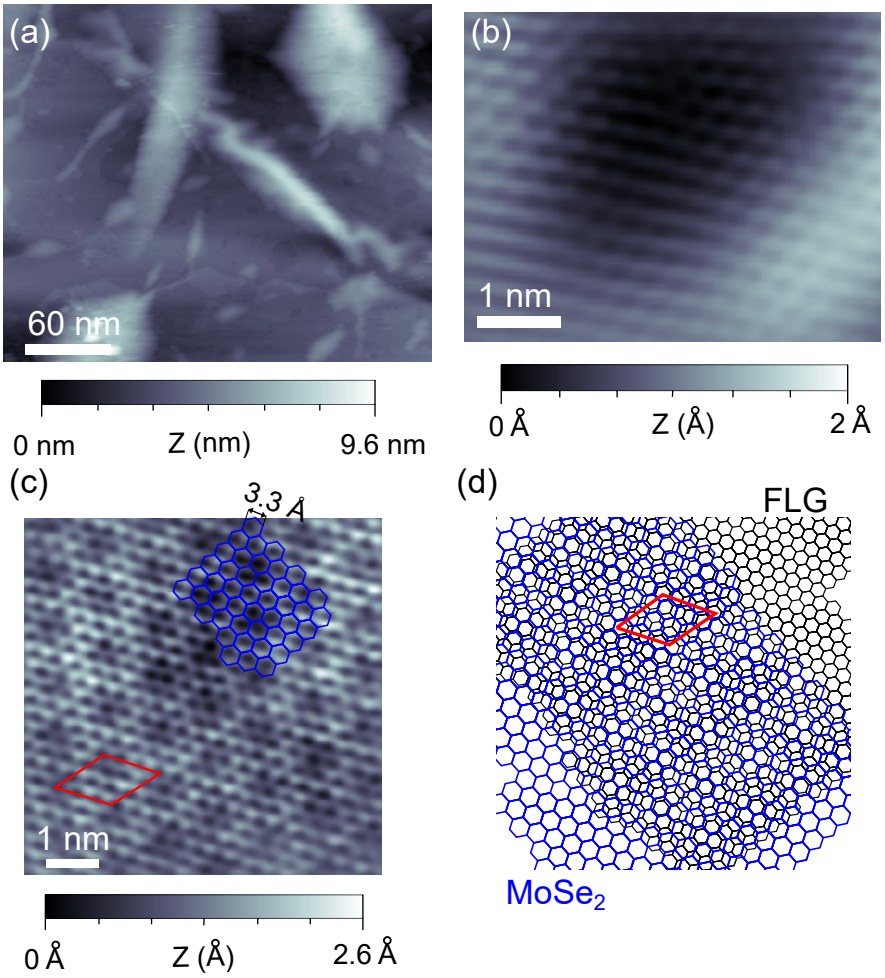


Figure 4.6: **Surface morphology.**(a) Typical constant current STM-image recorded on top of the $MoSe_2$/FLG surface. The heterostructure adapts smoothly to the substrate below, resulting in bubbles and ripples. The acquisition parameters for this image are -2.2 V and 4 pA. Atomically resolved STM-images recorded on flat areas (b) and (c). A lattice parameter of 3.3 Å is measured in agreement with what is expected for $MoSe_2$. A moiré pattern arising from the relative orientation between the TMD and graphene can be observed in (c) suggesting a better TMD/1LG interface quality than in (b). (d) Model of the moiré pattern. The primitive cell of this pattern is indicated in red. The acquisition parameters for the images were -1.3 V, 10 pA for image (b) and -1.4 V, 6 pA for image (c).

Figure 4.6a shows a constant current STM image recorded at 6 K on the $MoSe_2$/FLG surface. In general, we observed flat $\sim 20 \times 20$ nm$^2$ areas surrounded by foldings and bubbles. These structures result from the smooth adaptation of the heterostructure to the underlying Au(111) surface and the presence of residues from the fabrication process. Figure 4.6b and c show examples of atomically resolved STM-images recorded on two of

the flat areas in the sample. In both cases, we measure a lattice parameter of $3.3 \pm 0.2$ Å, which corresponds to the $MoSe_2$ lattice constant. The main difference between these areas is the apparition of a moiré pattern in (c) arising from the relative orientations between the TMD and graphene. Notice that in the image shown in 4.6b, atomic resolution can be obtained but with no signatures of the moiré pattern. This suggests a stronger coupling between the TMD and the FLG in the moiré region (figure 4.6c) than in those where the moiré is absent. We have highlighted the primitive lattice of the moiré pattern and determined that it is consistent with a relative angle of $\sim 5$ °. A model of this pattern is shown in figure 4.6d. We have superposed two hexagonal lattices corresponding to the $MoSe_2$ and FLG. In the vicinity of most of the bubbles, the imaging conditions become unstable. In some of these regions, we observe little sensitivity of the tunneling current to the distance between the sample and the tip. For instance, one order-of-magnitude variations in current were observed for distance variations of the order of 1 nm. This suggests electrostatic effects where the layer is pushed or pulled by the STM tip. In these areas, one has a high risk of crashing the tip into the substrate.

## 4.5 LT STM-induced light emission of $MoSe_2$/1LG

### 4.5.1 First experimental evidence

Figure 4.7a shows an STML spectrum obtained on a flat $10 \times 10$ nm$^2$ area of the $MoSe_2$/FLG surface (figure 4.7b). The spectrum is composed of two sharp resonances separated by 30 meV. We fitted these lines using Voigt profiles to precisely determine the resonances positions and FWHM. We obtained $E_1 = 1.659$ eV $\pm$ 1 meV and $\Gamma_1 = 11 \pm 1$ meV for the first peak, and $E_2 = 1.630$ eV$\pm$1 meV and $\Gamma_2 = 14 \pm 1$ meV for the second one. A comparison with the PL measurements on the same sample allows us to assign these peaks to $X^0$ and $X^*$, respectively. In all of our measurements, we estimate a quantum yield of $\sim 10^{-8}$ photons/e$^-$ assuming a detection efficiency of $\sim 15\%$ (see section 2.5.7). As a comparison, STML measurements on single molecules deposited on a NaCl/Ag(111) sample show yields that are at least 4 orders of magnitude larger [179]. Furthermore, a relatively low current ($< 100$ pA) needed to be used in order to preserve the integrity of the TMD layer. The low efficiency of this emission, together with the necessity of using moderate excitation currents might partially explain the difficulty of observing intrinsic luminescence of TMDs in previous attempts. The weakness of this emission also underlines the necessity to have a setup allowing for the precise in-situ alignment of the lens with respect to the probed sample area (section 2.5.7).

Interestingly, the STML spectrum is smooth and does not display multiple resonances, unlike its PL counterpart. This is a direct consequence of the local nature of the excitation. In essence, one is not sensitive to the spatial averaging which is at the heart of optical

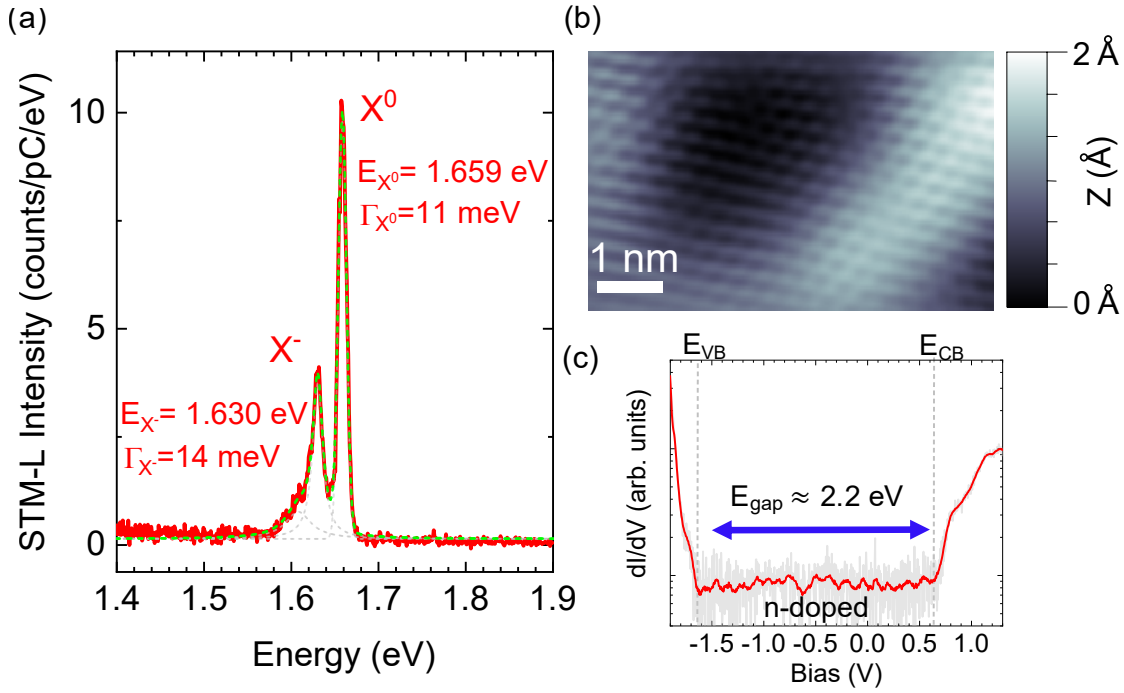


Figure 4.7: **First STML spectrum of $MoSe_2$.**(a) STML spectrum recorded of monolayer $MoSe_2$/FLG/Au(111) (shown in red). The acquisition parameters were -2.8 V and 90 pA. Each peak is fitted with Voigt profiles (shown in dashed gray), the cumulative fit is shown as a dashed green line. The parameters extracted from each fit are shown next to the corresponding resonance. (b) Atomically resolved STM-image of the area on which the spectrum was recorded. This image was acquired under a bias Voltage -1.3 V and at a current of 10 pA. (c) Differential conductance spectrum taken on the explored region. The spectrum is shown on logarithmic scale to facilitate the determination of the band's onsets. The raw data is shown in gray. For clarity, we smoothed this data, and the result is shown in red. From the band-onsets, we determined an electronic bandgap of 2.2 eV.

measurements. However, there are still signatures of inhomogeneous broadening in the peaks. Indeed, even though we observe much sharper widths than those obtained in PL, these values are still far from the homogeneous linewidth expected for $MoSe_2$/1LG ($\sim$ 300 $\mu$eV). Instead, the quality of the interface between the heterostructure and the Au(111) probably contributes to the broadening of the peak. Moreover, the presence of plasmons can also play a role in shortening the excitonic lifetimes through the Purcell effect.

Figure 4.7c shows a differential conductance spectrum taken in the same area. For all the dI/dV spectra acquired in this section, we used the same procedure as in reference [26] to determine the band onsets. This procedure can be summarized as follows:

- First, we represent the spectrum on a logarithmic scale. A rigid vertical offset was applied to avoid running into negative values.
- To estimate the floor level of the conductance, we calculated the average value and the standard deviation of the noise inside the gap.

- We defined a $2\sigma$ threshold from which we consider that the signal is sufficiently different from the noise. We use this to determine $E_{VB,2\sigma}$ and $E_{CB,2\sigma}$ which correspond to the values for which the signal is exactly $2\sigma$ above the floor level.

- Finally, we used linear fits of the bands within a range of $E_{VB,2\sigma} - \Delta E < E < E_{VB,2\sigma}$ and $E_{CB,2\sigma} < E < E_{CB,2\sigma} + \Delta E$. $\Delta E$ was chosen so that the $R^2$ of the fits is not smaller than 0.95.

- The onset of the bands is then defined as the intersection between the linear fit and the floor level. We have marked these values with the gray dashed vertical lines in figure 4.7c.

Using this procedure, we determined a bandgap of $2.2 \pm 0.1$ eV all over the sampled region (i.e., this value does not vary depending on the position with respect to the moiré pattern). This value closely matches what has been reported in similar systems [26]. Moreover, the proximity between the Fermi level and the conduction band indicates that the $MoSe_2$ layer is n-doped. This is not surprising since exfoliated $MoSe_2$ layers are expected to carry residual n-doping [27, 28, 29]. This measurement, together with the STML spectrum, allows us to draw two conclusions. First, the trion resonance is likely originating from a negatively charged trion. From now on, we are going to change the notation we have used for the trion $X^*$ to explicitly account for its charge sign ($X^-$). We can safely rule out "current-induced" trions since the current employed during this acquisition (90 pA) corresponds to the average passage of 1 electron every 2 ns. This is well above the characteristic lifetime of excitons and trions in $MoSe_2$ and $MoSe_2$/1LG, which we have seen is $\sim 2$ ps (See section 3.4). Second, we can estimate the local binding energy of the excitons by simply subtracting the electronic bandgap from the optical bandgap obtained in STML. We estimate an average difference between the STS bandgap and the optical bandgap of $\sim 540$ meV. Notice that this is the first example where the binding energy can be deduced from simultaneous atomically resolved electronic and photonic measurements, preventing any ensemble averaging effects.

This value is within the reported binding energies for similar systems estimated from the comparison between STS and large-scale PL measurements (See table 4.2). However, it largely exceeds the binding energies deduced from PL, DR, and PLE measurements (see chapter 3). This invites a reinterpretation of what is measured with STS. As discussed in chapter 2, different phenomena can be behind this discrepancy:

- **Determination of the band onsets:**

  STS is weakly sensitive to electrons with in-plane momentum $k_\parallel \neq 0$, therefore the determination of the bandgap at K is non-trivial. This could lead to an overestimation of the bandgap.

- **STS interpretation:**

  We might be measuring modifications of the local electronic structure due to the transient injection of a charge. A similar process is observed in single molecules [180]. This contrasts with the purely optical measurements of the electronic bandgap, where the TMD remains neutral.

- **Locality of STML vs PL:** We observe similar values for the binding energy in STML and PL indicating that the discrepancy does not arise from the non-local nature of PL.

We want to emphasize that this result remains the first observation of intrinsic emission from TMDs with atomic resolution.

| System | substrate | Binding energy (meV) | Exp. technique | reference |
|---|---|---|---|---|
| $MoSe_2$/2LG | SiC | 550 | STS,PL | [26] |
| hBN/$MoSe_2$/1LG | hBN | 150 | PL, DR | See Ch. 3 |
| $MoSe_2$/2LG | hBN | 155 | PL, DR | See Ch. 3 |

Table 4.2: Binding energies of $MoSe_2$/BLG on different substrates.

### 4.5.2 Homogeneity of the emission on flat areas

To explore the effect of the local environment and ensure the reproducibility of our measurements, we acquired several spectra on different locations over the sample. In particular, we focused on three $5 \times 5$ nm$^2$ flat areas in the heterostructure. A scheme of these regions and atomically resolved constant current STM images are shown in figure 4.8a. To distinguish between the measurements taken on each area, we assigned them numbers from 1 to 3, as shown in the figure. Regions 1 and 2 are located few tens of nm away from each other whereas region 3 is separated by more than 1 $\mu$m from the others. A selection of STML spectra acquired in each region is shown in figure 4.8b. The corresponding positions on which the spectra were recorded are indicated in the STM images with the colored marks.

Let us first discuss regions 1 and 2. In general, we observe that both the position and width of the resonances remain unchanged at small separation distances. In region 2, we observe a moiré pattern indicating a better TMD/FLG interface than in region 1. As a result, we observe a narrowing of the emission from 11 meV in region 1 to 9 meV in region 2. The image acquired in region 3 also reveals a moiré pattern. Surprisingly, we observe a massive 70 meV redshift in the $X^0$-line emission. Notice that similarly large variations in the $X^0$ emission were observed in PL (figure 4.5). The difference

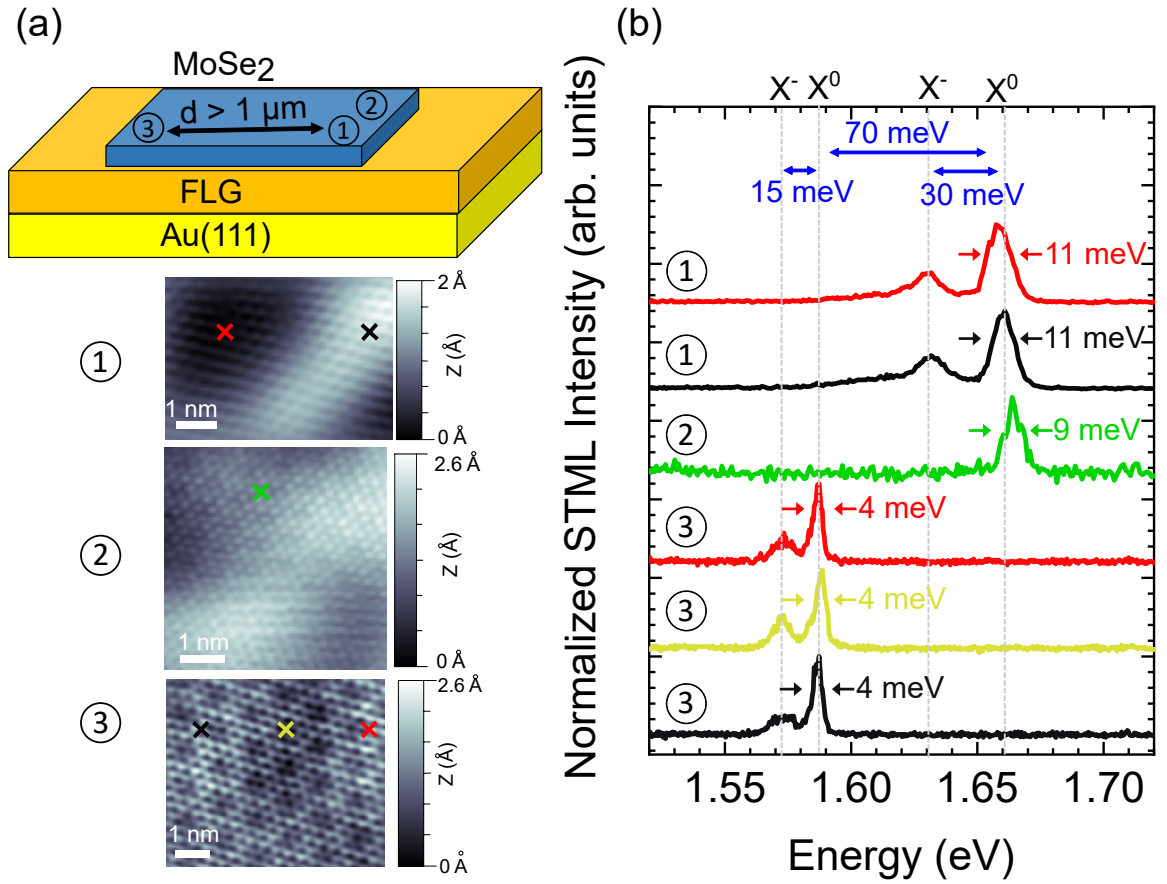


Figure 4.8: **Spatial dependence of the emission.**(a) Top: Scheme of the heterostructure. We focused on three regions, marked from 1 to 3. Regions 1 and 2 correspond to the same area whereas region 3 is located more than 1 $\mu$m away. Atomically resolved images of each region are shown in the bottom part of figure (a). The acquisition parameters for these images were from top to bottom: -1.3 V, 10 pA (region 1), -1.4 V, 4.1 pA (region 2) and -1.4 V, 6 pA for region 3. (b) Selected STML spectra recorded on regions 1 (top three spectra) and 2 (bottom two spectra). The corresponding positions on which the spectra were acquired are shown in the STM images and follow the colored marks. The spectra are characterized by two resonances separated by 30 meV (15 meV) in regions 1 and 2 (region 3). The acquisition parameters for the spectra were: -2.8 V, 90 pA (region 1), -2.8 V 100 pA (region 2) and -2.9 V 90 pA (region 3).

between the STML data acquired in region 2 and region 3, cannot be assigned to a different TMD/FLG interface and rather indicates that it is the interface between the heterostructure and the gold substrate that is at play. Dielectric screening induced by the proximity of a metallic environment is known to generate substantial redshift of TMD emission lines (a phenomenon that we discussed for $MoSe_2$/Au interface in reference [9]). We speculate, that the change in the emission energy of the $X^0$-line originates from this phenomenon which therefore indicates a better interface between the heterostructure and the Au substrate in region 3. This is also consistent with the narrowing of the linewidths from 11 meV in region 1 down to 4 meV in region 3 (Let us point out that this is the narrowest value to our knowledge in non-capped samples). Indeed, emission

line broadening arises when TMDs are located in an inhomogeneous environment. A sharp emission line is an indication of more homogeneous $MoSe_2$/FLG/Au(111) interfaces. Following a similar reasoning, redshifted narrow emission lines may also be attributed to localized excitons, which can be due to defects (absent in the image of region 3) or to moiré trapped excitons. Indeed, the emission from moiré trapped excitons may be very narrow (< meV) because of their long lifetimes. Here, the presence of graphene may reduce their lifetime to few ps, resulting in linewidths close to few $\sim$ meV. Overall, these observations indicate that the interface quality, either within the heterostructure or between the heterostructure and the Au surface, plays a crucial role in the exciton emission.

Let us now discuss the lower energetic features that accompany the $X^0$-line observed in the spectra of figure 4.8b. In region 1, the 30 meV redshifted peak can readily be assigned to a trion. The n-doping identified in the dI/dV spectrum in figure 4.7 suggests a negatively charged trion ($X^-$). The disappearance of this trion in region 2 can be well explained by the better interface with graphene that leads to static charge transfer between the layers as discussed in chapter 3. In region 3, a peak appears again but it is located 15 meV below $X^0$ instead of 30 meV. In the previous paragraph, we concluded that region 3 is affected by a massive screening due to the better coupling with the gold substrate. As observed for $MoSe_2$/1LG in figure 3.13, an increased screening reduces the trion binding energy. We, therefore, assign the 15 meV lower energetic feature in region 3 to a screened trion[1]. In region 3, the good interface with the gold substrate has a direct effect on the electron redistribution in the TMD/FLG heterostructure that may lead to a larger n-doping compared to region 2 where the trion is absent. This provides the conditions necessary to form trions and explains the presence of the $X^-$-line in region 3.

Interestingly, inside each region, we observe no appreciable change in the position of the resonances over distances as large as 30 nm, even at different points of the moiré pattern. A possible explanation for this is related to the period of the pattern itself. Indeed, in our case, the moiré pattern periodicity is comparable to the excitonic Bohr radius in TMDs. This could mean that the excitons 'feel' the averaged effect of the superlattice.

The conclusions drawn in this section are based on a solid but limited number of data sets. Considering the complexity of the processes at play and the highly changing morphology of the sample at the 5-100 nm scale, a definitive assignment of the different

[1]We can safely rule out biexcitons as candidates. Indeed, these quasiparticles require excitons to interact with each other, which is favored in high-density regimes. In our case, at 100 pA, we can safely rule out such a process. As a broad estimation, to form a biexciton one would need to form at least two excitons within $\sim$ 2 ps from each other -for longer times, excitons will recombine-. Supposing a formation rate of 1 $e^-$/exciton, this would imply a current of $\sim$ 320 nA which is above the 0.1 nA used in figure 4.8.

spectral features -especially the one identified as $X^-$- requires further investigations on $MoSe_2$/FLG/Au(111) samples having more homogeneous interfaces.

### 4.5.3 Emission from inhomogeneous areas

In section 4.4.1, we saw that the fabrication process and the smooth adaptation of the heterostructure to the substrate result in a landscape characterized by flat areas surrounded by ripples and bubbles. Consequently, the PL spectra are "contaminated" by emission arising from these inhomogeneities, rendering the observation of intrinsic features complex. So far, we have shown that the local nature of STML allows us to overcome these difficulties by avoiding these macroscopic defects. However, it could be interesting to investigate the emission from qualitatively different areas and observe the modification they produce in the luminescence of the TMD. This is not a simple task since there is a risk of crashing the tip onto the layer. Indeed, there might be situations where the bubbles are sufficiently decoupled from the electrodes to render stable STM measurements nearly impossible.

Figure 4.9a shows a 3D view of a $50 \times 40 nm^2$ area containing a flat area next to a TMD bubble. This image reveals an approximate bubble height of 1 nm. We recorded STML spectra at the two locations marked by crosses (blue on the bubble, red on the flat area). The resulting spectra are shown in figure 4.9b. The spectrum recorded on top of the flat area is composed of one resonance located at 1.590 eV. This resonance is assigned to the $X^0$ recombination. In the bubble (shown in blue), we observe two peaks located at 1.587 eV and 1.547 eV. The first peak corresponds to a redshifted $X^0$, probably due to the slightly higher strain in the bubble. The lower peak is only visible in the vicinity of the bubble, and we associate it with a localized exciton $X^L$.

Moreover, we observe a 3-fold increase of the STML signal with respect to the flat areas when measuring on top of the bubble. This increase is due to the decoupling nature of the bubble which reduces energy transfer towards the substrate. This difference in luminescence is compatible with the one observed in PL measurements between TMD and TMD/1LG. This allows us to investigate the difference between coupled and decoupled areas at the atomic scale. Besides, the appearance of $X^L$ suggests that the exciton is emitted in close vicinity of the tip, as spectra acquired a few nm apart provide different emission features.

The STML signal drastically changes in the vicinity of sharper inhomogeneities such as ripples and cracks in the layer. Figure 4.9c shows an STM image of an area containing bigger defects. Scanning over these areas can be challenging since the tip struggles to regulate the current. To counteract this, we measured STML spectra while scanning over a 5x5 $nm^2$ area at constant current instead of fixing the tip position. Figure 4.9d shows two STML spectra acquired in these conditions over the highlighted areas shown in figure

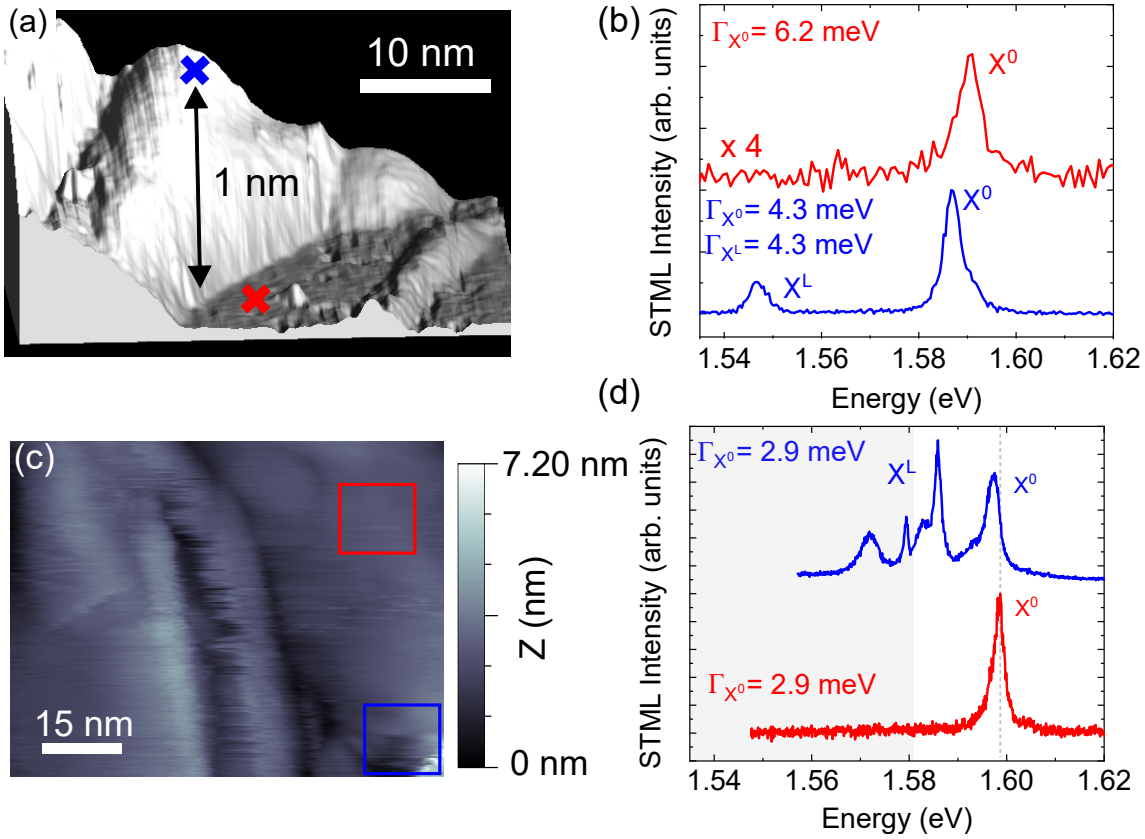


Figure 4.9: **Inhomogeneous emission in TMDs**(a) STM-image of an $MoSe_2$/FLG surface presenting a bubble. The image was acquired under a bias voltage of -2.1V and a current setpoint of 4 pA. An inset shows a profile of the surface taken along the line connecting the blue and red marks. (b)Normalized STML spectra recorded at the positions marked in the previous image. The scaling factor between the $X^0$ peak in the two spectra is 4, shown in the top panel. The red (blue) spectrum was acquired under a bias voltage of -3.2 V and a current setpoint of 4 pA (10 pA). (c) STM-image of the $MoSe_2$/FLG surfaces displaying a folding and a damaged part of the layer. The acquisition parameters were -1.85 V and 5 pA. (d) STML spectra taken while scanning on the areas highlighted by the colored squares. In the damaged area, the spectrum is composed of many peaks arising from localized excitons. Both spectra were acquired under a bias voltage of -1.85 V and a current setpoint of 5 pA.

4.9c. In the reference region (red area), the spectrum is composed of a single resonance corresponding to $X^0$. The absence of lower energy features suggests that this area is sufficiently far away from edge-related effects.

In contrast, in the anomalous region (blue area), we observe an STML spectrum composed of multiple sharp resonances with widths varying from 2.9 meV in the case of the $X^0$-line, down to $\sim$ 700 $\mu$eV in the case of the $X^L$-line. Similar observations have been reported in highly strained TMDs [30]. These peaks stem from quantum-dot-like states that may behave as single-photon sources. Correlation measurements would be required to confirm this hypothesis.

We want to point out that regions like these are readily found all over the heterostructure. This explains the inhomogeneous character of the emission when probed through diffraction-limited techniques. Besides, our measurements suggest that the origin of the localized emission $X^L$ in TMDs originates from macroscopic structures such as ripples, bubbles, and cracks measuring several nanometers across. In contrast, we have, at this stage, no indications that allow us to link SPS in TMDs to atomic-scale defects.

### 4.5.4 Origin of the luminescence

Let us now investigate the physical process that gives rise to the luminescence. To this end, the voltage dependence of the emission is crucial as this characteristic is generally different depending on the excitation mechanism (see section 4.2.5). In all STML spectra presented so far, a negative bias voltage was used. We also investigated voltages ranging from 1.6 V up to 3.5 V and at least two orders of magnitude variations in current. No light emission was observed under any of the explored parameter space. This already suggests a mechanism mediated by carrier injection in the conduction or valence band. To explore further this mechanism we recorded a series of spectra at different negative bias voltages (shown in figure 4.10b) recorded at the position shown in figure 4.10a. The gray dashed lines mark the positions of the $X^0$ and $X^-$-resonances and are given as a guide for the eye. We observe an onset of the luminescence at approximately -1.65 V. At this voltage and up to -1.7 V, only low energy peaks located 30 to 50 meV below the $X^0$-line are observed. These peaks may be assigned either to localized excitons and/or trions and may originate from surrounding inhomogeneities observed in the STM image. As we continue to increase the bias, we observe a drastic change in the shape of the spectra. Indeed, the $X^0$-line appears at -1.75 V and becomes dominant for lower voltages. Furthermore, the lower energetic features related to localized excitons and trions disappear entirely. This phenomenon will be discussed in section 4.5.5. For the moment, let us focus first on the $X^0$ emission. Figure 4.10c shows a differential conductance spectrum taken in the same spot as the STML. We have overlayed with this spectrum the integrated intensity of the $X^0$ line as a function of the applied bias. The similar evolution between the conductance and the intensity indicates that excitons are more efficiently excited as we increase the bias from the valence band maximum. In fact, the onset of the band coincides very well with the onset of the $X^0$ emission.

This observation, together with the absence of STML at positive bias, suggests an emission arising from hole injection in the VB. We propose an excitation mechanism in three steps (figure 4.10d):

1. **Electron extraction.** When the bias matches the onset of the VB, an electron can be extracted, leaving a positively charged hole in the VB.

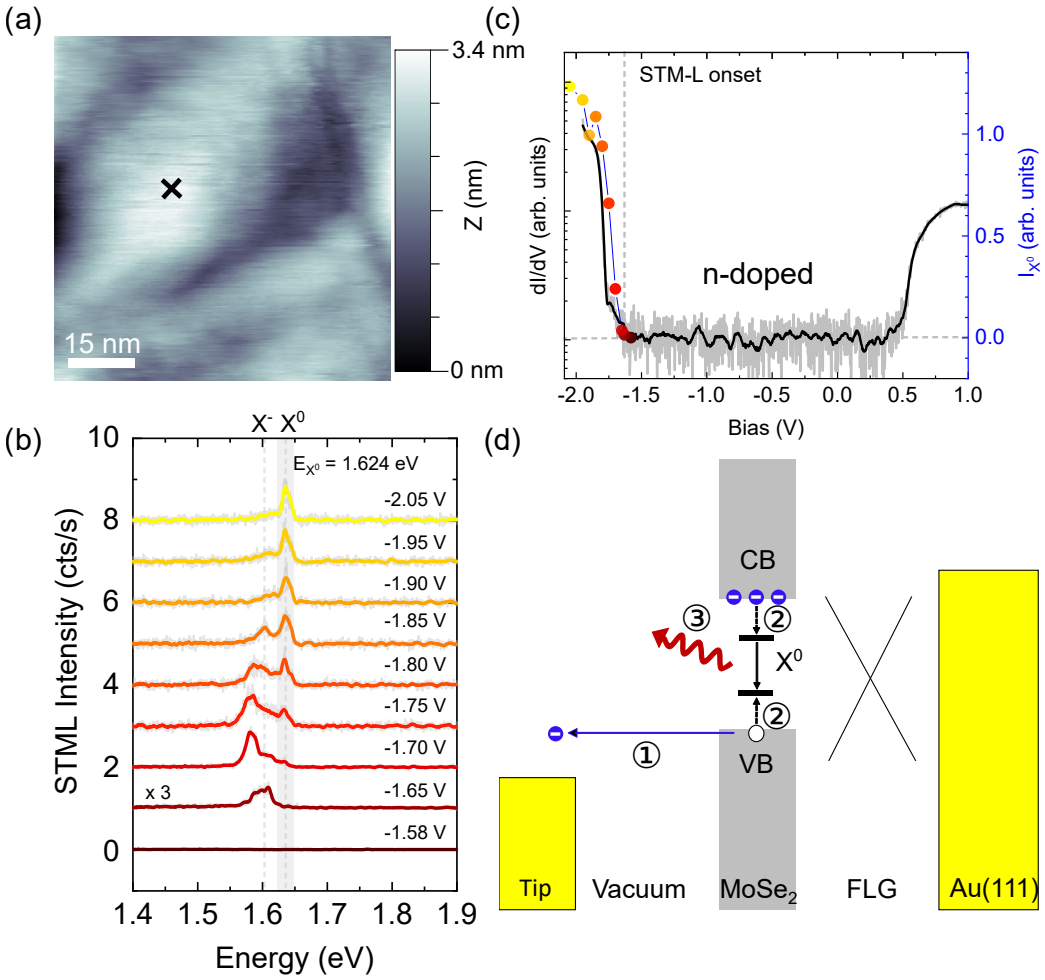


Figure 4.10: **Excitation mechanism.**(a) STM-image of a patch on the $MoSe_2$/FLG surface. The image was acquired under a bias voltage of -2 V and a current setpoint of 5 pA.(b)STML spectra recorded at different biases on the marked position in (a). The dashed lines correspond to the position of the $X^0$ and $X^-$ resonances and are left as a guide for the eye. These spectra were recorded at a setpoint current of 30 pA. (c) Differential conductance spectrum taken on the same location as in (b). The spectrum is overlayed with the integrated intensity of the $X^0$ line as a function of the applied voltage. The close agreement between the two supports a charge injection scenario for the excitation mechanism. The color code corresponds to the one used in figure (b). (d) Energy diagram of the excitation mechanism. First, an electron is extracted from the valence band, leaving a hole behind. Second, an exciton is then formed when native electrons in the TMD bind with the hole. Finally, the exciton recombines, emitting a photon.

2. **Exciton formation.** This hole then interacts electrostatically with native dopants in the heterostructure. From the dI/dV spectrum, we can deduce that the layer is n-doped[2]. Therefore, the Coulomb interaction between the native electrons and the hole results in exciton formation. Notice that this process is valid for trion formation as well. Indeed, as the exciton is formed, there could be a situation in which it interacts with native dopants and forms a trion.

[2]The Fermi level is closer to the conduction band than to the valence band.

3. **Exciton recombination.** Once formed, $X^0$ can recombine radiatively, resulting in the observed luminescence.

An energy diagram summarizing this process is shown in figure 4.10d.

### 4.5.5 Comments on filtering effect

Finally, let us comment on the disappearance of lower energetic peaks in the STML spectra presented in figure 4.10d. As mentioned before, this series of spectra were acquired at constant current. This means that as we vary the voltage, the tip-sample distance increases. Figure 4.11a shows the variations in the tip height as a function of the bias voltage during the acquisition of the previous spectra. In total, the tip-sample distance increases by 1 nm during the acquisition. It is well known that the tip-sample distance has an important impact on the coupling between gap plasmons localized at the STM junction and excitons localized within this junction. This plasmon-exciton coupling impacts the radiative lifetime of the excitons, an effect known as the Purcell effect. Below we investigate the possibility that the disappearance of these peaks is directly linked to this change in the Purcell factor.

The enhancement of the luminescence by a plasmonic structure has been studied before in the context of single-molecule fluorescence [181]. In the STM junction, the presence of the NCP (see section 2.5) provides a continuum of states with which the molecule can couple. As a result, the radiative recombination rate of the molecule increases. The extent to which this rate is affected depends on the photon emission probability in the absence of the plasmonic structure. This effect could be at play for TMDs as well, assuming that the radiative decay rises in the close vicinity of the tip. The main difference with single molecules is that the excitonic lifetimes are already short in bare TMDs. Indeed, for $MoSe_2$/1LG we have shown for $X^0$ that $\tau_{X^0}^{\text{rad}} = 5$ ps. In the proximity of the STM tip, we can expect these lifetimes to become even shorter. This can lead to a situation where the radiative decay of normally long-lived species is favored compared with the energy transfer towards graphene. This allows us to define two regimes: A regime dominated by the energy transfer to graphene (designed as the filtering regime) and a regime dominated by the shortening of the radiative lifetimes (designed as the nanocavity regime). This is depicted in figure 4.11b.

To investigate this effect further, we studied the luminescence from a bubble as we approach the tip. To do so, we kept the voltage constant at -2.2 V and increased the applied current. A reference spectra taken on the bubble is shown in figure 4.11c. The spectra are characterized by two transitions located at 1.596 eV and 1.541 eV that we assign to $X^0$ and a localized exciton $X^L$ respectively. Figure 4.11d shows the ratio between the integrated intensity of the peaks and the current applied as a function of the current. We observe that the efficiency of the localized exciton emission increases with the current.

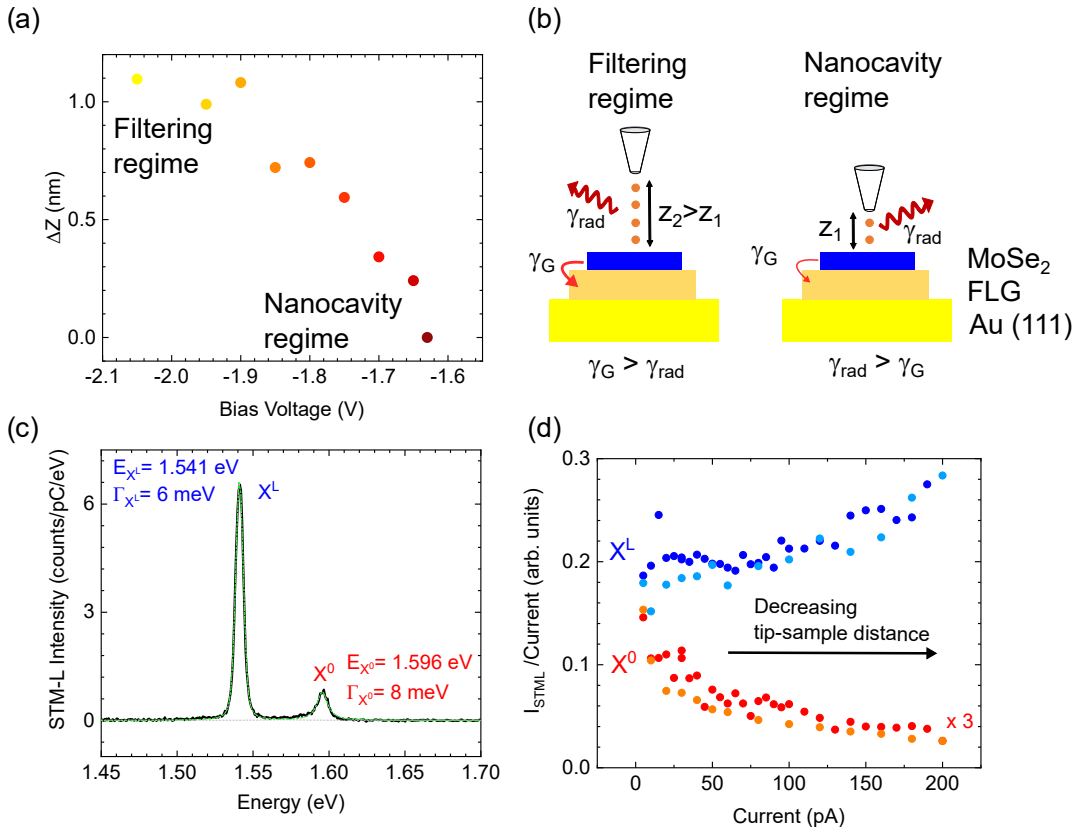


Figure 4.11: **Tailoring the excitonic dynamics.** (a) Distance variation of the tip height during the bias dependence spectra in figure 4.10d. (b) Scheme of the junction illustrating two regimes. At large tip-sample separations, the dynamics are dominated by the energy transfer rate to graphene $\gamma_G$. The Purcell effect increases the radiative recombination rate $\gamma_{rad}$ at shorter distances. (c) STML spectrum acquired on top of a bubble. The acquisition parameters were -2.2 V and 10 pA. (d) Ratio between the integrated intensity of the $X^0$ (red) and the $X^L$ (blue) emission lines and the current as a function of the current. The dark (clear) blue and red circles correspond to the continuous increasing (decreasing) of the applied current. These spectra were acquired at a bias voltage of -2.2 V.

This is consistent with a scenario in which radiative recombination of long-lived excitons becomes more efficient in the proximity of the tip. In the case of $X^0$, the efficiency slowly reduces when the current is increased. This reduction of the $X^0$ *efficiency* is due to a saturation of the light *intensity* with current. Moreover, we observe that this measurement is non-destructive as we obtain qualitatively the same behavior when decreasing the current. To understand these observations, let us consider the case of $MoSe_2$/FLG in the absence of plasmonic structures. In this scenario, we can write:

$$\begin{cases} \eta_{X^0} \propto \frac{\gamma_{X^0,rad}}{\gamma_{X^0,rad}+\gamma_G} \sim 1 \\ \eta_{X^L} \propto \frac{\gamma_{X^L,rad}}{\gamma_{L,rad}+\gamma_G} \approx 0 \end{cases} . \tag{4.2}$$

Where $\gamma_{X^0,rad}$, $\gamma_{X^L,rad}$, $\gamma_G$ are the radiative recombination rate of $X^0$, the radiative recombination rate of $X^L$ and the energy transfer rate towards graphene. $\eta_{X^0}$ and $\eta_{X^L}$

are respectively the emission efficiencies of each excitonic species. In the previous chapter, we have seen that $\gamma_{X^0,rad} \sim \gamma_G > \gamma_{X^L,rad}$. When the tip approaches, all the radiative recombination rates will increase due to the Purcell effect. Therefore, both $\eta_{X^0}$ and $\eta_{X^L}$ will increase. As a result, the filtering effect of graphene is reduced, and photon emission from long-lived species ensues. Moreover, since $X^0$ already has a yield $\eta \sim 1$, the emission efficiency of this quasiparticle will quickly saturate. To further evaluate the validity of this scenario, a theoretical study of the plasmon/TMD coupling would be required.

Another possible scenario to explain the presence and disappearance of the $X^L$ peak as a function of the tip position would consider electrostatic effects generated by the proximity of the tip with the substrate. Nevertheless, further measurements on other samples and under more controlled conditions are required to prove this point further.

## 4.6 Conclusion

In this chapter, we presented an STML investigation of monolayer $MoSe_2$/graphene heterostructures deposited on gold. We demonstrated that it is possible to achieve intrinsic emission from a van der Waals heterostructure while preserving the ultimate resolution of the STM. This was achieved thanks to a careful design of the sample architecture. As expected, graphene provides a smooth surface on which the monolayer $MoSe_2$ is deposited, while also acting as a decoupling layer. Furthermore, due to the relatively small separation ($\sim 1$ nm) between the TMD and the gold substrate, one may benefit from some of the plasmonic enhancement of the junction. Using PL, we showed that the sample displays complicated emission arising from inhomogeneities in the sample. This highlights the importance of the interface quality between the heterostructure and the gold substrate in the emission.

The STML spectra were characterized by emission arising from the neutral exciton $X^0$ as well as the negatively charged trion $X^-$. In all of our observations, we observed an emission yield for $MoSe_2$ close to $10^{-8}$ photons/$e^-$, a very low value compared to usual STML reports. We exploited the comparison between STML and low temperature STS to measure the local excitonic binding energy obtaining a value close to 540 meV. This is similar to what has been reported using combined approaches between PL and STS. This means that we can rule out the non-locality of PL as a source for the large discrepancy between bandgaps. This discrepancy may therefore find its origin either in the inability of STS to resolve $k_\parallel$ or in the specific nature of STS gap that involves transient local charging of the TMD. A definitive statement regarding the origin of the discrepancy remains to be established.

We have also shown that STML spectra display emission lines significantly sharper than those observed using PL in the same sample. This is a direct consequence of the ultimate resolution of STML in which we are essentially immune to spatial averaging effects.

Moreover, we showed that the efficiency, the linewidths, and the emission energies of the spectra strongly depend on the quality of the different interfaces: heterostructure/Au, TMD/FLG, and the bubbles. For instance, we observed that the heterostructure/Au interface induces large (up to 70 meV) variations in the exciton emission energy arising from dielectric screening. This is also evidenced by the reduction of the trion binding energy from 30 meV down to 15 meV. The interface between $MoSe_2$/FLG on the other hand determines the linewidths we observe. A signature of a clean interface is the apparition of moiré patterns. Finally, in the bubbles, we observed contributions from localized excitons as well as a 3-fold enhancement of the $X^0$ luminescence. This emphasizes the decoupling role of these macroscopic defects. We conclude that localized emission observed in PL arise from these macroscopic defects.

Finally, a voltage dependence study of the luminescence allows us to demonstrate that the emission from the heterostructure was induced by the injection of holes into the TMD. Once injected, they would quickly bind to native dopants (electrons) in the TMD, forming excitons in the process. At bias above -1.75 V, the luminescence arose not only from $X^0$ but also from other lower energy features that we assign to $X^-$ and localized emission $X^L$. At higher bias, these features disappeared giving rise to single-line emission similar to the one observed in PL for TMD/1LG. We understand this effect in terms of a tip-controlled filtering effect. At low bias, the tip is in proximity with the sample which could reduce the radiative lifetime of long-lived excitonic species. At high bias, the tip has receded and graphene filtering takes over, resulting in the same behavior explained in chapter 4. Our work addressed some of the questions mentioned in section 4.1. However, it also raised many more that we discuss in the perspectives of this thesis. This result paves the way for new investigations into the optical properties of 2D materials with ultimate in-plane resolution.

Chapter 5

# Conclusion

In this manuscript, we reported on the study of the interlayer coupling in TMD/graphene heterostructures at the sub-nm scale. This thesis is based on two main chapters. Chapter 3 is dedicated to the investigation of the interlayer coupling in TMD/graphene heterostructures using optical spectroscopies. Chapter 4 is dedicated to the study of the optical properties of TMD/graphene using STML.

In chapter 3, we showed that the coupling with graphene has two major effects on the luminescence properties of the TMD. These are the complete neutralization of the TMD due to graphene and a filtering arising from energy transfer of long-lived excitonic species to graphene. As a result, low-temperature PL spectra of different TMDs display single- and narrow-emission lines arising from the neutral exciton. Since this process is also true for TMDs displaying spin-forbidden excitons. Our results suggest that the mechanism behind the interlayer coupling in TMD/graphene is compatible with Dexter energy transfer.

Furthermore, we showed that graphene enables efficient non-radiative paths for both excitons in the light cone as well as hot-excitons with momentum outside of the light cone. Using a combined approach between time-resolved photoluminescence spectroscopy, differential reflectance contrast, and spatially-resolved photoluminescence spectroscopy, we were able to estimate a transfer time of cold excitons to graphene in the order of $\tau_G \sim$ few ps.

Remarkably, all the physical effects (filtering, reduction of the binding, PL quenching, etc...) that we observe occur using only one single layer of graphene. In a nutshell, adding extra layers of graphene and/or a top hBN layer marginally affects the aforementioned physical processes. This establishes TMD/1LG as a photostable heterostructure that can be readily contacted and that is compatible with STML studies.

In chapter 4, we continued our investigations into TMD/FLG using STML at low temperatures and in UHV conditions. We were able to demonstrate for the first time, the intrinsic STM-induced luminescence of a vdW heterostructure while preserving the atomic resolution. A goal that until now had not been reached. We then exploited the ultimate resolution provided by STML to investigate the effect of the atomic-scale landscape on the luminescence of the TMD.

First, we showed that the interface between the TMD and graphene plays an important role in broadening the emission lines. In clean interfaces, a Moiré pattern was observed

together with a reduction of the peak linewidths from 11 meV in areas with no Moiré pattern down to 4 meV in the best areas we found. These linewidths are comparable to those obtained in high-quality hBN-capped samples. Second, we showed that the quality of the interfaces (e.g., TMD/FLG and FLG/Au) plays an important role in the emission properties of the heterostructure. Our results suggest that the interface between the heterostructure with gold strongly defines the screening felt by the excitons. This can be evidence in both PL and STML, where variations in the excitonic emission energy of the order of 70 meV were observed.

Finally, we were able to explore the effect of macroscopic defects such as bubbles and cracks of the TMD on the excitonic emission. We observed that these inhomogeneities result in STML spectra composed of different peaks that may arise from localized excitons. Interestingly, some of these macroscopic defects displayed spectra with linewidths close to 700 $\mu$eV. This merits further investigations as these could be a sign of the SPS hosted by TMDs. Our results provide us with a clear understanding of the origin of complex features observed in PL spectra.

Finally, we investigated the mechanism that gives rise to the observed luminescence. A voltage dependence revealed that excitonic emission is induced through hole injection into $MoSe_2$. This is only possible due to the n-doped character of the TMD which acts as a reservoir of electrons for the hole to interact with. Moreover, we observed signs of atomic-scale control of the luminescence of TMDs. By changing the tip-sample distance, we observed emission from different excitonic species suggesting a non-negligible interaction between excitons and the metallic tip. Overall, our studies establish TMD/graphene as a platform to investigate light-matter interaction at the nanoscale.

## 5.1 Perspectives

In the following, I will discuss some of the perspectives related to our investigations.

### 5.1.1 Interlayer coupling mechanisms in TMD/1LG

So far, our results point towards a charge tunneling mediated process at the hearth of TMD/1LG coupling. However, at this moment, we do not have definitive proof. An ideal experiment to address this point would consist in the precise control of the interlayer separation. At large separations ($>$ 1 nm) tunneling becomes inefficient and we could investigate the effect of Foerster energy transfer in TMD/1LG. To do so, one could imagine using hBN as a spacer and investigate how the dynamics change at different separations as shown in figure 5.1.

Going a step further, one could characterize nanoscopic bubbles in the TMD and use STML to obtain information on the exciton emission efficiency at different TMD/graphene

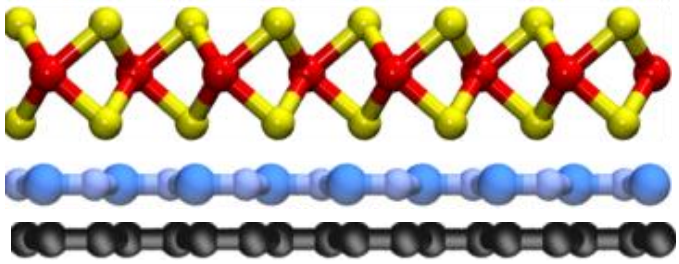

Figure 5.1: **Distance dependence interlayer coupling**. Scheme illustrating a vdW heterostructure composed of monolayer TMD/hBN/1LG. By varying the number of hBN layers one can tune the coupling in the heterostructure.

separations. These experiments could pinpoint the mechanisms at play in TMD/1LG heterostructures.

### 5.1.2 Valley depolarization and decoherence in TMD

We have briefly seen that TMD/graphene heterostructures display robust degrees of valley coherence and polarization. However, the underlying mechanisms for depolarization remain unknown. In chapter 2, we described all of the processes that can lead to depolarization in semiconductors. Currently, the main candidates to explain the depolarization process are the exchange interaction and phonon-induced intervalley scattering. A temperature dependence study could shine light on the mechanisms at play.

### 5.1.3 Effect of the tip on the excitonic dynamics.

We have seen that depending on the tip-distance separation, we were able to induce and suppress the luminescence from trions and localized defects. It would be interesting to investigate this effect in more detail and understand to which extent we can control the excitonic dynamics. For instance, we could imagine generating local strain in the monolayer and use it to localize excitons. Moreover, since the tip is bound to exert large strain gradients at the nm scale, it could have a considerable impact on slightly decoupled vdW heterostructures.

### 5.1.4 Investigations of the STS bandgap

We have shown that the discrepancy between the binding energies measured using STS and optical spectroscopies is not linked to the non-locality of PL. A detailed investigation on the onset of the gap using variable-height STS could give supplementary insights. In our investigations, we observed a peculiar phenomenon when measuring the differential

conductance spectra of the $MoSe_2$/FLG heterostructure. dI/dV spectra acquired at different points of the surface were characterized by a series of in-gap states below the Fermi level of the TMD. Figure 5.2 shows two dI/dV spectra acquired at different tip-sample separations on the surface of the heterostructure. The peaks present Gaussian profiles and have typical widths of 40 mV. Moreover, their resonances shift towards lower energies when the tip approaches the surface.

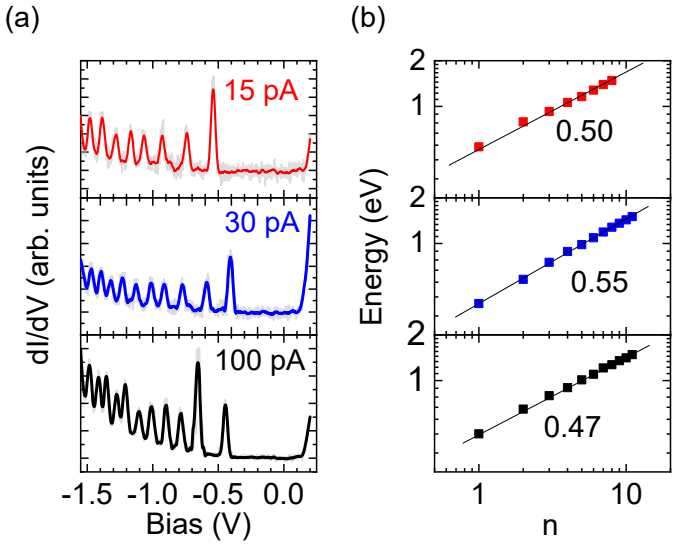


Figure 5.2: **Tip-induced gap states** (a)Differential conductance spectra acquired with an current setpoint of 15 pA (top), 30 pA (middle) and 100 pA (bottom). (b) Energy position of the peaks in the spectra shown in (a) as a function of the quantum number N.

We observe this behavior almost everywhere in the sample, and no correlation between the imaging conditions, the STML, and the apparition of these peaks was observed. Moreover, there is an absence of such resonances at positive bias. Following these observations, we decided to investigate the dependence of these resonances on the tip-sample distance. We perform measurements varying either the initial current setpoint or the size of the sampled bias range in order to change the tip-sample separation. Figure 5.2a shows three sets of dI/dV spectra recorded on the same spot and at different current setpoints. At higher currents (closer to the surface), more resonances appear within the same energy window. Moreover, we observe that the spacing between the peaks is not constant. Figure 5.2b shows the position of the peaks as a function of the principal quantum number N in a logarithmic scale. Indeed, we observe that the series of peaks follow a power law of the form $N^{0.5}$. This is verified for all tip heights sampled during our measurement. Similar observations have been reported in the context of Landau levels in monolayer graphene and graphite in the presence of a magnetic field [182, 183]. However, this is scenario is unlikely in our case due to our sample's composition (FLG) and the absence of the resonances at positive bias as well as at the Dirac point. Instead, these levels may arise from tip-induced states in the TMD as briefly discussed in section 1.8. Moreover, we observe

tunability of the position of these resonances with high degrees of reproducibility. Figure 5.3 shows the energy position of the peaks as a function of the tip-sample distance.

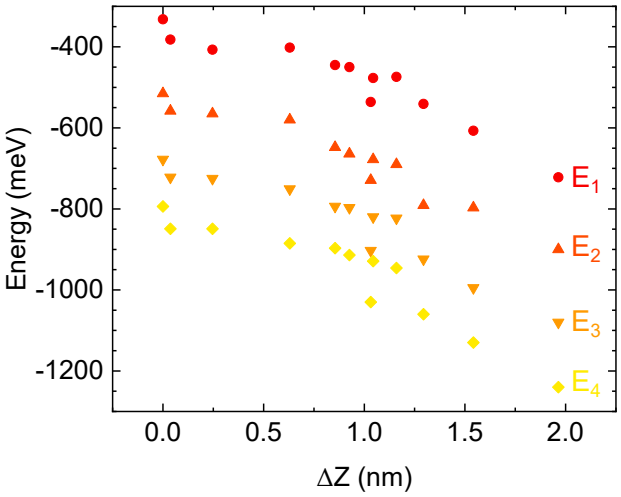


Figure 5.3: **Distance dependence** Distance dependence study on the resonances position.

### 5.1.5 Investigating dark TMDs

We can also investigate dark TMDs using STML. The emission spectra of W-based TMDs are composed of a manifold of peaks arising from different excitonic quasiparticles, including dark excitons. It could be interesting to address them with atomic resolution. We have started some preliminary studies on W-based TMDs. Figure 5.4a shows an optical image of a sample consisting of a monolayer of $WS_2$ deposited onto a thin Au(111)/mica substrate. This sample was fabricated using the dry transfer method and annealed at 200°C during 6h. In contrast to the previous sample, the TMD is directly in contact with the Au substrate. As a result, large areas of the sample are composed of bubbles and foldings. A constant current STM image of a relatively flat area is shown in figure 5.4b. The folding in the image suggests a poorer quality of the interface. Figure 5.4c shows a PL (black) and an STM-L (blue) spectrum taken on this area. The PL spectrum is characterized by a small resonance at 2.10 eV and a large and broad peak located 30 meV below. The former can be assigned to the recombination of the neutral exciton $X^0$. The latter stems from a combined contribution of different excitonic particles. Indeed, we have seen that the low temperature luminescence of $WS_2$ is composed of a manifold of peaks arising from different excitonic species such as trions ($X^*$), dark excitons ($X^D$), biexcitons ($XX$) among others. In non-capped samples, these resonances merge due to inhomogeneous broadening. This gives rise to the broad peak below the $X^0$ line.

However, the STM-L spectrum displays much sharper and smoother peaks due to the local nature of the excitation. Figure 5.4d shows a close-up of the STM-L spectrum

where one can identify three peaks. Comparing with reports on hBN-capped samples (ref), we tentatively assign these transitions to a screened $X^0$ (2.050 eV), a spin-forbidden dark exciton $X^D$ (1.989 eV), and a localized exciton $X^L$(1.968 eV). The massive redshift is likely due to a combination of different effects such as the presence of the tip, the proximity of the folding, and the coupling with the substrate below. The overall shape of the spectrum remains constant all over the studied region. Surprisingly, we observe peaks as sharp as 1 meV which is comparable to what has been reported in state-of-the-art hBN-capped $WS_2$ monolayers in PL experiments. We rule out the presence of multi-excitonic complexes since the currents employed in these measurements are below 1 nA. The presence of $X^D$ does not come as a surprise since this transition is expected to be efficiently excited in STM-L. This is because $X^D$ has a dipole that is aligned perpendicular to the layer and, therefore, can couple more efficiently with the tunneling electrons and tip-induced plasmons. Figure 5.4e shows a differential conductance spectrum taken on the same area as the STM-L. We observe an electronic bandgap of $E_G \sim 3$ eV. This gives rise to an estimated local binding energy close to $E_b \sim 1$ eV. However, this massive value probably comes from an overestimation of the bandgap. Notice the instability of the STM measurements and the total absence of atomic resolution. More detailed measurements in clean areas are needed to estimate the binding energy accurately. However, these results ultimately show that STM-L can be obtained in dark TMDs as well. This opens the door for investigations into the physics of more complex excitonic particles.

### 5.1.6 Molecules on TMD

We can also investigate the role of adsorbates in the excitonic dynamics of TMDs. We have seen that adsorbates in the substrate can act as traps for excitons and induce photodoping of the heterostructure. However, there could be situations in which these molecules undergo energy transfer with excitons in the TMD as well. We could explore how this energy transfer changes depending on the difference between the energy gap of the molecule and the bandgap of the TMD. Beyond this, TMDs can be used as a non-ionic decoupling layer for the molecules ( Figure 5.5a). Our techniques provide the perfect tool to investigate molecule/TMD hybrid heterostructures with the necessary spatial resolution. Along these lines, we deposited $H_2Pc$ molecules onto 1L- and 3L-$WS_2$. These molecules possess a $C_2$ symmetry due to the presence of two hydrogen atoms along with one of the molecular axis (figure 5.5b). The STML spectra on these molecules are then defined by two perpendicular dipoles oriented in-plane, denoted $Q_x$ and $Q_y$. $Q_x$ corresponds to the dipole aligned with the hydrogen axis. We were able to excite both $Q_x$ and $Q_y$ in the 3L- and 1L- domains (figure 5.5c), and perhaps more interestingly, we were able to simultaneously observe luminescence from $WS_2$ corresponding to the peak we tentatively assign in the previous example to the dark exciton. This offers a whole new playground

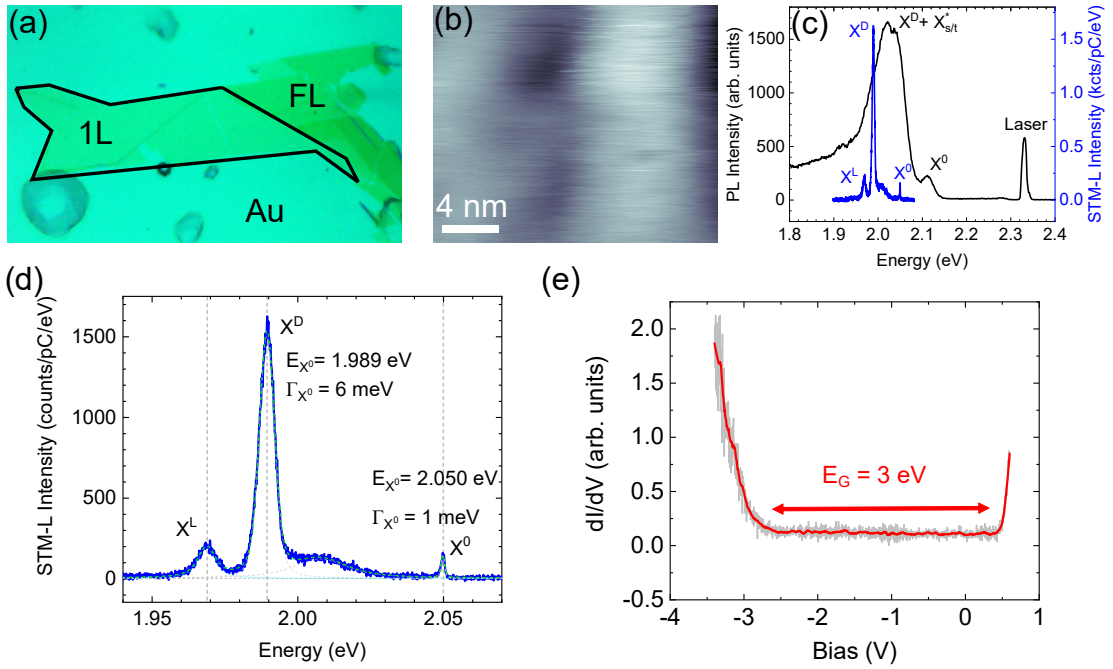


Figure 5.4: **STM-L of monolayer $WS_2$.**(a) Optical image of a monolayer of $WS_2$ deposited on top of a thin Au film. (b) STM image of a locally flat area in the vicinity of a folding. The acquisition parameters for the image are -2.6 V and 7 pA. (c) PL and STM-L spectra recorded on the area shown in (b). The PL spectrum was recorded under a CW excitation of 532 nm wavelength. The STM-L spectrum was acquired under a bias of -3.4 V and a current setpoint of 17 pA. (d) Close-up of the STM-L spectrum (blue). Each resonance was fitted using a Voigt profile. The resulting fits are shown in dashed gray lines for individual peaks and a dashed green line for the cumulative fit. (e) Differential conductance spectrum was taken on the same area as the STM-L. An electronic bandgap of 3 eV can be determined.

where we can investigate energy transfer between 0D and 2D systems.

### 5.1.7 Interlayer excitons and Moiré excitons

Interlayer excitons arise when the electron and the hole are spatially localized in different layers (figure 5.6). These excitons are known to exhibit longer lifetimes than their intralayer counterparts. Moreover, they possess dipoles oriented perpendicular to the plane of the heterostructure. This makes them ideal candidates to investigate using STML since this technique is expected to be optimal for dipoles aligned along the STM junction. Using the transferring techniques that we have described in chapter 2, one can build virtually any combination of 2D layers. We could think of engineering the local landscape through Moiré patterns and investigate its effect on the dynamics of both intra- and interlayer excitons as well as other more exotic quasiparticles.

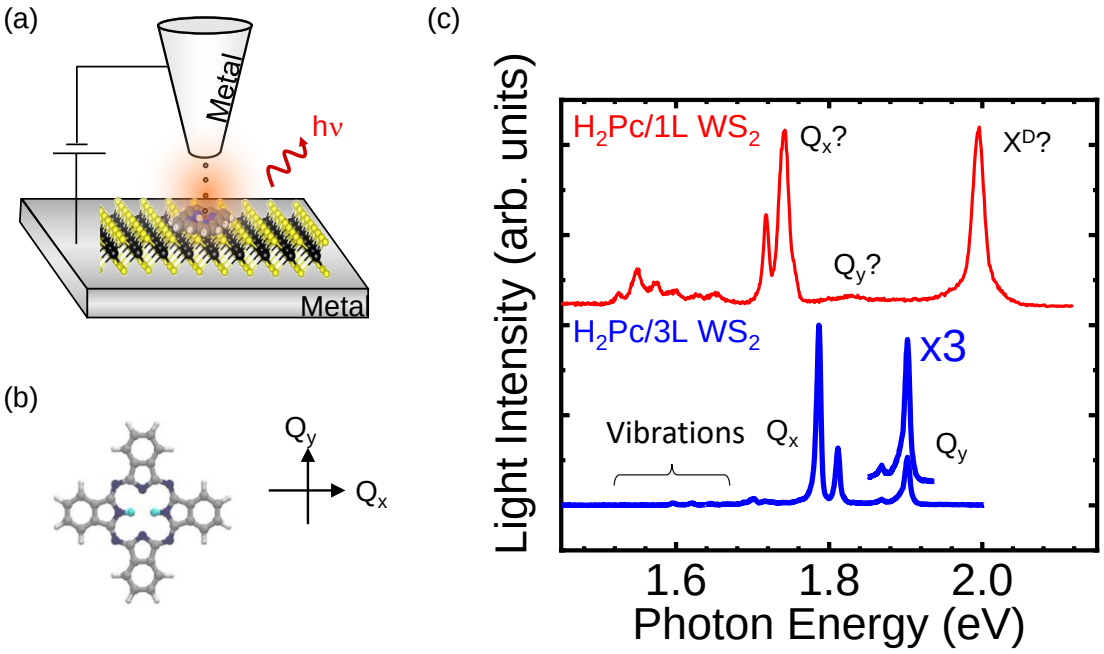


Figure 5.5: **$H_2Pc$ on $WS_2$.** (a) Scheme showing an $H_2Pc$ molecule deposited on top of monolayer TMD. The luminescence is then induced using the STM tip.(b) Graphic representation of the molecule. (c) STML spectra acquiresd on $H_2Pc$ when its deposited onto a 3L of $WS_2$ (blue) and on a 1L of $WS_2$ (red).

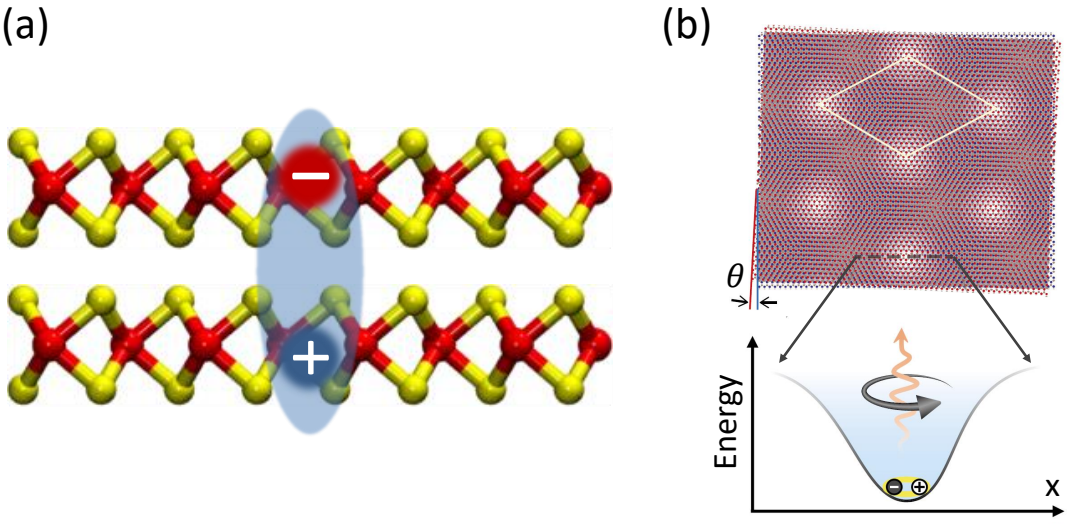


Figure 5.6: (a) Scheme illustrating an interlayer exciton. The electron and the hole are spatially separated in two different layers. (b) Scheme illustrating Moiré trapped excitons. Figure extracted from [184]

### 5.1.8 Single photon sources in vdW heterostructures

A natural follow-up to our work would be to address single-photon sources present in monolayer TMDs. Now that one has a technique with sufficient resolution to do so.

Appendix A

# Bardeen Formalism for the tunneling current

In this appendix, I will present the main points in Bardeen's formalism.

## A.1 Tunneling current

In this section, I will summarize the approach to model the tunneling current between two electrodes. The first work was done by John Bardeen in 1961 [137] following the experimental work of Giaever [138] regarding tunneling between two superconductors separated by a thin oxide film. Bardeen set the theoretical basis for the development of the theory behind tunneling current by describing it in terms of probability of transfer.

### A.1.1 Bardeen's formalism

The idea behind Bardeen's formalism is to model an electron in a tunneling junction. The tunneling junction consists of a thin oxide layer that separates two metal electrodes. Note that this situation is analogous to an STM junction. The tip and the sample being the electrodes and the vacuum in between acting as the insulator. To make the analogy clearer I am going to call electrode A "tip" and electrode B "sample" (see figure A.1a).

Let us consider now the situation where both electrodes are separated by a large distance d. At the surface of the electrode, the electron encounters a potential barrier that prevents it from escaping the surface. Notice that the problem can be reduced to a 1D problem since the potential is essentially "felt" along one dimension. In this case, Schrodinger's equation for an electron at the tip can be expressed as:

$$i\hbar\frac{\partial\Psi(z,t)}{\partial t} = \left[-\frac{\hbar^2}{2m}\frac{\partial^2}{\partial z^2} + V_T(z)\right]\Psi(z,t) \tag{A.1}$$

Where $V(z)$ is the potential at the surface of the electrode. Since the potential does not depend on time, we can separate the spatial and the time dependent parts of the wavefunction. We can therefore express the eigen-wavefunctions of the electron in the tip as:

$$\Psi^T(z,t) = \sum_n c_n\psi_n^T(z)e^{-\frac{i}{\hbar}E_nt} \tag{A.2}$$

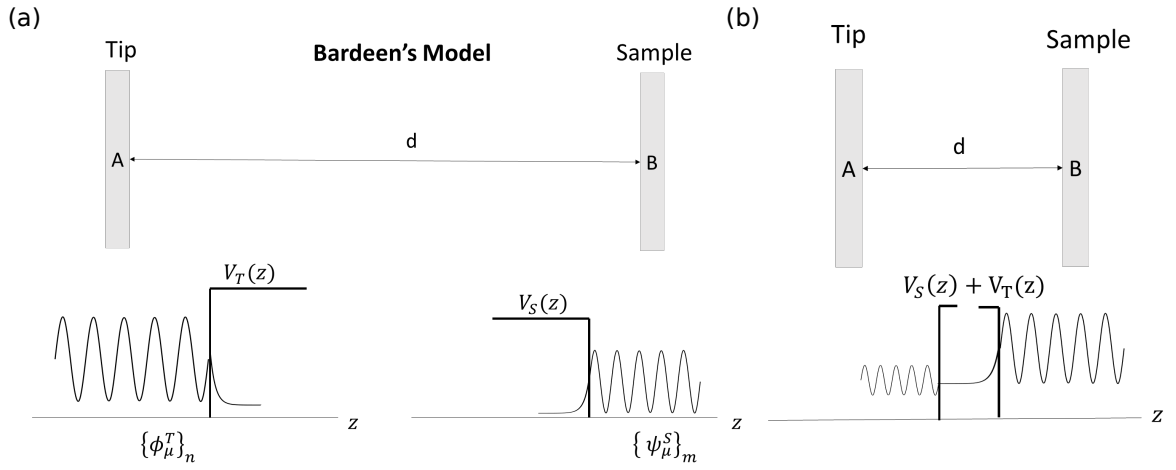


Figure A.1: Bardeen's model for a tunneling junction. (a) Two electrodes A and B separated by a large distance "d". An electron's wave function has an exponentially decaying solution near the surface of the electrode. (b) If the distance d between the electrodes is small enough, there is a non-negligible probability (which depends on the transfer matrix $M_{\mu\nu}$) for the electron to tunnel into the other electrode.

where $\psi_n^T(z)$ is the n-th eigenfunction of the equation with eigenvalue $E_n$. Each one of the eigen-wavefunctions $\psi_n^T(z)$ can be calculated by solving the stationary Schrodinger's equation:

$$\left[-\frac{\hbar^2}{2m}\frac{\partial^2}{\partial z^2} + V_T(z)\right]\psi_n^T(z) = E_n\psi_n^T(z,t) \tag{A.3}$$

Similarly, for an electron in the sample electrode we can write:

$$\Phi^S(z,t) = \sum_m c_m\phi_m^S(z)e^{-\frac{i}{\hbar}E_m t} \tag{A.4}$$

where $\phi_m^S(z)$ is the eigen-wavefunction of the electron at the sample and it satisfies the equation:

$$\left[-\frac{\hbar^2}{2m}\frac{\partial^2}{\partial z^2} + V_S(z)\right]\phi_m^S(z) = E_m\phi_m^S(z,t) \tag{A.5}$$

If we consider for a moment that the potential at the tip is a constant potential barrier such that $V_T(z) = V_0\Theta(z - z_T) > E$ where $\Theta(z - z_T)$ is Heaviside's step-function we can write:

$$\begin{cases} -\frac{\hbar^2}{2m}\frac{\partial^2}{\partial z^2}\psi_n(z) = E_n\psi_n(z,t) & z \leq z_T \\ \left[-\frac{\hbar^2}{2m}\frac{\partial^2}{\partial z^2} + V_0\right]\psi_n(z) = E_n\psi_n(z,t) & z \geq z_T \end{cases}$$

The solution in the barrier region is given by an exponentially decaying function of the form:

$$\psi_n^T(z) = \psi_n^T(z_T)e^{-kz} \tag{A.6}$$

where $k = \sqrt{\frac{(V_0-E)2m}{\hbar^2}}$. A completely analogous development can be applied to an electrode in the sample. Let us consider now the situation where an electron is in the sample in a state $\psi_\sigma^S(z)$ and the tip approaches adiabatically. At first, the isolated systems, tip, and sample have each their own basis of eigenfunctions $\psi_\sigma^S(z)$ and $\phi_\mu^T(z)$ respectively. As they get closer (in the order of the decay length $\lambda = 1/k$ of the exponential) they get coupled and this coupling mixes the states of the isolated systems (figure A.1b). Meaning that $\psi_\sigma^S(z)$ and $\phi_\mu^T(z)$ are no longer stationary solutions of the coupled system whose equation is given by:

$$i\hbar\frac{\partial\Psi(z,t)}{\partial t} = \left[-\frac{\hbar^2}{2m}\frac{\partial^2}{\partial z^2} + V_T(z) + V_S(z)\right]\Psi(z,t) \tag{A.7}$$

In other words, because of the coupling, there is a non-zero probability for the electron in the sample to tunnel into the tip (figure A.1b) [1]. We assume that the wavefunction $\Psi(z,t)$ of an electron in the coupled system can be written as a linear combination of the solutions for the isolated systems[2] such that:

$$\Psi(z,t) = \sum_\sigma a_\sigma(t)\phi_\sigma^S(z)e^{-i\frac{E_\sigma t}{\hbar}} + \sum_\mu b_\mu(t)\psi_\mu^T(z)e^{-i\frac{E_\mu t}{\hbar}} \tag{A.8}$$

To simplify the calculation, we make three assumptions:

1. The electron on the sample electrode is prepared in the state $\phi_\sigma^S(z)$ and has been for a long time. This means that

$$\forall\mu\ ,\ b_\mu(t\leq 0) = 0$$

$$\forall\sigma'\ ,\ a_{\sigma'}(t\leq 0) = \delta_{\sigma\sigma'}$$

2. At t=0 we approach the tip adiabatically to the sample. This can be modelled by introducing the potential of the tip as an slowly growing potential $V_T(t) = V_T e^{t\frac{0^+}{\hbar}}$ where $V_T$ is a constant. The latter allows means that the coefficient $a_\sigma(t)$ does not changes appreciably in time: $\frac{d}{dt}a_\sigma(t) \approx 0$ and therefore $a_\sigma(t) \approx a_\sigma(0) = a_\sigma(-\infty)$

3. In his original derivation, Bardeen assumes that the isolated wavefunctions of the tip and the sample are approximately orthogonal $\left\langle\psi_\mu^T\middle|\phi_\sigma^S\right\rangle \approx 0$. This assumption is key as it makes our expression for the wave-function self consistent [3].

[1] Completely analogous to an electromagnetic wave undergoing total internal reflection. If one approaches a second medium near the surface of reflection, the decaying exponential solution can propagate in the medium.

[2] This is not the case since we have not proven that this constitutes a C.S.C.O. ($\phi_\sigma^S(z)$ and $\phi_\mu^T(z)$ are solutions of $T+V_S$ and $T+V_T$ and not from $T+V_S+V_T$).

[3] Notice that this means the tip has a negligible effect on the sample.

Introducing equation A.8 into A.7 and projecting onto a tip state $\left\langle \psi_\mu^T \right|$ we can write:

$$i\hbar \frac{d}{dt} b_\mu(t) = \left\langle \psi_\mu^T \right| V_T(t) \left| \phi_\sigma^S \right\rangle e^{-\frac{i}{\hbar}(E_\sigma^S - E_\mu^T)t} + \sum_{\lambda=1}^{\infty} b_\lambda \left\langle \psi_\mu^T \right| V_S \left| \phi_\lambda^S \right\rangle e^{-\frac{i}{\hbar}(E_\sigma^S - E_\mu^T)t} \tag{A.9}$$

This equation can be solved iterative, in this derivation we will only consider first order terms and develop it as a time-dependent perturbation[4], this allows us to rewrite it in the form:

$$i\hbar \frac{d}{dt} b_\mu(t) = M_{\mu\sigma} e^{-\frac{i}{\hbar}(E_\sigma^S - E_\mu^T + i0^+)t} \tag{A.10}$$

where

$$M_{\mu\sigma} = \left\langle \psi_\mu^T \right| V_T \left| \phi_\sigma^S \right\rangle \tag{A.11}$$

$M_{\mu\sigma}$ represents then the probability to transition from $\left|\phi_\sigma^S\right\rangle$ to $\left|\psi_\mu^T\right\rangle$. To calculate the coefficient $b_\mu$, it suffices to integrate over time equation A.10:

$$b_\mu(t) = M_{\mu\sigma} \frac{e^{-\frac{i}{\hbar}(E_\sigma^S - E_\mu^T + i0^+)t}}{E_\sigma^S - E_\mu^T + i0^+} \tag{A.12}$$

The probability to tunnel from the sample to the tip is given by $|b_\mu(t)|^2$:

$$|b_\mu(t)|^2 = |M_{\mu\sigma}|^2 \frac{e^{20^+ \frac{t}{\hbar}}}{(E_\sigma^S - E_\mu^T)^2 + (0^+)^2} \tag{A.13}$$

From this expression and using the fact that

$$\lim_{\epsilon \to 0^+} \frac{\epsilon}{x^2 + \epsilon^2} = \pi \delta(x)$$

we can compute the transition probability per unit time for the electron:

$$\Gamma_{\mu\sigma} = \frac{2\pi}{\hbar} \delta(E_\mu^T - E_\sigma^S) |M_{\mu\sigma}|^2 \tag{A.14}$$

This is the well-known Fermi's Golden Rule for elastic processes (assured by the delta function). This expression represents the rate of transition from a state on the sample to one on the tip (This formalism remains completely analogous for the case in which the electron tunnels from the tip to the sample). To complete this calculation, we must take into account the fact that there is a continuum of states in the sample and in the tip, each state with its own occupation probability. In other words, an electron can tunnel only if it comes from an occupied state on the sample and goes to an unoccupied state on the tip (and vice-versa). This means we should add the probability distribution associated with tip and sample occupation numbers. This is done by introducing Fermi-Dirac distribution into the expression for the rate:

[4]We neglect therefore the second term on the right.

$$\Gamma_{\mu\sigma}^{S\to T} = \frac{2\pi}{\hbar} \underbrace{\delta(E_\mu^T - E_\sigma^S)}_{\text{elastic tunneling condition}} |M_{\mu\sigma}|^2 \times \overbrace{f(E_\sigma^S + eV)}^{\text{Occupied sample states}} \times \underbrace{(1 - f(E_\mu^T))}_{\text{Unoccupied tip states}}$$

Notice that we have also added the fact that there is a voltage V applied between the tip and the sample. By symmetry

$$\Gamma_{\mu\sigma}^{T\to S} = \frac{2\pi}{\hbar} \underbrace{\delta(E_\sigma^S - E_\mu^T)}_{\text{elastic tunneling condition}} |M_{\mu\sigma}|^2 \times \overbrace{f(E_\mu^T)}^{\text{Occupied tip states}} \times \underbrace{(1 - f(E_\sigma^S + eV))}_{\text{Unoccupied sample states}}$$

These two expressions represent the electron transfer rate from the tip to the sample and vice-versa. To construct a complete expression for the tunneling current, we need to sum over all possible contributions:

- States of the tip.
- States of the sample.
- Spin: Every energy state can be filled with two electrons with a different spin.

With these in mind, we can write:

$$I = \underbrace{2 \times e}_{\text{Accounts for charge and spin}} \times \overbrace{(\sum_{\mu,\sigma} \Gamma_{\mu\sigma}^{S\to T}}^{\text{Current from sample to tip}} - \overbrace{\sum_{\mu,\sigma} \Gamma_{\mu\sigma}^{T\to S})}^{\text{Current from tip to sample}}$$

where we have assumed that $|M_{\mu\sigma}|^2 = |M_{\sigma\mu}|^2$. Substituting each expression for the transfer rates we obtain:

$$I = \frac{4\pi e}{\hbar} \sum_{\mu,\sigma} \delta(E_\sigma^S - E_\mu^T) |M_{\mu\sigma}|^2 (f(E_\sigma^S + eV) - f(E_\mu^T)) \tag{A.15}$$

We can identify three main terms in this expression; each one of them accounting for a different part of the tunneling process. The first term with the delta assures conservation of energy and it is the main reason why this type of tunneling is called elastic. The third term regarding the Fermi-Dirac distribution accounts for the availability of states: you can only tunnel from an occupied to an unoccupied state. The middle term is perhaps the richer one since this term is related to the probability of transferring an electron and it depends on the coupling between tip and sample states through the potential $V_T(z,t)$. Indeed, we can simplify this a bit further this expression by making the relevant approximations of our measuring conditions: low temperatures and low bias.

- First let us introduce an integral into the summation by using the fact that:

$$\delta(E_\sigma^S - E_\mu^T) = \iint dE dE' \delta(E - E_\sigma^S) \delta(E' - E_\mu^T) \delta(E - E')$$

This allows us to write:

$$I = \frac{4\pi e}{\hbar} \sum_{\mu,\sigma} \iint dE dE' \delta(E - E_\sigma^S)\delta(E' - E_\mu^T)\delta(E - E')|M_{\mu\sigma}|^2 (f(E_\sigma^S + eV) - f(E_\mu^T)) \tag{A.16}$$

We can simplify further by integrating over $E'$:

$$I = \frac{4\pi e}{\hbar} \sum_{\mu,\sigma} \int dE \delta(E - E_\sigma^S)\delta(E - E_\mu^T)|M_{\mu\sigma}|^2 (f(E_\sigma^S + eV) - f(E_\mu^T)) \tag{A.17}$$

- At low temperatures we can consider the fermi-Dirac distribution as a Heaviside function.

$$(f(E + eV) - f(E)) = \frac{1}{e^{\frac{E-eV}{kT}} + 1} - \frac{1}{e^{\frac{E}{kT}} + 1} \approx \Theta(E + eV) - \Theta(E)$$

this allows us to write:

$$I = \frac{4\pi e}{\hbar} \sum_{\mu,\sigma} \int_{E_F^T}^{E_F^T + eV} dE \delta(E - E_\sigma^S)\delta(E - E_\mu^T)|M_{\mu\sigma}|^2 \tag{A.18}$$

rewriting this expression in terms of the fermi energy of the sample we get:

$$I = \frac{4\pi e}{\hbar} \sum_{\mu,\sigma} \int_0^{eV} d\epsilon \delta(\epsilon + E_F^S - E_\sigma^S)\delta(\epsilon + E_F^S - E_\mu^T)|M_{\mu\sigma}|^2 \tag{A.19}$$

- Finally if we suppose the applied bias is small we can write:

$$I \approx \frac{4\pi}{\hbar} e^2 V \sum_{\mu,\sigma} \delta(E_\sigma^S - E_F^S - eV)\delta(E_\mu^T - E_F^T)|M_{\mu\sigma}|^2 \tag{A.20}$$

This expression for the tunneling current however is still incomplete. The only element that remains to be calculated is the tunneling matrix $M_{\mu\sigma}$. This is not so trivial as in general, this can depend on the geometry of the tip and its electronic structure. This is where Tersoff and Haman's work [109] made a fundamental step further into the formalism to model an STM junction. They show that if the electronic structure of the tip is approximated to a sphere (s-orbitals), the matrix element can be considered as a constant. This has been done under the supposition that only the outermost states of the tip overlap with the sample states, however, this is a questionable assumption[5]. I will now present a summary of Tersoff and Haman's work.

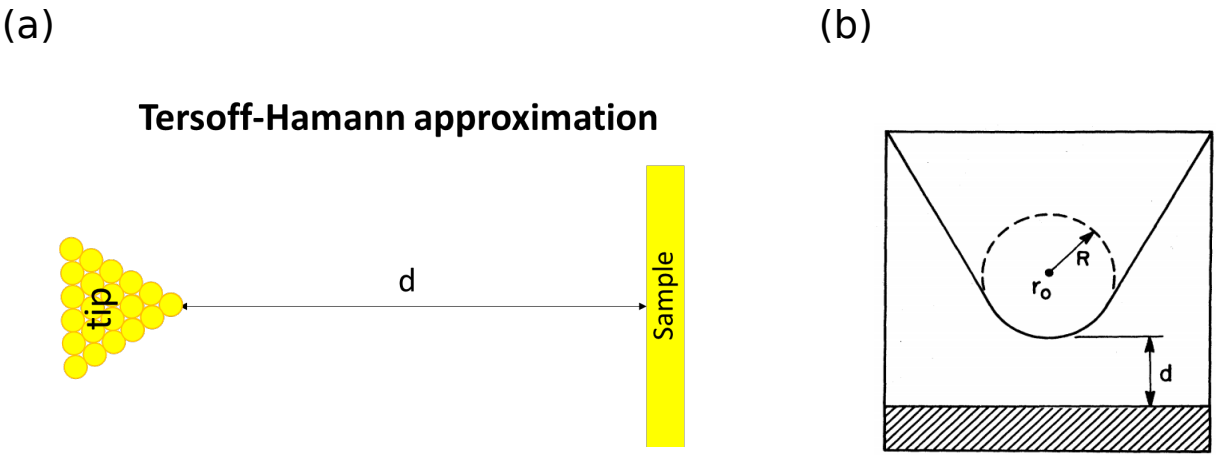


Figure A.2: (a) Instead of a flat electrode, we consider now the shape of the tip. (b) Tersoff-Hamann's approximation supposes that the tip electronic structure is well represented by spherical states [109].

### Tersoff and Hamann's approximation

To understand Tersoff and Hamann's approach, let us begin with a toy model first of an ideal probe. Consider a simple case where the tip is a point-probe at position $\vec{r}_0$. If the probe can be modeled by an extremely localized function around a position $\vec{r}_0$, then the matrix element will be proportional to the value of the wavefunction of the sample state

$$M_{\mu\sigma} \propto \psi_\sigma^S(\vec{r}_0)$$

and therefore the tunneling current can be expressed like this:

$$I \propto \sum_{\mu\sigma} \left|\psi_\sigma^S(\vec{r}_0)\right|^2 \delta(E_\sigma^S - E_F^S - eV)\delta(E_\mu^T - E_F^T) \propto DoS(E_F^S + eV)DoS(E_F^T)$$

In this toy model, we can see that the tunneling current is proportional to the density of states $DoS(E) = \sum_\mu \delta(E_\mu - E)$. This result, despite its triviality, tells us that if the influence of the probe is negligible, an STM image represents contour plots of the density of states of the sample. This simple interpretation motivates us to look for the real effect of the tip on Bardeen's transfer matrix. To do that, let's go back to the expression of the tunneling matrix and use Schrödinger's equation:

$$M_{\mu\sigma} = \left\langle \psi_\mu^T \right| V_T \left| \phi_\sigma^S \right\rangle = \int d^3\vec{r}\, \psi_\mu^{T*} V_T \phi_\sigma^S \tag{A.21}$$

[5]In fact, Chen proved that this is not the case and other states should be added to fully explain corrugation in STM-images [139]

$$= \int d^3\vec{r}\phi_\sigma^S \left( E_\mu^T + \frac{\hbar^2}{2m}\frac{\partial^2}{\partial z^2} \right) \psi_\mu^{T*}$$

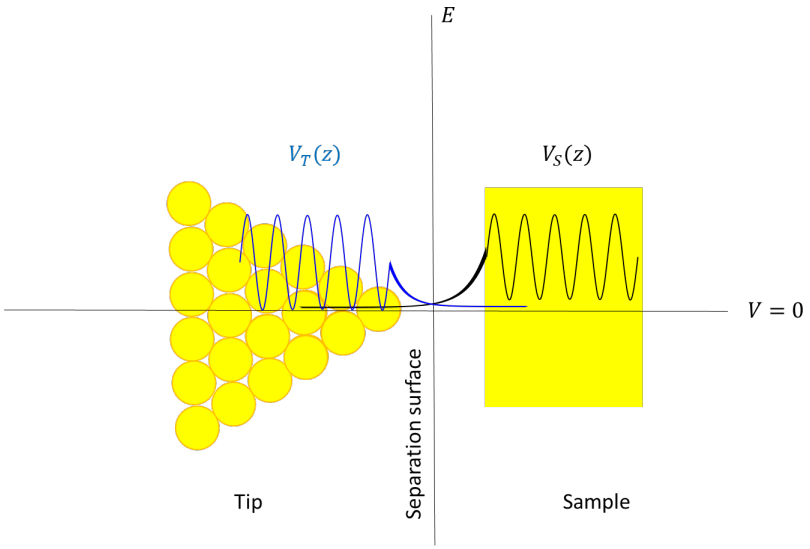


Figure A.3: The separation surface is defined as the surface from where the potential of the tip (sample respectively) does not affect the sample (tip) side. In other words, $V_S(z)V_T(z) = 0 \ \forall z$.

Two important steps are to be taken now:

- Energy conservation imposes $E_\mu^T = E_\sigma^S$.
- In the formalism developed before we know that:

$$-\frac{\hbar^2}{2m}\frac{\partial^2\phi_\sigma^S}{\partial z^2} + U_S\phi_\sigma^S = E_\sigma^S\phi_\sigma^S$$

  It is here that Bardeen introduces the notion of a separation surface. It is defined as a surface from where we can neglect the influence of the sample (or tip) potential on the tip (sample) side [6]. Therefore on the tip side $U_S = 0$.

This allows us to write:

$$M_{\mu\sigma} = \int_{ontip} d^3\vec{r}\frac{\hbar^2}{2m}\left( -\psi_\mu^{T*}\frac{\partial^2\phi_\sigma^S}{\partial z^2} + \phi_\sigma^S\frac{\partial^2\psi_\mu^{T*}}{\partial z^2} \right) \tag{A.22}$$

$$M_{\mu\sigma} = \frac{\hbar^2}{2m}\int dxdy\left( \phi_\sigma^S\frac{\partial\psi_\mu^{T*}}{\partial z} - \psi_\mu^{T*}\frac{\partial\phi_\sigma^S}{\partial z} \right) \tag{A.23}$$

where the integral is taken on any surface in the vacuum barrier. This expression tells us that we can relate the transfer matrix to probability currents. This is an important

[6] This is equivalent to say that $V_S V_T = 0$ in any point of space.

result that will be crucial when applying Tersoff-Hamann's approximation. To model the states of the surface they propose the following:

- They expand the surface wavefunctions as a series:

$$\psi_\sigma^S = \frac{1}{\sqrt{\Omega}} \sum_G a_G e^{(\kappa^2+|k_G|^2)^{\frac{1}{2}} z} e^{i\vec{k}_G \cdot \vec{r_S}} \tag{A.24}$$

  In this expression $\kappa = \frac{\sqrt{2m\phi}}{\hbar}$ is the minimum decay length of the wavefunction in a vacuum, $\phi$ is the crystal's work function, $\Omega$ is the volume, and $\vec{k}_G = \vec{k} - \vec{G}$ is a vector that relates the surface's Bloch vector of the state and a reciprocal lattice vector.

- For the tip, they assume it to have spherical shape (figure A.2):

$$\phi_\mu^T = \frac{1}{\sqrt{\Omega_t}} c_t \frac{\kappa R e^{\kappa R}}{\kappa |\vec{r} - \vec{r}_0|} e^{-\kappa|\vec{r}-\vec{r}_0|} \tag{A.25}$$

  $\Omega_t$ is the probed volume, $c_t$ is a normalization factor and the rest of the parameters are defined as above. Notice that they assumed the same workfunction for the tip and for the sample.

We proceed to develop the the tip's wavefunction as a series in the same manner as for the surface's wavefunction and we introduce it into equation (A.23). The resulting expression for the tunneling matrix can be summarized as follows:

$$M_{\sigma\mu} = (constant) \times \psi_\sigma^S(\vec{r}_0) \tag{A.26}$$

which means that in this approximation we can consider the tunneling matrix as a constant (equation A.20) and therefore:

$$I = \frac{4\pi e}{\hbar} |M|^2 \int_0^{eV} dE_F DoS^S(E_F - eV) DoS^T(E_F) \tag{A.27}$$

This means that for a spherical tip, we can interpret the STM current signal as a convolution of the density of states of the tip and sample at a particular energy (given by the bias) and at the probe position. In other words, we are sensitive to the **Local Density of States** (LDOS).

### WKB approximation

The final element towards a more complete theory for STM is to consider the potential barrier. Indeed, the matrix element $M = \left\langle \psi_\mu^T \right| V_T(z) \left| \phi_\sigma^S \right\rangle$ has three main ingredients:

1. The surface electronic structure encrypted in the term $\left|\phi_\sigma^S\right\rangle$ (Treated exactly).

2. The tip electronic structure encrypted in the term $\left\langle \psi_\mu^T \right|$ (Tersoff-Hamann approximation).

3. The shape of the potential barrier $V_T(z)$.

To take this into account one can use the WKB (Wentzel-Kramers-Brillouin) approximation. For a slowly varying potential in space, the corresponding wavefunction should also slowly vary in space relative to the constant potential case. If we model the tunnel barrier using the WKB approximation, we obtain the following expression for the tunneling current:

$$I_t \propto \int_{-\infty}^{\infty} dE DoS^T(E - eV) DoS^S(E)(f(E - eV) - f(E))T(z, E, V) \tag{A.28}$$

where T(z, E, V) is the transmission coefficient which encompasses the dependence on the shape of the barrier. At low temperature, we can reduce this expression to:

$$I_t \propto \int_0^{eV} DoS^S(E)T(z, E, V)dE \tag{A.29}$$

For a barrier with a trapezoidal shape, we can compute the transmission coefficient using WKB approximation:

$$T(z, E, V) \propto e^{-2z\sqrt{\frac{2m}{\hbar}(\phi - E + \frac{eV}{2})}} \tag{A.30}$$

This expression means that the transmission sensitively depends on the electron energy. The higher the energy, the higher the probability of tunneling. In the limit of low voltages, the expression A.28 becomes:

$$I_t \propto e^{-2z\sqrt{\frac{2m}{\hbar}(\phi_{eff})}} \tag{A.31}$$

To get an idea of the effect of such coefficient, first, let us rewrite this in terms of a decay constant k: $I_t \propto e^{-kz}$ and perform a small back-of-the-envelope calculation. For silver and gold $\phi_{eff}$ is typically $\approx 5eV$ [140]. With this, we can estimate $k \approx 22.9nm$. This means that for a variation of $\Delta z = \pm 0.1$ nm we get $\frac{I(z+\Delta z)}{I(z)} \propto e^{\mp 2.3}$. This explains the extreme sensitivity of STM.

# Fabrication of samples for STM

As mentioned in the introduction, we tried many different sample architectures during my Ph.D., looking for the perfect trade-off between decoupling the TMD monolayers while preserving conditions on which we can perform STM measurements. In the beginning, we designed two sample architectures fulfilling the aforementioned conditions.

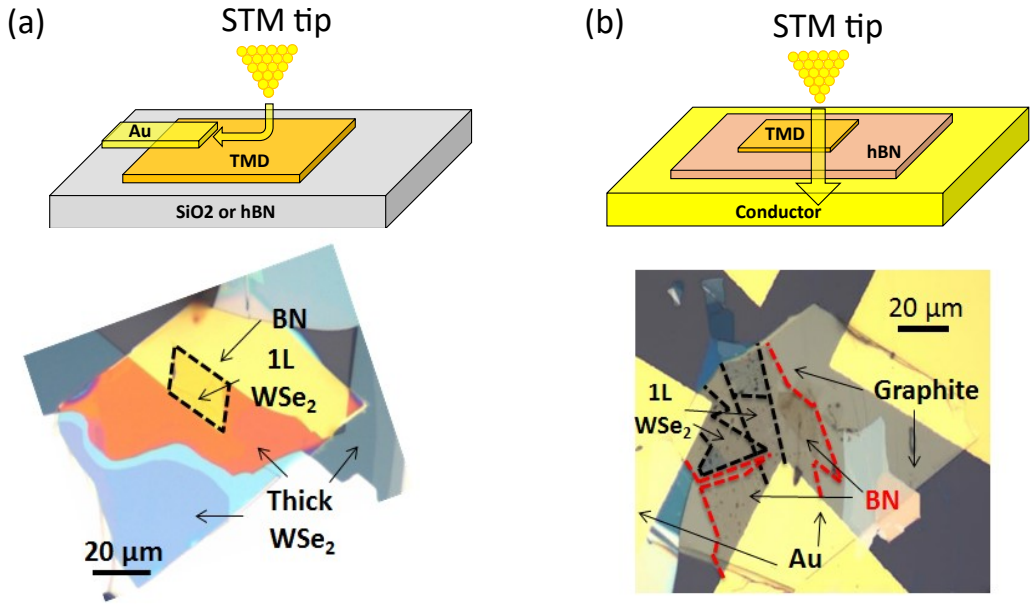


Figure B.1: **STM-compatible samples.** (a) Top: Scheme of a lateral configuration. The current travels along the sample. Bottom: optical image of monolayer $WSe_2$ on hBN. This sample was later contacted with gold as shown in the top scheme. (b) Top: Scheme of a vertical transport configuration. Bottom: Optical image of monolayer $WSe_2$ on graphite with a few layers of hBN as a decoupling element.

## B.1 Lateral contacts

In this case, the TMD is on a non-conductive substrate (hBN or $SiO_2$). Gold contacts are then evaporated onto the TMD. The idea is that when a bias voltage is applied, the generated current will travel along with the TMD towards the contacts (see figure B.1a). To improve the electronic mobility, the choice of substrate is essential. Indeed, it has been shown that inhomogeneities on rough substrates reduce the transport properties of TMDs relative to smoother substrates such as hBN [53].

## B.2 Vertical contacts

In this configuration, the TMD is directly deposited onto a conductive substrate. Few-layer hBN can be used as a spacer to reduce the interaction between the TMD and the metal. In this case, the current passes through the TMD/hBN heterostructure (see figure B.1b). During my Ph.D. I used four different types of substrate:

1. Graphene/Graphite: Graphene and few-layer graphene are known to make excellent contacts for TMD-based devices. Due to their 2D nature, an atomically sharp interface is formed between them, significantly reducing contact resistance. Moreover, it provides a flat substrate that is suitable for STM measurements. Graphene and graphite flakes were exfoliated on $Si/SiO_2$ (90 nm thick), and then a TMD layer was deposited on top. Gold contacts were then evaporated on the graphene/graphite electrodes.

2. Evaporated Au: Au was evaporated on top of a $Si/SiO_2$ (90 nm thick) wafer, and a TMD was exfoliated on top or transferred onto it.

3. Au(111) on Mica: Here, I took commercial gold on mica and deposited my sample on top. Gold on mica presents flatter areas than the evaporated ones.

4. Indium Tin Oxide (ITO): ITO is a semitransparent conductive substrate. The idea to use ITO came from a collaboration with Eric le Moal at ISMO Paris. This collaboration proved to be fruitful as room temperature STM-induced luminescence of $MoSe_2$ monolayers was demonstrated[13].

# Bibliography


[1] K. Novoselov et al., "Electric Field Effect in Atomically Thin Carbon Films", in: Science 306 (2004), pp. 666 –669, ISSN: 0036-8075, DOI: 10.1126/science.1102896, eprint: https://science.sciencemag.org/content/306/5696/666.full.pdf, URL: https://science.sciencemag.org/content/306/5696/666.

[2] C. R. Dean et al., "Boron nitride substrates for high-quality graphene electronics", in: Nature Nanotechnology 5.*10* (Oct. 2010), pp. 722–726, ISSN: 1748-3395, DOI: 10.1038/nnano.2010.172, URL: https://doi.org/10.1038/nnano.2010.172.

[3] A. K. Geim and I. V. Grigorieva, "Van der Waals heterostructures", in: Nature 499.*7459* (July 2013), pp. 419–425, ISSN: 1476-4687, DOI: 10.1038/nature12385, URL: https://doi.org/10.1038/nature12385.

[4] Yuan Cao et al., "Unconventional superconductivity in magic-angle graphene superlattices", in: Nature 556.*7699* (Apr. 2018), pp. 43–50, ISSN: 1476-4687, DOI: 10.1038/nature26160, URL: https://doi.org/10.1038/nature26160.

[5] Jeong Min Park et al., "Tunable strongly coupled superconductivity in magic-angle twisted trilayer graphene", in: Nature 590.*7845* (Feb. 2021), pp. 249–255, ISSN: 1476-4687, DOI: 10.1038/s41586-021-03192-0, URL: https://doi.org/10.1038/s41586-021-03192-0.

[6] "Interlayer excitons and how to trap them", in: Nature Materials 19.*6* (June 2020), pp. 579–579, ISSN: 1476-4660, DOI: 10.1038/s41563-020-0701-0, URL: https://doi.org/10.1038/s41563-020-0701-0.

[7] H Baek et al., "Highly energy-tunable quantum light from moiré-trapped excitons", in: Science advances 6.*37* (2020), eaba8526.

[8] Guillaume Froehlicher, Etienne Lorchat, and Stéphane Berciaud, "Charge Versus Energy Transfer in Atomically Thin Graphene-Transition Metal Dichalcogenide van der Waals Heterostructures", in: Phys. Rev. X 8 (1 Jan. 2018), p. 011007, DOI: 10.1103/PhysRevX.8.011007, URL: https://link.aps.org/doi/10.1103/PhysRevX.8.011007.

[9] Etienne Lorchat et al., "Filtering the photoluminescence spectra of atomically thin semiconductors with graphene", in: Nature Nanotechnology 15.*4* (Apr. 2020), pp. 283–288, ISSN: 1748-3395, DOI: 10.1038/s41565-020-0644-2, URL: https://doi.org/10.1038/s41565-020-0644-2.

[10] Luis Enrique Parra López et al., "Single-and narrow-line photoluminescence in a boron nitride-supported MoSe _2/graphene heterostructure", in: Comptes Rendus. Physique 22.*S4* (2021), pp. 1–12.

[11] Michael C. Chong et al., "Ordinary and Hot Electroluminescence from Single-Molecule Devices: Controlling the Emission Color by Chemical Engineering", in: Nano Letters 16.*10* (2016), PMID: 27652517, pp. 6480–6484, DOI: 10.1021/acs.nanolett.6b02997, eprint: https://doi.org/10.1021/acs.nanolett.6b02997, URL: https://doi.org/10.1021/acs.nanolett.6b02997.

[12] Yang Zhang et al., "Visualizing coherent intermolecular dipole–dipole coupling in real space", in: Nature 531.*7596* (Mar. 2016), pp. 623–627, ISSN: 1476-4687, DOI: 10.1038/nature17428, URL: https://doi.org/10.1038/nature17428.

[13] Delphine Pommier et al., "Scanning Tunneling Microscope-Induced Excitonic Luminescence of a Two-Dimensional Semiconductor", in: Phys. Rev. Lett. 123 (2 July 2019), p. 027402, DOI: 10.1103/PhysRevLett.123.027402, URL: https://link.aps.org/doi/10.1103/PhysRevLett.123.027402.

[14] Ricardo Javier Peña Román et al., "Tunneling-current-induced local excitonic luminescence in p-doped WSe2 monolayers", in: Nanoscale 12 (25 2020), pp. 13460–13470, DOI: 10.1039/D0NR03400B, URL: http://dx.doi.org/10.1039/D0NR03400B.

[15] Renaud Péchou et al., "Plasmonic-Induced Luminescence of MoSe2 Monolayers in a Scanning Tunneling Microscope", in: ACS photonics 7.*11* (2020), pp. 3061–3070.

[16] Nils Krane et al., "Electronic Structure and Luminescence of Quasi-Freestanding MoS2 Nanopatches on Au(111)", in: Nano Letters 16.*8* (2016), PMID: 27459588, pp. 5163–5168, DOI: 10.1021/acs.nanolett.6b02101, eprint: https://doi.org/10.1021/acs.nanolett.6b02101, URL: https://doi.org/10.1021/acs.nanolett.6b02101.

[17] Bruno Schuler et al., "Electrically driven photon emission from individual atomic defects in monolayer WS2", in: Science Advances 6.*38* (2020), DOI: 10.1126/sciadv.abb5988, eprint: https://advances.sciencemag.org/content/6/38/eabb5988.full.pdf, URL: https://advances.sciencemag.org/content/6/38/eabb5988.

[18] Sven Aeschlimann et al., "Direct evidence for efficient ultrafast charge separation in epitaxial WS2/graphene heterostructures", in: Science Advances 6.*20* (2020), DOI: 10.1126/sciadv.aay0761, eprint: https://advances.sciencemag.org/content/6/20/eaay0761.full.pdf, URL: https://advances.sciencemag.org/content/6/20/eaay0761.

[19] C Robert et al., “Exciton radiative lifetime in transition metal dichalcogenide monolayers”, in: Physical Review B 93.*20* (2016), p. 205423.

[20] Archana Raja et al., “Coulomb engineering of the bandgap and excitons in two-dimensional materials”, in: Nature Communications 8.*1* (May 2017), p. 15251, ISSN: 2041-1723, DOI: 10.1038/ncomms15251, URL: https://doi.org/10.1038/ncomms15251.

[21] Samuel Brem et al., “Exciton relaxation cascade in two-dimensional transition metal dichalcogenides”, in: Scientific reports 8.*1* (2018), pp. 1–8.

[22] Cédric Robert et al., “Fine structure and lifetime of dark excitons in transition metal dichalcogenide monolayers”, in: Physical review B 96.*15* (2017), p. 155423.

[23] D Lagarde et al., “Carrier and polarization dynamics in monolayer MoS 2”, in: Physical review letters 112.*4* (2014), p. 047401.

[24] Philipp Nagler et al., “Zeeman splitting and inverted polarization of biexciton emission in monolayer WS 2”, in: Physical review letters 121.*5* (2018), p. 057402.

[25] H. H. Fang et al., “Control of the Exciton Radiative Lifetime in van der Waals Heterostructures”, in: Phys. Rev. Lett. 123 (6 Aug. 2019), p. 067401, DOI: 10.1103/PhysRevLett.123.067401, URL: https://link.aps.org/doi/10.1103/PhysRevLett.123.067401.

[26] Miguel M. Ugeda et al., “Giant bandgap renormalization and excitonic effects in a monolayer transition metal dichalcogenide semiconductor”, in: Nature Materials 13.*12* (Dec. 2014), pp. 1091–1095, ISSN: 1476-4660, DOI: 10.1038/nmat4061, URL: https://doi.org/10.1038/nmat4061.

[27] Akshay Singh et al., “Coherent Electronic Coupling in Atomically Thin $MoSe_2$”, in: Phys. Rev. Lett. 112 (21 May 2014), p. 216804, DOI: 10.1103/PhysRevLett.112.216804, URL: https://link.aps.org/doi/10.1103/PhysRevLett.112.216804.

[28] Jason S. Ross et al., “Electrical control of neutral and charged excitons in a monolayer semiconductor”, in: Nature Communications 4.*1* (Feb. 2013), p. 1474, ISSN: 2041-1723, DOI: 10.1038/ncomms2498, URL: https://doi.org/10.1038/ncomms2498.

[29] M. Grzeszczyk et al., “The effect of metallic substrates on the optical properties of monolayer MoSe2”, in: Scientific Reports 10.*1* (Mar. 2020), p. 4981, ISSN: 2045-2322, DOI: 10.1038/s41598-020-61673-0, URL: https://doi.org/10.1038/s41598-020-61673-0.

[30] Carmen Palacios-Berraquero et al., “Large-scale quantum-emitter arrays in atomically thin semiconductors”, in: Nature communications 8.*1* (2017), pp. 1–6.

[31] Ruitao Lv et al., "Two-dimensional transition metal dichalcogenides: Clusters, ribbons, sheets and more", in: Nano Today 10.*5* (2015), pp. 559 –592, ISSN: 1748-0132, DOI: https://doi.org/10.1016/j.nantod.2015.07.004, URL: http://www.sciencedirect.com/science/article/pii/S1748013215000961.

[32] P. Ajayan, P. Kim, and Banerjee K., "Nanometer resolution in luminescence microscopy of III-V heterostructures", in: Physics Today 69.*9* (2016), pp. 38–44, DOI: 10.1063/PT.3.3297, URL: https://doi.org/10.1063/PT.3.3297.

[33] Jia-Sheng Sun et al., "Self-cleaning by harnessing wrinkles in two-dimensional layered crystals", in: Nanoscale 10.*1* (2018), pp. 312–318.

[34] S. J. Haigh et al., "Cross-sectional imaging of individual layers and buried interfaces of graphene-based heterostructures and superlattices", in: Nature Materials 11.*9* (Sept. 2012), pp. 764–767, ISSN: 1476-4660, DOI: 10.1038/nmat3386, URL: https://doi.org/10.1038/nmat3386.

[35] A. V. Kretinin et al., "Electronic Properties of Graphene Encapsulated with Different Two-Dimensional Atomic Crystals", in: Nano Letters 14.*6* (2014), PMID: 24844319, pp. 3270–3276, DOI: 10.1021/nl5006542, eprint: https://doi.org/10.1021/nl5006542, URL: https://doi.org/10.1021/nl5006542.

[36] Kin Fai Mak et al., "Optical spectroscopy of graphene: From the far infrared to the ultraviolet", in: Solid State Communications 152.*15* (2012), Exploring Graphene, Recent Research Advances, pp. 1341–1349, ISSN: 0038-1098, DOI: https://doi.org/10.1016/j.ssc.2012.04.064, URL: https://www.sciencedirect.com/science/article/pii/S0038109812002700.

[37] P. R. Wallace, "The Band Theory of Graphite", in: Phys. Rev. 71 (9 May 1947), pp. 622–634, DOI: 10.1103/PhysRev.71.622, URL: https://link.aps.org/doi/10.1103/PhysRev.71.622.

[38] Guillaume Froehlicher, "Optical spectroscopy of two-dimensional materials: graphene, transition metal dichalcogenides and van der Waals heterostructures", PhD thesis, Strasbourg, 2016.

[39] A. H. Castro Neto et al., "The electronic properties of graphene", in: Rev. Mod. Phys. 81 (1 Jan. 2009), pp. 109–162, DOI: 10.1103/RevModPhys.81.109, URL: https://link.aps.org/doi/10.1103/RevModPhys.81.109.

[40] M. I. Katsnelson, K. S. Novoselov, and A. K. Geim, "Chiral tunnelling and the Klein paradox in graphene", in: Nature Physics 2.*9* (Sept. 2006), pp. 620–625, ISSN: 1745-2481, DOI: 10.1038/nphys384, URL: https://doi.org/10.1038/nphys384.

[41] Kin Fai Mak et al., "Measurement of the Optical Conductivity of Graphene", in: Phys. Rev. Lett. 101 (19 Nov. 2008), p. 196405, DOI: 10.1103/PhysRevLett.101.196405, URL: https://link.aps.org/doi/10.1103/PhysRevLett.101.196405.

[42] John David Jackson, Classical electrodynamics; 2nd ed. New York, NY: Wiley, 1975, URL: https://cds.cern.ch/record/100964.

[43] Dresselhaus, M. ; Dresselhaus G. ; Jorio A., Group Theory: Application to the Physics of Conc Springer Berlin Heidelberg, 2007, URL: https://books.google.fr/books?id=SPiqKWk_h2sC.

[44] Andrea C. Ferrari and Denis M. Basko, "Raman spectroscopy as a versatile tool for studying the properties of graphene", in: Nature Nanotechnology 8.*4* (Apr. 2013), pp. 235–246, ISSN: 1748-3395, DOI: 10.1038/nnano.2013.46, URL: https://doi.org/10.1038/nnano.2013.46.

[45] Michele Lazzeri and Francesco Mauri, "Nonadiabatic Kohn Anomaly in a Doped Graphene Monolayer", in: Phys. Rev. Lett. 97 (26 Dec. 2006), p. 266407, DOI: 10.1103/PhysRevLett.97.266407, URL: https://link.aps.org/doi/10.1103/PhysRevLett.97.266407.

[46] Pedro Venezuela, Michele Lazzeri, and Francesco Mauri, "Theory of double-resonant Raman spectra in graphene: Intensity and line shape of defect-induced and two-phonon bands", in: Phys. Rev. B 84 (3 July 2011), p. 035433, DOI: 10.1103/PhysRevB.84.035433, URL: https://link.aps.org/doi/10.1103/PhysRevB.84.035433.

[47] D. M. Basko, "Theory of resonant multiphonon Raman scattering in graphene", in: Phys. Rev. B 78 (12 Sept. 2008), p. 125418, DOI: 10.1103/PhysRevB.78.125418, URL: https://link.aps.org/doi/10.1103/PhysRevB.78.125418.

[48] A. Das et al., "Monitoring dopants by Raman scattering in an electrochemically top-gated graphene transistor", in: Nature Nanotechnology 3.*4* (Apr. 2008), pp. 210–215, ISSN: 1748-3395, DOI: 10.1038/nnano.2008.67, URL: https://doi.org/10.1038/nnano.2008.67.

[49] D. M. Basko, S. Piscanec, and A. C. Ferrari, "Electron-electron interactions and doping dependence of the two-phonon Raman intensity in graphene", in: Phys. Rev. B 80 (16 Oct. 2009), p. 165413, DOI: 10.1103/PhysRevB.80.165413, URL: https://link.aps.org/doi/10.1103/PhysRevB.80.165413.

[50] C. E. Ekuma, and D. Gunlycke, "First-Principles-Based Method for Electron Localization: Application to Monolayer Hexagonal Boron Nitride", in: Phys. Rev. Lett. 118 (10 Mar. 2017), p. 106404, DOI: 10.1103/PhysRevLett.118.106404, URL: https://link.aps.org/doi/10.1103/PhysRevLett.118.106404.

[51] Darshana Wickramaratne, Leigh Weston, and Chris G. Van de Walle, "Monolayer to Bulk Properties of Hexagonal Boron Nitride", in: The Journal of Physical Chemistry C 122.*44* (10 Mar. 2018), pp. 25524–25529, DOI: 10.1021/acs.jpcc.8b09087, eprint:

https://doi.org/10.1021/acs.jpcc.8b09087, URL: https://doi.org/10.1021/acs.jpcc.8b09087.

[52] Alexander S. Mayorov et al., "Micrometer-Scale Ballistic Transport in Encapsulated Graphene at Room Temperature", in: Nano Letters 11.*6* (10 Mar. 2011), PMID: 21574627, pp. 2396–2399, DOI: 10.1021/nl200758b, eprint: https://doi.org/10.1021/nl200758b, URL: https://doi.org/10.1021/nl200758b.

[53] Jiamin Xue et al., "Scanning tunnelling microscopy and spectroscopy of ultra-flat graphene on hexagonal boron nitride", in: Nature Materials 10.*4* (10 Apr. 2011), pp. 282–285, ISSN: 1476-4660, DOI: 10.1038/nmat2968, URL: https://doi.org/10.1038/nmat2968.

[54] Régis Decker et al., "Local Electronic Properties of Graphene on a BN Substrate via Scanning Tunneling Microscopy", in: Nano Letters 11.*6* (10 Mar. 2011), PMID: 21553853, pp. 2291–2295, DOI: 10.1021/nl2005115, eprint: https://doi.org/10.1021/nl2005115, URL: https://doi.org/10.1021/nl2005115.

[55] F. Cadiz et al., "Excitonic Linewidth Approaching the Homogeneous Limit in $MoS_2$-Based van der Waals Heterostructures", in: Phys. Rev. X 7 (2 May 2017), p. 021026, DOI: 10.1103/PhysRevX.7.021026, URL: https://link.aps.org/doi/10.1103/PhysRevX.7.021026.

[56] J. Ribeiro-Soares et al., "Group theory analysis of phonons in two-dimensional transition metal dichalcogenides", in: Phys. Rev. B 90 (11 July 2014), p. 115438, DOI: 10.1103/PhysRevB.90.115438, URL: https://link.aps.org/doi/10.1103/PhysRevB.90.115438.

[57] Andrea Splendiani et al., "Emerging Photoluminescence in Monolayer MoS2", in: Nano Letters 10.*4* (10 Mar. 2010), PMID: 20229981, pp. 1271–1275, DOI: 10.1021/nl903868w, eprint: https://doi.org/10.1021/nl903868w, URL: https://doi.org/10.1021/nl903868w.

[58] Kin Fai Mak et al., "Atomically Thin $MoS_2$: A New Direct-Gap Semiconductor", in: Phys. Rev. Lett. 105 (13 Sept. 2010), p. 136805, DOI: 10.1103/PhysRevLett.105.136805, URL: https://link.aps.org/doi/10.1103/PhysRevLett.105.136805.

[59] Gang Wang et al., "Colloquium: Excitons in atomically thin transition metal dichalcogenides", in: Rev. Mod. Phys. 90 (2 Apr. 2018), p. 021001, DOI: 10.1103/RevModPhys.90.021001, URL: https://link.aps.org/doi/10.1103/RevModPhys.90.021001.

[60] Gui-Bin Liu et al., "Three-band tight-binding model for monolayers of group-VIB transition metal dichalcogenides", in: Phys. Rev. B 88 (8 Aug. 2013), p. 085433, DOI: 10.1103/PhysRevB.88.085433, URL: https://link.aps.org/doi/10.1103/PhysRevB.88.085433.

[61] Z. Y. Zhu, Y. C. Cheng, and U. Schwingenschlögl, "Giant spin-orbit-induced spin splitting in two-dimensional transition-metal dichalcogenide semiconductors", in: Phys. Rev. B 84 (15 Oct. 2011), p. 153402, DOI: 10.1103/PhysRevB.84.153402, URL: https://link.aps.org/doi/10.1103/PhysRevB.84.153402.

[62] Ashish Arora et al., "Exciton band structure in layered MoSe 2: from a monolayer to the bulk limit", in: Nanoscale 7.*48* (10 Mar. 2015), pp. 20769–20775, DOI: 10.1103/PhysRevLett.118.106404, URL: https://link.aps.org/doi/10.1103/PhysRevLett.118.106404.

[63] Yi Zhang et al., "Direct observation of the transition from indirect to direct bandgap in atomically thin epitaxial MoSe 2", in: Nature Nanotechnology 9.*2* (10 Feb. 2014), pp. 111–115, ISSN: 1748-3395, DOI: 10.1038/nnano.2013.277, URL: https://doi.org/10.1038/nnano.2013.277.

[64] Kin Fai Mak et al., "Control of valley polarization in monolayer MoS2 by optical helicity", in: Nature Nanotechnology 7.*8* (10 Aug. 2012), pp. 494–498, ISSN: 1748-3395, DOI: 10.1038/nnano.2012.96, URL: https://doi.org/10.1038/nnano.2012.96.

[65] Maciej Koperski et al., "Optical properties of atomically thin transition metal dichalcogenides: observations and puzzles", in: Nanophotonics 6.*6* (10 Mar. 2017), pp. 1289–1308, DOI: doi:10.1515/nanoph-2016-0165, URL: https://doi.org/10.1515/nanoph-2016-0165.

[66] M Goryca et al., "Revealing exciton masses and dielectric properties of monolayer semiconductors with high magnetic fields", in: Nature communications 10.*1* (10 Mar. 2019), pp. 1–12, DOI: 10.1103/PhysRevLett.118.106404, URL: https://link.aps.org/doi/10.1103/PhysRevLett.118.106404.

[67] A. V. Stier et al., "Magnetooptics of Exciton Rydberg States in a Monolayer Semiconductor", in: Phys. Rev. Lett. 120 (5 Feb. 2018), p. 057405, DOI: 10.1103/PhysRevLett.120.057405, URL: https://link.aps.org/doi/10.1103/PhysRevLett.120.057405.

[68] C. Robert et al., "Measurement of the spin-forbidden dark excitons in MoS2 and MoSe2 monolayers", in: Nature Communications 11.*1* (10 Aug. 2020), p. 4037, ISSN: 2041-1723, DOI: 10.1038/s41467-020-17608-4, URL: https://doi.org/10.1038/s41467-020-17608-4.

[69] Frederick Wooten, Optical properties of solids, vol. 118, Academic press, Mar. 2013, p. 106404, DOI: 10.1103/PhysRevLett.118.106404, URL: https://link.aps.org/doi/10.1103/PhysRevLett.118.106404.

[70] Krishna P Dhakal et al., "Confocal absorption spectral imaging of MoS 2: optical transitions depending on the atomic thickness of intrinsic and chemically doped MoS 2", in: Nanoscale 6.*21* (10 Mar. 2014), pp. 13028–13035, DOI: 10.1103/PhysRevLett.118.106404, URL: https://link.aps.org/doi/10.1103/PhysRevLett.118.106404.

[71] Etienne Lorchat, "Optical spectroscopy of heterostructures based on atomically-thin semiconductors", PhD thesis, Strasbourg, Mar. 2019, p. 106404, DOI: 10.1103/PhysRevLett.118.106404, URL: https://link.aps.org/doi/10.1103/PhysRevLett.118.106404.

[72] Bo Peng et al., "Thermal conductivity of monolayer MoS 2, MoSe 2, and WS 2: interplay of mass effect, interatomic bonding and anharmonicity", in: RSC advances 6.*7* (10 Mar. 2016), pp. 5767–5773, DOI: 10.1103/PhysRevLett.118.106404, URL: https://link.aps.org/doi/10.1103/PhysRevLett.118.106404.

[73] David J Griffiths and Darrell F Schroeter, Introduction to quantum mechanics, vol. 118, Cambridge University Press, Mar. 2018, p. 106404, DOI: 10.1103/PhysRevLett.118.106404, URL: https://link.aps.org/doi/10.1103/PhysRevLett.118.106404.

[74] Timothy C. Berkelbach, Mark S. Hybertsen, and David R. Reichman, "Theory of neutral and charged excitons in monolayer transition metal dichalcogenides", in: Phys. Rev. B 88 (4 July 2013), p. 045318, DOI: 10.1103/PhysRevB.88.045318, URL: https://link.aps.org/doi/10.1103/PhysRevB.88.045318.

[75] A. Molina-Sánchez and L. Wirtz, "Phonons in single-layer and few-layer $MoS_2$ and $WS_2$", in: Phys. Rev. B 84 (15 Oct. 2011), p. 155413, DOI: 10.1103/PhysRevB.84.155413, URL: https://link.aps.org/doi/10.1103/PhysRevB.84.155413.

[76] J. S. Blakemore, "Semiconducting and other major properties of gallium arsenide", in: Journal of Applied Physics 53.*10* (10 Mar. 1982), R123–R181, DOI: 10.1063/1.331665, eprint: https://doi.org/10.1063/1.331665, URL: https://doi.org/10.1063/1.331665.

[77] Alexey Chernikov et al., "Exciton Binding Energy and Nonhydrogenic Rydberg Series in Monolayer $WS_2$", in: Phys. Rev. Lett. 113 (7 Aug. 2014), p. 076802, DOI: 10.1103/PhysRevLett.113.076802, URL: https://link.aps.org/doi/10.1103/PhysRevLett.113.076802.

[78] Keldysh L.V., "Coulomb interaction in thin semiconductor and semimetal films", in: JETP 29.*11* (10 Mar. 1979), p. 658, DOI: 10.1103/PhysRevLett.118.106404, URL: https://link.aps.org/doi/10.1103/PhysRevLett.118.106404.

[79] Lucio Claudio Andreani, Francesco Tassone, and Franco Bassani, "Radiative lifetime of free excitons in quantum wells", in: Solid State Communications 77.*9* (10 Mar. 1991), pp. 641 –645, ISSN: 0038-1098, DOI: https://doi.org/10.1016/0038-1098(91)90761-J, URL: http://www.sciencedirect.com/science/article/pii/003810989190761J.

[80] Ashish Arora et al., "Excitonic resonances in thin films of WSe 2: from monolayer to bulk material", in: Nanoscale 7.*23* (10 Mar. 2015), pp. 10421–10429, DOI: 10.1103/PhysRevLett.118.106404, URL: https://link.aps.org/doi/10.1103/PhysRevLett.118.106404.

[81] John R. Schaibley et al., "Valleytronics in 2D materials", in: Nature Reviews Materials 1.*11* (10 Aug. 2016), p. 16055, ISSN: 2058-8437, DOI: 10.1038/natrevmats.2016.55, URL: https://doi.org/10.1038/natrevmats.2016.55.

[82] Yehuda B. Band and Yshai Avishai, "9 - Electronic Properties of Solids", in: Quantum Mechanics with Applications to Nanotechnology and Information Science, ed. by Yehuda B. Band and Yshai Avishai, vol. 118, Amsterdam: Academic Press, Mar. 2013, pp. 381 –544, ISBN: 978-0-444-53786-7, DOI: https://doi.org/10.1016/B978-0-444-53786-7.00009-5, URL: http://www.sciencedirect.com/science/article/pii/B9780444537867000095.

[83] , Jaroslav Fabian, and S. Das Sarma, "Spintronics: Fundamentals and applications", in: Rev. Mod. Phys. 76 (2 Apr. 2004), pp. 323–410, DOI: 10.1103/RevModPhys.76.323, URL: https://link.aps.org/doi/10.1103/RevModPhys.76.323.

[84] M. Z. Maialle, E. A. de Andrada e Silva, and L. J. Sham, "Exciton spin dynamics in quantum wells", in: Phys. Rev. B 47 (23 June 1993), pp. 15776–15788, DOI: 10.1103/PhysRevB.47.15776, URL: https://link.aps.org/doi/10.1103/PhysRevB.47.15776.

[85] M. M. Glazov et al., "Spin and valley dynamics of excitons in transition metal dichalcogenide monolayers", in: physica status solidi (b) 252.*11* (2 Apr. 2015), pp. 2349–2362, DOI: 10.1002/pssb.201552211, eprint: https://onlinelibrary.wiley.com/doi/pdf/10.1002/pssb.201552211, URL: https://onlinelibrary.wiley.com/doi/abs/10.1002/pssb.201552211.

[86] M. M. Glazov et al., "Exciton fine structure and spin decoherence in monolayers of transition metal dichalcogenides", in: Phys. Rev. B 89 (20 May 2014), p. 201302, DOI: 10.1103/PhysRevB.89.201302, URL: https://link.aps.org/doi/10.1103/PhysRevB.89.201302.

[87] C. R. Zhu et al., "Exciton valley dynamics probed by Kerr rotation in $WSe_2$ monolayers", in: Phys. Rev. B 90 (16 Oct. 2014), p. 161302, DOI: 10.1103/PhysRevB.90.161302, URL: https://link.aps.org/doi/10.1103/PhysRevB.90.161302.

[88] Cong Mai et al., "Many-Body Effects in Valleytronics: Direct Measurement of Valley Lifetimes in Single-Layer MoS2", in: Nano Letters 14.*1* (2 Apr. 2014), PMID: 24325650, pp. 202–206, DOI: 10.1021/nl403742j, eprint: https://doi.org/10.1021/nl403742j, URL: https://doi.org/10.1021/nl403742j.

[89] Kha Tran et al., "Disorder-dependent valley properties in monolayer $WSe_2$", in: Phys. Rev. B 96 (4 July 2017), p. 041302, DOI: 10.1103/PhysRevB.96.041302, URL: https://link.aps.org/doi/10.1103/PhysRevB.96.041302.

[90] T. Yu and M. W. Wu, "Valley depolarization dynamics and valley Hall effect of excitons in monolayer and bilayer $MoS_2$", in: Phys. Rev. B 93 (4 Jan. 2016), p. 045414, DOI: 10.1103/PhysRevB.93.045414, URL: https://link.aps.org/doi/10.1103/PhysRevB.93.045414.

[91] Kathleen M. McCreary et al., "Understanding Variations in Circularly Polarized Photoluminescence in Monolayer Transition Metal Dichalcogenides", in: ACS Nano 11.*8* (2 Apr. 2017), PMID: 28763189, pp. 7988–7994, DOI: 10.1021/acsnano.7b02554, eprint: https://doi.org/10.1021/acsnano.7b02554, URL: https://doi.org/10.1021/acsnano.7b02554.

[92] Hans Tornatzky, Anne-Marie Kaulitz, and Janina Maultzsch, "Resonance Profiles of Valley Polarization in Single-Layer $MoS_2$ and $MoSe_2$", in: Phys. Rev. Lett. 121 (16 Oct. 2018), p. 167401, DOI: 10.1103/PhysRevLett.121.167401, URL: https://link.aps.org/doi/10.1103/PhysRevLett.121.167401.

[93] G. Kioseoglou et al., "Optical polarization and intervalley scattering in single layers of MoS2 and MoSe2", in: Scientific Reports 6.*1* (2 Apr. 2016), p. 25041, ISSN: 2045-2322, DOI: 10.1038/srep25041, URL: https://doi.org/10.1038/srep25041.

[94] G. Kioseoglou et al., "Valley polarization and intervalley scattering in monolayer MoS2", in: Applied Physics Letters 101.*22* (2 Apr. 2012), p. 221907, DOI: 10.1063/1.4768299, eprint: https://doi.org/10.1063/1.4768299, URL: https://doi.org/10.1063/1.4768299.

[95] G. Kioseoglou et al., "Spin effects in MoS2 and WS2 single layers", in: physica status solidi (RRL) – 10.*1* (2 Apr. 2016), pp. 111–119, DOI: 10.1002/pssr.201510291, eprint: https://onlinelibrary.wiley.com/doi/pdf/10.1002/pssr.201510291, URL: https://onlinelibrary.wiley.com/doi/abs/10.1002/pssr.201510291.

[96] Matthias Paur et al., "Electroluminescence from multi-particle exciton complexes in transition metal dichalcogenide semiconductors", in: Nature communications 10.*1* (2 Apr. 2019), pp. 1–7, DOI: 10.1103/RevModPhys.76.323, URL: https://link.aps.org/doi/10.1103/RevModPhys.76.323.

[97] Kai Hao et al., "Neutral and charged inter-valley biexcitons in monolayer MoSe2", in: Nature Communications 8.*1* (2 June 2017), p. 15552, ISSN: 2041-1723, DOI: 10.1038/ncomms15552, URL: https://doi.org/10.1038/ncomms15552.

[98] Zhipeng Li et al., "Revealing the biexciton and trion-exciton complexes in BN encapsulated WSe2", in: Nature Communications 9.*1* (2 Sept. 2018), p. 3719, ISSN: 2041-1723, DOI: 10.1038/s41467-018-05863-5, URL: https://doi.org/10.1038/s41467-018-05863-5.

[99] E. Courtade et al., "Charged excitons in monolayer $WSe_2$: Experiment and theory", in: Phys. Rev. B 96 (8 Aug. 2017), p. 085302, DOI: 10.1103/PhysRevB.96.085302, URL: https://link.aps.org/doi/10.1103/PhysRevB.96.085302.

[100] Ziliang Ye et al., "Efficient generation of neutral and charged biexcitons in encapsulated WSe2 monolayers", in: Nature Communications 9.*1* (2 Sept. 2018), p. 3718, ISSN: 2041-1723, DOI: 10.1038/s41467-018-05917-8, URL: https://doi.org/10.1038/s41467-018-05917-8.

[101] D Vaclavkova et al., "Singlet and triplet trions in WS2 monolayer encapsulated in hexagonal boron nitride", in: Nanotechnology 29.*32* (2 June 2018), p. 325705, DOI: 10.1088/1361-6528/aac65c, URL: https://link.aps.org/doi/10.1103/RevModPhys.76.323.

[102] Joanna Jadczak et al., "Probing negatively charged and neutral excitons in MoS2/hBN and hBN/MoS2/hBN van der Waals heterostructures", in: Nanotechnology 32.*14* (2 Apr. 2021), p. 145717, DOI: 10.1103/RevModPhys.76.323, URL: https://link.aps.org/doi/10.1103/RevModPhys.76.323.

[103] G. Wang et al., "In-Plane Propagation of Light in Transition Metal Dichalcogenide Monolayers: Optical Selection Rules", in: Phys. Rev. Lett. 119 (4 July 2017), p. 047401, DOI: 10.1103/PhysRevLett.119.047401, URL: https://link.aps.org/doi/10.1103/PhysRevLett.119.047401.

[104] Matteo Barbone et al., "Charge-tuneable biexciton complexes in monolayer WSe2", in: Nature Communications 9.*1* (2 Sept. 2018), p. 3721, ISSN: 2041-1723, DOI: 10.1038/s41467-018-05632-4, URL: https://doi.org/10.1038/s41467-018-05632-4.

[105] Trevor B. Arp et al., "Electron–hole liquid in a van der Waals heterostructure photocell at room temperature", in: Nature Photonics 13.*4* (2 Apr. 2019), pp. 245–250, ISSN: 1749-4893, DOI: 10.1038/s41566-019-0349-y, URL: https://doi.org/10.1038/s41566-019-0349-y.

[106] Yiling Yu et al., "Room-Temperature Electron–Hole Liquid in Monolayer MoS2", in: ACS Nano 13.*9* (2 Apr. 2019), PMID: 31483608, pp. 10351–10358, DOI: 10.1021/acsnano.9b04124, eprint: https://doi.org/10.1021/acsnano.9b04124, URL: https://doi.org/10.1021/acsnano.9b04124.

[107] Alexander W. Bataller et al., "Dense Electron–Hole Plasma Formation and Ultralong Charge Lifetime in Monolayer MoS2 via Material Tuning", in: Nano Letters 19.*2* (2 Apr. 2019), pp. 1104–1111, DOI: 10.1021/acs.nanolett.8b04408, eprint: https://doi.org/10.1021/acs.nanolett.8b04408, URL: https://doi.org/10.1021/acs.nanolett.8b04408.

[108] Carmen Palacios-Berraquero, "Atomically-thin quantum light emitting diodes", in: Rev. Mod. Phys. 76 (2 Apr. 2018), pp. 71–89, DOI: 10.1103/RevModPhys.76.323, URL: https://link.aps.org/doi/10.1103/RevModPhys.76.323.

[109] J. Tersoff and D. R. Hamann, "Theory of the scanning tunneling microscope", in: Phys. Rev. B 31 (2 Jan. 1985), pp. 805–813, DOI: 10.1103/PhysRevB.31.805, URL: https://link.aps.org/doi/10.1103/PhysRevB.31.805.

[110] Antal A. Koos et al., "Influence of Native Defects on the Electronic and Magnetic Properties of CVD Grown MoSe2 Single Layers", in: The Journal of Physical Chemistry C 123.*40* (2 Apr. 2019), pp. 24855–24864, DOI: 10.1021/acs.jpcc.9b05921, eprint: https://doi.org/10.1021/acs.jpcc.9b05921, URL: https://doi.org/10.1021/acs.jpcc.9b05921.

[111] Chendong Zhang et al., "Probing Critical Point Energies of Transition Metal Dichalcogenides: Surprising Indirect Gap of Single Layer WSe2", in: Nano Letters 15.*10* (2 Apr. 2015), PMID: 26389585, pp. 6494–6500, DOI: 10.1021/acs.nanolett.5b01968, eprint: https://doi.org/10.1021/acs.nanolett.5b01968, URL: https://doi.org/10.1021/acs.nanolett.5b01968.

[112] Sara Barja et al., "Identifying substitutional oxygen as a prolific point defect in monolayer transition metal dichalcogenides", in: Nature Communications 10.*1* (2 July 2019), p. 3382, ISSN: 2041-1723, DOI: 10.1038/s41467-019-11342-2, URL: https://doi.org/10.1038/s41467-019-11342-2.

[113] Ming-Hui Chiu et al., "Determination of band alignment in the single-layer MoS2/WSe2 heterojunction", in: Nature Communications 6.*1* (2 July 2015), p. 7666, ISSN: 2041-1723, DOI: 10.1038/ncomms8666, URL: https://doi.org/10.1038/ncomms8666.

[114] Chendong Zhang et al., "Engineering Point-Defect States in Monolayer WSe2", in: ACS Nano 13.*2* (2 Apr. 2019), PMID: 30689361, pp. 1595–1602, DOI: 10.1021/acsnano.8b07595, eprint: https://doi.org/10.1021/acsnano.8b07595, URL: https://doi.org/10.1021/acsnano.8b07595.

[115] Shuai Zhang et al., "Defect Structure of Localized Excitons in a $WSe_2$ Monolayer", in: Phys. Rev. Lett. 119 (4 July 2017), p. 046101, DOI: 10.1103/PhysRevLett.119.046101, URL: https://link.aps.org/doi/10.1103/PhysRevLett.119.046101.

[116] Albert F. Rigosi et al., "Electronic band gaps and exciton binding energies in monolayer $Mo_xW_{1-x}S_2$ transition metal dichalcogenide alloys probed by scanning tunneling and optical spectroscopy", in: Phys. Rev. B 94 (7 Aug. 2016), p. 075440, DOI: 10.1103/PhysRevB.94.075440, URL: https://link.aps.org/doi/10.1103/PhysRevB.94.075440.

[117] Chendong Zhang et al., "Direct Imaging of Band Profile in Single Layer MoS2 on Graphite: Quasiparticle Energy Gap, Metallic Edge States, and Edge Band Bending", in: Nano Letters 14.*5* (2 Apr. 2014), PMID: 24783945, pp. 2443–2447, DOI: 10.1021/nl501133c, eprint: https://doi.org/10.1021/nl501133c, URL: https://doi.org/10.1021/nl501133c.

[118] Xiaolong Liu et al., "Point Defects and Grain Boundaries in Rotationally Commensurate MoS2 on Epitaxial Graphene", in: The Journal of Physical Chemistry C 120.*37* (2 Apr. 2016), pp. 20798–20805, DOI: 10.1021/acs.jpcc.6b02073, eprint: https://doi.org/10.1021/acs.jpcc.6b02073, URL: https://doi.org/10.1021/acs.jpcc.6b02073.

[119] Min Hong et al., "Quasi-freestanding, striped WS2 monolayer with an invariable band gap on Au(001)", in: Nano Research 10.*11* (2 Nov. 2017), pp. 3875–3884, ISSN: 1998-0000, DOI: 10.1007/s12274-017-1601-8, URL: https://doi.org/10.1007/s12274-017-1601-8.

[120] Heather M. Hill et al., "Band Alignment in MoS2/WS2 Transition Metal Dichalcogenide Heterostructures Probed by Scanning Tunneling Microscopy and Spectroscopy", in: Nano Letters 16.*8* (2 Apr. 2016), PMID: 27298270, pp. 4831–4837, DOI: 10.1021/acs.nanolett.6b01007, eprint: https://doi.org/10.1021/acs.nanolett.6b01007, URL: https://doi.org/10.1021/acs.nanolett.6b01007.

[121] R. M. Feenstra and Joseph A. Stroscio, "Tunneling spectroscopy of the GaAs(110) surface", in: Journal of Vacuum Science & Technology B: Microelectronics Processing and Ph 5.*4* (2 Apr. 1987), pp. 923–929, DOI: 10.1116/1.583691, eprint: https://avs.scitation.org/doi/pdf/10.1116/1.583691, URL: https://avs.scitation.org/doi/abs/10.1116/1.583691.

[122] R. Dombrowski et al., "Tip-induced band bending by scanning tunneling spectroscopy of the states of the tip-induced quantum dot on InAs(110)", in: Phys. Rev. B 59 (12 Mar. 1999), pp. 8043–8048, DOI: 10.1103/PhysRevB.59.8043, URL: https://link.aps.org/doi/10.1103/PhysRevB.59.8043.

[123] Joseph A. Stroscio, R. M. Feenstra, and A. P. Fein, "Electronic Structure of the Si(111)2 × 1 Surface by Scanning-Tunneling Microscopy", in: Phys. Rev. Lett. 57 (20 Nov. 1986), pp. 2579–2582, DOI: 10.1103/PhysRevLett.57.2579, URL: https://link.aps.org/doi/10.1103/PhysRevLett.57.2579.

[124] Yi Pan et al., "Quantum-Confined Electronic States Arising from the Moiré Pattern of MoS2–WSe2 Heterobilayers", in: Nano Letters 18.*3* (2 Apr. 2018), PMID: 29415536, pp. 1849–1855, DOI: 10.1021/acs.nanolett.7b05125, eprint: https://doi.org/10.1021/acs.nanolett.7b05125, URL: https://doi.org/10.1021/acs.nanolett.7b05125.

[125] Dacen Waters et al., "Flat Bands and Mechanical Deformation Effects in the Moiré Superlattice of MoS2-WSe2 Heterobilayers", in: ACS Nano 14.*6* (2 Apr. 2020), PMID: 32496750, pp. 7564–7573, DOI: 10.1021/acsnano.0c03414, eprint: https://doi.org/10.1021/acsnano.0c03414, URL: https://doi.org/10.1021/acsnano.0c03414.

[126] Randall M. Feenstra et al., "Acquisition and analysis of scanning tunneling spectroscopy data—WSe2 monolayer", in: Journal of Vacuum Science & Technology A 39.*1* (2 Apr. 2021), p. 011001, DOI: 10.1116/6.0000684, eprint: https://doi.org/10.1116/6.0000684, URL: https://doi.org/10.1116/6.0000684.

[127] And J. Fernández-Rossier, "Electronic properties of the $MoS_2$-$WS_2$ heterojunction", in: Phys. Rev. B 87 (7 Feb. 2013), p. 075451, DOI: 10.1103/PhysRevB.87.075451, URL: https://link.aps.org/doi/10.1103/PhysRevB.87.075451.

[128] Debora Pierucci et al., "Band Alignment and Minigaps in Monolayer MoS2-Graphene van der Waals Heterostructures", in: Nano Letters 16.*7* (7 Feb. 2016), PMID: 27281693, pp. 4054–4061, DOI: 10.1021/acs.nanolett.6b00609, eprint: https://doi.org/10.1021/acs.nanolett.6b00609, URL: https://doi.org/10.1021/acs.nanolett.6b00609.

[129] Høgni C. Kamban and Thomas G. Pedersen, "Interlayer excitons in van der Waals heterostructures: Binding energy, Stark shift, and field-induced dissociation", in: Scientific Reports 10.*1* (7 Mar. 2020), p. 5537, ISSN: 2045-2322, DOI: 10.1038/s41598-020-62431-y, URL: https://doi.org/10.1038/s41598-020-62431-y.

[130] Xiaoping Hong et al., "Ultrafast charge transfer in atomically thin MoS 2 /WS 2 heterostructures", in: Nature Nanotechnology 9.*9* (7 Sept. 2014), pp. 682–686, ISSN: 1748-3395, DOI: 10.1038/nnano.2014.167, URL: https://doi.org/10.1038/nnano.2014.167.

[131] Philipp Nagler et al., "Interlayer exciton dynamics in a dichalcogenide monolayer heterostructure", in: 2D Materials 4.*2* (7 June 2017), p. 025112, DOI: 10.1088/2053-1583/aa7352, URL: https://doi.org/10.1088/2053-1583/aa7352.

[132] R. F. Frindt, "Single Crystals of MoS2 Several Molecular Layers Thick", in: Journal of Applied 37.*4* (7 Feb. 1966), pp. 1928–1929, DOI: 10.1063/1.1708627, eprint: https://doi.org/10.1063/1.1708627, URL: https://doi.org/10.1063/1.1708627.

[133] Yuan Huang et al., "Reliable Exfoliation of Large-Area High-Quality Flakes of Graphene and Other Two-Dimensional Materials", in: ACS Nano 9.*11* (7 Feb. 2015), PMID: 26336975, pp. 10612–10620, DOI: 10.1021/acsnano.5b04258, eprint: https://doi.org/10.1021/acsnano.5b04258, URL: https://doi.org/10.1021/acsnano.5b04258.

[134] Andres Castellanos-Gomez et al., "Deterministic transfer of two-dimensional materials by all-dry viscoelastic stamping", in: 2D Materials 1.*1* (7 Apr. 2014), p. 011002, DOI: 10.1088/2053-1583/1/1/011002, URL: https://doi.org/10.1088%2F2053-1583%2F1%2F1%2F011002.

[135] G. Wang et al., "Giant Enhancement of the Optical Second-Harmonic Emission of $WSe_2$ Monolayers by Laser Excitation at Exciton Resonances", in: Phys. Rev. Lett. 114 (9 Mar. 2015), p. 097403, DOI: 10.1103/PhysRevLett.114.097403, URL: https://link.aps.org/doi/10.1103/PhysRevLett.114.097403.

[136] Ji Eun Lee et al., "Optical separation of mechanical strain from charge doping in graphene", in: Nature Communications 3.*1* (7 Aug. 2012), p. 1024, ISSN: 2041-1723, DOI: 10.1038/ncomms2022, URL: https://doi.org/10.1038/ncomms2022.

[137] J. Bardeen, "Tunnelling from a Many-Particle Point of View", in: Phys. Rev. Lett. 6 (2 Jan. 1961), pp. 57–59, DOI: 10.1103/PhysRevLett.6.57, URL: https://link.aps.org/doi/10.1103/PhysRevLett.6.57.

[138] Ivar Giaever, "Electron Tunneling Between Two Superconductors", in: Phys. Rev. Lett. 5 (10 Nov. 1960), pp. 464–466, DOI: 10.1103/PhysRevLett.5.464, URL: https://link.aps.org/doi/10.1103/PhysRevLett.5.464.

[139] C. Julian Chen, "Effects of m≠0 tip states in scanning tunneling microscopy: The explanations of corrugation reversal", in: Phys. Rev. Lett. 69 (11 Sept. 1992), pp. 1656–1659, DOI: 10.1103/PhysRevLett.69.1656, URL: https://link.aps.org/doi/10.1103/PhysRevLett.69.1656.

[140] W.M.H. Sachtler, G.J.H. Dorgelo, and A.A. Holscher, "The work function of gold", in: Surface Science 5.*2* (7 Feb. 1966), pp. 221 –229, ISSN: 0039-6028, DOI: http://dx.doi.org/10.1016/0039-6028(66)90083-5, URL: http://www.sciencedirect.com/science/article/pii/0039602866900835.

[141] Michael Chong, "Electrically driven fluorescence of single molecule junctions", PhD thesis, Strasbourg, Feb. 2016, p. 075451, DOI: 10.1103/PhysRevB.87.075451, URL: https://link.aps.org/doi/10.1103/PhysRevB.87.075451.

[142] John Lambe and S. L. McCarthy, "Light Emission from Inelastic Electron Tunneling", in: Phys. Rev. Lett. 37 (14 Oct. 1976), pp. 923–925, DOI: 10.1103/PhysRevLett.37.923, URL: https://link.aps.org/doi/10.1103/PhysRevLett.37.923.

[143] Benjamin Doppagne, "Hyper-resolved fluorescence microscopy with STM", PhD thesis, Strasbourg, Feb. 2020, p. 075451, DOI: 10.1103/PhysRevB.87.075451, URL: https://link.aps.org/doi/10.1103/PhysRevB.87.075451.

[144] And J. Fernández-Rossier, "Modern Plasmonics", in: Modern Plasmonics, ed. by N.V. Richardson and Stephen Holloway, vol. 4, Handbook of Surface Science, North-Holland, Feb. 2014, p. i, DOI: https://doi.org/10.1016/B978-0-444-59526-3.00016-1, URL: https://www.sciencedirect.com/science/article/pii/B9780444595263000161.

[145] B. Novotny L. Hecht, Principles of Nano-Optics, ed. by N.V. Richardson and Stephen Holloway, vol. 4, Handbook of Surface Science, Cambridge: Cambridge University Press, Feb. 2006, p. i, DOI: https://doi.org/10.1016/B978-0-444-59526-3.00016-1, URL: https://www.sciencedirect.com/science/article/pii/B9780444595263000161.

[146] R. W. Rendell, D. J. Scalapino, and B. Mühlschlegel, "Role of Local Plasmon Modes in Light Emission from Small-particle Tunnel Junctions", in: Phys. Rev. Lett., Handbook of Surface Science 41 (25 Dec. 1978), ed. by N.V. Richardson and Stephen Holloway, pp. 1746–1750, ISSN: 1573-4331, DOI: 10.1103/PhysRevLett.41.1746, URL: https://link.aps.org/doi/10.1103/PhysRevLett.41.1746.

[147] Peter Johansson, R. Monreal, and Peter Apell, "Theory for light emission from a scanning tunneling microscope", in: Phys. Rev. B, Handbook of Surface Science 42 (14 Nov. 1990), ed. by N.V. Richardson and Stephen Holloway, pp. 9210–9213, ISSN: 1573-4331, DOI: 10.1103/PhysRevB.42.9210, URL: https://link.aps.org/doi/10.1103/PhysRevB.42.9210.

[148] Richard Berndt, James K. Gimzewski, and Peter Johansson, "Inelastic tunneling excitation of tip-induced plasmon modes on noble-metal surfaces", in: Phys. Rev. Lett., Handbook of Surface Science 67 (27 Dec. 1991), ed. by N.V. Richardson and Stephen Holloway, pp. 3796–3799, ISSN: 1573-4331, DOI: 10.1103/PhysRevLett.67.3796, URL: https://link.aps.org/doi/10.1103/PhysRevLett.67.3796.

[149] Kazuyuki Meguro et al., "Origin of multiple peaks in the light emission spectra of a Au(111) surface induced by the scanning tunneling microscope", in: Phys. Rev. B, Handbook of Surface Science 65 (16 Apr. 2002), ed. by N.V. Richardson and Stephen Holloway, p. 165405, ISSN: 1573-4331, DOI: 10.1103/PhysRevB.65.165405, URL: https://link.aps.org/doi/10.1103/PhysRevB.65.165405.

[150] Wenli Deng et al., “STM-induced photon emission from self-assembled porphyrin molecules on a Cu (100) surface”, in: The Journal of chemical physics, Handbook of Surface Science 117.*10* (7 Feb. 2002), ed. by N.V. Richardson and Stephen Holloway, pp. 4995–5000, ISSN: 1573-4331, DOI: https://doi.org/10.1016/B978-0-444-59526-3.00016-1, URL: https://www.sciencedirect.com/science/article/pii/B9780444595263000161.

[151] Guillaume Schull, Michael Becker, and Richard Berndt, “Imaging Confined Electrons with Plasmonic Light”, in: Phys. Rev. Lett., Handbook of Surface Science 101 (13 Sept. 2008), ed. by N.V. Richardson and Stephen Holloway, p. 136801, ISSN: 1573-4331, DOI: 10.1103/PhysRevLett.101.136801, URL: https://link.aps.org/doi/10.1103/PhysRevLett.101.136801.

[152] Christoph Große et al., “Dynamic control of plasmon generation by an individual quantum system”, in: Nano letters, Handbook of Surface Science 14.*10* (7 Feb. 2014), ed. by N.V. Richardson and Stephen Holloway, pp. 5693–5697, ISSN: 1573-4331, DOI: https://doi.org/10.1016/B978-0-444-59526-3.00016-1, URL: https://www.sciencedirect.com/science/article/pii/B9780444595263000161.

[153] Michael C. Chong et al., “Narrow-Line Single-Molecule Transducer between Electronic Circuits and Surface Plasmons”, in: Phys. Rev. Lett., Handbook of Surface Science 116 (3 Jan. 2016), ed. by N.V. Richardson and Stephen Holloway, p. 036802, ISSN: 1573-4331, DOI: 10.1103/PhysRevLett.116.036802, URL: https://link.aps.org/doi/10.1103/PhysRevLett.116.036802.

[154] Yang Zhang et al., “Visualizing coherent intermolecular dipole–dipole coupling in real space”, in: Nature, Handbook of Surface Science 531.*7596* (7 Feb. 2016), ed. by N.V. Richardson and Stephen Holloway, pp. 623–627, ISSN: 1573-4331, DOI: https://doi.org/10.1016/B978-0-444-59526-3.00016-1, URL: https://www.sciencedirect.com/science/article/pii/B9780444595263000161.

[155] X. H. Qiu, G. V. Nazin, and W. Ho, “Vibrationally Resolved Fluorescence Excited with Submolecular Precision”, in: Science, Handbook of Surface Science 299.*5606* (7 Feb. 2003), ed. by N.V. Richardson and Stephen Holloway, pp. 542–546, ISSN: 0036-8075, DOI: 10.1126/science.1078675, eprint: https://science.sciencemag.org/content/299/5606/542.full.pdf, URL: https://science.sciencemag.org/content/299/5606/542.

[156] D. L. Abraham et al., “Nanometer resolution in luminescence microscopy of III-V heterostructures”, in: Applied Physics Letters, Handbook of Surface Science 56.*16* (7 Feb. 1990), ed. by N.V. Richardson and Stephen Holloway, pp. 1564–1566, ISSN: 1573-4331, DOI: 10.1063/1.103154, eprint: https://doi.org/10.1063/1.103154, URL: https://doi.org/10.1063/1.103154.

[157] Lars Montelius, Mats-Erik Pistol, and Lars Samuelson, "Low-temperature luminescence due to minority carrier injection from the scanning tunneling microscope tip", in: Ultramicroscopy, Handbook of Surface Science 42-44 (7 Feb. 1992), ed. by N.V. Richardson and Stephen Holloway, pp. 210–214, ISSN: 0304-3991, DOI: https://doi.org/10.1016/0304-3991(92)90269-P, URL: https://www.sciencedirect.com/science/article/pii/030439919290269P.

[158] R. Berndt and J. K. Gimzewski, "Injection luminescence from CdS(112¯0) studied with scanning tunneling microscopy", in: Phys. Rev. B, Handbook of Surface Science 45 (24 June 1992), ed. by N.V. Richardson and Stephen Holloway, pp. 14095–14099, ISSN: 1573-4331, DOI: 10.1103/PhysRevB.45.14095, URL: https://link.aps.org/doi/10.1103/PhysRevB.45.14095.

[159] J. K. Gimzewski et al., "Photon emission with the scanning tunneling microscope", in: Zeitschrift für Physik B Condensed Matter, Handbook of Surface Science 72.*4* (7 Dec. 1988), ed. by N.V. Richardson and Stephen Holloway, pp. 497–501, ISSN: 1431-584X, DOI: 10.1007/BF01314531, URL: https://doi.org/10.1007/BF01314531.

[160] Inger Ekvall et al., "Preparation and characterization of electrochemically etched W tips for STM", in: Measurement Science and Technology, Handbook of Surface Science 10.*1* (7 Jan. 1999), ed. by N.V. Richardson and Stephen Holloway, pp. 11–18, ISSN: 1573-4331, DOI: 10.1088/0957-0233/10/1/006, URL: https://doi.org/10.1088/0957-0233/10/1/006.

[161] Hanbury Brown R. and Twiss R. Q., "A Test of a New Type of Stellar Interferometer on Sirius", in: Nature, Handbook of Surface Science 178 (4541 Nov. 1956), ed. by N.V. Richardson and Stephen Holloway, pp. 1476–4687, ISSN: 1573-4331, DOI: 10.1038/1781046a0, URL: https://doi.org/10.1038/1781046a0.

[162] Carino Ferrante et al., "Picosecond energy transfer in a transition metal dichalcogenide-graphene heterostructure revealed by transient Raman spectroscopy", in: arXiv preprint arXiv:2101. Handbook of Surface Science 4 (7 Feb. 2021), ed. by N.V. Richardson and Stephen Holloway, p. i, ISSN: 1573-4331, DOI: https://doi.org/10.1016/B978-0-444-59526-3.00016-1, URL: https://www.sciencedirect.com/science/article/pii/B9780444595263000161.

[163] Heather M. Hill et al., "Exciton broadening in $WS_2$/graphene heterostructures", in: Phys. Rev. B, Handbook of Surface Science 96 (20 Nov. 2017), ed. by N.V. Richardson and Stephen Holloway, p. 205401, ISSN: 1573-4331, DOI: 10.1103/PhysRevB.96.205401, URL: https://link.aps.org/doi/10.1103/PhysRevB.96.205401.

[164] Wenjing Zhang et al., "Ultrahigh-Gain Photodetectors Based on Atomically Thin Graphene-MoS2 Heterostructures", in: Scientific Reports, Handbook of Surface Science 4.*1* (7 Jan. 2014), ed. by N.V. Richardson and Stephen Holloway, p. 3826, ISSN: 2045-2322, DOI: 10.1038/srep03826, URL: https://doi.org/10.1038/srep03826.

[165] Dominik Metten et al., "Probing built-in strain in freestanding graphene monolayers by Raman spectroscopy", in: physica status solidi (b), Handbook of Surface Science 250.*12* (7 Feb. 2013), ed. by N.V. Richardson and Stephen Holloway, pp. 2681–2686, ISSN: 1573-4331, DOI: https://doi.org/10.1002/pssb.201300220, eprint: https://onlinelibrary.wiley.com/doi/pdf/10.1002/pssb.201300220, URL: https://onlinelibrary.wiley.com/doi/abs/10.1002/pssb.201300220.

[166] Sunmin Ryu et al., "Atmospheric Oxygen Binding and Hole Doping in Deformed Graphene on a SiO2 Substrate", in: Nano Letters, Handbook of Surface Science 10.*12* (7 Feb. 2010), ed. by N.V. Richardson and Stephen Holloway, PMID: 21069971, pp. 4944–4951, ISSN: 1573-4331, DOI: 10.1021/nl1029607, eprint: https://doi.org/10.1021/nl1029607, URL: https://doi.org/10.1021/nl1029607.

[167] Weiyi Lin et al., "Electron redistribution and energy transfer in graphene/MoS2 heterostructure", in: Applied Physics Letters, Handbook of Surface Science 114.*11* (7 Feb. 2019), ed. by N.V. Richardson and Stephen Holloway, p. 113103, ISSN: 1573-4331, DOI: https://doi.org/10.1016/B978-0-444-59526-3.00016-1, URL: https://www.sciencedirect.com/science/article/pii/B9780444595263000161.

[168] Guillaume Froehlicher and Stéphane Berciaud, "Raman spectroscopy of electrochemically gated graphene transistors: Geometrical capacitance, electron-phonon, electron-electron, and electron-defect scattering", in: Phys. Rev. B, Handbook of Surface Science 91 (20 May 2015), ed. by N.V. Richardson and Stephen Holloway, p. 205413, ISSN: 1573-4331, DOI: 10.1103/PhysRevB.91.205413, URL: https://link.aps.org/doi/10.1103/PhysRevB.91.205413.

[169] Th Förster, "Zwischenmolekulare energiewanderung und fluoreszenz", in: Annalen der physik, Handbook of Surface Science 437.*1-2* (7 Feb. 1948), ed. by N.V. Richardson and Stephen Holloway, pp. 55–75, ISSN: 1573-4331, DOI: https://doi.org/10.1016/B978-0-444-59526-3.00016-1, URL: https://www.sciencedirect.com/science/article/pii/B9780444595263000161.

[170] David L Dexter, "A theory of sensitized luminescence in solids", in: The journal of chemical ph Handbook of Surface Science 21.*5* (7 Feb. 1953), ed. by N.V. Richardson and Stephen Holloway, pp. 836–850, ISSN: 1573-4331, DOI: https://doi.org/10.1016/B978-0-444-59526-3.00016-1, URL: https://www.sciencedirect.com/science/article/pii/B9780444595263000161.

[171] Yilei Li et al., "Measurement of the optical dielectric function of monolayer transition-metal dichalcogenides: $MoS_2$, $MoSe_2$, $WS_2$, and $WSe_2$", in: Phys. Rev. B, Handbook of Surface Science 90 (20 Nov. 2014), ed. by N.V. Richardson and Stephen Holloway, p. 205422, ISSN: 1573-4331, DOI: 10.1103/PhysRevB.90.205422, URL: https://link.aps.org/doi/10.1103/PhysRevB.90.205422.

[172] Malte Selig et al., "Theory of optically induced Förster coupling in van der Waals coupled heterostructures", in: Physical Review B, Handbook of Surface Science 99.*3* (7 Feb. 2019), ed. by N.V. Richardson and Stephen Holloway, p. 035420, ISSN: 1573-4331, DOI: https://doi.org/10.1016/B978-0-444-59526-3.00016-1, URL: https://www.sciencedirect.com/science/article/pii/B9780444595263000161.

[173] Etienne Lorchat et al., "Room-Temperature Valley Polarization and Coherence in Transition Metal Dichalcogenide–Graphene van der Waals Heterostructures", in: ACS Photonics, Handbook of Surface Science 5.*12* (7 Feb. 2018), ed. by N.V. Richardson and Stephen Holloway, pp. 5047–5054, ISSN: 1573-4331, DOI: 10.1021/acsphotonics.8b01306, eprint: https://doi.org/10.1021/acsphotonics.8b01306, URL: https://doi.org/10.1021/acsphotonics.8b01306.

[174] I. Paradisanos et al., "Prominent room temperature valley polarization in WS2/graphene heterostructures grown by chemical vapor deposition", in: Applied Physics Letters, Handbook of Surface Science 116.*20* (7 Feb. 2020), ed. by N.V. Richardson and Stephen Holloway, p. 203102, ISSN: 1573-4331, DOI: 10.1063/5.0002396, eprint: https://doi.org/10.1063/5.0002396, URL: https://doi.org/10.1063/5.0002396.

[175] G. Wang et al., "Polarization and time-resolved photoluminescence spectroscopy of excitons in MoSe2 monolayers", in: Applied Physics Letters, Handbook of Surface Science 106.*11* (7 Feb. 2015), ed. by N.V. Richardson and Stephen Holloway, p. 112101, ISSN: 1573-4331, DOI: 10.1063/1.4916089, eprint: https://doi.org/10.1063/1.4916089, URL: https://doi.org/10.1063/1.4916089.

[176] D. Basko et al., "Förster energy transfer from a semiconductor quantum well to an organic material overlayer", in: The European Physical Journal B - Condensed Matter and Comple Handbook of Surface Science 8.*3* (7 Apr. 1999), ed. by N.V. Richardson and Stephen Holloway, pp. 353–362, ISSN: 1434-6036, DOI: 10.1007/s100510050700, URL: https://doi.org/10.1007/s100510050700.

[177] David S. Hecht and Richard B. Kaner, "Solution-processed transparent electrodes", in: MRS Bulletin, Handbook of Surface Science 36.*10* (7 Feb. 2011), ed. by N.V. Richardson and Stephen Holloway, 749–755, ISSN: 1573-4331, DOI: 10.1557/mrs.2011.211, URL: https://www.sciencedirect.com/science/article/pii/B9780444595263000161.

[178] S Palleschi et al., “On the role of nano-confined water at the 2D/SiO2 interface in layer number engineering of exfoliated MoS2 via thermal annealing”, in: 2D Materials, Handbook of Surface Science 7.*2* (7 Feb. 2020), ed. by N.V. Richardson and Stephen Holloway, p. 025001, ISSN: 1573-4331, DOI: https://doi.org/10.1016/B978-0-444-59526-3.00016-1, URL: https://www.sciencedirect.com/science/article/pii/B9780444595263000161.

[179] Li Zhang et al., “Electrically driven single-photon emission from an isolated single molecule”, in: Nature Communications, Handbook of Surface Science 8.*1* (7 July 2017), ed. by N.V. Richardson and Stephen Holloway, p. 580, ISSN: 2041-1723, DOI: 10.1038/s41467-017-00681-7, URL: https://doi.org/10.1038/s41467-017-00681-7.

[180] Jascha Repp et al., “Molecules on Insulating Films: Scanning-Tunneling Microscopy Imaging of Individual Molecular Orbitals”, in: Phys. Rev. Lett., Handbook of Surface Science 94 (2 Jan. 2005), ed. by N.V. Richardson and Stephen Holloway, p. 026803, ISSN: 1573-4331, DOI: 10.1103/PhysRevLett.94.026803, URL: https://link.aps.org/doi/10.1103/PhysRevLett.94.026803.

[181] Pascal Anger, Palash Bharadwaj, and Lukas Novotny, “Enhancement and Quenching of Single-Molecule Fluorescence”, in: Phys. Rev. Lett., Handbook of Surface Science 96 (11 Mar. 2006), ed. by N.V. Richardson and Stephen Holloway, p. 113002, ISSN: 1573-4331, DOI: 10.1103/PhysRevLett.96.113002, URL: https://link.aps.org/doi/10.1103/PhysRevLett.96.113002.

[182] T. Matsui et al., “STS Observations of Landau Levels at Graphite Surfaces”, in: Phys. Rev. Lett., Handbook of Surface Science 94 (22 June 2005), ed. by N.V. Richardson and Stephen Holloway, p. 226403, ISSN: 1573-4331, DOI: 10.1103/PhysRevLett.94.226403, URL: https://link.aps.org/doi/10.1103/PhysRevLett.94.226403.

[183] Guohong Li and Eva Y. Andrei, “Observation of Landau levels of Dirac fermions in graphite”, in: Nature Physics, Handbook of Surface Science 3.*9* (7 Sept. 2007), ed. by N.V. Richardson and Stephen Holloway, pp. 623–627, ISSN: 1745-2481, DOI: 10.1038/nphys653, URL: https://doi.org/10.1038/nphys653.

[184] Kyle L. Seyler et al., “Signatures of moiré-trapped valley excitons in MoSe2/WSe2 heterobilayers”, in: Nature, Handbook of Surface Science 567.*7746* (7 Mar. 2019), ed. by N.V. Richardson and Stephen Holloway, pp. 66–70, ISSN: 1476-4687, DOI: 10.1038/s41586-019-0957-1, URL: https://doi.org/10.1038/s41586-019-0957-1.

[185] Fabian Cadiz et al., "Ultra-low power threshold for laser induced changes in optical properties of 2D molybdenum dichalcogenides", in: 2D Materials, Handbook of Surface Science 3.*4* (7 Oct. 2016), ed. by N.V. Richardson and Stephen Holloway, p. 045008, ISSN: 1573-4331, DOI: 10.1088/2053-1583/3/4/045008, URL: https://doi.org/10.1088/2053-1583/3/4/045008.

[186] Zheyuan Chen et al., "Energy transfer from individual semiconductor nanocrystals to graphene", in: ACS nano, Handbook of Surface Science 4.*5* (7 Feb. 2010), ed. by N.V. Richardson and Stephen Holloway, pp. 2964–2968, ISSN: 1573-4331, DOI: https://doi.org/10.1016/B978-0-444-59526-3.00016-1, URL: https://www.sciencedirect.com/science/article/pii/B9780444595263000161.

[187] François Federspiel et al., "Distance Dependence of the Energy Transfer Rate from a Single Semiconductor Nanostructure to Graphene", in: Nano Letters, Handbook of Surface Science 15.*2* (7 Feb. 2015), ed. by N.V. Richardson and Stephen Holloway, PMID: 25607231, pp. 1252–1258, ISSN: 1573-4331, DOI: 10.1021/nl5044192, eprint: https://doi.org/10.1021/nl5044192, URL: https://doi.org/10.1021/nl5044192.

[188] M. Fox, Optical Properties of Solids, ed. by N.V. Richardson and Stephen Holloway, vol. 4, Oxford Master Series in Physics, OUP Oxford, Feb. 2010, p. i, ISBN: 9780199573363, DOI: https://doi.org/10.1016/B978-0-444-59526-3.00016-1, URL: https://books.google.fr/books?id=K9YJ950kBDsC.

[189] JK Gimzewski et al., "Enhanced photon emission in scanning tunnelling microscopy", in: EPL (Europhysics Letters), Handbook of Surface Science 8.*5* (7 Feb. 1989), ed. by N.V. Richardson and Stephen Holloway, p. 435, ISSN: 1573-4331, DOI: https://doi.org/10.1016/B978-0-444-59526-3.00016-1, URL: https://www.sciencedirect.com/science/article/pii/B9780444595263000161.

[190] Jiaqi He et al., "Electron transfer and coupling in graphene–tungsten disulfide van der Waals heterostructures", in: Nature Communications, Handbook of Surface Science 5.*1* (7 Nov. 2014), ed. by N.V. Richardson and Stephen Holloway, p. 5622, ISSN: 2041-1723, DOI: 10.1038/ncomms6622, URL: https://doi.org/10.1038/ncomms6622.

[191] L Jiao et al., "Molecular-beam epitaxy of monolayer MoSe2: growth characteristics and domain boundary formation", in: New Journal of Physics, Handbook of Surface Science 17.*5* (7 May 2015), ed. by N.V. Richardson and Stephen Holloway, p. 053023, ISSN: 1573-4331, DOI: 10.1088/1367-2630/17/5/053023, URL: https://doi.org/10.1088/1367-2630/17/5/053023.

[192] Tobias Korn et al., "Low-temperature photocarrier dynamics in monolayer MoS2", in: Applied Physics Letters, Handbook of Surface Science 99.*10* (7 Feb. 2011), ed. by N.V. Richardson and Stephen Holloway, p. 102109, ISSN: 1573-4331, DOI: https://doi.org/10.1016/B978-0-444-59526-3.00016-1, URL: https://www.sciencedirect.com/science/article/pii/B9780444595263000161.

[193] Der-Hsien Lien et al., "Large-area and bright pulsed electroluminescence in monolayer semiconductors", in: Nature communications, Handbook of Surface Science 9.*1* (7 Feb. 2018), ed. by N.V. Richardson and Stephen Holloway, pp. 1–7, ISSN: 1573-4331, DOI: https://doi.org/10.1016/B978-0-444-59526-3.00016-1, URL: https://www.sciencedirect.com/science/article/pii/B9780444595263000161.

[194] Yanping Liu et al., "Recent Progress in the Fabrication, Properties, and Devices of Heterostructures Based on 2D Materials", in: Nano-Micro Letters, Handbook of Surface Science 11.*1* (7 Feb. 2019), ed. by N.V. Richardson and Stephen Holloway, p. 13, ISSN: 2150-5551, DOI: 10.1007/s40820-019-0245-5, URL: https://doi.org/10.1007/s40820-019-0245-5.

[195] M. Massicotte et al., "Picosecond photoresponse in van der Waals heterostructures", in: Nature Nanotechnology, Handbook of Surface Science 11.*1* (7 Jan. 2016), ed. by N.V. Richardson and Stephen Holloway, pp. 42–46, ISSN: 1748-3395, DOI: 10.1038/nnano.2015.227, URL: https://doi.org/10.1038/nnano.2015.227.

[196] K S Novoselov and A H Castro Neto, "Two-dimensional crystals-based heterostructures: materials with tailored properties", in: Physica Scripta, Handbook of Surface Science T146 (7 Jan. 2012), ed. by N.V. Richardson and Stephen Holloway, p. 014006, ISSN: 1573-4331, DOI: 10.1088/0031-8949/2012/t146/014006, URL: https://doi.org/10.1088%2F0031-8949%2F2012%2Ft146%2F014006.

[197] V Perebeinos, "Metal dichalcogenides: Two dimensions and one photon", in: Nature nanotechno Handbook of Surface Science 10.*6* (7 Feb. 2015), ed. by N.V. Richardson and Stephen Holloway, pp. 485–486, ISSN: 1573-4331, DOI: https://doi.org/10.1016/B978-0-444-59526-3.00016-1, URL: https://www.sciencedirect.com/science/article/pii/B9780444595263000161.

[198] C. Robert et al., "Optical spectroscopy of excited exciton states in $MoS_2$ monolayers in van der Waals heterostructures", in: Phys. Rev. Materials, Handbook of Surface Science 2 (1 Jan. 2018), ed. by N.V. Richardson and Stephen Holloway, p. 011001, ISSN: 1573-4331, DOI: 10.1103/PhysRevMaterials.2.011001, URL: https://link.aps.org/doi/10.1103/PhysRevMaterials.2.011001.

[199] Matthew R. Rosenberger et al., "Quantum Calligraphy: Writing Single-Photon Emitters in a Two-Dimensional Materials Platform", in: ACS Nano, Handbook of Surface Science 13.*1* (7 Feb. 2019), ed. by N.V. Richardson and Stephen Holloway, pp. 904–912, ISSN: 1573-4331, DOI: 10.1021/acsnano.8b08730, eprint: https://doi.org/10.1021/acsnano.8b08730, URL: https://doi.org/10.1021/acsnano.8b08730.

[200] S Schwarz et al., "Electrically pumped single-defect light emitters in WSe2", in: 2D Materials, Handbook of Surface Science 3.*2* (7 Feb. 2016), ed. by N.V. Richardson and Stephen Holloway, p. 025038, ISSN: 1573-4331, DOI: https://doi.org/10.1016/B978-0-444-59526-3.00016-1, URL: https://www.sciencedirect.com/science/article/pii/B9780444595263000161.

[201] R. S. Sundaram et al., "Electroluminescence in Single Layer MoS2", in: Nano Letters, Handbook of Surface Science 13.*4* (7 Feb. 2013), ed. by N.V. Richardson and Stephen Holloway, PMID: 23514373, pp. 1416–1421, ISSN: 1573-4331, DOI: 10.1021/nl400516a, eprint: https://doi.org/10.1021/nl400516a, URL: https://doi.org/10.1021/nl400516a.

[202] Junyong Wang, Ivan Verzhbitskiy, and Goki Eda, "Electroluminescent devices based on 2D semiconducting transition metal dichalcogenides", in: Advanced Materials, Handbook of Surface Science 30.*47* (7 Feb. 2018), ed. by N.V. Richardson and Stephen Holloway, p. 1802687, ISSN: 1573-4331, DOI: https://doi.org/10.1016/B978-0-444-59526-3.00016-1, URL: https://www.sciencedirect.com/science/article/pii/B9780444595263000161.

[203] Hong Wang et al., "Two-dimensional heterostructures: fabrication, characterization, and application", in: Nanoscale, Handbook of Surface Science 6 (21 Feb. 2014), ed. by N.V. Richardson and Stephen Holloway, pp. 12250–12272, ISSN: 1573-4331, DOI: 10.1039/C4NR03435J, URL: http://dx.doi.org/10.1039/C4NR03435J.

[204] Ruoyu Yue, "Molecular Beam Epitaxy Growth of Transition Metal Dichalcogenides", PhD thesis, The University of Texas at Dallas, Jan. 2017, p. i, DOI: https://doi.org/10.1016/B978-0-444-59526-3.00016-1, URL: https://www.sciencedirect.com/science/article/pii/B9780444595263000161.

[205] M Koperski et al., "Single photon emitters in exfoliated WSe2 structures", in: Nature nanotechnology, Handbook of Surface Science 10.*6* (7 Feb. 2015), ed. by N.V. Richardson and Stephen Holloway, pp. 503–506, ISSN: 1573-4331, DOI: https://doi.org/10.1016/B978-0-444-59526-3.00016-1, URL: https://www.sciencedirect.com/science/article/pii/B9780444595263000161.

[206] Yu-Ming He et al., “Single quantum emitters in monolayer semiconductors”, in: Nature nanotechnology, Handbook of Surface Science 10.*6* (7 Feb. 2015), ed. by N.V. Richardson and Stephen Holloway, pp. 497–502, ISSN: 1573-4331, DOI: https://doi.org/10.1016/B978-0-444-59526-3.00016-1, URL: https://www.sciencedirect.com/science/article/pii/B9780444595263000161.

[207] Santosh Kumar, Artur Kaczmarczyk, and Brian D Gerardot, “Strain-induced spatial and spectral isolation of quantum emitters in mono-and bilayer WSe2”, in: Nano letters, Handbook of Surface Science 15.*11* (7 Feb. 2015), ed. by N.V. Richardson and Stephen Holloway, pp. 7567–7573, ISSN: 1573-4331, DOI: https://doi.org/10.1016/B978-0-444-59526-3.00016-1, URL: https://www.sciencedirect.com/science/article/pii/B9780444595263000161.

Luis Enrique PARRA LOPEZ

# Tailoring the luminescence of atomically-thin semiconductors with sub-nanometer resolution.


## Résumé

Dans cette thèse, nous présentons une étude des propriétés optiques des hétérostructures de van der Waals avec une résolution sub-nanométrique. Pour y parvenir, nous utilisons une approche unique combinant des spectroscopies optiques résolues spatialement et temporellement. Nous utilisons ces techniques pour caractériser des hétérsotructures de van der Waals composées d'une monocouche de dichalcogénure de métaux de transition (TMD) coupleé à une ou plusieurs couches du graphène. Tout d'abord, nous montrons comment nous fabriquons ces hétérostructures. Ensuite, nous caractérisons en profondeur le couplage entre les couches de ces hétérostructures à basse température. Nous étudions ensuite la luminescence induite par une pointe de microscope à effet tunnel (STML) afin de sonder l'effet de l'environnement nanoscopique sur les propriétés optiques de nos échantillons. Ce travail met en évidence la richesse de la physique des hétérostructures de van der Waals et ouvre la voie à des études où des matériaux 2D peuvent être sondés à l'échelle atomique.


Mots-clés : spectroscopie de photoluminescence, STM, optoelectronique, STML, materiaux 2D, graphene, dicalcogenures de metaux de transition, heterostructures de van der Waals, transfert de charge, transfert d'énergie.


## Résumé en anglais

In this thesis, we present an investigation of the optical properties of van der Waals heterostructures with sub-nm resolution. To achieve this, we use a unique approach combining time- and spatially-resolved optical spectroscopies together with STM-induced luminescence (STML). We use these techniques to characterize van der Waals heterostructures made from a monolayer transition metal dichalcogenides (TMDs) coupled to graphene mono- or few-layers. First, we show how we fabricate these heterostructures. Then, we thoroughly characterize the interlayer coupling in various heterostructures at low temperatures. We then use STML to investigate the effect of the nanoscopic landscape on the optical properties of TMD-based heterostructures. This work sheds light on the rich physics in van der Waals heterostructures and paves the way for investigations where 2D-materials can be probed at the nanoscale.


Key words: Photoluminescence spectroscopy, STM, optoelectronics, STM-induced luminescence, two dimensional materials, graphene, transition metal dichalcogenides, van der Waals heterostructures, charge transfer, energy transfer.